Università degli
Studi di Genova

Doctorate in Sciences and Technologies of
Chemistry and Materials

UniGe
DCCI

PhD Thesis

UniGe
DIFAR

Spectroscopic techniques and chemometrics for the development of non-destructive analytical strategies for forensic, environmental and material analysis

Cycle: XXXVIII

Curriculum: Pharmaceutical, Food
and Cosmetic Sciences

Candidate: Sara Gariglio

Supervisors: Prof. Monica Casale
Dr. Cristina Malegori

A nonna Puccia,
che oggi sarebbe sicuramente stata
la più orgogliosa di tutti

ABSTRACT

The core of this PhD thesis explores how near-infrared (NIR) spectroscopy, when integrated with advanced chemometric and data-driven approaches, can overcome its traditional limitations and emerge as a powerful, multidimensional analytical tool in complex and unconventional contexts. By moving beyond the traditional view of NIR as a secondary or low-specificity technique, the work demonstrates how its capabilities can be expanded and adapted for complex, heterogeneous and non-traditional analytical scenarios.

The research begins by critically examining the hierarchical view that often governs the selection of spectroscopic techniques. Through forensic case studies on bloodstain ageing, near infrared (NIR), ultraviolet-visible (UV-Vis) and Raman spectroscopies are systematically compared across different substrates and environmental conditions. The findings do not reveal a hierarchy, but a complementarity between techniques. Experimental design and multivariate analysis of variance demonstrate that environmental parameters and substrate of deposition significantly influence ageing models, reinforcing the need for context-aware analytical strategies in forensic applications.

The thesis then extends NIR analysis into the spatial and temporal domain through the application of hyperspectral imaging (HSI) in the field of plant physiology and the ecology of non-vascular plants. In particular, HSI enables the visualisation of complex, non-linear moisture dynamics that depart from classical diffusion models when applied to the study of dehydration of epiphytic organisms, such as lichens and bryophytes. Pixel-based and image-based approaches reveal fine-scale heterogeneities and suggest biologically mediated drying behaviours, highlighting the potential of NIR-HSI in the study of living systems.

The most original contribution addresses a long-standing but poorly answered question: the penetration depth of NIR radiation in layered materials. Using custom 3D-printed stratified polymer systems, this work provides the first systematic, image-based and quantitative investigation of NIR-HSI penetration. Classical chemometric methods (principal component analysis, classical least squares, partial least squares) are integrated with convolutional neural networks to capture the complex, non-linear nature of radiation propagation. The results demonstrate that light can significantly penetrate under samples' surface, thus taking NIR-HSI forward from its classical surface-only interpretation and introducing the possibility of applying it as a 3D spectral tomography.

Overall, this thesis proposes a conceptual and methodological shift in NIR spectroscopy. By embracing complexity rather than reducing it, the work opens new perspectives for the application of NIR and hyperspectral techniques in forensic science, environmental analysis, materials science and beyond.

RIASSUNTO

Questa tesi di dottorato esplora come la spettroscopia nel vicino infrarosso (NIR), quando integrata con approcci chemiometrici avanzati, possa superare i suoi limiti tradizionali ed emergere come un potente strumento per risolvere problemi analitici complessi. Anziché trattare il NIR come una tecnica secondaria, il lavoro lo ricolloca nello scenario scientifico attuale, presentandolo come una piattaforma dinamica in grado di fornire informazioni dense di significato chimico e fisico.

Attraverso casi di studio forensi sull'invecchiamento delle macchie di sangue, le spettroscopie nel vicino infrarosso (NIR), nell'UV-visibile (UV-Vis) e Raman vengono confrontate in modo sistematico su vari substrati e in diverse condizioni ambientali. I risultati evidenziano una complementarità tra le varie spettroscopie presentate. L'uso di un disegno sperimentale associato a un'analisi multivariata della varianza dimostra che i parametri ambientali e il substrato di deposizione influenzano in modo significativo i modelli di invecchiamento delle macchie di sangue, rafforzando la necessità di strategie analitiche che tengano conto delle condizioni ambientali e contestuali nelle applicazioni forensi.

La tesi estende poi l'analisi NIR alla dimensione spaziale e temporale attraverso l'imaging iperspettrale (HSI). Applicato allo studio della disidratazione in comunità epifitiche (licheni e briofite), l'HSI consente la visualizzazione di dinamiche complesse di gestione dell'acqua tra diverse comunità epifitiche. Gli approcci pixel-based e image-based rivelano eterogeneità e suggeriscono che l'essiccamento di queste specie avvenga attraverso meccanismi biologici complessi, mettendo in evidenza il potenziale della NIR-HSI nello studio di sistemi viventi.

A seguire la tesi affronta una questione finora scarsamente studiata: la profondità di penetrazione della radiazione NIR associata ad HSI in materiali stratificati. Utilizzando sistemi polimerici multicomponente realizzati mediante stampa 3D, questo lavoro fornisce la prima indagine sistematica e quantitativa della penetrazione del NIR-HSI. Metodi chemiometrici classici (analisi delle componenti principali, minimi quadrati classici, minimi quadrati parziali) vengono integrati con le reti neurali, allo scopo di catturare la natura complessa e non lineare della propagazione della radiazione all'interno della materia. I risultati dimostrano che la luce è in grado di penetrare significativamente al di sotto della superficie dei campioni, portando l'HSI nel NIR a superare la sua classica interpretazione come tecnica esclusivamente superficiale e introducendo la possibilità di applicarla come una tomografia spettrale tridimensionale.

Nel complesso, questa tesi propone un cambiamento concettuale e metodologico nella spettroscopia NIR. Abbracciando la complessità anziché ridurla, il lavoro apre nuove prospettive per l'applicazione delle tecniche NIR e iperspettrali nella scienza forense, nell'analisi ambientale, nella scienza dei materiali e oltre.

SUMMARY

PREFACE

This PhD thesis critically re-evaluates and applies near-infrared (NIR) spectroscopy and hyperspectral imaging (HSI) in complex analytical scenarios. Traditionally considered a rapid but difficult to interpret technique, NIR spectroscopy is here reinterpreted as a powerful, information-rich approach capable of addressing challenging scientific questions when integrated with advanced chemometric data-driven methodologies. The thesis is built around the idea that the true potential of a spectroscopic technique does not reside solely in its instrumental configuration, but in the way data are interpreted, contextualised and combined.

Chapter 1 provides an overview of the state of the art in spectroscopy, with particular attention to NIR, ultraviolet-visible (UV-Vis) and Raman techniques. It discusses their physical principles, common applications and main limitations. The chapter then introduces the central research questions of the thesis, which concern three main themes: the complementarity of spectroscopic techniques in applied contexts, the potential of NIR-HSI for monitoring dynamic biological processes, and the largely unresolved issue of NIR penetration depth in layered and heterogeneous materials. These questions define the conceptual framework of the entire work.

Chapter 2 investigates the application of spectroscopy in a forensic context, focusing on the ageing of bloodstains with different spectroscopic techniques, on different substrates and under varying environmental conditions. A direct comparison of NIR with UV-Vis and Raman spectroscopies is performed to assess the strengths and limitations of each technique. In a first case study, UV-Vis and NIR spectroscopies are used individually and in combination to produce dating models for forensic bloodstains, demonstrating the potential of NIR spectroscopy in this research context. In a second case study, a systematic design of experiments is employed to evaluate the influence of temperature, humidity, illumination and substrate on spectral evolution, while regularised multivariate analysis of variance is used to statistically deconvolute their individual and combined effects. This chapter highlights the complementary nature of NIR, UV-Vis and Raman spectroscopies rather than establishing a rigid performance hierarchy among them.

In Chapter 3, the investigation moves from point-based spectroscopy to hyperspectral imaging (HSI) in the NIR region. NIR-HSI is applied in the field of plant physiology to the study of dehydration dynamics in epiphytic communities, consisting of lichens and bryophytes. This chapter explores the ability of hyperspectral techniques to capture both spatial and temporal variations in water content and distribution. By using multivariate analysis and a combination of image-based and pixel-based approaches, it reveals complex, non-linear drying behaviours that differ significantly from those observed in non-living materials. The results illustrate how NIR-HSI can be extended beyond traditional quantitative analysis to provide insights into dynamic biological and ecological processes, while also suggesting a complementary role of image-based and pixel-based approaches.

Chapter 4 addresses one of the least explored aspects of NIR-HSI: the penetration of radiation into matter. Custom-designed, 3D-printed stratified polymer samples are used to systematically investigate how NIR light propagates through multilayer systems of controlled thickness and composition. Classical chemometric methods such as principal component analysis, classical least squares and partial least squares are combined with convolutional neural networks to model both linear and non-linear aspects of the phenomenon. The findings demonstrate that NIR penetration depth is not a fixed value, but a conditional parameter governed by material properties, structural organisation and instrumental settings. This chapter proposes a novel, quantitative and reproducible framework for studying penetration in stratified media, with implications for a wide range of scientific fields.

Finally, Chapter 5 synthesises the key findings of the thesis and places them within a broader scientific context. The original contributions, methodological advances, limitations and future perspectives are discussed, emphasising the role of NIR spectroscopy and HSI as evolving tools at the interface of physics, chemistry and data science.

1 INTRODUCTION

In a world that moves at an ever-increasing pace, where tens of new food products, materials, and manufactured goods are developed and commercialised every day, analytical chemistry is required to respond to a growing demand for fast, versatile, and adaptable solutions [1]. The progressive acceleration of production cycles and decision-making processes has challenged traditional analytical workflows, emphasising the need for techniques capable of delivering reliable information within increasingly constrained timeframes [2]. In this context, the development of new high-throughput and flexible analytical tools has become a central objective of modern analytical chemistry [2].

To meet these evolving demands, a growing emphasis has been placed on analytical approaches capable of providing rapid and non-destructive access to chemical information [3]. Among these, spectroscopic techniques have emerged as particularly valuable tools [4,5], as they enable direct interrogation of matter through its interaction with electromagnetic radiation and provide direct insights with little to no sample preparation. Their ability to deliver rich, information-dense signals in short acquisition times has made spectroscopy a cornerstone of modern analytical science, especially in contexts where speed and versatility are critical [4,6]. Moreover, the high user-friendliness of spectroscopic instruments and interfaces makes them particularly suitable for use by non-specialised personnel in in-line and on-line configurations.

Being based on matter-radiation interaction, the choice of the incident wavelength(s) and of their intensity strictly determines the outcomes of an experiment. Indeed, several types of spectroscopic techniques have been historically developed, depending both on the specific wavelength ranges used for probing the analytes, and on the physical nature of the interaction between the sample and the radiation itself. As a result, the different types of spectroscopies, specifically ultraviolet–visible (UV–Vis), Raman, and infrared (IR), have often been considered as both complementary and counterposed, being each characterised by distinct strengths and inherent limitations [7–9]. It is, indeed, quite common in literature to find application papers where two different spectroscopic approaches are compared, in order to determine the “best” performing technique for the specific use. However, the comparison between different spectroscopic techniques should go beyond simple analytical performance [8,10–12], also offering insight into how information is generated, encoded, and extracted from matter. Therefore, comparisons should not just focus on instrumental features but encompass the relationship between the physical origin of the signal and the methods used to interpret it as well. A careful, data-informed comparison of the various techniques may indeed provide a clearer understanding of their respective roles in modern analytical chemistry and highlight opportunities for applying each method in non-conventional contexts.

Spectroscopic data come with an intrinsic richness of information, enclosed in peaks, bands and complex signals. Indeed, rather than delivering isolated analytical parameters, spectroscopic techniques generate complex data structures containing a wealth of chemical and physical information [13]. This represents a major advantage since it allows a comprehensive understanding of several features of the sample within a single analysis. Indeed, the increase in the amount of information present in the data widens their potential exploitability, while also introducing significant challenges in terms of interpretation and information extraction [14]. In particular, spectroscopic outcomes must be appropriately disentangled to be fully exploited [15]. For this reason, for a long time this characteristic was considered a limitation of spectroscopic techniques, as it required the statistical treatment of potentially large data matrices, associated with high computational demands and the need for specialised data handling strategies [15,16]. As a consequence, spectroscopy has historically been regarded with a certain degree of caution. In the current era of big data [2], however, this same complexity is increasingly seen not as a drawback but as a valuable source of analytical insight [17,18].

Within this framework, near-infrared (NIR) spectroscopy emerges as a paradigmatic example of a technique where the true analytical potential can only be fully appreciated through advanced data-driven interpretative strategies. At the same time, it represents one of the most emblematic examples of a technique whose complexity has often been mistaken for a limitation, while it actually embodies an extraordinary, yet still partially unexplored, analytical potential [19,20].

Indeed, NIR spectroscopy has long occupied an ambiguous position within the spectroscopic landscape [21]. Despite its intrinsic advantages in terms of speed and ease of use, it has often been perceived as a secondary technique, limited by broad, overlapping absorption bands and reduced chemical selectivity when compared to mid-infrared or Raman spectroscopy [22]. This perception has contributed to a historical underestimation of the true informational content encoded within NIR spectra, frequently relegating the technique to rapid screening applications rather than treating it as a fully-fledged analytical tool [23].

Over the last decades, NIR spectroscopy has undergone a profound transformation, driven by advances in instrumentation, optoelectronics, and computational power [20,22]. Modern NIR systems are no longer confined to laboratory environments, but are increasingly implemented in portable, handheld, and in-line configurations, broadening the range of possible applications [20,24–26]. In parallel, improvements in detector sensitivity and spectral resolution have progressively enhanced the quality of NIR data, allowing more subtle chemical and physical variations to be captured and exploited [27].

The present thesis is grounded in the conviction that the limitations traditionally attributed to NIR spectroscopy are not intrinsic to the technique itself, but rather arise from how NIR data are interpreted. Indeed, the rich, albeit highly convoluted, spectral signatures characteristic of the near-infrared region contain a level of chemical information that becomes accessible only through appropriate mathematical and multivariate approaches [28–30]. From this perspective, NIR spectroscopy should not be viewed merely as a complementary or rapid alternative to more established techniques, but as a versatile and powerful analytical platform whose full potential is unlocked through the integration of advanced data processing strategies.

Building on the considerations outlined above, the present thesis aims to explore the potential of near-infrared (NIR) spectroscopy as a versatile analytical platform capable of addressing complex chemical questions across different application domains.

The work is guided by three overarching and interconnected objectives, that are here presented and will be reconsidered in the General conclusions chapter.

First, NIR spectroscopy is critically evaluated in comparison with other spectroscopic techniques, such as UV-Vis and Raman. This comparison is held not only in terms of instrumental performances, but with a particular focus on how chemical information is encoded within the raw spectral data and the strategies required for its interpretation. This comparative approach is intended to highlight the relative strengths and limitations of each technique, as well as to identify scenarios in which NIR may offer unique advantages, challenging the traditional hierarchies of analytical methods. This comparison illustrates the potential of integrating different spectroscopic techniques into a unified analytical framework [3], where complementary approaches work together to provide a comprehensive characterization of all chemical and physical properties of a sample. Rather than selecting a single “best-performing” technique for each application, this strategy can simultaneously enhance analytical outcomes, improving sensitivity, precision, robustness, and reliability, while also deepening the chemical understanding of the analytical problems by approaching them from multiple perspectives at once.

Second, this thesis focuses on pushing the application of spectroscopic techniques, and in particular of NIR hyperspectral imaging (NIR-HSI), forward from the identification, quantification, and characterisation of chemical constituents to the possibility of describing and capturing chemical, biological and physical processes in a dynamic way. Through the development and application of multivariate and data-driven approaches that enable the extraction of meaningful chemical information from the complex NIR spectral signatures, the thesis seeks to demonstrate how the apparent complexity of NIR data can be turned into a powerful source of insight, pushing spectroscopic techniques outside the typical boundaries in which they have been historically confined. The final goal is to drive NIR spectroscopy forward from the classical applications for moisture quantification or specific analytes prediction, presenting it as a complete, versatile technique capable of providing invaluable insights even in complex situations where multiple processes might be happening at the same time.

As a third and final objective, the present thesis intends to demonstrate the applicability and versatility of NIR spectroscopy in non-conventional contexts, such as the underexplored aspects of radiation-matter interaction. This topic potentially allows for a significant broadening of the possible application fields for NIR spectroscopy, and it emphasises the practical impact of the work, that aims to reposition NIR as a fully-fledged analytical platform, capable of delivering results that are both scientifically rigorous and operationally efficient.

To provide a comprehensive and solid foundation for the studies presented in this thesis, the following sections of this introductory chapter will review the principles and characteristics of the spectroscopic techniques addressed, with particular emphasis on NIR spectroscopy and its integration with multivariate analytical approaches.

1.1 SPECTROSCOPIC TECHNIQUES

The interaction between electromagnetic radiation and matter represents the foundation of all spectroscopic techniques [31,32]. As a general overview, when a sample is exposed to light, a portion of the incident radiation may be absorbed, transmitted, scattered, re-emitted, or a combination of these [33]. The response of matter to radiation strictly depends both on the energy of the incoming photons and on the electronic, vibrational, or rotational states of the molecules involved [34,35]. As a consequence, each of these processes encodes specific chemical and physical information, which can be accessed and interpreted through appropriate experimental and analytical strategies, and which can therefore be exploited to resolve analytical problems and answer analytical questions.

In particular, absorption occurs when the energy of the incident photons matches the energy gap between two molecular states in the analytes, leading to transitions at the electronic, vibrational, or rotational levels. Electronic transitions, typically probed in the UV-Vis regions, provide information on chromophores and conjugated systems [36–38], while vibrational transitions, primarily explored in the IR and Raman regions, reveal details about molecular bonds, functional groups, and symmetry [39,40]. Scattering phenomena, including Rayleigh and Raman scattering, which convey information on polarizability and electronic structure of molecules, with Raman in particular allowing the characterisation of molecular vibrations and interactions even in transparent or weakly absorbing media [41]. On the other hand, emission, which refers to, for instance, fluorescence spectroscopy, will not be treated in this thesis, and will therefore not be further mentioned.

The wavelength-dependent response typical of each sample represents therefore a complex fingerprint of the unique chemical composition and structure of the specimen under analysis. The richness of this information, while offering powerful analytical potential, also demands careful interpretation, often requiring the integration of multivariate approaches to extract meaningful insights from overlapping or convoluted signals [28]. Understanding these fundamental interactions is essential to rationalise the choice of spectroscopic technique, to understand complementary features between techniques, and to design experiments that maximise information content while minimising limitations and artifacts.

1.1.1 Probing electronic transitions: UV-Vis spectroscopy

UV–Vis spectroscopy is based on the absorption of photons in the ultraviolet (~200–400 nm) and visible (~400–800 nm) regions of the electromagnetic spectrum, corresponding to electronic transitions within molecules [42,43]. In particular, when a molecule absorbs light in this region, electrons are promoted from occupied molecular orbitals to higher-energy unoccupied orbitals, typically involving π→π* or n→π* transitions in conjugated systems or functional groups [32,44]. The energy and intensity of these transitions are highly sensitive to the chemical environment, providing selective information about specific chromophores [42].

Due to its ease of use, reduced costs, and intuitiveness, UV–Vis spectroscopy has found widespread applications in both qualitative and quantitative analyses [45]. In particular, its strict dependence on the Beer-Lambert law, regulating the direct relation between radiation absorption and analyte concentration, ensured a widespread application of this technique across several fields of chemistry. UV-Vis spectroscopy is therefore commonly employed for the determination of known analytes' concentration, monitoring reaction kinetics, assessing sample purity, and detecting specific analytes in a solution [46]. The simplicity of sample preparation, combined with the availability of robust and relatively inexpensive instrumentation, has contributed to its pervasive use in chemical, biochemical, and industrial laboratories [44].

Despite these advantages, UV–Vis spectroscopy also presents limitations. Its sensitivity is often restricted to molecules containing suitable chromophores, and overlapping electronic transitions can complicate spectral interpretation. Intuitively, the Vis spectrum of a sample largely mirrors its colour, and it is therefore easy to understand that the co-presence of analytes with similar colours in the same sample hinders interpretability and sensitivity of the technique [44]. Additionally, UV-Vis spectroscopy provides limited structural information, as it does not directly probe vibrational or rotational states.

These constraints highlight the necessity of combining this strategy with complementary techniques presenting highly characteristic spectral signatures, such as IR or Raman spectroscopies, in order to obtain a more comprehensive characterisation of the molecular systems under analysis [32]. In this perspective, UV–Vis can be viewed as a fast and selective tool for probing specific electronic features, forming a foundational layer of analytical information that can be integrated with vibrational data for a more complete understanding of complex samples and to resolve interference issues [32].

1.1.2 The power of vibrations: IR and Raman spectroscopies

Vibrational spectroscopy encompasses techniques that probe the quantised vibrational energy levels of molecules, providing detailed information about chemical bonds, functional groups, and molecular structure as well. Mid-IR (MIR, 2500-25,000 nm or 4000-400 cm^{-1}) spectroscopy is based on the absorption of photons whose energy matches vibrational transitions of polar bonds, resulting in characteristic absorption bands. Each functional group within a molecule has a predictable vibrational signature, allowing both qualitative identification and quantitative analysis of polar analytes [47].

Raman spectroscopy, on the other hand, relies on inelastic scattering of photons, the Raman effect, precisely, rather than direct absorption. When an intense beam of monochromatic light interacts with a molecule, a small fraction of it is scattered back with a shift in energy corresponding to vibrational transitions. For its physical nature, Raman is sensitive also to non-polar bonds, given that they are characterised by a good polarizability, that are on the contrary weak or inactive in the MIR spectrum, making the two techniques highly complementary by nature [7,9].

Both MIR and Raman spectroscopy offer high chemical specificity and structural insight, making them invaluable for detailed molecular characterisation [47]. They are widely applied in fields ranging from organic and inorganic chemistry to materials science, food analysis, pharmaceuticals, and environmental monitoring. However, vibrational techniques also present practical limitations. In particular, MIR spectroscopy sometimes requires careful sample preparation, since solid samples need to be included in MIR-transparent supports (KBr) for transmission/absorption measurement, or samples may need to be pulverised to be used in the attenuated total reflectance (ATR) configuration [13]. Moreover, MIR spectra can be affected by water absorption, which might act as an interferent when the focus is not on the moisture content of the specimen. On the other hand, Raman signals are intrinsically weak, deriving from low-probability interactions, and may additionally suffer from fluorescence interference [48]. These constraints suggest the need of combining these vibrational techniques with other spectroscopic modalities, such as UV–Vis and NIR, to obtain a comprehensive understanding of complex samples.

By providing complementary perspectives on molecular structure [48], MIR and Raman spectroscopies set the stage for integrating vibrational information with UV-Vis and NIR data, ultimately enhancing the depth and reliability of chemical analyses.

1.1.3 A key player: NIR spectroscopy

NIR spectroscopy probes the interaction of matter with electromagnetic radiation in the approximate range 780–2500 nm (12,800–4000 cm^{-1} in wavenumber) [49]. Unlike UV-Vis, which is dominated by electronic transitions, or MIR, which primarily involves fundamental vibrational modes, NIR spectra arise largely from overtones and combination bands of fundamental vibrations. In particular, NIR absorption primarily depends on overtones and combination bands of vibrational modes associated with X–H bonds (C–H, O–H, N–H). These transitions are inherently weaker than fundamental vibrations in the MIR region, resulting in broad, overlapping spectral features [49,50] rather than sharp, distinctive peaks. While this lower resolution can complicate direct interpretation, it also allows rapid acquisition of bulk sample information. The resulting spectral signatures are highly information-dense, encoding contributions from multiple chemical groups and interactions simultaneously, therefore they carry rich chemical information that can be exploited for qualitative and quantitative analysis [50].

The NIR region occupies a unique position in the electromagnetic spectrum, namely between visible and IR radiations, thus bridging electronic and vibrational spectroscopy. This enables the technique to probe both molecular composition and certain structural or physical properties of the sample, often with minimal sample preparation. Combined with modern instrumentation capable of rapid, non-destructive measurements, these characteristics make NIR spectroscopy particularly well-suited for high-throughput and in-line analytical applications [26]. Indeed, NIR spectroscopy combines several practical advantages that complement its informational content. Measurements are typically fast, often requiring only a few seconds per sample, and are non-destructive, preserving the integrity of the analysed material [26]. The technique is compatible with a variety of sample forms, including solids, liquids, and powders, and modern instrumentation ranges from benchtop to portable or in-line systems [25]. This versatility, coupled with minimal sample handling, renders NIR an ideal tool for high-throughput screening, process monitoring, and applications where rapid feedback is essential.

As previously commented, historically NIR spectroscopy was often viewed as a secondary or auxiliary technique, limited by overlapping bands and relatively low selectivity compared to MIR or Raman methods [23]. It is indeed important to acknowledge that NIR spectroscopy is not exempt from intrinsic limitations that must be critically analysed. The broad and overlapping nature of NIR absorption bands reduces spectral specificity when compared to MIR or Raman techniques, and weak absorptivity can limit sensitivity for certain analytes. Furthermore, NIR spectra are strongly affected by physical factors such as particle size, scattering, temperature, and matrix composition, which may introduce non-linearities and confounding effects [19]. Nevertheless, rather than representing intrinsic weaknesses of the technique itself, these aspects highlight the need for advanced data interpretation strategies [20]. When properly modelled, the physical and chemical contributions embedded in NIR spectra can be disentangled and exploited separately and co-ordinately as valuable complementary sources of analytical information. By leveraging data-driven interpretation, NIR can provide detailed insights into chemical composition, structural features, and even dynamic processes, effectively repositioning it as a primary analytical tool rather than a mere rapid-screening method [13]. This perspective opens new possibilities for its application across diverse scientific and industrial contexts.

1.1.4 Hyperspectral imaging

Building on the principles of point-based spectroscopies, hyperspectral imaging (HSI) represents a natural and innovative extension, capturing not only the chemical information at each measurement point but also its spatial distribution across the sample [22]. This approach transforms spectroscopy from a purely point-based technique into a powerful imaging tool, capable of revealing heterogeneity and complex interactions within a sample [51]. Hyperspectral imaging systems can be associated to different spectroscopic modalities, such as UV-Vis, NIR, MIR and Raman. In this thesis, the focus will revolve around NIR-HSI, which has demonstrated significant potential in fields ranging from material characterisation to pharmaceutical, food and forensic applications [22,52,53]. However, it remains a relatively underexploited technique, offering new opportunities for high-dimensional analysis and the exploration of sample heterogeneity in ways that conventional NIR cannot achieve.

The combination of spectroscopy and imaging produces a three-dimensional dataset commonly referred to as a hypercube [54], a rich, multidimensional dataset that encodes both spectral and spatial information. From an instrumental perspective, this information can be acquired in different ways. In particular, three main acquisition strategies are commonly recognised: point-scanning (whiskbroom), line-scanning (pushbroom), and snapshot imaging systems [55]. In whiskbroom configurations, a single spatial point is analysed at a time, and a full spectrum is acquired sequentially for each pixel by mechanically scanning the sample in two spatial dimensions. While this approach offers high spectral fidelity and flexibility, it is intrinsically slow and therefore poorly suited for dynamic processes or large-area imaging [55]. Pushbroom systems, by contrast, acquire an entire spatial line simultaneously across all wavelengths, reconstructing the hyperspectral cube through the relative motion between the sample and the imaging system. Owing to their favourable compromise between acquisition speed, spectral resolution, and signal-to-noise ratio, pushbroom instruments represent the most widely adopted configuration for NIR-HSI, particularly in industrial and in-line applications [55]. Finally, snapshot imaging systems capture the full hyperspectral data cube in a single exposure, without the need for mechanical scanning. Although this strategy enables extremely fast acquisitions, it typically involves trade-offs in terms of spatial resolution, spectral resolution, or field of view [55], which may limit its applicability in high-precision analytical contexts.

Beyond acquisition geometry, the performance of an HSI system is strongly influenced by additional instrumental components, including illumination sources and detectors. In NIR-HSI, broadband halogen lamps are most commonly employed, providing stable and continuous illumination across the spectral range of interest, albeit at the cost of potential heating effects and non-uniform illumination [22]. Detector technology further plays a critical role, with InGaAs arrays representing the standard choice for NIR-HSI due to their sensitivity and robustness in the relevant wavelength range [56]. The interplay between these instrumental elements ultimately determines key performance parameters, such as spectral resolution, spatial resolution, signal-to-noise ratio, and acquisition speed, all of which must be carefully balanced according to the specific analytical objective.

Consequently, the choice of HSI instrumentation is not merely a technical detail, but a fundamental experimental decision that directly shapes the quality of the information encoded within the hyperspectral data.

However, regardless of the chosen strategy for data acquisition, the resulting hyperspectral image contains a full spectrum for each pixel, resulting in large, complex data matrices that require careful handling, pre-processing and processing [57]. The richness of hyperspectral data therefore comes with new analytical challenges. The high dimensionality and the strong collinearity inherent to spectra demand the use of chemometric methods for visualisation, pattern recognition, and quantitative modelling [57]. At the same time, hyperspectral imaging presents unique opportunities, enabling spatially resolved chemical mapping, identification of localised heterogeneities, and the investigation of dynamic or complex processes that would be difficult to study with point-based spectroscopy.

Within the data cube generated by HSI, one of the central challenges is how to exploit the spectral information contained in each pixel. Over the years, three main strategies for the analysis of hyperspectral data have been developed, namely image-based, pixel-based and object-based approaches [58,59]. These strategies are sometimes presented as complementary [60], while in other cases they are treated as mutually exclusive [61], evidencing an ongoing debate on how to most effectively exploit the complex information embedded in hyperspectral data cubes.

The image-based approach is grounded in the idea that an image can be considered as a form of massively replicated sampling [58]. Within this framework, each pixel is treated as a replicate measurement of the same sample represented by the entire image, and pixel level information is typically extracted and condensed into a unique descriptor representative of the whole image. This descriptor may be an average signal, a median signal, or even the outcome of multivariate data processing strategies, such as scores and/or loadings of a principal component analysis. This strategy offers several advantages, including the ability to condense in a single signal information from different areas of a sample, improve the spectral description of extended sample, and significantly reduce noise, thereby enhancing sensitivity compared to point-based spectroscopy. In addition, by collapsing the hyperspectral data cube into a conventional two-dimensional data matrix, the image-based approach enables the use of well-established chemometric workflows originally developed for point spectroscopy. Nevertheless, this strategy has been widely criticised for its limited exploitation of the information content of hyperspectral data. The process of extracting a single descriptor inherently smooths out local spectral extremes, effectively discarding the contribution of highly diverse pixels. While this may be advantageous for truly homogeneous samples, where extreme pixels often correspond to spectral artefacts, it represents a clear limitation when spatial heterogeneity carries chemically relevant information. Most importantly, this approach largely neglects the spatial dimension, which is one of the defining strengths of HSI.

In contrast, the pixel-based approach is founded on the assumption that each pixel within one image can be treated as an independent analytical sample [58]. This perspective preserves local variability and fully exploits the spatial information encoded in the hyperspectral cube. The approach is particularly powerful for heterogeneous systems, where subtle spatial differences may be chemically meaningful, but it also shows potential for nominally homogeneous samples. Indeed, the possibility of treating each pixel as an individual sample results in an unprecedented increase in effective sampling density, often yielding several thousands of spectra from a single image acquired in seconds. This increased sampling density is invaluable for the application of data-driven machine learning tools, which require huge amounts of data to be efficiently trained. However, this strategy is not without limitations. The assumption of contiguous pixel independence is frequently violated in practice, since most HSI systems rely on diffuse illumination sources (*e.g.,* halogen lamps), which can induce shadowing and scattering effects, especially on non-flat or irregular surfaces. These phenomena cause spatial mixing of spectral information, introducing correlations between neighbouring pixels and undermining the conceptual independence of individual measurements. Moreover, the indiscriminate inclusion of all pixels may propagate noisy or aberrant spectra into subsequent analysis. Finally, the pixel-based paradigm generates extremely large datasets, often comprising tens or hundreds of thousands of spectra per image, with the data volume increasing rapidly as the number of analysed images grows, posing significant computational and statistical challenges.

Within this context, the object-based approach emerges as an intermediate strategy [59]. This method consists of segmenting the hyperspectral image into meaningful regions, the objects, and subsequently treating each object as a single analytical entity using an image-based logic. Often, objects represent individual small samples present in the same image capture, while only rarely they represent different regions of interest of a single bigger sample. In any case, this approach allows a more refined exploitation of spatial information by simultaneously considering multiple regions of the same image, while still benefiting from dimensionality reduction and noise averaging. However, although object-based analysis represents a compromise between global averaging and fully pixel resolved analysis, it does not completely overcome the limitations associated with the image-based approach, as the intra-object variability is still largely suppressed during the averaging process.

As a result, none of the currently established strategies fully resolves the fundamental trade-off between spectral robustness, spatial resolution, and computational burden, leaving open a critical methodological gap in the effective exploitation of hyperspectral data. However, rather than identifying the existence of a single “optimal” strategy, the coexistence of image-based, pixel-based and object-based approaches highlights a more profound conceptual issue: hyperspectral data do not admit a unique, privileged representation. Each analytical perspective emphasises different aspects of the same physical reality, encoding complementary layers of chemical and structural information [60].

In this perspective, the present thesis does not seek to identify a universally superior paradigm, but rather to demonstrate that the real analytical power of HSI emerges from the coherent integration of these different viewpoints, which might be better regarded as synergistic rather than alternative. By systematically applying and comparing these frameworks across different case studies, this work therefore investigates how a multi-perspective interpretation of hyperspectral data may provide a richer, more robust, and chemically meaningful description of complex samples than any individual approach considered in isolation.

1.2 CHEMOMETRICS

The increasing richness and complexity of spectroscopic data, as well as their inherent multidimensional nature, make it evident that instrumental advances alone are not sufficient to fully exploit the chemical information encoded within spectral measurements, as already widely pointed out along this introductory chapter. As spectroscopic techniques evolve from simple signal generators to high-content analytical platforms, the role of data interpretation becomes central. In this context, chemometrics emerges not as an auxiliary computational tool, but as an integral part of the spectroscopic measurement itself, providing the conceptual and mathematical framework through which raw signals are transformed into chemically meaningful information.

Traditionally, as the word itself suggests, chemometrics has been rooted in a chemistry-driven vision of data analysis, where mathematical models are designed to represent, as much as possible, the underlying physicochemical structure of the system under investigation [62–64]. Classical multivariate methods, such as principal component analysis (PCA) and partial least squares (PLS) regression, have been developed not only for their predictive performance, but also for their interpretability, allowing the analyst to establish meaningful connections between spectral features and chemical phenomena. This emphasis on interpretability has long represented one of the defining strengths of classical chemometrics, enabling the training of models that do not merely predict, but also explain the information enclosed in the data [65,66].

However, it is crucial to acknowledge that the scientific landscape is rapidly changing also in this regard. The present thesis is positioned at the beginning of one of the most significant transitional phases for the field, arguably the most profound transformation in data analysis since the expansion of computational capabilities in the 1960s and then again in the late 1990s. These modern developments are progressively blurring the traditional boundaries between classical, chemistry-based chemometrics and the emerging paradigm of data-driven and deep learning approaches [67,68].

This topic remains highly controversial, with the scientific community divided between those who argue that deep learning, due to its limited interpretability, should not be considered as part of chemometrics [69] but rather of data science, since it betrays the original nature of chemometric approaches, which are rooted in extracting chemical meaning from data. On the other hand, there are those scientists who regard machine learning models as a natural extension of data-driven statistical analysis [70], and therefore as legitimate tools within the chemometric toolbox. This idea has been at the basis of the modern trend in machine learning algorithm development towards what is defined as “interpretable machine learning”. Regardless of one’s position within this debate, it is no longer possible to extricate modern chemometrics from this evolution, which is expected to become increasingly dominant as the volume and complexity of analytical data continues to grow.

In line with both the natural progression of personal scientific training and the temporal evolution of the field itself, the early stages of this thesis were strongly grounded in the consolidation of classical multivariate strategies, with a particular focus on model robustness, transparency, and chemical interpretability. The final part of the thesis, however, moves towards the exploration of modern deep learning frameworks, where modelling shifts towards a more mathematically driven perspective. Rather than representing a discontinuity, this transition is treated here as a conceptual evolution, in which the strengths of traditional chemometric thinking are deliberately carried into the deep learning domain. In this view, the work aims to contribute to the development of analytical models that combine the explanatory power of chemistry-based approaches with the flexibility and representational capacity of modern machine learning.

2 FORENSIC APPLICATIONS

The primary function of forensic sciences is to assist decision-makers in quantifying the nature of a criminal act and subsequently enabling informed decision-making based on the evaluation of evidence. However, it is insufficient to merely observe the forensic traces for them to attain relevance. Indeed, the crucial role of forensic practitioners is to assign the appropriate significance to these pieces of evidence through their decoding and understanding using specialised knowledge [71] and to communicate these results comprehensibly to non-scientists, such as judges or attorneys [72].

In the particular case of blood traces, the situation is analogous. It is widely acknowledged that blood is a crucial evidence in the field of forensic science, and its role has become even more important in recent decades due to the substantial advancements in DNA extraction, amplification, and sequencing [73]. However, in order to fully comprehend the significance of blood traces discovered at the scene and/or on objects involved in the incident, and to accurately estimate the value of the findings, it is imperative to verify whether these traces are related to the considered act of violence. The simple presence of bloodstains, and even the subsequent genetic analysis which may be used to associate them with a specific individual, may not be sufficient evidence in itself. This is because the circumstances of the formation of the analysed traces, and precisely the time of their creation, may often be questioned. Hence, ascertaining whether these traces were formed during the commission of the crime is frequently of paramount importance. It is possible to accomplish this aim by answering the question about the time elapsed since bloodstains deposition (TSD). The determination of the TSD of bloodstains is, indeed, a critical aspect of forensic practice, as it provides valuable information about the chronology of events at a crime scene. Specifically, it can either inform on the time frame in which a crime was committed or determine whether a blood trace from a suspect was created before, during, or after the criminal event. Consequently, it could assist prosecutors in establishing the innocence or culpability of a suspect [74].

The issue of bloodstains age is a well-established area of research in forensic science, with the initial attempts to establish the TSD dating back to the early 20th century [75]. A number of approaches have been posited to address this issue, including the quantification of RNA degradation [76,77], the evaluation of aspartic acid racemisation rate [78], the study of the circadian hormones [79], the assessment of enzyme activity [80], and the measurement of fluorescence lifetime [81,82]. A range of analytical techniques have been utilised in the attempt to identify a suitable method for estimating the age of bloodstains. These techniques include high-performance liquid chromatography (HPLC) [83,84], electron paramagnetic resonance (EPR) [85], immunoelectrophoresis [86], and atomic force microscopy [87]. Nevertheless, it should be noted that the aforementioned techniques are all time-consuming and require sample preparation, which in turn causes the destruction of the specimen under analysis. Consequently, they are not optimal for the forensic practice, which demands timely, on-scene, and repeatable analysis.

In this framework, spectroscopic techniques offer several significant advantages, including their rapidity, reproducibility, non-contact and non-destructive nature. Furthermore, these techniques have the potential to be rendered portable to a certain extent, and research in this area is progressing rapidly. Comprehensive reviews, including those by Bremmer *et al.* [88] as well as Zadora and Menżyk [89], have extensively delved into the ageing process of bloodstains and the spectroscopic techniques developed to ascertain their TSD; hence, they should serve as a fundamental source of information on this matter.

Ultraviolet-visible (UV-Vis) spectroscopy was arguably the primary and most extensively investigated technique employed by scientists to study the TSD of bloodstains [89], given that blood undergoes a colour change when exposed to air. This technique has been applied in both short (2 days [90]) and long (200 days [91]) time frames, with satisfactory results. Another well-studied technique is Raman spectroscopy, which has proven to be very precise and robust over short time periods [92], though it is less efficient for TSD larger than a couple of weeks due to increased sample fluorescence. The technique was further advanced by Menżyk et al [93], who proposed a strategy to overcome the sample degradation issue due to laser exposure. In addition, infrared (IR) spectroscopy was investigated as a possible technique for bloodstain dating as well, thanks to the medium infrared (MIR) spectroscopy capability to identify functional groups and changes in protein structure. This technique was primarily investigated in the attenuated total reflection (ATR) mode and has been demonstrated to be effective over medium to long time periods (ranging from two to six months from deposition) [94]. NIR spectroscopy may also prove useful in this context, since it can describe both protein structure and water evaporation, the two main processes which characterise blood ageing. However, the potential of this wavelength range has been investigated just in a limited number of studies [95–97].

Despite the various attempts that have been described, no single method nor the combination of several solutions has been universally adopted by the forensic community. This protracted impasse may be partially attributed to the fact that most of the proposed solutions have been presented through a purely scientific/analytical approach rather than through the perspective of forensic sciences. In other words, the models for blood dating were developed usually in laboratory conditions as a universal tool to solve the issue of time, overlooking the fact that forensic science is not as extrapolative as, for example, analytical chemistry, where a result can be predicted when setting up an experiment and developing a regression model. Rather, forensic science is retrodictive and contextual, and should be treated as such also in research. In particular, in the case of bloodstain dating, circumstantial characteristics which differ between one crime scene and the next – here primarily understood as the environmental conditions at the crime scene – render each particular case somewhat unique. Consequently, it is reasonable to hypothesise that they will be highly significant in determining the course and rate of blood degradation processes and thus will influence the sought-after answer: the bloodstain age.

In recent years, however, an alternative approach to address the dating challenge has been suggested, proposing a comprehensive shift in perspective [93,98,99]. The hypothesis under consideration is that the challenges stemming from the variability in aging kinetics can be mitigated by replacing the conventional dating methodology, which implies the comparison of each new sample to a global validated model, as briefly described above, with a case-specific comparative analysis. The fundamental concept underpinning this approach involves the assessment of the (dis)similarity between the stage of evidence decomposition and sets of reference materials, namely bloodstains obtained through supervised aging, with the objective of recreating the degradation conditions at the crime scene with the utmost accuracy. This suggests that each dating procedure would be customised for specific cases, with the objective of accommodating the unique characteristics of the examined traces. Consequently, this approach seeks to diminish the impact of external factors, such as environmental conditions and substrate nature, on the validity of the analysis to a significant degree. Nevertheless, the implementation of this tactic remains contingent upon the development of a methodology that facilitates the characterisation of the degree of degradation present in both the evidential and comparative bloodstains.

The present chapter of this thesis fits into the presented research topic, and in particular it articulates in two distinct but consecutive case studies that aim to answer the following crucial questions in bloodstain dating research:

1. Is NIR spectroscopy capable of effectively monitoring the process of blood degradation during the ageing process, thereby providing satisfactory dating models?
2. How do NIR spectroscopy performances compare with those of the most commonly used spectroscopic techniques in this field, *i.e.* UV-Vis and Raman spectroscopies?
3. Is the combination of different spectroscopic techniques a possible approach for enhancing the precision of bloodstains dating performances?
4. Is it possible to evaluate the effect of environmental conditions and substrate of deposition on the bloodstains ageing kinetics?
5. Is the effect of environmental conditions and substrate of deposition universal, or rather does each factor exert a distinct influence on each spectroscopic technique?

The present chapter concludes with a final section that draws upon the innovative perspective derived from the results presented and discussed to proposes a forensic dating protocol. This protocol, conceived as a compendium for best practices, has the potential to function as an analytical guideline, delineating the most efficacious dating approaches in accordance with contextual information and the properties of the bloodstain evidence in question. The objective of this initiative is twofold: firstly, to standardise the procedure for the secure collection, storage and preservation of forensic trace material intended for dating purposes; and secondly to provide guidelines for efficient and robust dating model development.

2.1 BLOODSTAINS DATING BY MEANS OF NIR AND UV-VIS SPECTROSCOPY – A CRITICAL COMPARISON

2.1.1 Introduction

The establishment of the timing of bloodstain deposition used to rely on visually comparing changes in blood colour [75,100]. However, these techniques were soon surpassed by more sophisticated and objective analytical techniques, including spectrophotometric [101,102], chromatographic [83,103], or spectroscopic approaches [92,104–106]. In a relatively short time, indeed, the methods of absorbance spectroscopy in the UV-Vis range [90,102,106–109] and vibrational spectroscopies, either Raman [92,93,98,110–112] or mid-infrared [94,113,114] became the primary tools for researchers attempting blood dating. These choices were led by the hypothesis that, following the evaporation of the aqueous component of plasma, the remaining part of the degrading blood consists primarily of red blood cells and the iron-containing protein haemoglobin. Time-dependent transformations of this tetrameric protein are reflected in Raman or UV-Vis spectra, showing characteristic changes during the formation of methaemoglobin or hemo- and hemichromes [115]. Concurrently, infrared spectroscopy demonstrated efficacy in the observation of the progression of dehydration of bloodstain residues and methaemoglobin formation in the subsequent ageing stages [97]. Considering the complementary nature of information provided by different spectroscopic techniques, it can be concluded that the combination of two analytical methods, with a focus on distinct aspects of blood degradation, could contribute to a more precise estimation of the age of the trace. It is noteworthy that, to date, no research team has opted to adopt this approach.

In this context, it is somewhat surprising that NIR radiation received reduced consideration, despite its ability to describe, among other features, protein structure and water content [116]. Indeed, only a small number of studies have applied this technique to bloodstain dating [95,97,104], utilising a variety of configurations (point analysis, hyperspectral image analysis), time frames (ranging from 19 days to one month), and diverse data analysis approaches (multivariate and univariate). In particular, the performances of NIR spectroscopy were never compared to those of the most affirmed techniques described above.

In consideration of the aforementioned background, the present study initially conducted a comparative analysis of the performances of NIR spectroscopy in bloodstain dating and TSD determination with those of UV-Vis spectroscopy. The primary objective of the present research is thus to evaluate the efficacy of NIR and UV-Vis spectroscopies in monitoring the degradation processes of blood and in verifying the effectiveness of predicting the age of bloodstains through the utilisation of individual methods. In order to evaluate this, blood samples were collected from healthy donors, and blooddrops ageing was monitored over a period of 16 days using both techniques. Subsequently, PLS regression was used to formulate models capable of predicting sample age from spectral information. The performance of the obtained models, expressed in the form of root mean square error of prediction (RMSEP), served as a quality evaluation parameter for each technique.

Afterwards, the two spectroscopic methods were combined to facilitate a more profound comprehension of the transformations that occur during bloodstain aging. At this stage, the study integrated spectroscopic data (including both NIR and UV-Vis) from a data fusion perspective in order to construct combined PLS models.

2.1.2 Results and discussion

2.1.2.1 Chemical interpretation of changes during aging

Prior to the utilisation of chemometric tools, a chemical interpretation of the recorded signals was conducted to comprehend the various aspects of blood degradation observable through specific analytical methods. Initially, this analysis was performed through visual observation of registered signals, considering either all analysed samples (**Figure 2.1A** and **C**) or one average spectrum for each time point (**Figure 2.1B** and **D**).

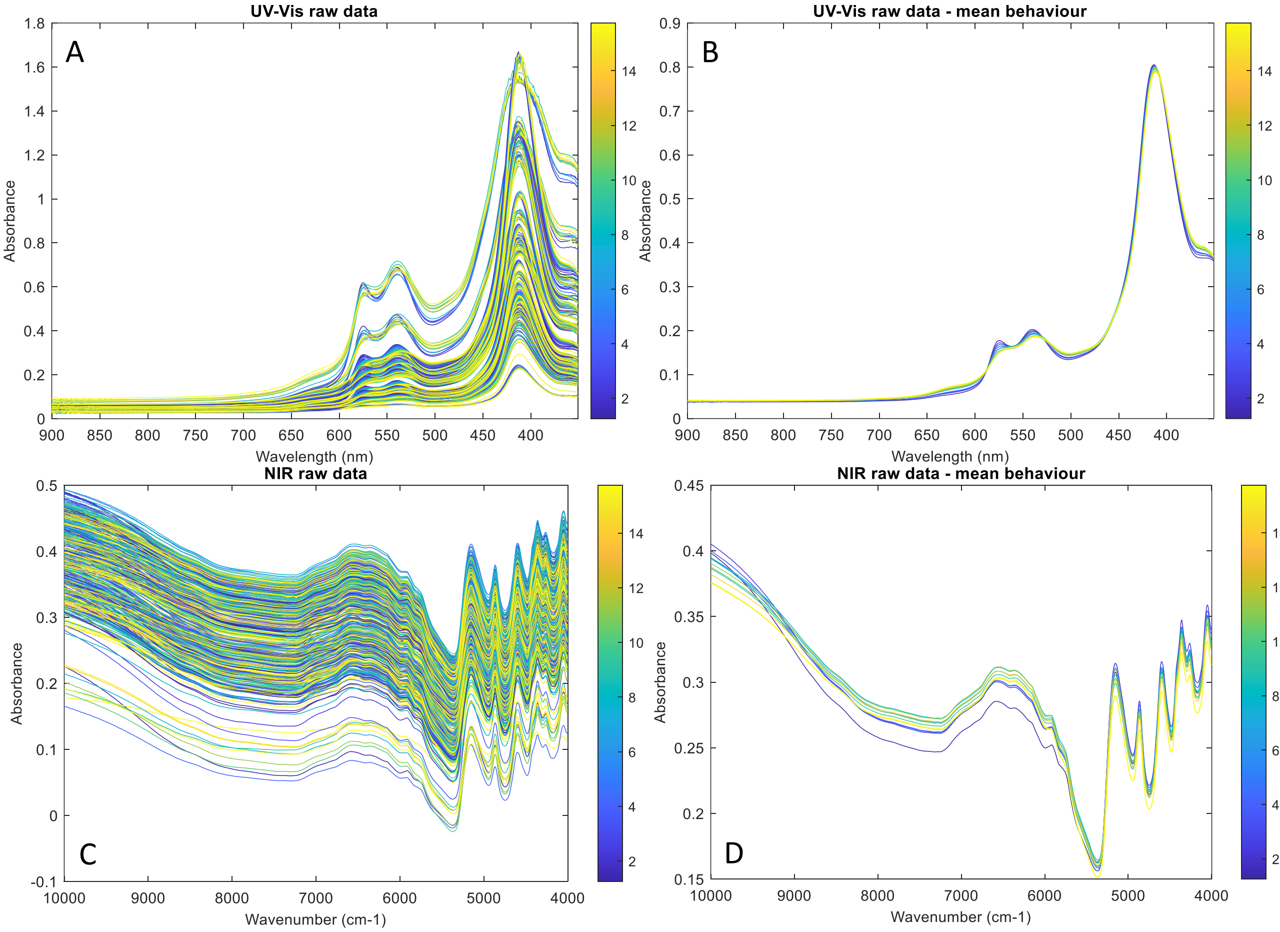

__Figure 2.1__: A: UV-Vis raw data; B: Average behaviour of UV-Vis data, obtained by averaging spectra for each time point; C: NIR raw data; D: Average behaviour of NIR data, obtained by averaging spectra for each time point. The graphs are coloured according to time, ranging from day 1 (dark blue) to day 16 (light yellow).

Time-dependent changes were readily observed in the UV-Vis spectra, even during visual inspection, both on individual spectra from all analysed bloodstains, registered for every time point (**Figure 2.1A**), and, even more evidently, on averaged spectra (**Figure 2.1B**). The most significant changes were observed especially within the 350 to 700 nm range. It is noteworthy that the Soret band's maximum, which is present at approximately 420 nm in "fresh" samples (blue in the figure), undergoes a shift in position during the process of sample degradation, thereby demonstrating a phenomenon referred to as a blue shift, *i.e.*, a shift characterised by the movement of the maximum towards lower wavelengths [115]. These changes were accompanied by distortions in the 500-650 nm region, which encompasses, among others, the so-called Q-bands [102]. These can be further categorised into the alpha (α) and beta (β) bands, whose maxima correspond to 542 and 576 nm, respectively, in "fresh" bloodstains dominated by oxyhaemoglobin. In the case of these bands, time-dependent changes involved an intensity decrease, a broadening, and the tendency to merge into one band with increasing TSD. This feature constituted the spectral indication of methaemoglobin formation. A transformation of oxyhaemoglobin to methaemoglobin (metHb) was detected also in an incremental rise in the absorbance extinction coefficient at a wavelength of approximately 630 nm [117]. All the aforementioned observations remained consistent with previous literary reports [90,102,106–109]. Both the Q-bands and the Soret band are interpreted as π/π^* transitions, arising from electron delocalisation extending across the tetrapyrrole ring of porphyrins [118]. It is evident that these bands demonstrated a high degree of sensitivity to structural alterations, which occur particularly during ligand exchange processes at the nitrogen atoms level of pyrrole rings. Consequently, the distortions resulting from the formation of new haemoglobin derivatives over time are entirely justified.

The raw NIR spectra are presented in **Figure 2.1C**, which illustrates the spectral signatures corresponding to all the analysed bloodstains, and in **Figure 2.1D**, which presents averaged colour-coded signals based on the time elapsed since deposition. A visual evaluation of the averaged spectra indicates that while certain spectral changes are immediately apparent, their interpretation is considerably more challenging compared to that for UV-Vis spectroscopy, particularly in the absence of a preliminary signal processing stage. It is notable that a decline in intensity over time is evident in the range of 10,000-9500 cm^{-1}, followed by the presence of an isosbestic point [97] around 9500 cm^{-1}. It is noteworthy that between 8000-6500 cm^{-1}, the region where the O–H stretching first overtone vibration region is located, the absorbance appears to remain relatively constant, despite the anticipated decline over time due to water evaporation. Nevertheless, it is important to acknowledge the possibility that at least a portion of the observed variability in this spectral region might be attributable to scattering effects. As is commonly understood, pre-processing of NIR spectra is a crucial preliminary step before engaging in any advanced data analysis. This is due to the fact that the process of acquiring spectra is vulnerable to distortions caused by variations in the path length of electromagnetic radiation stemming from alterations in measurement geometry, sample thickness, or its physical properties [119], which may be the case in this instance. Another potential explanation for the observed deviation from expected spectral changes is the presence, within the range of approximately 6000-5700 cm^{-1}, of bands corresponding to protein structures such as haemoglobin, albumin, and globulin connected to the first overtone of C–H stretching vibrations [97]. Conversely, at approximately 5200 cm^{-1}, where the maximum of the water band is observed, arising from the combination band of O–H stretching and O–H bending, the anticipated behaviour can be discerned. In fact, within this region, the absorbance intensity diminishes over time as a results of water loss occurring as the samples undergoes the process of ageing. In comparison to the first O–H stretching overtone, the more pronounced correlation of this combination band with ageing may be attributable to its higher intensity in the NIR spectrum. Indeed, this spectral region has previously been employed by Botonjic-Sehic *et al*. [104] to estimate the TSD of bloodstains. Finally, between 5000–4000 cm^{-1}, protein absorption bands are present. In this region, bands can be attributed to the N–H bending second overtone, the combination of C–H stretching and C=O stretching, and the combination of C–O stretching, N–H in-plane bending and C–N stretching [22]. It can be posited that the observed decrease in intensity of these bands with the age of the bloodstains can be explained by the degradation of protein structures, such as haemoglobin, albumin, and/or globulin [97].

This preliminary chemical exploration of recorded signals resulted in the conclusion that both the tested methods exhibited some potential in answering the question of time elapsed since bloodstain deposition. The application of chemometric tools was imperative in order to achieve this objective.

2.1.2.2 Unsupervised analysis

Chemometric analysis commenced with an exploratory approach. PCA was applied in particular to deconvolute the main sources of variance within the spectral dataset. The results of the PCA on the raw data are displayed in **Figure 2.2** for UV-Vis spectroscopy and in **Figure 2.3** for NIR spectroscopy.

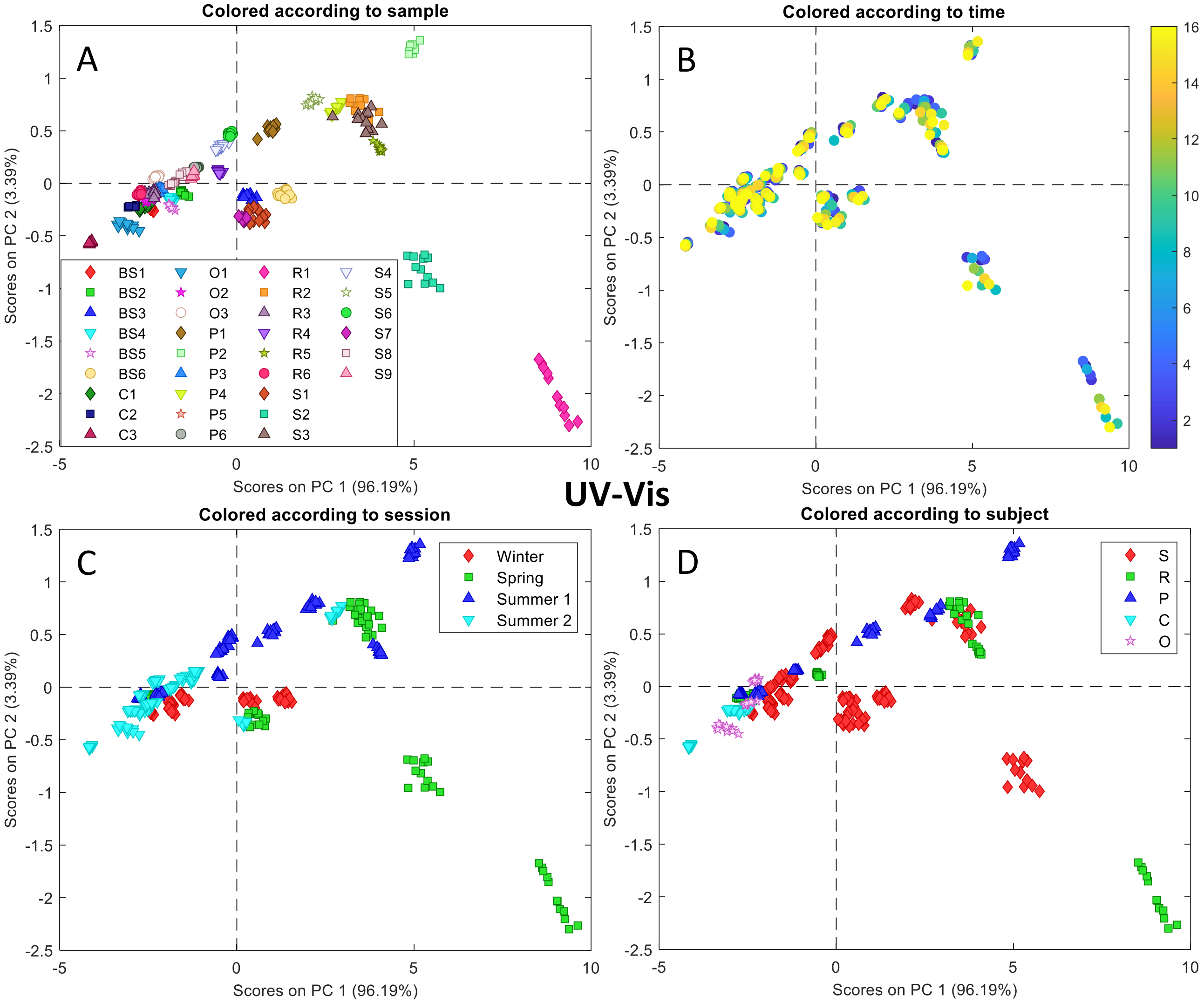

*__Figure 2.2__: Score scatter plots for raw UV-Vis data. A: Score scatter plot coloured according to sample (*i.e.*, single bloodstain); B: Score scatter plot coloured according to TSD; C: Score scatter plot coloured according to analytical session; D: Score scatter plot coloured according to different subject. Each score scatter plot has its own legend for colour codification.*

A visual analysis of the score plots indicates that UV-Vis spectra are characterised by a pronounced grouping within the PC space connected to the sample, as clearly illustrated in **Figure 2.2A**. This finding suggests that the primary source of variability in the dataset is attributable to individual differences in the spectra of the bloodstains. When comparing this figure to **Figure 2.2C** and **2.2D**, displaying the data coloured according to subject identity and analytical session of analysis, respectively, it is noteworthy that the discussed behaviour is not subject- nor session-dependent. In fact, two bloodstains from the same subject collected during the same analytical session (for instance, R1 and R2 in **Figure 2.2A**) are sometimes found to be further apart on the score space than two bloodstains from different subjects collected during different analytical sessions (for instance, P4 and R2 in **Figure 2.2A**). This robust grouping is likely associated with the physical characteristics of the samples, particularly the thickness of the blood layer on the substrate. Indeed, blood was manually smeared on thin glass supports prior to analysis, and smear thickness could not be kept constant nor measured analytically during data analysis. This experimental aspect, however, should not be regarded as a limitation of the study, since it mirrors the situation in real-case scenarios, when blood is of course deposited in a non-controlled fashion with consequently varying physical properties.

No other trend could be revised in the PCA space, probably masked by the strong effect of subject. Indeed, no significant grouping nor tendency can be observed neither in **Figure 2.2C** nor **2.2D**. this assertion can be made with equal validity in the case of **Figure 2.2B**, showcasing the data coloured according to the time of analysis. This last result may appear surprising when compared to the results displayed in the raw spectra analysis, which demonstrated a strong correlation between spectral signature and TSD, but it in fact reflects the significant enhancement in the description of the data when applying the average. In particular, if going back to Figure 2.1A after these observations, it is evident that the predominant effect of the sample can be discerned, in the form of intensity distortion for different samples. These distortions are represented by the well-defined series of time-resolved spectra presented in the figure. These observations underscore the necessity to implement a specific signal pre-processing technique to eliminate the effect of the samples. In particular, conventional line pre-processing by means of standard normal variate (SNV) transform [120] was employed, followed by a pre-processing specific to solving this problem, namely class centering. As outlined in the Materials and methods section (2.1.3) of this chapter, class centering is a column mean centering applied to each of the class whose variance is unwanted. In this case, the class is the sample. The purpose of this process is to normalise for the class mean and thus remove its effect from the dataset.

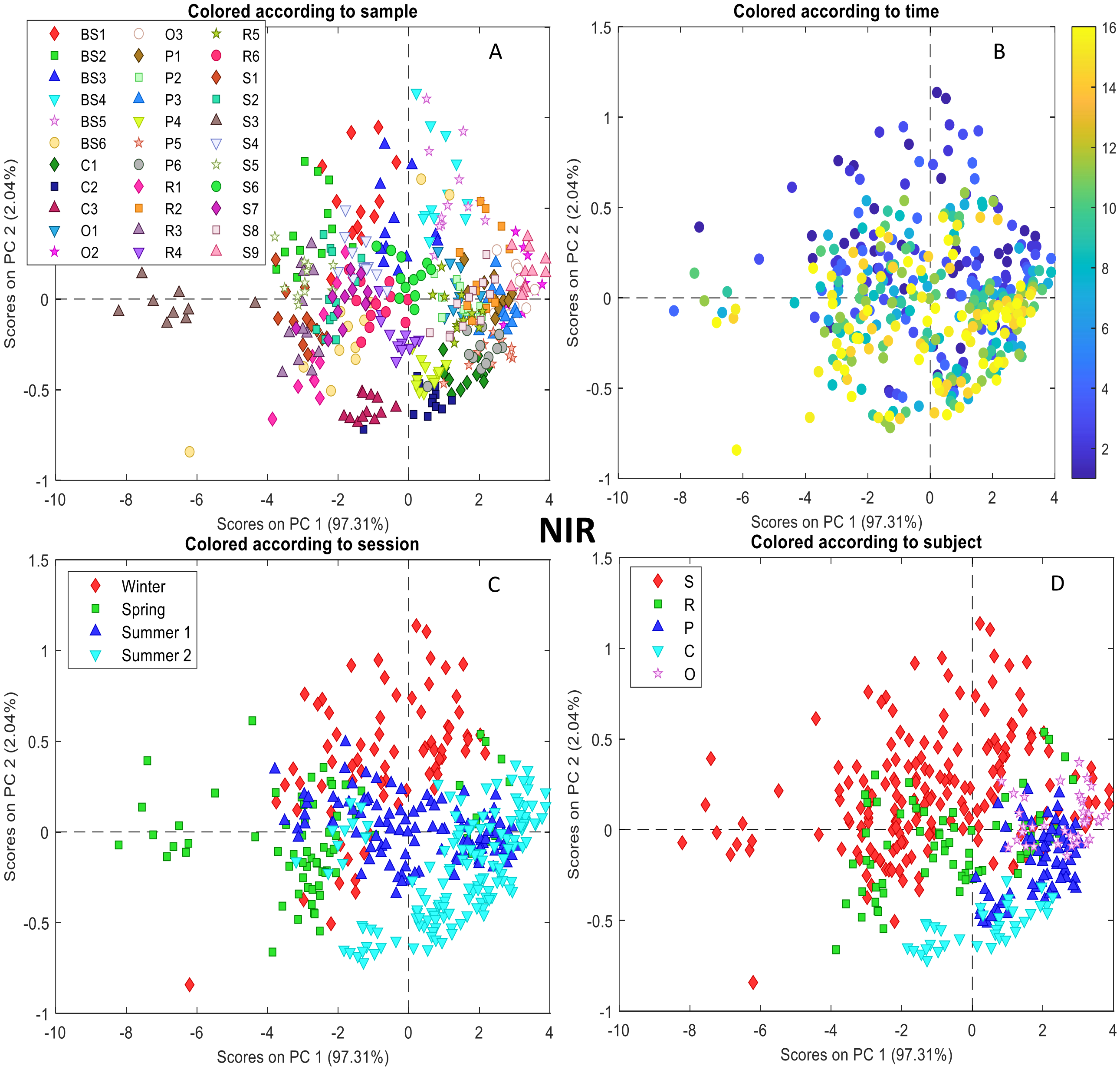

***Figure 2.3**: Score scatter plots for raw NIR data. A: Score scatter plot coloured according to sample (i.e., single bloodstain); B: Score scatter plot coloured according to TSD; C: Score scatter plot coloured according to analytical session; D: Score scatter plot coloured according to different subject. Each score scatter plot has its own legend for colour codification.*

On the contrary, the grouping connected to sample observed in the PC space of the score plots obtained by NIR data (**Figure 2.3A**) is minimal. When colouring the score space according to the four analytical sessions (**Figure 2.3C**) there is some indication of grouping, with data from the same analytical session occupying the same region of the PC space. However, all the groups exhibit at least some overlap, and the situation is not nearly as critical as that observed for sample grouping in UV-Vis spectroscopy. The same can be stated when considering the effect of the subject in **Figure 2.3 D**, wherein the five subjects remain partially grouped in contiguous regions of the PC space, but each group presents a good overlap with the others. Furthermore, the variability connected to the time trend is not dominant (**Figure 2.3B**), yet a suggestion of trend can be identified along PC2, which generally presents “fresh” samples at positive values (blue in the figure) and aged samples at negative values (yellow in the figure). The inability to identify a significant source of variability in the results of PCA for NIR spectroscopy further corroborates the observation derived from the analysis of raw spectra, namely that scattering effects predominate in this technique, and thar data must be subjected to pre-processing to ensure satisfactory chemometric results. In particular, the SNV transform line pre-processing, which is conventionally employed to address this issue, was applied to the NIR data for further analysis.

After implementation of the appropriate signal pre-processing on each technique’s data matrix, PCA was repeated, and the results are illustrated in **Figure 2.4** for UV-Vis spectroscopy and in **Figure 2.5** for NIR spectroscopy.

Comparing **Figure 2.2A** to **Figure 2.4A**, both representing the PC space coloured according to sample, but before and after pre-processing, respectively, it is immediately apparent that the pretreatment used on UV-Vis spectra solved the problem of the substantial systematic difference between samples. Indeed, the predominant source of variability can now be readily identified to be the time trend, as demonstrated in **Figure 2.4B**. Specifically, the TSD information results explained along PC1, with “fresh” samples (blue in the figure) positioned at positive values of scores on this component and aged samples (yellow in the figure) situated at negative scores. **Figure 2.4B** and **2.4C**, on the other hand, do not display any significant grouping, neither in terms of analytical session nor subject. This finding is consistent with the observation made from the PCA on raw data.

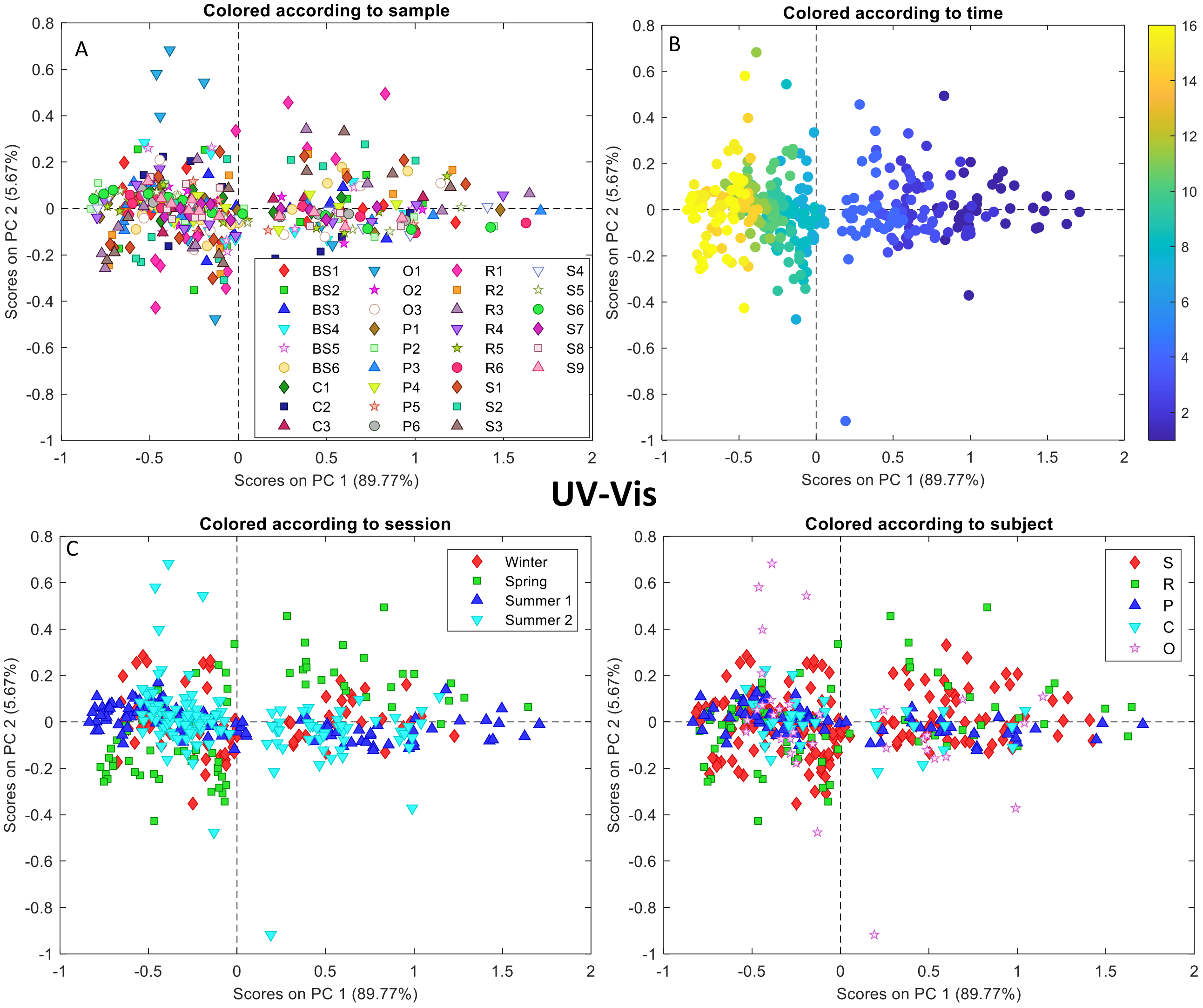

Figure 2.4*: Score scatter plots for pre-processed (SNV transform + class centering) UV-Vis data. A: Score scatter plot coloured according to samples (i.e., single bloodstain); B: Score scatter plot coloured according to TSD; C: Score scatter plot coloured according to analytical session; D: Score scatter plot coloured according to different subject. Each score scatter plot has its own legend for colour codification.*

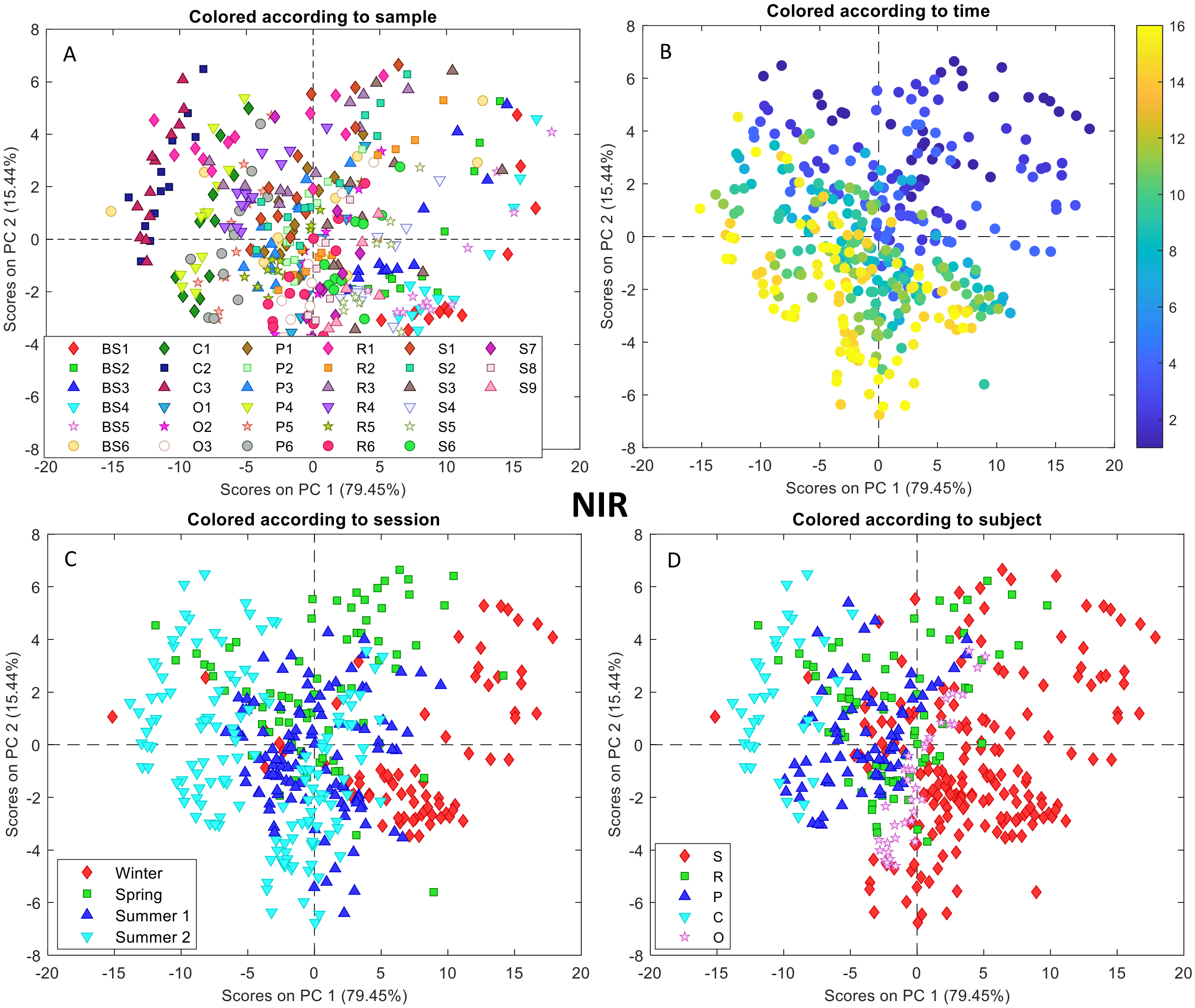

*Figure 2.5: Score scatter plots for pre-processed (SNV transformed) NIR data. A: Score scatter plot coloured according to sample (*i.e.*, single bloodstain); B: Score scatter plot coloured according to TSD; C: Score scatter plot coloured according to analytical session; D: Score scatter plot coloured according to different subject. Each score scatter plot has its own legend for colour codification.*

Analysing PCA results on NIR data, as shown in **Figure 2.5**, pre-processing was beneficial also in this instance. The temporal trend was evidenced, as illustrated in **Figure 2.5B**, where it is evident that TSD has become a significant source of variability for both PC1 and PC2, thereby demonstrating the time trend in an oblique direction. The “fresh” samples (in blue in the figure) are positioned at positive values of both PC1 and PC2, while the aged samples (in yellow in the figure) are situated at negative values of both components.

Grouping according to sample was correctly dealt with by the pre-processing (**Figure 2.5A**), while the minor grouping according to analytical session and subject exhibited a marginal improvement, though not complete elimination, following the pre-processing (**Figure 2.5C** and **2.5D**).

An interesting outcome that can be drawn from PCA results of both techniques, irrespective of the pre-processing, is that blood donors have a low influence on NIR spectroscopy and almost no influence at all on UV-Vis spectroscopy. This may provide a preliminary indication that interindividual differences can be accounted for by chemometric processing. Conversely, the minimal influence ascribed to the analytical session is unsurprising, given that the experiments were carried out in controlled laboratory conditions. The substantial overlap observed between session can thus be interpreted as an indication of repeatability.

Subsequently, loadings of the PCA models obtained on pre-processed data, reported in **Figure 2.6**, were analysed for both spectroscopic techniques. It is important to underline that the loading profiles depicted in **Figure 2.6**, which are utilised for band attribution, are derived from pre-processed data. To circumvent the risk for misinterpretation arising from pre-processing artefacts [15], the pre-processing was reversed to generate the graphs, thereby ensuring a more precise reflection of the spectral signatures of raw data.

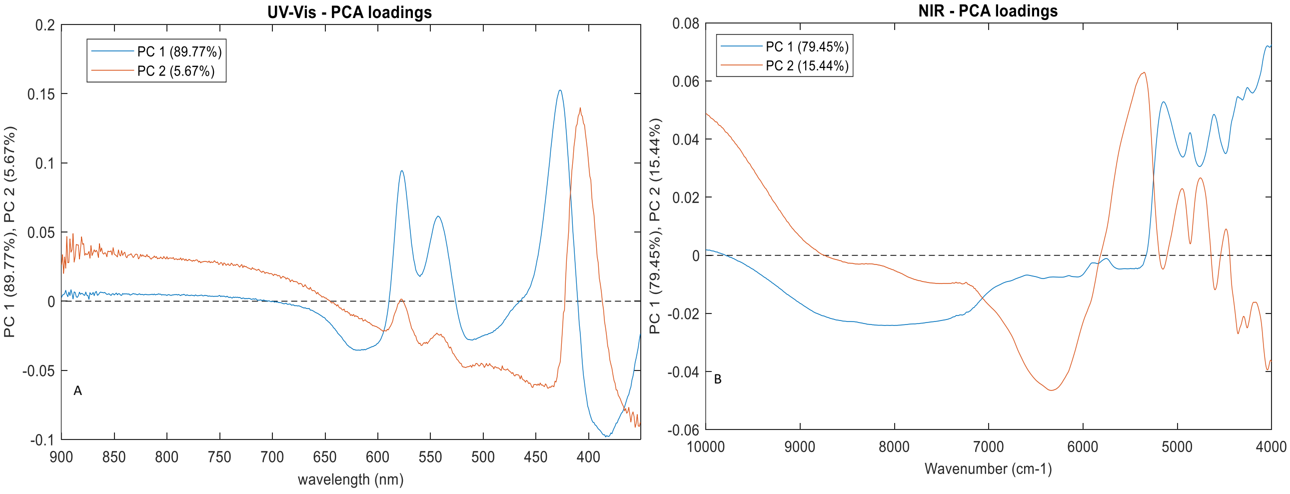

Figure 2.6: *PCA loading line plots. A: Loadings for PC1 and PC2 (pre-processing = SNV transform + class centering) for UV-Vis spectroscopy; B: Loadings for PC1 and PC2 (pre-processing = SNV transform) for NIR spectroscopy.*

For UV-Vis spectroscopy, the PC1 loadings (**Figure 2.6A**) display a negative contribution from the metHb band, as evidenced by the negative peak observed at approximately 630 nm. This finding suggests that samples with negative PC1 values, *i.e.* aged samples, are characterised by higher concentrations of methaemoglobin. Conversely, the Q bands exhibited a positive contribution to PC1, thereby emphasising that “fresh” samples, positioned at positive values on this PC, are characterised by higher intensity levels at these specific wavelengths. In a similar manner, the Soret band demonstrates a positive contribution at approximately 440 nm, underlining the higher contribution of this band for “fresh” samples. A thorough examination of the scores and loadings reveals that higher absorbances in the metHb band and higher wavenumbers in the maximum of the Soret band are indicative of aged samples. Conversely, higher absorbances in the Q-bands are typical for newly deposited samples. This finding aligns with observations derived from visual interpretation of spectra (section 2.1.2.1). Although reported for the sake of comprehensiveness, PC2 loadings contributed little to the interpretation of the data, as evidenced by the absence of variability in this principal component, as illustrated in **Figure 2.4**.

Upon investigating the PCA loadings derived from NIR data (**Figure 2.6B**), it becomes discernible that the protein bands, spanning the range of approximately 4000 cm^{-1} to approximately 5200 cm^{-1}, are predominantly contributing to PC1. In particular, higher values of PC1 are indicative of samples exhibiting heightened protein band intensity; upon performing a joined interpretation with the score plot, it can be observed that this area of the orthogonal space corresponds to newly deposited bloodstains. Indeed, these bloodstains present higher intensities in those bands connected to lower protein degradation. Conversely, the aged samples characterised by higher levels of degradation can be found at negative values of PC1. When PC2 is considered, loadings demonstrate higher contributions from the water stretching and bending combination band at approximately 5500 cm^{-1}, for which higher intensities result in higher scores on PC2. The opposite behaviour can be observed for the band around 6300 cm^{-1}, attributed to the N–H stretching vibration of amide groups, which exhibit negative PC2 loadings. When the score plot is considered for a joint interpretation, newly deposited samples display higher scores on PC2, thereby confirming their higher content of water, as reflected by the higher intensities observed in the water band during the analysis of raw spectral data. Furthermore, the negative contribution of amide bonds supports the hypothesis of a structural degradation of proteins during the ageing process.

In summary, PCA was able to emphasise the paramount importance of pre-processing in order to deal with unwanted effects in the data. It also highlighted a critical sample effect on UV-Vis data that could not be evidenced in NIR data. Moreover, PCA confirmed the suitability of both instrumental techniques for describing the evolution of blood samples during the ageing process, as evidenced by the time trend dependence of scores evidenced in the PC space. Nevertheless, in order to achieve the modelling objective of the study and to make a comparison of the dating performance of the two techniques, it was necessary to apply supervised regression techniques.

2.1.2.3 Supervised analysis

The first step of the supervised analysis involved optimising regression models to predict the TSD using the data from each instrument separately. The regression results were therefore optimised with an instrument-tailored approach to maximise the performance of both techniques. To this end, the samples were divided into independent training and test sets. The former contained three subjects and three analytical sessions for a total of 216 spectra, while the latter contained two additional subjects and one analytical session for a total of 72 spectra.

The initial phase of the regression training consisted in the optimisation of the pre-processing stage, which was conducted separately for the two analytical techniques. A total of 92 combinations of pre-processing were evaluated, and the optimal combination was chosen by minimising RMSECV. When RMSECV was not significantly different between the top-ranking models, the configuration that displayed the lowest complexity was selected. The pre-processing approach that proved to be most effective for UV-Vis data was found to be first derivative followed by normalisation (Norm1) and then by class centering, resulting in a RMSECV of 0.97 days and displaying 5 significant latent variables. Notably, of the 92 pre-processing combinations, the half encompassing class centering exhibited superior performance in comparison to the remaining half. This outcome underscores the crucial role of addressing the bias caused by the physical differences among samples in order to extract the desired information, thereby validating the efficacy of class centering as a solution to this issue.

Consequently, UV-Vis data required a “strong” pre-processing to ensure the attainment of satisfactory results. While this may not pose a significant challenge from a computational perspective, since the calculation speed of chemometric software is no longer problematic, the main issue resides in the equation of the pre-processing itself. Indeed, the calculation necessitates the estimation of the global mean of the time trend, thereby requiring the complete time trend to be analysed. Indeed, the mean spectrum of a specific bloodstain varies according to the number of sampling times considered and the time range those acquisitions cover. It is imperative that the number of sampling points and the time covered correspond for the training and test sets in order to ensure the correct application of the pre-processing. Nevertheless, while acquiring the complete time trend is not problematic in an experimental setup, it is in fact impossible in real-case scenarios. The necessity of applying a dating technique implies in fact the impossibility of following the evolution of the unknown sample for the entirety of its ageing process. It is therefore essential to evaluate the performance of UV-Vis spectroscopy in both situations, *i.e.* with and without using this pre-processing, in order to gain information that could be valuable whenever the proposed methods might be transferred to the forensic practice.

For this reason, the best model that did not use class centering was kept for further consideration as well. In this case, the optimal pre-processing combination resulted to be normalisation (Norm1) followed by the first derivative, which resulted in a model with RMSECV = 1.67 days and a total of 9 significant latent variables. The increased complexity, in conjunction with an almost double cross-validation error, serves to emphasise the augmented strain on the regression algorithm in efficiently predicting TSD. This outcome serves to substantiate once again the conclusion that the physical features associated with the samples have a considerable impact on UV-Vis data.

Conversely, the outcomes derived from NIR spectroscopy were more unambiguous. In this case, the best pre-processing approach resulted to be the application of the first derivative followed by SNV transform, which yielded a RMSECV of 2.20 days and exhibited a complexity of 5 significant latent variables. The investigation revealed that no model using class centering was evaluated as one of top 20 optimal solutions, thereby substantiating the negligible impact of class effects on NIR spectroscopy. This outcome corroborates the PCA results, indicating a strong independence of NIR spectroscopy results from the choice of pre-processing, thereby rendering the technique more robust than UV-Vis spectroscopy.

The three selected models where then subjected to a permutation test, and all proved to be significantly different ($p < 0.005$) when compared to a model constructed from the same dataset using randomisation. The specifications of the models are documented in **Table 2.1**.

***Table 2.1**: Summary of figures of merit for the selected regression models.*

Data	**Pre-processing**	**Latent Variables**	**RMSEC (days)**	**RMSECV (days)**	**RMSEP (days)**	**R^2**
UV-Vis A	1st derivative + norm1 + class centering	5	0.74	0.96	1.67	0.96
UV-Vis B	Norm1 + 1st derivative	9	1.18	1.67	3.18	0.88
NIR	1st derivative + SNV transform	5	2.03	2.20	2.30	0.83

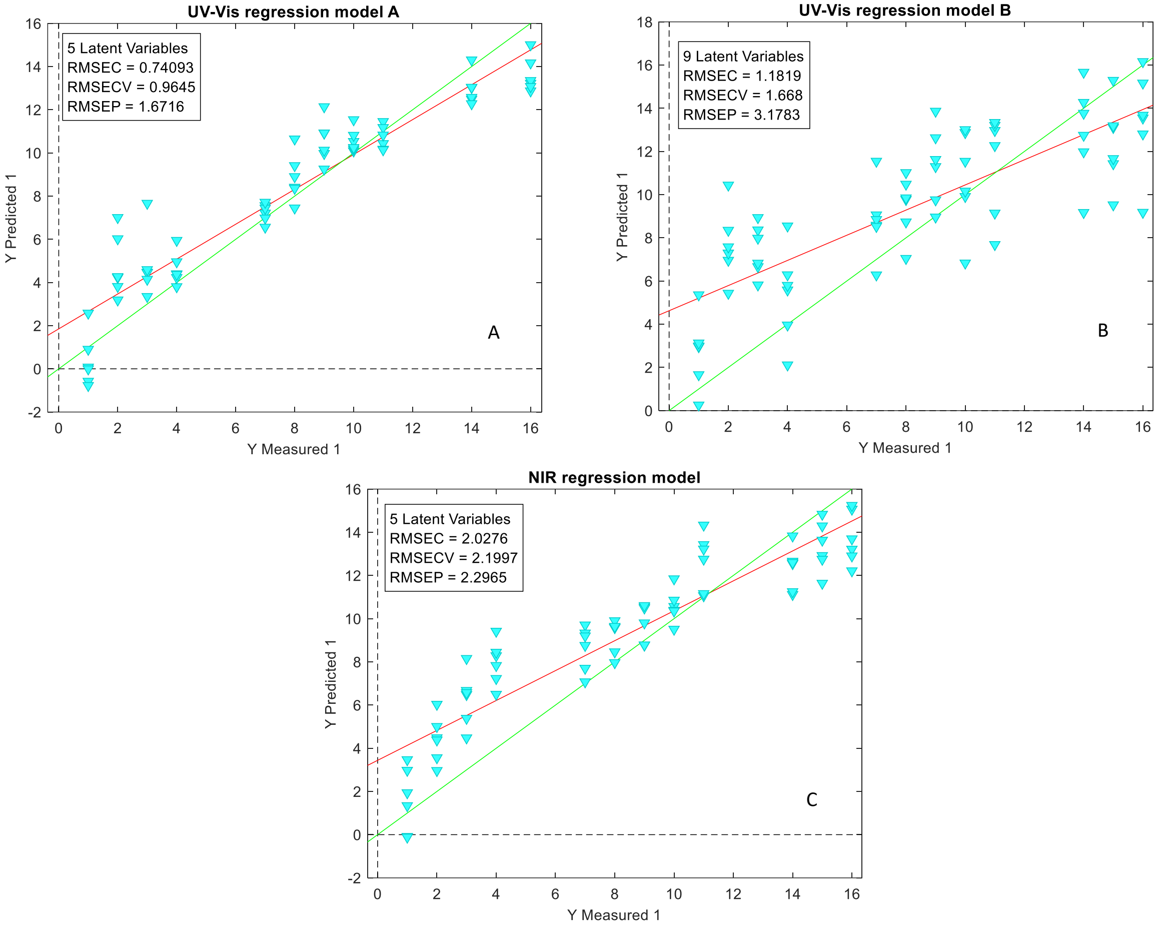

***Figure 2.7**: Results of the PLS regression models on the test set. A: Model for UV-Vis data, pre-processing = 1st derivative + norm1 + class centering; B: Model for UV-Vis data, pre-processing = Norm1 + 1st derivative; C: Model for NIR data, pre-processing = 1st derivative + SNV transform.*

Finally, the models were applied to the test set in order to verify their prediction ability of the models and the accuracy with which bloodstain age could be assessed. The results of the prediction are summarised in **Table 2.1** and in **Figure 2.7**. In particular UV-Vis, when treated with a combination of pre-processing techniques which encompassed the use of class centering, provided the most precise method for bloodstain dating, demonstrating a RMSEP of 1.67 days, *i.e.*, about 40 hours. Conversely, when class centering was not applied, UV-Vis spectroscopy yielded a prediction error of 3.18 days, equivalent to approximately 76 hours. NIR spectroscopy presented an RMSEP of 2.30 days, which is equivalent to 55 hours. The satisfactory dating results obtained on the test set, which contains blood from two different donors than the ones used in the training set, lend support to the hypothesis that the influence of the donor on the blood ageing process is reduced. This suggests that satisfactory dating models could be obtained using blood from different donors that the one of the unknown samples. However, this hypothesis must be confirmed by further analysis on a wider cohort of subjects.

The findings of this study demonstrate that both NIR and UV-Vis spectroscopies have the capacity to predict the TSD of bloodstains with satisfactory performances. When class centering was applied, UV-Vis spectroscopy was identified as the most accurate method for obtaining the blood dating, yielding a prediction error of 40 hours in comparison to the 50 hours observed for NIR spectroscopy. The models' dating performances align with what was reported in previous literature, where the RMSEP for the models developed for NIR data was approximately 2.7 days [97], and for the UV-Vis achieved RMSEPs oscillating around one day [90,91,107,121]. Conversely, when class centering is not applied, RMSEP for UV-Vis spectroscopy reaches 76 hours, which is significantly worse than the 50 hours of NIR spectroscopy. The robustness of NIR spectroscopy is further substantiated by the observation that the variation between RMSE in calibration, cross-validation and prediction is minimal when compared to that observed in UV-Vis spectroscopy, both with and without the application of class centering (see **Table 2.2**). Indeed, a low delta between RMSEC, RMSECV and RMSEP generally signifies a reduced probability of model overfitting [122] and thus an enhanced robustness of the model.

With regard to latent variables, it is noteworthy that the model for NIR and the one for UV-Vis data exhibit the same complexity when class centering is applied. Conversely, the complexity is higher when class centering is not applied. This finding suggests that, without using this pre-processing, the PLS algorithm experiences greater difficulty in isolating the variability associated with the time trend, having to deal with a substantial confounding factor given by the systematic difference.

***Table 2.2**: Difference of RMSEC, RMSECV and RMSEP for the selected regression models. * = lower difference among the models considered.*

Data	Pre-processing	RMSECV – RMSEC	RMSEP – RMSECV	RMSEP – RMSEC
UV-Vis A	1st derivative + norm1 + class centering	0.22	0.71	0.93
UV-Vis B	Norm1 + 1st derivative	0.48	1.51	1.99
NIR	1st derivative + SNV transform	0.17*	0.10*	0.27*

2.1.2.4 Data fusion

A combination approach was finally adopted, applying low- and mid-level fusion of NIR and UV-Vis data. The data were fused by the concatenation of matrices, and the model optimisation process was repeated. Both low and mid-level data fusion models were developed either avoiding or allowing the use of class centering, and the best model was selected according to RMSECV, determined through sample-wise cross-validation.

For this particular data processing stage, the data were divided into the same training and test set that has been utilised in the preceding supervised analysis step. Consequently, the construction, selection, and optimisation of models were conducted on training set data, and subsequently the selected models were applied to the independent test set in order to evaluate the prediction ability of the models themselves.

Two distinct approaches were employed for low-level data fusion:

1. Spectroscopic data were pre-processed prior to fusion, employing the pre-processing method previously identified during individual PLS calibration. The data fusion regression model was directly calculated without reiterating the pre-processing optimisation step;
2. The raw data matrices were concatenated, and the pre-processing optimisation was repeated as described for the individual models. In this case, class centering was excluded from the pre-processing options.

The results for the two approaches are shown in **Figure 2.8A** and **B** respectively and the figures of merit pertaining to the models are reported in **Table 2.3**. Specifically, the model constructed using the first approach demonstrated satisfactory cross-validation outcomes, exhibiting an RMSECV of 0.91 days (~22 h). The second approach presented 1^{st} derivative followed by normalisation as the best pre-processing option and produced a model with an almost double RMSECV (1.78 days, ~43 h). When the two models were applied to the test set, they displayed a RMSEP of 1.62 days (~39 h) and 2.82 days (~68 h), respectively.

These results bring to the conclusion that, in the context of this particular application, the integration of low-level data fusion did not yield substantial improvements in the estimation of time from deposition. Indeed, even when class centering is employed, the RMSEP was of about 39 hours, which is a non-significant reduction in the prediction error when compared to what happens when the dating is conducted exclusively using UV-Vis. Moreover, the method that did not apply class centering had an RMSEP higher than the 50 hours obtained by NIR alone.

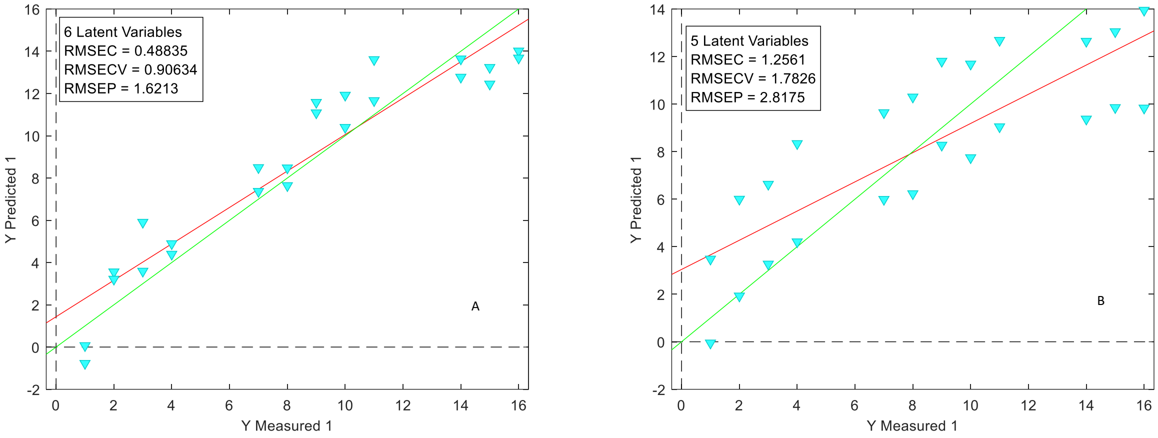

***Figure 2.8**: PLS regression models obtained from low-level data fusion. A: model calculated with approach one; B: model calculated with approach two.*

In the context of mid-level data fusion, two distinct approaches were employed to calculate the models also in this case. One approach included the use of class centering, while the other one avoided it. In particular, the first approach consisted in the concatenation of the 5 significant latent variables obtained by the best PLS regression model for NIR spectroscopy with the 5 significant latent variables obtained by the best PLS regression model for UV-Vis spectroscopy encompassing the use of class centering. The second approach fused still the same latent variables for the NIR model with the 9 significant latent variables obtained by the best PLS regression model for UV-Vis spectroscopy without the use of class centering.

The results of PLS regression on mid-level fused data are shown in **Figure 2.9**, and their figures of merit are documented in **Table 2.3**. The two new models exhibited five significant latent variables each and demonstrated a RMSECV of 1.04 days (~25 h) and 2.14 days (~51 h) respectively. When employed for the purpose of prediction, the two models yielded a RMSEP of 1.48 days (~36h) hours and 2.29 days (~55 h), respectively.

These data reveal a decrease in RMSEP, reaching 36 hours when class centering is applied. This value represents the lowest recorder in the present study. Consequently, in this case, the technique combination enhanced the dating performances of the models, leading to a reduction in error of approximately 5 hours when compared to the results achieved through UV-Vis alone. On the contrary, when no class centering was applied, the RMSEP of the fused model was of approximately 55 hours, which was 5 hours higher than the results obtained with NIR spectroscopy alone. This finding suggests that the combination of techniques does not offer any advantage in this case. This result is of paramount importance, since it emphasises that, even in the best possible scenario in which class centering is applied, the use of both NIR and UV-Vis spectroscopy should be preferred than the application of UV-Vis alone. This underscores the potential for NIR spectroscopy and the combination of techniques to enhance the performance of bloodstains dating in forensic practice.

***Table 2.3**: Summary of figures of merit for the low-level and mid-level data fusion regression models.*

Data	Pre-processing	Latent Variables	RMSEC (days)	RMSECV (days)	RMSEP (days)
Low-level data fusion	UV-Vis: 1st derivative + norm1 + class centering; NIR: 1st derivative + SNV transform	5	0.49	0.91	1.62
Low-level data fusion	1st derivative + norm1	5	1.26	1.78	2.82
Mid-level data fusion	UV-Vis: 1st derivative + norm1 + class centering; NIR: 1st derivative + SNV transform	5	0.85	1.04	1.48
Mid-level data fusion	UV-Vis: norm1 + 1st derivative; NIR: 1st derivative + SNV transform	5	1.38	2.14	2.29

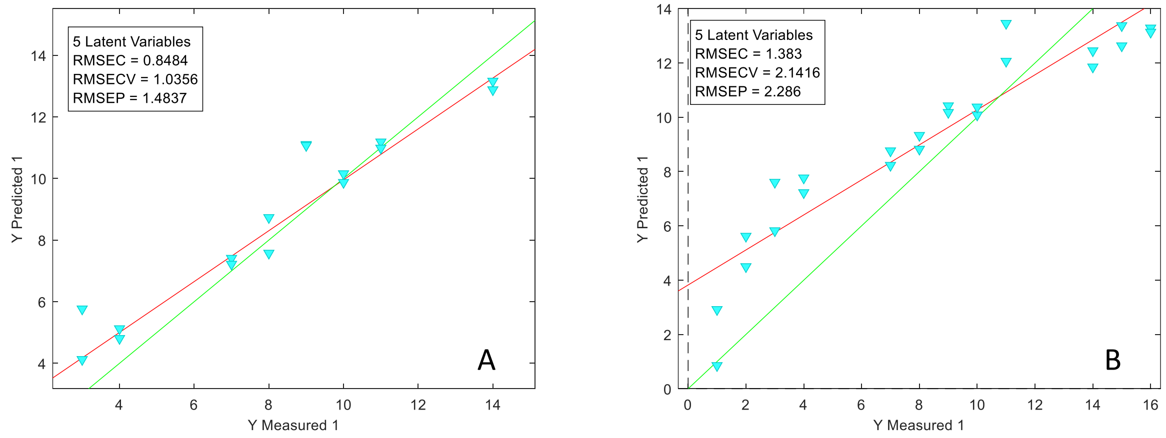

***Figure 2.9**: Results of PLS-R models calculated on mid-level fused data. A: Model obtained including class centering in the pre-processing; B: Model obtained without using class centering in the pre-processing.*

2.1.2.5 The concept of confidence interval in multivariate regression

In the forensic context, the concept of confidence interval is crucial to understand the significance of analytical evidence in the real-case scenarios. Indeed, studies regarding the issue of confidence interval have been carried out in several fields of forensic research, such as entomology [123], anthropology [124], DNA evidence [125,126], death time estimation [127,128] and documentoscopy [129]. While the calculation of a confidence interval is well established in univariate analysis, its calculation is trickier when multivariate analysis is concerned, and only one study concerning documentoscopy [129] deals with this issue in a PLS-DA context.

In chemometric practice, it is commonly accepted to use RMSEP as an estimation of a regression model precision, and this figure of merit is sometimes referred to as the “uncertainty” of a model. However, RMSEP (**Equation 2.1**) is actually an indication of the standard deviation of the error of the prediction [130], analogous to the standard deviation of the model ($s_{y/x}$, **Equation 2.2**) in univariate calibration, as can be observed by their equations:

$$RMSEP = \sqrt{\frac{\sum_{i=1}^{P}(y_i - \hat{y_i})^2}{P}} \tag{2.1}$$

$$s_{x/y} = \sqrt{\frac{\sum_{i=1}^{N}(y_i - \hat{y_i})^2}{N-2}} \tag{2.2}$$

Where:

- P is the total number of samples in the test set of the multivariate calibration;
- y_i is the known value for sample i;
- $\hat{y_i}$ is the predicted value for sample i;
- N is the total number of samples in the test set of the univariate calibration.

In univariate calibration, the semi-amplitude of the confidence interval for a predicted value depends on two factors: the standard error of the regression and the leverage of the prediction point. In particular, it is obtained from the standard deviation of the regression by multiplying it by the critical value of the Student or Z distribution at the desired confidence level and by the square root of the leverage of the prediction point.

Therefore, to maintain the analogy in multivariate calibration, RMSEP as well should be multiplied for the critical t or z value and the leverage to obtain the semi-amplitude of the confidence interval:

$$y = y_p \pm t_p * L * RMSEP \qquad (2.3a)$$

$$y = y_p \pm z_p * L * RMSEP \qquad (2.3b)$$

Clearly, such a calculation would enlarge the final confidence interval if compared to the use of RMSEP alone. For example, in the case of the models proposed in this thesis for NIR and UV-Vis spectroscopy, the confidence intervals would be 4.57 days for NIR (RMSEP = 2.29 days), 6.95 days for UV-Vis with class centering (RMSEP = 1.67 days) and 36.74 days for UV-Vis without class centering (RMSEP = 3.18 days).

From these results several comments may arise. Firstly, as expected, the confidence interval is way higher than the RMSEP, and therefore using RMSEP as a confidence interval might lead to an overestimation of the general performances of a multivariate regression model. More importantly, the dependence of the confidence interval on the leverage, which is not a constant but rather a model-dependant statistic, implies that the results of a method comparison might vary significantly if this comparison is done either on RMSEP or on the confidence interval. Indeed, a model with a lower RMSEP may however be characterised by a higher leverage, thus reversing the final outcome. Indeed, for instance, in our case study we have lower RMSEP for UV-Vis spectroscopy compared to NIR spectroscopy, while this situation is completely opposed when considering the confidence interval. Lastly, while the model constructed with UV-Vis spectroscopy without the use of class centering might appear an acceptable model when only RMSEP is observed, the confidence interval underlines that the model cannot be used in prediction, since the uncertainty associated with the measure is higher that the timespan covered by the measure itself.

The observations reported in this paragraph should serve as a warning to chemometricians and may hopefully open up research towards a standardisation of confidence interval analysis for multivariate regression analysis. However, this topic was not pursued further during my PhD research, therefore it will not be given further consideration in this thesis.

2.1.3 Materials and methods

2.1.3.1 Sampling

Blood samples were obtained from five healthy volunteers, 3 males and 2 females, aged between 25 and 41 years (average = 31). Blood was directly extracted from the fingertip by puncturing the dermis with a lancet and was subsequently recovered using a quantitative pipette. The blood was the deposited for analysis without the addition of any anticoagulant agent. For each donor, the process of blood deposition was carried out at least three times in order to account for variability.

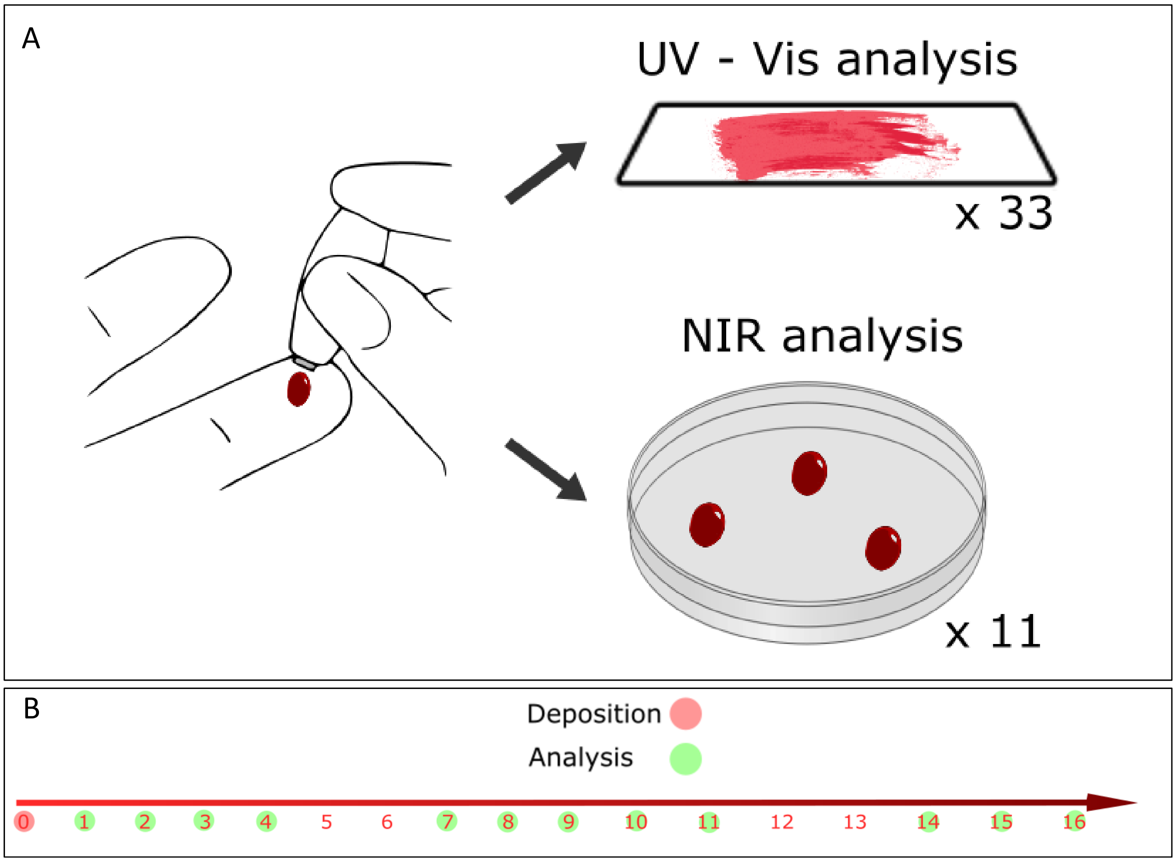

Figure 2.10. *A: Visual schematisation of sampling procedure, with indication of samples' numerosity; B: Measurement scheme along time. A red circle indicates the day of sample deposition, while a green circle indicates a day during which samples were analysed. No analysis was done on day 0.*

For analysis by means of UV-Vis spectroscopy, 20 µl aliquots of blood were deposited onto glass slides (Pearl Microscope Slides – 1.0-1.2 mm thickness) and immediately smeared with the assistance of another glass slide to obtain a thin layer of blood. For analysis by means of NIR spectroscopy, 20 µl aliquots of blood were deposited directly onto optical glass (Precision Cell, Hellma Analytics, Milan – Italy) and left to dry. The process of sample preparation is visually summarised in **Figure 2.10A**.

After the process of blood deposition, the samples were permitted to dry in the dark and at controlled laboratory conditions (T = 20±2°C, humidity = 41±2%). The samples were deposited on day 0 (Monday) and analysed with both UV-Vis and NIR spectroscopies at 24-hours intervals during working days, commencing on day 1. The measurement scheme is illustrated in **Figure 2.10B**. The samples were monitored over a period of 16 days, with a total of 12 sampling times.

The analytical procedure was repeated on four sessions, once during winter period (December 2022), once during the spring period (March 2023), and twice during the summer period (June 2023 and July 2023). It should be noted that not all subjects provided blood in all sessions, as is detailed in **Table 2.4**. Each subject provided three bloodstains per technique for each session, with the exception of subject S in the winter session, when they provided six samples for each technique (symbolised by * in **Table 2.4**). In total, 33 bloodstains were analysed with each technique over the course of the study.

***Table 2.4**: Sampling scheme according to blood donor per session. Each cell of the table contains the number of bloodstains each donor provided in each session.*

	Subject “S”	**Subject “R”**	**Subject “P”**	**Subject “C”**	**Subject “O”**
Winter session	6				
Spring session	3	3			
Summer session 1	3	3	3		
Summer session 2				3	3

2.1.3.2 Instrumentation

UV-Vis analysis was performed with a Cary-100 UV-Vis Spectrophotometer (Agilent Technologies, Santa Clara, CA, USA) equipped with a horizontal sampling integrating sphere working in the diffuse reflection mode. The range of spectral acquisition was 350–900 nm, with a data interval of 1.0 nm. The averaging time was 0.1 s, with a scan rate of 600 nm/min. The spectral bandwidth was 4.0 nm. The glass support was fixed vertically on a sample holder, ensuring that the layer of blood covered the whole window as homogeneously as possible. Additionally, a disk made of Spectralon® was positioned behind the glass substrate, thereby serving as a highly reflective material, with the objective of maximising the amount of radiation reaching the integrating sphere and the detector, through transflection. The position of the sample on the holder was maintained constant day by day. Three consecutive replicates were taken at every sampling time, with a total of 975 spectra collected in the UV-Vis spectral range (26 bloodstains × 3 repetitions × 12 days of analysis + 1 bloodstain × 3 repetitions × 12 days of analysis).

NIR analyses were conducted utilising a NIRFlex Solids FT-NIR spectrophotometer, BUCHI (BUCHI s.r.l, Flawil, Switzerland), operating in the transflection mode. In order to obtain transflection, the bloodstains were covered by a transflector, an accessory made of 360L steel with a fixed path length. The range of spectral acquisition was 4000-10,000 cm^{-1}, with a data interval of 4.0 cm^{-1} and a number of scans per measurement equal to 32. A of 3 mm diameter window reducer was employed in the analysis to ensure that the analysed sample completely covered the measuring window. Samples were analysed in triplicate on a daily basis, slightly moving the sample between replicates, resulting in a total of 972 spectra collected within the NIR spectral range.

2.1.3.3 Data analysis

2.1.3.3.1Data organisation and exploration

Spectral data were organised into data matrices using MATLAB®, version 2023a (The MathWorks, Natick, MA, USA). UV-Vis and NIR data were organised in two independent matrices with samples on the rows (972 rows) and variables on the columns, with 551 wavelengths for UV-Vis data and 1501 wavenumbers for NIR data. Subsequently, the mean of the three instrumental replicates was calculated, thus yielding a mean spectrum for each sample on a specific day. The resulting matrices had 324 rows, while the number of columns remained unchanged. The obtained data matrices were subjected to multivariate data analysis using the PLS-Toolbox 9.2 software (Eigenvector Research Inc., Manson, WA, USA) in the MATLAB® environment.

Initially, the NIR spectra were converted from the transflectance scale to the pseudo-absorbance scale (Log (1/R)), in order to enhance interpretability of the results [131]. Subsequently, exploratory data analysis was conducted through PCA [66]. In this study, the technique was initially implemented on raw data, with the objective of identifying patterns and differentiating the impact of different factors, including subject, analytical session, single bloodstain, and time on the distribution of samples in the score plot.

Subsequently, the data underwent a pre-processing stage, with the objective of eliminating any unwanted sources of variability and accentuate the effect of time since deposition. The following classical line pre-processing techniques were tested: SNV [120] transform, Savitzky-Golay 1st and 2nd derivative [132], as detailed below, in conjunction with a column scaling technique referred to as class centering. Class centering is a groupwise column pre-processing technique that aims to account for systematic differences between samples due to physical factors, such as the manual deposition of the blood stains. This mathematical transform aims to centre the samples according to the mean of each class [133,134], as detailed in **Equation 2.4**:

$$\lambda_{BS\, t_i\, cc} = \lambda_{BS\, t_i} - \frac{\sum_{i=1}^{n} \lambda_{BS\, t_i}}{n} \qquad (2.4)$$

where $\lambda_{BS\, t_i\, cc}$ is the class centred absorbance value at wavelength λ for sample BS at time i, $\lambda_{BS\, t_i}$ is the absorbance value at wavelength λ for sample BS at time i and *n* is the total number of sampling points.

Subsequently, the PCA was reiterated following the pre-processing of the data.

2.1.3.3.2 Multivariate regression

Subsequently, PLS regression models were calculated. PLS regression is a technique that relates the two data matrices, one containing the observed the observed spectral data (X variables) and the other containing the time for deposition (Y variable) through a linear multivariate model [65,135].

To build the regression model, data were split into a training and a test set. The training set comprised the data from the first three analytical sessions (“Winter”, “Spring” and “Summer 1”, see **Table 2.4**) and the data from three out of five subjects (subjects “S”, “P” and “R”, one female and two male) for a total of 21 bloodstains followed for 12 sampling times, resulting in 252 spectra. The test set was selected to be entirely independent from the training set; consequently, the two subjects not included in the training set (“C” and “O”), analysed in the last analytical sessions (“Summer 2”), were used, resulting in a total of 6 bloodstains followed for 12 days, yielding 72 spectra.

The calibration of the PLS regression model was performed on the training set. The initial stage was the optimisation of pre-processing technique through the model optimiser option of the PLS Toolbox. In particular, the following pre-processing strategies were considered:

- 1st derivative, Savitzky-Golay algorithm with 11 points window and 2nd grade interpolating function [132];
- 2nd derivative, Savitzky-Golay algorithm with 11 points window and 2nd grade interpolating function [132];
- SNV transform [120];
- Normalisation obtained by division of each variable by the sum of the absolute value of all selected variables for the given sample. This results in a vector with an area under the curve equal to 1 [136] (Norm1 in the text);
- Normalisation obtained by extracting the square root of the sum of the squared value of all the selected variables for a given sample. The function returns a vector of length equal to 1 [136] (Norm2 in the text);

Those pre-processing strategies were explored either alone or in combination, with or without class centering (**Equation 2.4**). Mean centering always followed the implementation of pre-processing on each data matrix. Model construction without any pre-processing apart from mean centering was also investigated as a potential approach. The combination of the described options resulted in the construction of 92 models for each technique. To avoid overestimation of the model's performances due to overfitting during cross-validation, this stage was carried out leaving one sample out at each iteration of the process. In detail, at each step of the iteration, a model was constructed, with all sampling times of one bloodstain excluded. The excluded data were then used in prediction, and a root mean square error in cross validation (RMSECV) was calculated. After the process was repeated for all bloodstains, an average RMSECV was calculated and designated as the final RMSECV for that specific model. This cross-validation technique will be referred in the text as sample-wise cross-validation. The model to be used in prediction was determined by identifying the model that minimised the RMSECV and, when RMSECV of the top-ranking models did not differ significantly, the model with the lowest number of latent variables was selected.

In order to perform a more in-depth evaluation of the reliability of the model performances, a permutation test was applied on the chosen models. The permutation test is a statistical test that involves randomising the order of the rows in the data matrix X, but not in the response matrix Y. this process is employed to ascertain whether the selected model is significantly different in terms of performances when compared to a model randomly built from the same data [137]. In this study, a permutation test was conducted utilising the built-in tool of the PLS_Toolbox 9.2 (Eigenvector Research Inc., Manson, WA, USA) [138].

The final models were then applied to the test set in order to evaluate the prediction ability of the regression. Root mean square error in prediction (RMSEP) was calculated on the test set data and used as an indication of the dating ability of the model.

2.1.3.3.3 Data fusion

Then, techniques combination explored. First, low-level data fusion [139] was employed, which entails the concatenation of variables through the juxtaposition of matrices. This procedure can be directly applied when the same sample is analysed with more than one analytical technique, simply by constructing a new matrix with all variables on the columns. Conversely, some precautions must be taken when analysing different samples with the two techniques, even though they may be the same type. In the context of the present study, different bloodstains were analysed with UV-Vis and NIR spectroscopy. Consequently, a strategy was devised to address the samples analysed with these two techniques as the same sample.

In this study, the information for a specific subject at a specific time was considered as a unique sample. For instance, as demonstrated in **Figure 2.11**, for subject S in Summer Session 1, an average spectrum of the three single bloodstains produced by this subject (S1, S2, S3) was calculated at each sampling time, yielding a unique spectrum for subject S at each sampling time for both techniques. The unique spectra were then concatenated, juxtaposing UV-Vis and NIR wavelengths in the final matrix, which had a number of rows that was one third of the starting matrix (96) and a number of columns that was the sum of the number of variables of UV-Vis and NIR spectra (2052). The division of the training and test sets was executed in accordance with the strategy previously outlined for the non-fused matrices, yielding 6 samples x 12 sampling points = 72 rows in the training set and 2 samples x 12 sampling points = 24 rows in the test set.

Following the concatenation of the variables, a new PLS-R model was calculated on the fused training set data. Pre-processing on the fused variables was undertaken using two different approaches:

1. The fusion of already pre-processed data, achieved by employing the same pre-processing techniques that were selected following the optimisation procedure conducted for individual PLS models. Consequently, the NIR and UV-visible pre-processing are optimised independently, and subsequently a single model is calculated on the fused data by applying mean centering only as additional pre-processing.

2. Raw data from both NIR and UV-Vis spectroscopies are fused, and then the pre-processing optimisation process is repeated on the fused matrix as previously described. consequently, the NIR and UV-Vis spectra are subjected to the same pre-processed procedures, and the model is selected based on the optimal pre-processing strategy for the combined data. The final low-level data fusion regression model was selected minimising the RMSECV, calculated using sample-wise cross-validation as previously described.

Also in this case, the performance of the models were evaluated through the implementation of a permutation test. The final step of low-level data fusion was to apply the model on the test set and calculate the RMSEP with the ultimate objective of assessing the efficacy of low-level data fusion in improving the performance of bloodstain dating.

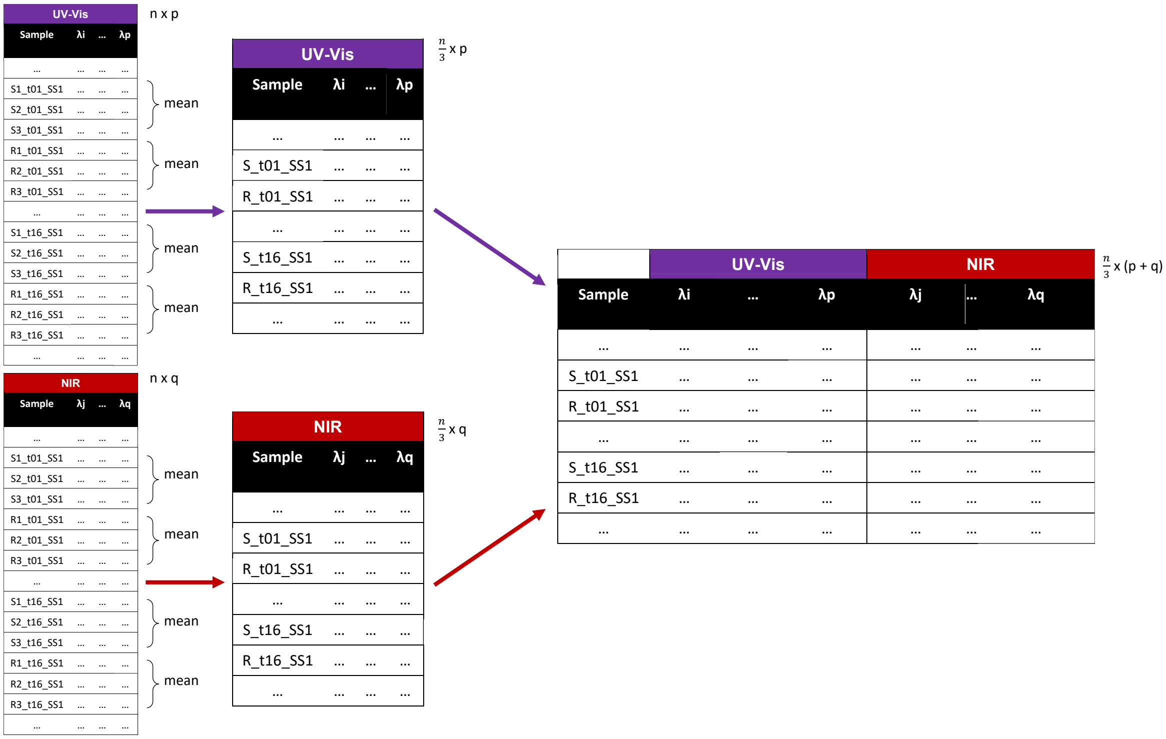

Figure 2.11: Graphical representation of the process of low-level data fusion.

Lastly, mid-level data fusion was implemented. Mid-level data fusion is a data concatenation technique which uses independent regression models built on the same samples analysed with different techniques and brings together the respective significant latent variables with the aim of building a new regression model [139]. Once more, in order to apply this technique, it was necessary to render the samples analysed with UV-Vis and NIR spectroscopies confrontable. The same strategy described for low-level data fusion was therefore applied. In this case, no further pre-processing optimisation was needed, given that the use of latent variables obtained from an already optimised regression model signifies that the data must undergo independent pre-processing. The samples were divided into training and test sets, as previously described for low-level data fusion. Then, a new PLS regression model was trained on the new variables using sample-wise cross-validation for model selection and permutation test for model evaluation. Finally, the model was applied to the test set data, and the RMSEP was calculated to assess mid-level data fusion potential in improving dating agilities for forensic bloodstains.

2.1.4 Conclusions

The present study attempted bloodstains dating for forensic purposes by utilising two complementary spectroscopic tools, namely UV-Vis and NIR spectroscopies. This complementarity arose from the different capabilities of the methods in monitoring degradation processes. Indeed, the former primarily tracked the structural changes in haemoglobin, while the latter provided information about the loss of the aqueous part of the bloodstain. Indeed, as demonstrated by the presented research, the combination of the information provided by the two spectroscopic ranges, which are mutually complementary, helped to estimate the age of bloodstains with a greater degree of accuracy.

The first objective of the present research was to compare the capabilities of both methods, applied independently, in dating bloodstains. In order to evaluate their performances, PLS regression models, and more precisely RMSEP, were used as a qualitative indication of the performance of these techniques. Consequently, it was possible to identify certain differences between UV-Vis and NIR spectroscopy in the context of bloodstain dating. The superiority of UV-Vis with class centering suggested its potential as a leading method (RMSEP ~ 40 hours), provided the right pre-processing strategies are employed. On the other hand, NIR spectroscopy (RMSEP ~ 50 hours) exhibits robustness and relative independence from pre-processing steps, indicating its resilience in forensic applications. Even more interesting is that both UV-Vis and NIR spectroscopies showed a good degree of independence of results from blood donors. This observation holds great promise, suggesting the possibility to use blood samples for ageing studies and practical blood dating obtained from subjects different than the individuals who left traces at the scene of an incident. It is evident that the study of a greater cohort of subjects would be needed to better account for biological variability and therefore to draw solid conclusions in this respect. Nevertheless, these results can be regarded as proof that blood donors may not be influential in building a model for bloodstain dating.

The second stage of the research involved the merging of spectroscopic data in the context of data fusion, to verify whether UV-Vis and NIR spectroscopies combination would enhance the process of estimating time elapsed since bloodstain deposition. Mid-level data fusion technique was demonstrated to reduce RMSEP, reaching a value of 36 hours when class centering was applied to UV-Vis datasets. This represents the lowest value obtained in this study. This finding served to corroborate the initial hypothesis regarding the potential enhancement of blood age estimates through the implementation of complementary spectroscopic methods, delineating further research paths.

In order to advance this research, it would be necessary to explore the synergies between different spectroscopic methods and advanced chemometric approaches (*e.g.*, data fusion) with a view to developing a more comprehensive and accurate bloodstain dating methodology. This multidimensional approach has the potential to refine forensic practices and strengthen the reliability of age estimation in criminal investigations, thereby laying the foundation for future endeavours to bridge the gap between laboratory findings and real-world forensic challenges.

2.2 UNDERSTANDING THE EFFECT OF ENVIRONMENTAL CONDITIONS AND DEPOSITION SUBSTRATE ON BLOODSTAINS AGEING

2.2.1 Introduction

Despite the undeniable advantages of using spectroscopies for bloodstains dating, as previously discussed in this chapter, the technique can be affected by interferences arising both from the background and from the environmental conditions in which specimens are stored between deposition and analysis. Indeed, one of the main strengths of spectroscopy is the ability to analyse blood samples directly on their deposition substrate without extraction or other preparation steps. However, this characteristic may also imply a non-negligible background contribution to the spectral signature, which depends on sample presentation (*e.g.* thickness, volume, penetration into the substrate) and possibly on the wavelength range used for analysis. In forensic practice, blood is expected to be found on a variety of surfaces, many of which have their own spectral features that could obscure blood signals [140].

As expected, UV-Vis spectroscopy is the most affected by changes in background colour, while this limitation can be overcome by using IR spectroscopy [97]. Only a few studies have explicitly considered substrate characteristics. Among them, Manis *et al.* [95] employed NIR spectroscopy combined with hyperspectral imaging to investigate blood-substrate interactions and demonstrated that bloodstains aged on hydrophilic substrates (*e.g.*, cotton) can be described with dating models yielding better predictive performances than those on hydrophobic substrates (*e.g.*, polyester). Similarly, Mengual-Pujante *et al.* [141] explored the use of absorbent substrates (cotton, filter paper, and regular paper) through ATR-Fourier transform IR (ATR-FT-IR) spectroscopy, showing that non-rigid, absorbent supports are ideal for the ATR measurements since they allow the use of the sample without resuspension or sample damage. They also demonstrated that regression models trained without accounting for the substrate, *i.e.* models that combine samples on cotton, paper, and filter paper, perform worse than those developed for each substrate separately. Using the same technique, bloodstain ageing on three types of soil substrates was also investigated [114], producing separate models for each soil type. Gautam et al [142] applied the same approach using Raman spectroscopy to predict TSD for bloodstains deposited on facial tissue, floor tile, and linoleum, confirming that absorbent substrates provide better predictive outcomes than non-absorbent ones.

These findings support the hypothesis that the background may not only introduce spectral interferences but also influence the aging kinetics of bloodstains, either accelerating or slowing chemical transformations in the sample. This latter aspect is crucial: while spectral interferences can be corrected through chemometric approaches, chemical and physical alterations in blood degradation kinetics can compromise the feasibility of global models capable of addressing diverse scenarios.

Therefore, the study of ageing kinetics and of the factors that may modify it is of paramount importance. In this context, temperature, humidity and light exposure are the most frequently studied factors, and their influence on bloodstain degradation and dating has been repeatedly reported [89,140]. For instance, three studies [113,114,141] developed dating models using ATR-FT-IR spectroscopy on samples stored either under laboratory conditions or outdoor conditions. However, temperature and humidity were not monitored, preventing firm conclusions about their actual effects. The main objective of these studies was in fact to increase sample variability to improve model robustness, yet the impact of this variability on ageing was largely overlooked. Moreover, both Mengual-Pujante *et al.* [141] and Lin *et al.* [113] observed that merging models derived from indoor and outdoor samples led to poorer dating performance, suggesting that the conditions may indeed affect the ageing rate. The role of storage temperature in bloodstain ageing has also been explored using UV-Vis [115,143], and Raman spectroscopy [112,144], but in all cases, temperature and/or humidity were examined individually and with the sole aim of producing single dating models. Consequently, both the individual and combined effects and interactions among the factors, such as temperature, humidity, illumination and substrate, remain unaddressed. This information would however be extremely relevant in real-case scenarios, and even more if we consider that clear guidelines for forensic practitioners are needed in order to ensure efficient sampling and on-scene proof collection.

Such an in-depth understanding of factors' effects and their interaction can be carried out by means of design of experiment (DoE) and analysis of variance (ANOVA) [145], and when dealing with multivariate dataset, such as those deriving from spectroscopic techniques, multivariate analysis of variance techniques such as ANOVA simultaneous component analysis (ASCA), multivariate ANOVA (MANOVA) and regularised MANOVA (RMANOVA) are the most suitable [146–148]. In particular, MANOVA is a statistical method employed to explore factors effect and their interrelations when samples are described with multiple variables [147,149]. Compared to ASCA [146,150], arguably the most used approach in this application field, MANOVA has the advantage of considering eventual interaction between variables along the whole process, including the dimension reduction step, potentially providing more precise results. However, MANOVA is limited by the fact that it can only be applied when the number of samples is (much) higher than that of variables to obtain reliable statistics from the results [148]. RMANOVA overcomes this drawback by applying a shrinkage function, thus maintaining the information and becoming applicable even when the number of variables is (much) larger than the number of samples [146,148].

These approaches have already been proven useful in several fields of research, such as food chemistry [151–153] and biology [154,155]. In particular, one study proved that the application of ASCA on NIR spectra of honey was able to discriminate and describe the effect of temperature, irradiation, adulteration and time on honey samples [156]. However, to date only one study [93] has applied these techniques in a forensic framework. In particular, RMANOVA was used to determine whether an acquisition configuration in Raman spectroscopy yielded better result than the classical configuration for bloodstain dating. No application of those techniques have, to date, ever been applied to ruling out the effect of environmental conditions and substrate of deposition on bloodstain ageing.

In the described context, this study aims at analysing, quantifying and comparing the effects of climatic conditions (intended as covariation of temperature and humidity), illumination and substrate of deposition of samples on forensic bloodstains ageing process, in order to rule out which of the factors have a significant effect and focusing on their interactions. To reach this goal, bloodstains were deposited on four substrates (cotton, polyblend fabric, glass and metal) and aged in four different environmental conditions, controlling temperature, humidity, and illumination and mimicking the real day-night alternance by means of a climatic chamber equipped with a solar lamp. The ageing of all samples was followed for two weeks, for a total of fourteen sampling times, by means of a portable NIR spectrophotometer and a benchtop Raman microscope. This experimental scheme allows, as an additional outcome, to study the differences in factors' effects with respect to the chosen analytical technique. It is important to notice that, to address the significance, all the studied effects were compared both with typical statistical thresholds (p value) and with the effect of subject, treated as a dummy factor. This data processing strategy was intended to verify if the importance of evaluating environmental conditions and substrate of deposition is greater than that of blood donor.

2.2.2 Results and discussion

2.2.2.1 Experimental protocol

The backgrounds used for deposition were two fabric substrates, namely cotton and polyblend, one glass substrate, namely microscope glass slides, and one metal substrate, namely table knife blades, adding up to a total of four different materials. After deposition, samples were immediately stored in a climate chamber, a device designed to maintain controlled temperature, humidity and illumination at specified levels for a defined period of time, with the possibility of programming parameters to vary during the day and mimic a natural day-night alternation.

During this study, two climatic conditions were considered in terms of temperature and humidity: one with lower temperature and higher humidity (cold and wet – CW) and one with higher temperature and lower humidity (hot and dry – HD). Illumination had two different configurations as well:

1. through a glass window, mimicking indirect exposure to sunlight, as may happen within a building (indoor – I);
2. direct illumination, mimicking direct exposure to sunlight, as may happen in open air (outdoor – O).

Each setup mimicked the day-night alternation by means of cycles of 12-hours cycles of light and dark, switching respectively on and off a UV lamp and alternating warmer temperature and lower humidities when the lamp was on, to colder temperatures and higher humidities when it was off. The conditions were combined in all possible pairs, thus resulting in a total of four analytical sessions.

***Table 2.5**: Detail of temperature, humidity and illumination conditions in the four analytical sessions.*

Condition name	**Day**			**Night**		
	Temperature (°C)	***Humidity (RH%)***	***Illumination (lamp / window)***	***Temperature (°C)***	***Humidity (RH%)***	***Illumination (lamp / window)***
HD_O	35	60	On / no	20	75	Off / no
HD_I	35	60	On / yes	20	75	Off / yes
CW_O	20	75	On / no	10	90	Off / no
CW_I	20	75	On / yes	10	90	Off / yes

The specific temperature, humidity and light configuration during day and night for each session are detailed in **Table 2.5**.

As shown in **Table 2.5**, temperature and humidity were not considered as separate factors, but were allowed to covary, thereby mimicking realistic conditions in the Mediterranean area. Therefore, the combination of these two conditions was considered as a single factor, referred to as “T&RH” throughout the text. This approach was adopted to reproduce real-world conditions as closely as possible, in which temperature and humidity are inherently correlated and tend to covary.

Consequently, the configuration of the whole experiment followed a full-factorial design of experiments (DoE) [145] with three qualitative factors: two at two levels (T&RH and illumination) and one at four levels (substrate). All factors and levels are reported in **Table 2.6**.

***Table 2.6**: Summary of correspondences between levels of each factor.*

Factor	**Factor name**	**Levels**			
		-1	***-0.33***	***+0.33***	***+1***
T&RH	A	CW	/	/	HD
Illumination	B	Lamp off	/	/	Lamp on
Substrate	C	Cotton	Polyblend	Metal	Glass

This design matrix was repeated for each of the two studied subjects. The subject may be considered as a fourth factor at two levels (A and B), though its effect was not of interest. Indeed, while it is possible that the subject might have an effect on blood ageing, this factor is rarely controllable in real-case scenarios, since the blood source might be unknown or unavailable. Therefore, the subject was treated as a dummy variable in the present study, meaning that other factors were considered significant only when they were statistically significant and their effect exceeded that of the subject. Although the use of a higher number of subjects with more diverse characteristics would be preferrable for model development, this was not the aim of the current work, which instead focuses on proposing an analytical strategy and not a ready-to-use model.

2.2.2.2 Data exploration

2.2.2.2.1 Profiles observation

First, the evolution of spectra over time was analysed both for NIR and Raman spectroscopies, to visually confirm the ability of the selected methods to describe the ageing process. To this aim, the spectra were averaged, yielding one average spectrum for each sampling time, which was then plotted and colour-coded according to time (in hours), as illustrated in **Figure 2.12**.

Both NIR and Raman spectra already showed a clear time dependence when raw signals were examined. In particular, NIR spectra exhibited a total intensity effect (**Figure 2.12A**), with aged samples (yellow in the figure) showing lower transflectance values compared to "fresh" ones (blue in the figure). This effect was most likely due to the combined influence of water evaporation caused by sample drying over time and scattering changes resulting from the cracking of bloodstains. The application of SNV transform (**Figure 2.12B**) further emphasised the effect of time, highlighting the presence of a strongly absorbing region between 1200 and 1400 nm, attributable to the second overtone of O–H stretching.

Regarding Raman spectroscopy, **Figure 2.12C** showed a clear total intensity effect together with a multiplicative effect related to the time trend, with aged samples displaying higher signal intensities due to increased fluorescence in aged blood samples, as already reported in the literature [92,93,157,158]. One possible explanation for this phenomenon was the accumulation of haemoglobin (Hb) degradation products that exhibit stronger natural fluorescence than oxyhaemoglobin (oxyHb), which was the main form found in "fresh" blood. According to previous studies [159–161], one of these fluorescent Hb byproducts was hemichrome, which resulted from natural blood degradation [158] and showed strong fluorescence [162]. Moreover, further degradation may continue over time, leading to the formation of additional heavily degraded Hb forms that displayed fluorescent properties, possibly due to the breakdown of its subunits and the release of iron ions [159–161].

After baseline correction using automatically weighted least squares (AWLS), age-dependent spectral alterations became more evident. These spectral changes, particularly evident within the 300–1700 cm^{-1} region, provided molecular insight into the degradation pathways of haemoglobin and could serve as valuable markers for estimating the age of bloodstains in forensic applications [93,158,163]. Notably, the band around 377–380 cm^{-1}, attributed to vibrational modes characteristic of methaemoglobin (metHb), showed a progressive increase in intensity over time, reflecting the gradual auto-oxidation of oxyHb to metHb during blood degradation [158]. In the 900–1000 cm^{-1} region, variations were observed in the relative intensities of the bands at approximately 976 cm^{-1} and 1003 cm^{-1}. The band near 976 cm^{-1}, associated with heme aggregation and degradation products, increased in intensity relative to the phenylalanine ring-breathing mode at 1003 cm^{-1}, which remained relatively stable. The intensity ratio between these two bands therefore served as an additional metric to differentiate bloodstains according to their age, indicating progressive heme aggregation and structural changes within haemoglobin derivatives. Notably, bands associated with non-heme components of Hb, such as the amide I band at approximately 1655 cm^{-1}, exhibited minimal variability over time. Their relative stability suggested that the protein backbone remained largely unaffected during the early stages of *ex vivo* degradation, and that the observed spectral changes primarily originated from the heme prosthetic group and its immediate environment.

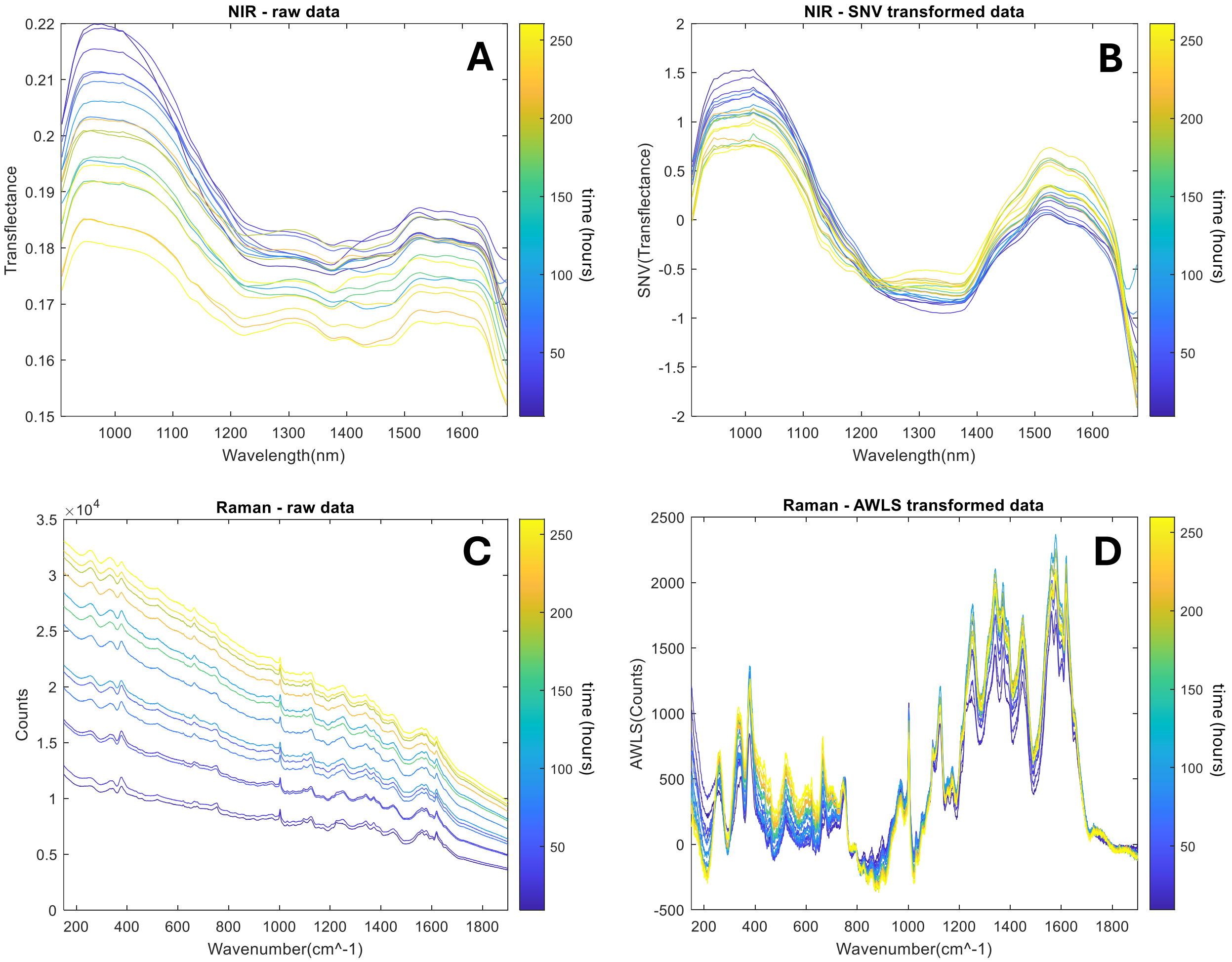

Figure 2.12*: Spectral profiles of samples averaged over time. A: Raw NIR spectra; B: SNV transformed NIR spectra; C: Raw Raman spectra; D: AWLS transformed Raman spectra. Spectra are colour-coded according to sampling time in hours.*

These findings highlighted the suitability of Raman spectroscopy as a complement to the temporal information obtained from NIR spectroscopy, with both methodologies offering a valuable framework for tracking the influence of external factors on the aging process of bloodstains – an approach that may be further enhanced through multivariate analysis techniques.

2.2.2.2.2 PCA

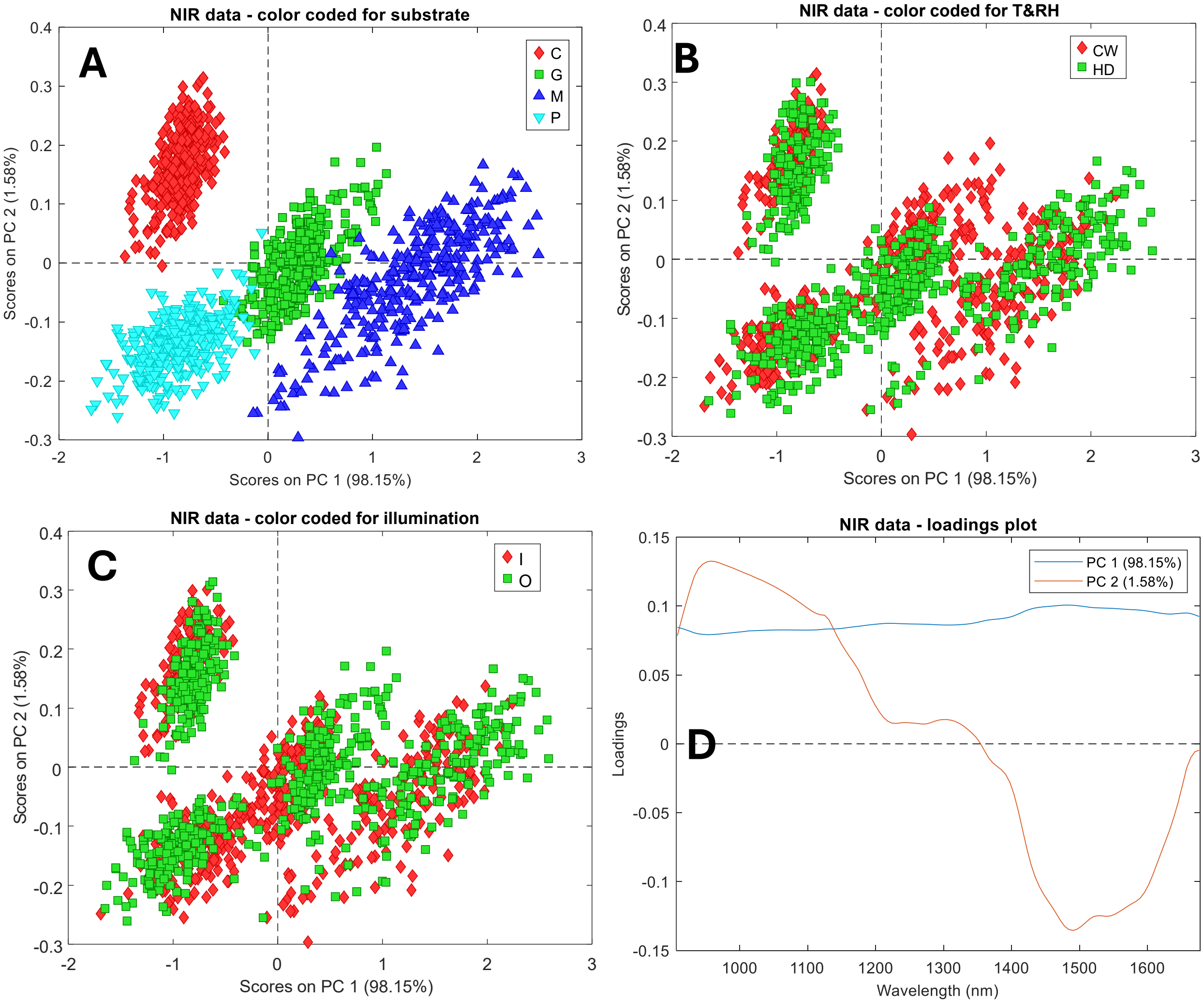

***Figure 2.13**: Score and loading plots obtained from PCA on raw data for NIR spectroscopy, colour-coded for the different factors and levels under analysis. A: Score scatter plot colour-coded according to substrate (C = cotton, G = glass, M = metal, P = polyblend fabric); B: Score scatter plot colour-coded according to T&RH; C: Score scatter plot colour-coded according to illumination; D: Loading line plot.*

The exploration of the data continued with the application of PCA, which was used to identify groupings within the data and to make an initial evaluation of the main sources of variability for the two techniques. **Figure 2.13** and **Figure 2.14** display the resulting score and loading plots for NIR and Raman spectroscopies respectively.

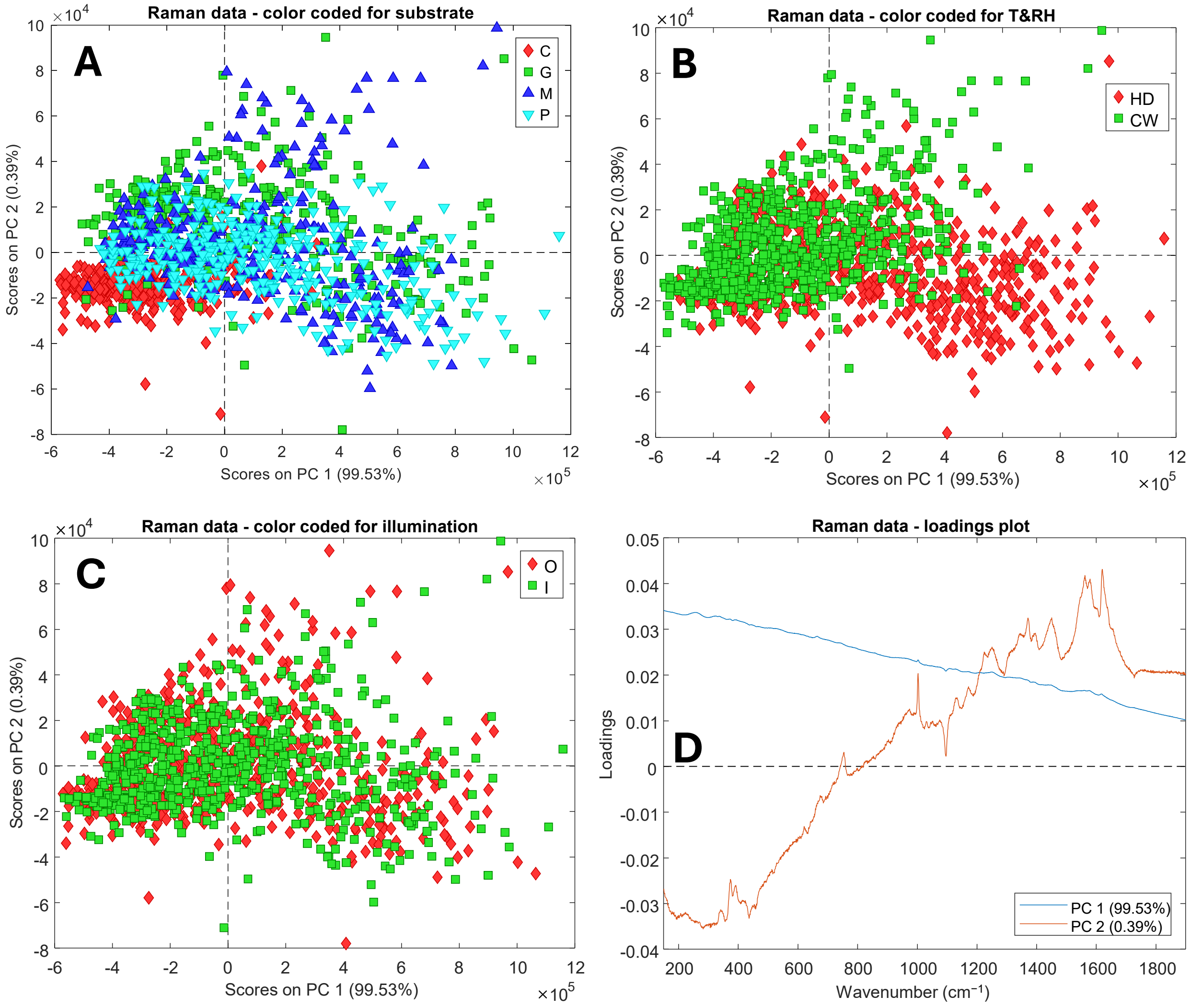

Figure 2.14*: Score and loading plots obtained from PCA on raw data for Raman spectroscopy, colour-coded for the different factors and levels under analysis. A: Score scatter plot colour-coded according to substrate (C = cotton, G = glass, M = metal, P = polyblend fabric); B: Score scatter plot colour-coded according to T&RH; C: Score scatter plot colour-coded according to illumination; D: Loading line plot.*

The score plots obtained for NIR spectroscopy revealed that the main source of variability associated with this analytical technique was the difference between substrates (**Figure 2.13A**). In particular, PC1 differentiated between fabrics substrates (cotton and polyblend) and non-absorbing substrates (glass and metal), while PC2 distinguished cotton from all the other substrates. Examining the loadings, it was observed that PC1 explained a total intensity effect. This suggested that global reflectance depended on the substrate, and probably reflected the physical interaction of radiation with the material, which justified the distinction between fabrics and non-absorbing substrates. This difference likely originated form the fact that fabrics are less reflective than glass and metal. Conversely, the loadings on PC2 mostly displayed bands; therefore, this principal component likely summarised the chemical information, explaining the differences between substrates. Indeed, cotton, which had the most distinctive spectral signature compared to the other materials used, was the substrate with higher scores on this component.

Regarding the other two factors of interest, some shifts were visible for T&RH and illumination as well, along both PC1 and PC2 (**Figure 2.13B** and **2.13C**), suggesting that the effects of these two factors were also related to chemical and physical proprieties. However, the effect of substrate appeared to be too strong compared to that of T&RH and illumination, which were therefore masked and could not be clearly distinguished in the PCA space.

When considering results obtained from Raman spectroscopy, the main source of variability was more difficult to identify. In particular, in **Figure 2.14A**, where the samples in the PCA space are coloured according to substrate, the effect of this factor was in this case limited to cotton, which formed a group at negative values of PC1 and PC2, while the other three materials overlapped, covering the remaining PC space. Conversely, some differences and grouping were also observed when considering the T&RH factor, as displayed in **Figure 2.14B**, where samples from the HD level (red in the figure) showed higher values of PC1 and lower values of PC2 compared to samples from the CW level (green in the figure). This suggested that this factor might have had a high influence on Raman spectroscopy. In contrast, grouping could not be identified for the illumination factor (**Figure 2.14C**). However, this lack of grouping could not be taken as evidence of a non-significant of the factor overall, since it might have accounted for a smaller portion of the variability not captured by PCA.

From the analysis of loadings (**Figure 2.14D**) it resulted that PC1 explained a total intensity effect combined with a multiplicative one due to fluorescence. This suggested that sample of the HD level (red in the figure), which were located at more positive values of PC1, might have been characterised by a faster increase in fluorescence. Since an increase in fluorescence is connected to the ageing process, as discussed in the previous section, a higher fluorescence in HD samples may indicate that the blood stored under this condition underwent a faster ageing compared to that stored in the CW condition, thus suggesting that changes in temperature and humidity indeed modified the ageing kinetics. A similar observation was derived from PC2, whose loadings described a multiplicative effect, again associated with the ageing of samples, previously as described.

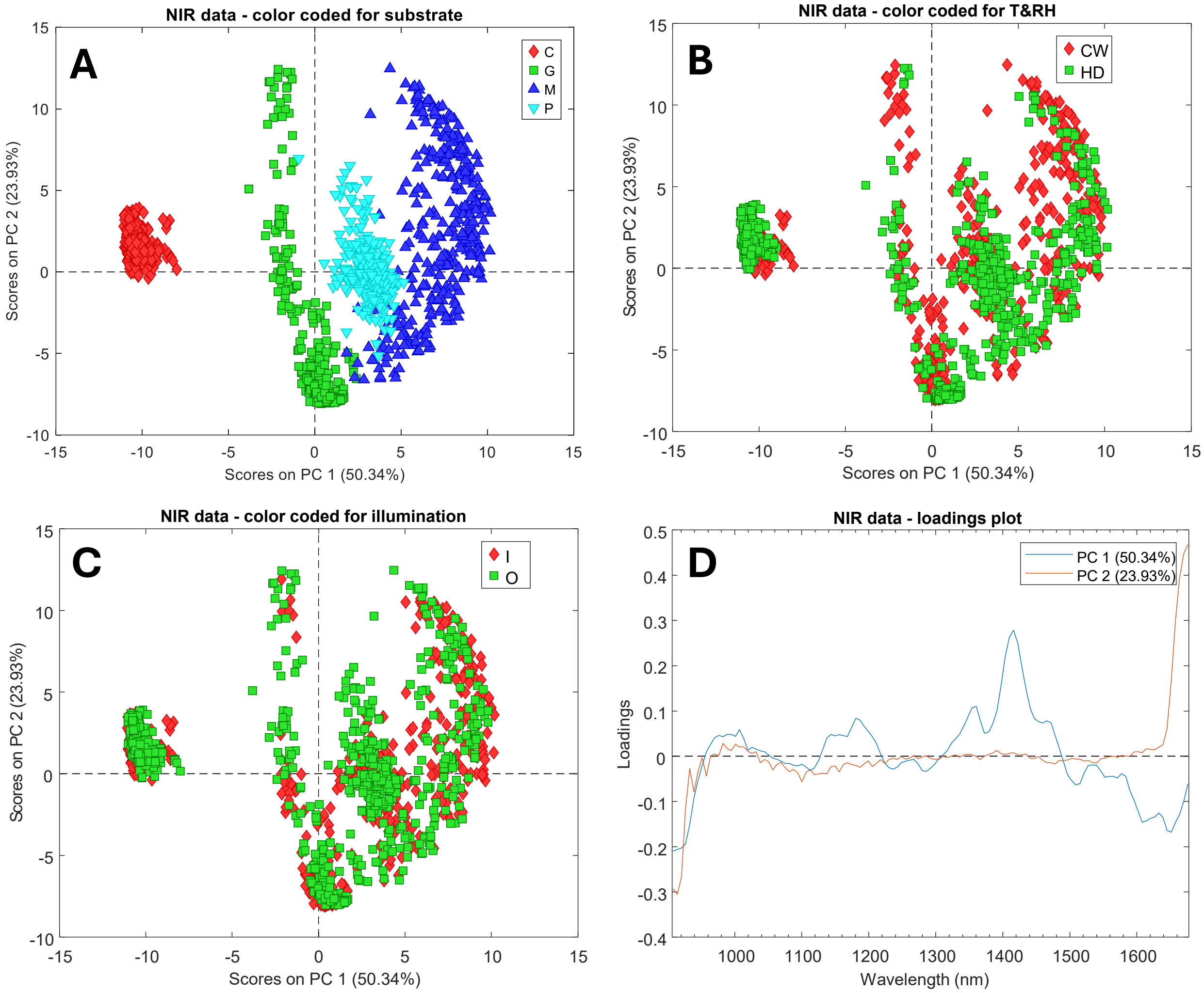

***Figure 2.15**: Score and loading plots obtained from PCA on SNV transformed data for NIR spectroscopy, colour-coded for the different factors and levels under analysis. A: Score scatter plot colour-coded according to substrate (C = cotton, G = glass, M = metal, P = polyblend fabric); B: Score scatter plot colour-coded according to T&RH; C: Score scatter plot colour-coded according to illumination; D: Loading line plot.*

The comments drawn from the PCA built on raw data – motivated by the intention to interpret the chemical phenomenon without the presence of possible interferences or artefacts introduced by the algebraic transformations typical of pre-processing [131] – were also confirmed repeating PCA for both NIR and Raman spectroscopies on pre-processed data.

In particular, NIR data were pre-processed using the SNV transform and were subsequently subjected to PCA. The results of this analysis were illustrated in **Figure 2.15**, which presents the corresponding score and loading plots. From the score plots, it was evident that the application of pre-processing had promoted a clearer separation of factor-related information, which was now primarily captured by PC1 and was mainly associated with the background (**Figure 2.15A**). Similarly to the raw data, grouping could not be clearly identified according to either T&RH (**Figure 2.15B**) or illumination (**Figure 2.15C**). When examining the loading plot (**Figure 2.15D**), PC1 revealed three bands around 1350-1450 nm, likely corresponding to the spectral signature of the background materials. A comparison between this profile to that previously reported in **Figure 2.13D** showed that the use of SNV transform effectively mitigated the total intensity effect identified earlier, thereby enhancing the visibility of the chemically relevant features in the PCA results. Conversely, PC2 did not display any characteristic pattern and appeared to represent mainly noise concentrated at the extremes of the wavelength range.

Raman spectra where pre-processed using the automatically weighted least squares (AWLS) method [164] and then re-analysed through PCA (**Figure 2.16**). In this case as well, the application of the pre-processing did not alter the information represented in the score plots compared with that observed for the raw data. The main outcome was an improved deconvoluting the information associated with the substrate, which was now primarily captured by PC2. The inspection of **Figure 2.16A** confirmed that only cotton, located at positive values of PC2, could be clearly distinguished from the other substrates, which remained largely overlapped in the lower portion of the PC space. This suggested that Raman was capable of discerning the substrate influence when the substrate was absorbent, while partially (polyblend fabric) or completely (glass and metal) non-absorbing materials did not significantly affect the spectral signature of the blood.

Conversely, the application of the pre-processing reduced the grouping associated to the T&RH factor (**Figure 2.16B**), supporting the hypothesis that its effect was linked to the baseline shift evident in the raw data ad eliminated by the AWLS correction. No grouping was observed when the data were colour-coded according to illumination (**Figure 2.16C**), confirming what had been previously observed in the raw data.

When examining the loading plot (**Figure 2.16D**), it became apparent that PC1 contained chemical information mainly associated with the 1200-1600 cm^{-1} range, whereas PC2 showed a strong contribution from a sharp peak around 1100 cm^{-1}, which was subsequently confirmed to be characteristic of cotton absorption. This observation further substantiates that the dominant course of variability in this component was indeed the information related to the absorbing background.

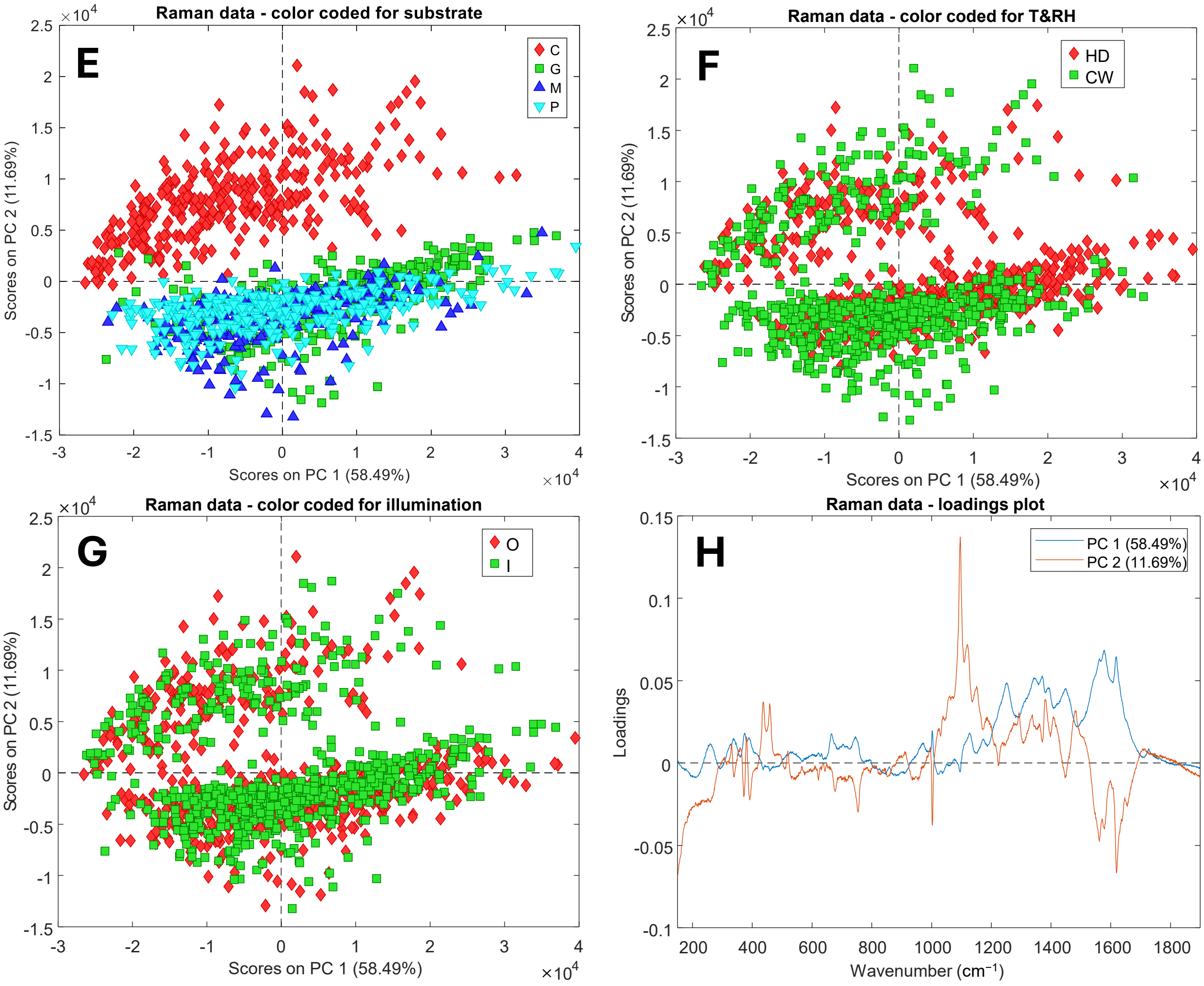

__Figure 2.16__: Score and loading plots obtained from PCA on AWLS transformed data for Raman spectroscopy, colour-coded for the different factors and levels under analysis. A: Score scatter plot colour-coded according to substrate (C = cotton, G = glass, M = metal, P = polyblend fabric); B: Score scatter plot colour-coded according to T&RH; C: Score scatter plot colour-coded according to illumination; D: Loading line plot.

Subsequently, all score plots were colour-coded according to time trend, and the results are reported in **Figure 2.17**. No clear time trend could be identified in the score plots for NIR data, neither when data were kept raw (**Figure 2.17A**) nor when they were pre-processed using the SNV transform (**Figure 2.17C**). In particular, in raw data only the group of samples corresponding to cotton showed some information associated to time, which was represented along PC2, with "fresh" samples at positive values (blue in the figure) and aged samples nearer to 0 (yellow in the figure). When data were pre-processed, a hint of trend could still be observed in the cotton group, along PC1, with aged samples at more negative score values and "fresh" samples at less negative score values. Information about the time trend could also be partially observed in the glass group, with aged samples condensed at negative values of PC2 and "fresh" samples spread across positive PC2 scores.

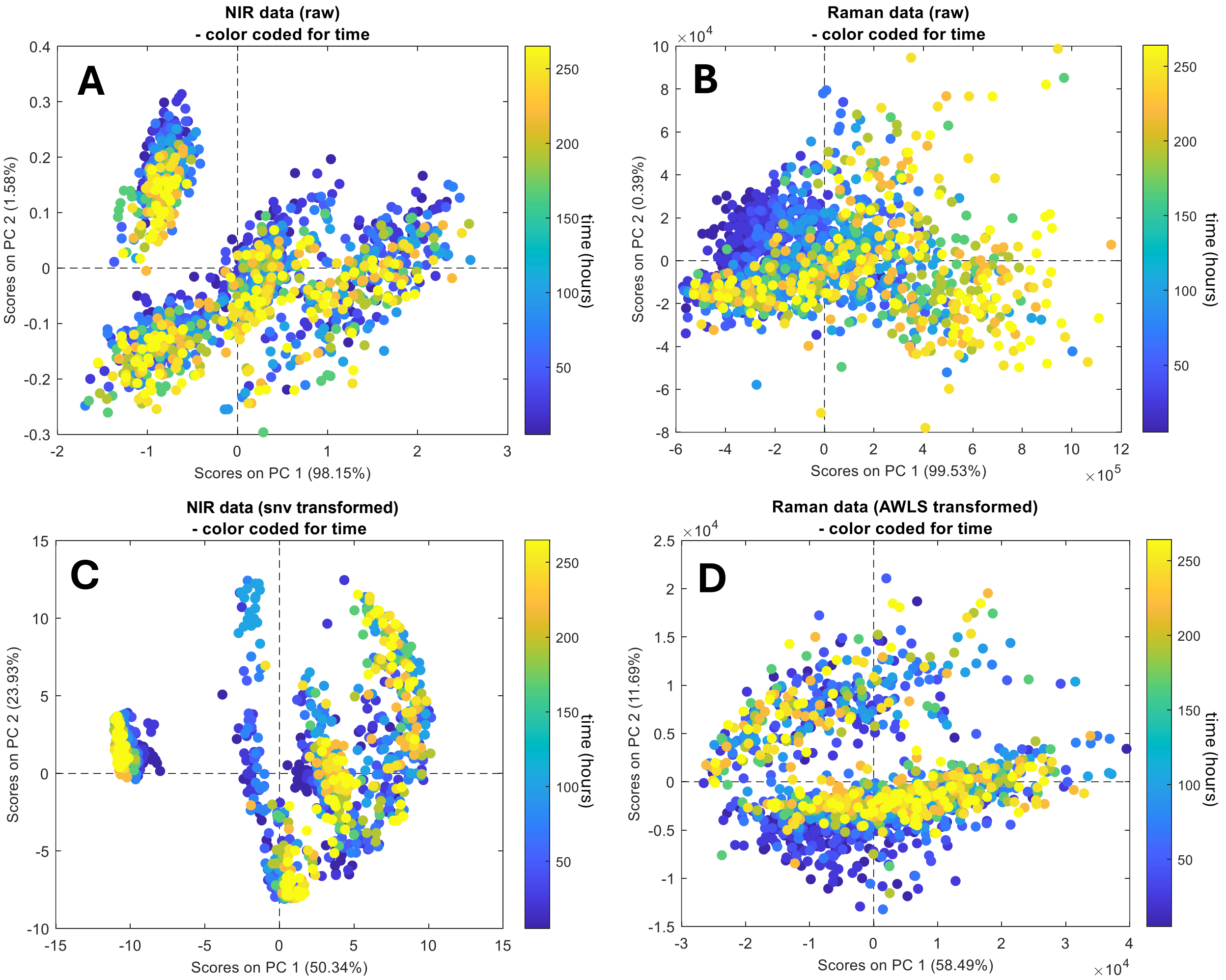

***Figure 2.17**: Score scatter plots colour coded according to measurement time. A: NIR raw data; B: Raman raw data; C: 1st derivative + SNV transformed NIR data; D: AWLS transformed Raman data.*

Conversely, for Raman data, the information related to the time trend appeared to represent the main source of variability on raw data. Indeed, if the group corresponding to cotton in the third quadrant of the PC space is ignored, the remaining substrates presented “fresh” samples at negative values of PC1 and aged samples at positive values of this component. This was also confirmed by comparing these results to the loading plot previously discussed (**Figure 2.14D**), where PC1 described a total intensity effect, which was also the main variation associated to ageing of samples. On the other end, the time trend was lost when data were pre-processed using AWLS (**Figure 2.17D**).

Despite the valuable insights that were provided regarding the effect of factors on the distribution of variability within the spectral signature, PCA proved to be insufficient for fully deconvoluting the information associated with individual factors and their levels, whether applied to raw or pre-processed data. This indicated that more sophisticated variance deconvolution techniques were required to achieve the intended outcomes.

2.2.2.3 Factors analysis

2.2.2.3.1 Extraction of features

The first step towards deconvoluting the effect of factors involved feature extraction and concatenation by means of partial least squares regression, with the aim of obtaining a single signal representing the entire ageing process for each blood sample (see the Materials and methods section for further details). To this end, a regression model was trained for each of the sixteen experimental conditions for both instruments, resulting in a total of 32 regression models. The figures of merit of the resulting models are reported in **Table 2.7** and **2.8** in for NIR and Raman spectroscopy, respectively.

The optimal number of significant latent variables was determined for each of the 32 models by minimising the RMSECV/RMSEC ratio. Across all models, the minimum number of latent variables selected NIR spectroscopy was three, for both pre-processing strategies, *i.e.* SNV transform alone or 1st derivative followed by SNV transform. For Raman spectroscopy, the minimum number of latent variables across all models was 3 for raw data and 2 for AWLS transformed data. Since an identical number of features had to be extracted for all samples, the number of latent variables was set to the minimum value identified across all models, ensuring consistency, and the corresponding RMSECV was calculated (RMSECV* in **Table 2.7 and 2.8**).

***Table 2.7**: Model results for NIR spectroscopy. LV* and RMSECV* represent the number of chosen latent variables and the RMSECV of the model when the number of latent variables was kept constant across all conditions.*

Condition	**1st derivative + SNV transform**				**SNV transform**				**Selected pre-processing**
	LV	***RMSECV***	***LV****	***RMSECV****	***LV***	***RMSECV***	***LV****	***RMSECV****	
C_HD_I	6	8.5	3	20.7	6	7.8	3	19.1	1st derivative + SNV transform
C_HD_O	5	9.0	3	15.9	9	6.0	3	15.0	
C_CW_I	6	13.0	3	33.3	5	24.1	3	39.6	
C_CW_O	5	18.2	3	34.2	6	30.5	3	37.1	
G_HD_I	3	34.1	3	34.1	4	29.6	3	32.2	SNV transform
G_HD_O	4	35.3	3	44.5	6	13.9	3	21.5	
G_CW_I	4	69.5	3	65.0	4	58.8	3	62.0	
G_CW_O	4	45.4	3	43.4	5	28.5	3	42.5	
M_HD_I	3	57.1	3	57.1	5	56.8	3	61.0	1st derivative + SNV transform
M_HD_O	3	54.5	3	54.5	5	40.6	3	54.3	
M_CW_I	3	54.3	3	54.3	3	68.9	3	68.9	
M_CW_O	4	64.3	3	72.6	5	76.7	3	75.8	
P_HD_I	6	12.3	3	23.4	7	12.1	3	15.5	1st derivative + SNV transform
P_HD_O	4	23.1	3	26.6	6	15.6	3	17.7	
P_CW_I	4	46.6	3	53.3	5	45.3	3	54.5	
P_CW_O	4	52.7	3	65.2	6	51.5	3	78.1	

The best pre-processing strategy was then selected for each substrate by choosing the pre-processing that minimised RMSECV at the identified number of LVs. For NIR spectroscopy, the best pre-processing was found to be the 1st derivative followed by SNV transform for cotton, metal and polyblend substrates, whereas SNV transform alone was optimal for the glass substrate. For Raman spectroscopy, the use of raw data proved to be the best choice across all conditions.

To verify robustness, the features extraction procedure was repeated three times, each time increasing the number of selected LVs by one. Results were comparable, thus demonstrating the stability of the selected approach. For this reason, only results corresponding to 3 LVs will be presented hereafter.

Although the objective of the regression step was not to develop fully reliable dating models for the different conditions, but rather to enable the extraction of features for use in the subsequent processing step, the performance of all models was considered sufficiently satisfactory to proceed, with an average RMSECV around 15% of the calibration range for both spectroscopic techniques.

***Table 2.8**: Model results for Raman spectroscopy. LV* and RMSECV* represent, respectively, the number of chosen latent variables and the RMSECV of the model when the number of latent variables is equal to LV*.*

Condition	**AWLS**				**Raw**				**Selected pre-processing**
	LV	***RMSECV***	***LV****	***RMSECV****	***LV***	***RMSECV***	***LV****	***RMSECV****	
C_HD_I	3	66.9	3	66.9	2	76.8	2	76.8	Raw
C_HD_O	3	51.8	3	51.8	2	66.2	2	66.2	
C_CW_I	3	36.0	3	36.0	2	61.0	2	61.0	
C_CW_O	3	38.1	3	38.1	3	41.9	2	52.4	
G_HD_I	3	33.3	3	33.3	2	45.5	2	45.5	Raw
G_HD_O	3	29.7	3	29.7	3	33.3	2	42.5	
G_CW_I	4	29.3	3	37.7	3	44.0	2	56.0	
G_CW_O	3	34.4	3	34.4	3	30.0	2	35.4	
M_HD_I	3	24.0	3	24.0	2	40.7	2	40.7	Raw
M_HD_O	3	30.2	3	30.2	2	41.5	2	41.5	
M_CW_I	3	30.8	3	30.8	3	37.2	2	45.0	
M_CW_O	3	34.8	3	34.8	3	34.6	2	39.7	
P_HD_I	3	31.3	3	31.3	3	38.7	2	39.9	Raw
P_HD_O	3	28.1	3	28.1	3	28.0	2	37.8	
P_CW_I	3	30.2	3	30.2	3	36.8	2	46.6	
P_CW_O	3	46.0	3	46.0	3	43.0	2	58.4	

As an additional outcome, the evaluation of the model performances provided valuable insights into the differences between the two analytical techniques. In particular, NIR spectroscopy performed exceptionally well on absorbing substrates, namely cotton (average RMSECV < 10% of calibration range), followed by polyblend (average RMSECV ~ 15% of calibration range), which exhibited intermediate absorbing properties. Conversely, metal yielded the poorest performance (average RMSECV ~24% of calibration range), likely due to its high reflectance and scattering characteristics, which interfered with the NIR spectra and hindered the regression capabilities.

On the other hand, Raman spectroscopy showed good performances on non-absorbing substrates, as indicated by comparable cross-validation errors for glass (average RMSECV ~11% of calibration range), metal (average RMSECV ~13% of calibration range) and polyblend fabric (average RMSECV ~13% of calibration range), whereas cotton performed worse (average RMSECV ~18% of calibration range), particularly under hot and dry conditions.

These findings highlighted that NIR and Raman spectroscopies exhibited contrasting behaviours with respect to substrate, showcasing a complementary performance with respect to absorbing and non-absorbing substrates. This outcome emphasised the necessity of selecting the most appropriate spectroscopic method on a case-by-case basis, after careful consideration of situation-specific factors such as substrate of deposition.

2.2.2.3.2 RMANOVA

The resulting data matrix, containing a single signal representing the blood ageing kinetics for each combination of factor levels, was subjected to RMANOVA in order to deconvolute of the effects of factors and their interactions, as reported in **Table 2.9**.

***Table 2.9**: Summary of RMANOVA results for NIR and Raman spectroscopies. Cells with a grey background refer to results for the dummy variable. ** = $p < 0.01$; * = $p < 0.01$ and $Effect_{factor} > Effect_{dummy}$.*

Factor	**NIR**		**Raman**	
	Effect (%)	***P value***	***Effect (%)***	***P value***
Dummy	2.4	0.026*	3.4	0.046*
Dummy × substrate	4.5	0.51	4.5	0.87
Dummy × T&RH	0.6	0.96	3.7	0.03*
Dummy × illumination	0.5	0.99	3.4	0.046*
Substrate	33.2	0.00001**	46.5	0.00001**
T&RH	5.2	0.0002**	12.5	0.00001**
Illumination	7.0	0.00001**	2.3	0.29
Substrate × T&RH	22.6	0.00001**	13.9	0.0009**
Substrate × illumination	18.4	0.00001**	7.9	0.088
T&RH × illumination	5.6	0.0002**	2.1	0.4

From a statistical perspective, it was apparent that virtually all experimental conditions tested (substrate, T&RH, illumination) exerted a significant effect on the kinetics of bloodstain ageing. In particular, substrate emerged as the most significant factor for both NIR and Raman spectroscopies. This factor accounted for the largest part of the variance and corroborated the trends observed in PCA.

Similarly, the effect of T&RH was found to be significant with both techniques, although it was slightly more pronounced for Raman spectroscopy. The influence of T&RH on Raman spectroscopy was consistent with the PCA results. Conversely, for NIR spectroscopy, the effect of T&RH was not readily apparent in PCA; however, the results of RMANOVA demonstrated a significant effect of this factor, indicating that the feature extraction step was instrumental in retrieving the information related to the ageing kinetics from the spectra. The results obtained confirmed that temperature and humidity conditions had a substantial impact on the rate of blood ageing kinetics, as suggested by previous studies [89].

In contrast to T&RH and substrate, which displayed similar behaviours across the two spectroscopic techniques, direct exposure of bloodstains to light exerted a significant effect only on NIR spectra. Specifically, its influence ranked second in importance for this analytical technique, after substrate, whereas Raman spectra appeared unaffected by the illumination conditions. This discrepancy between the two spectroscopic techniques may be explained by assuming that, when temperature and humidity were maintained constant, the primary effect of direct illumination was to accelerate water evaporation. Consequently, the high sensitivity of NIR spectroscopy to water content rendered it more susceptible to an accelerated sample drying. In contrast, Raman spectra do not exhibit any characteristic water absorption band and were therefore uninfluenced by the illumination factor.

Regarding the interaction between factors, all pairwise interactions were significant for NIR spectroscopy, while only interactions not involving illumination were significant for Raman spectroscopy, coherently with the lack of significance of illumination for this technique. This observation suggests that blood ageing is a complex phenomenon, whose kinetics is influenced by several factors interacting among each other. This highlights the necessity of considering environmental, illumination and substrate conditions together within a comprehensive experimental framework, ideally adopting a DoE approach, in order to properly account for complex factor interactions during model development.

As an additional outcome, the dummy variable representing subject variability was found to have p-values in the range $0.03 < p < 0.05$, and it was never significant in combination with the other factors when evaluated by NIR spectroscopy, whereas its combination with substrate and T&RH showed low significance ($0.03 < p < 0.05$) for Raman spectroscopy. Most importantly, the effects of all primary factors of interest exhibited a magnitude that widely exceeded that of the dummy variable. This comparison underscored the critical importance of environmental conditions and deposition substrate, whose effects should be rigorously controlled in any statistical model developed to evaluate bloodstain ageing, and may even surpass the influence of interindividual variability.

2.2.3 Materials and methods

2.2.3.1 Sampling and instrumentation

Blood samples were obtained by fingertip puncture, and the biological fluid was collected using a quantitative pipette set to 20 µl and immediately deposited for analysis without the addition of any anticoagulant agent. Four substrates were employed: two fabrics (cotton and polyblend), one glass substrate (Pearl Microscope Slides, 1.0~1.2 mm thickness) and one metal substrate (table knife). Fabric substrates were thoroughly washed at least twice prior to use to ensure comparability with commonly worn clothes. Blood was drawn in triplicate from each donor for each substrate, resulting in a total of 2 donors × 4 substrates × 3 replicates = 24 samples. The studied subjects were both healthy females, aged 31 (A) and 26 (B).

Following deposition, samples were immediately stored in a KMF 115 constant climate chamber (Binder GmbH, Tuttlingen, Germany) to age under controlled environmental conditions. Within the storage chamber, a SUNLIGHT 430 W metal-halide lamp (SIGMA Tech, Warsaw, Poland) was positioned for sample irradiation. The lamp had a nominal power of 450 W, with a final intensity of 55 W/m^2 for UVA radiation, 10 W/m^2 for UVB, 120’000 Lux for visible light, and 850 W/m^2 for solar spectrum radiation.

The combination of factors studied, *i.e.* T&RH at two levels, illumination at two levels, substrate at four levels, and subject at two levels, totalled 32 experimental conditions. Since each condition was analysed in triplicate, the final number of independent samples amounted to 96. Samples were collected across four analytical session, and their ageing was monitored for 12 days. They were analysed 14 times during this period, with higher frequency in the first five days post-deposition and lower frequency during the subsequent 7 days. Specifically, samples were analysed after 5, 24, 29, 48, 53, 72, 77, 96, 101, 169, 193, 217, 241 and 265 hours post-deposition.

NIR analyses were conducted using an OnSite-W MicroNIR® (VIAVI Solutions Inc., Chandler, AZ, US) spectrophotometer, operated with the VIAVI MicroNIR™ Pro v3.2 software. The spectral acquisition range was 908-1676 nm, with a spectral resolution of 6.15 nm over 125 spectral points. The scan count was set to 200 and the integration time to 10 ms. Samples were analysed in triplicate each day, slightly repositioning the sample between replicates. The three instrumental replicates for each analysis were then averaged.

All measurement were performed in transflection mode. Transflection was achieved by adjusting the instrument configuration to the substrate, in order to preserve sample integrity and ensure repeatability while maximising signal intensity (**Figure 2.18**). For cotton and polyblend, measurements were performed by placing a white reference material

(Spectralon®) beneath the fabric and positioning the MicroNIR directly on the bloodstain (**Figure 2.18A**). For glass, the microscope slide containing the sample was placed directly on the MicroNIR, with the bloodstain covered by the Spectralon® (**Figure 2.18B**). In both cases, the presence of the white reference ensured that the radiation passing through the sample would be transmitted back to the detector. For metal, the MicroNIR was positioned on top of the sample (**Figure 2.18C**), without using Spectralon®, since the knife's metallic surface was sufficiently large to prevent light dispersion.

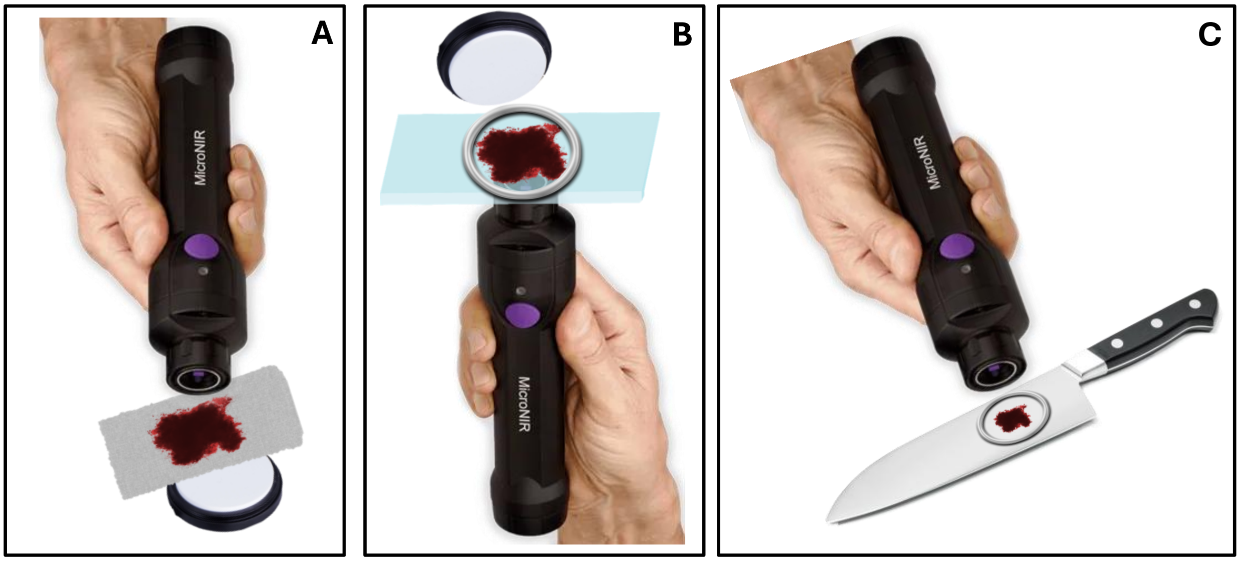

***Figure 2.18**: Visual representation of measurement configuration for different substrates (A: cotton and polyblend fabric; B: glass slide; C: metal knife). The figure shows the use of a round metal spacer to prevent the instrument from touching the specimen when it was not absorbed by the substrate and therefore subject to fracturing and damaging.*

Blank substrates, *i.e.* those without bloodstains on them, were maintained in the climatic chamber alongside the samples, and they were measured prior to sample analysis and every 10 minutes during the measurements, in order to account for temperature and humidity variations while samples were kept under laboratory conditions for instrumental analysis. Blanks were analysed in the same configuration as samples and used as a "reference scan". Dark scans were recorder with the lamp off mode. Consequently, transflectance was calculated from the sample spectra as in **Equation 2.5**

$$\lambda_T = \frac{\lambda_S - \lambda_D}{\lambda_B - \lambda_D} \qquad (2.5)$$

where λ_T is the transflectance value at wavelength λ, λ_S is the intensity of the sample spectrum at wavelength λ, λ_D is the intensity of the dark scan at wavelength λ, and λ_B is the intensity of the blank sample at wavelength λ.

In parallel, samples were analysed using an inVia Raman Microscope (Renishaw, New Mills, UK). The spectra were recorded in the wavenumber range 150–1900 cm^{-1}, comprising a total of 1846 wavenumbers. Excitation was provided via a 785-nm laser line, and 0.5% of the initial laser power (68 mW) was used to irradiate the sample. The instrument was configured for 3 acquisitions of 10 seconds each, resulting in a total analysis time of approximately 7 minutes. No instrumental replicates were acquired due to the relatively long measurement duration; hence, 96 samples × 14 sampling times yielded 1344 Raman spectra. The microscope was operated with a 50× objective (NA = 0.75) and its confocal lenses were manually focused each time to ensure that the detector was completely covered by the bloodstain.

2.2.3.2 Chemometric treatment

2.2.3.2.1Data exploration

All data pre-processing, processing, and chemometric analyses were performed using in-house scripts developed in the MATLAB® environment, version R2024b (The MathWorks, Natick, MA, USA), together with the PLS_Toolbox 9.5 software (Eigenvector Research Inc., Manson, WA, USA).

Initially, spectral signatures were analysed by averaging samples across time to reduce variability, and the spectra were visually inspected to identify significant bands and regions associated with the time trend and macroscopic differences among sessions and materials. Various pre-processing techniques and combination of them were tested to enhance differences among spectra and to minimise unwanted signal variations. The tested pre-processing strategies were the SNV transform [120], Savitzky-Golay first and second derivatives (3rd order polynomial, 7 points window) [132], normalisation to unit length and to unit area for NIR spectroscopy, and the aforementioned methods plus baseline correction using asymmetric least squares (ALS) smoothing or automatically weighted least squares (AWLS) [164] for Raman spectroscopy.

Subsequently, PCA [58,66] was applied on the entire dataset. Score plots were examined to investigate grouping and clustering within the data and to identify factors responsible for the main directions of variability, whereas loading plots were analysed to determine variables associated with each factor.

2.2.3.2.2 Features extraction

To study the effect of factors on bloodstain ageing, each sample, *i.e.,* a bloodstain in one level of substrate, T&RH, light and subject, needed to be represented by a single signal summarising its evolution over time, from sampling point 1 to 14. The signals obtained for all levels of all factors could then be compared using chemometric strategies, thereby isolating the effect of each factor on blood degradation. This objective was achieved through feature extraction.

Feature extraction is a data compression technique that involved applying a chemometric model to summarise information from a large number of variables into fewer new variables, derived from the combinations of the original ones and retaining most of their variability [165]. The model employed to extract information could be unsupervised or supervised. Unsupervised feature extraction methods, most commonly PCA, aim at describing the underlying data structure without focusing on specific factors. Supervised features extraction methods can involve classification or regression techniques. They incorporate class labels or a response variable into the feature extraction process, either enhancing the ability to discriminate classes or focusing the new variables on quantitative information [165]. The most frequently used chemometric techniques in this context include supervised PCA [166], LDA (linear discriminant analysis) [167] or PLS-DA (partial least squares discriminant analysis) [168] for classification, and PLS [169] for regression.

In this study, PLS regression [65,135] was employed as the feature extraction technique, with the aim of focusing on spectral variations associated with the passage of time. To this end, a PLS regression model was constructed for each condition, resulting in a total of 16 models. Calculating individual PLS models for each condition allowed extraction of time trend information without smoothing out the effect of other factors. Each model was cross validated using a venetian blinds scheme with five blocks. The selection of pre-processing and the number of significant latent variables (LVs) was determined for each model by observing the trend of root mean square error in cross validation (RMSECV) and comparing it with that of root mean square error in calibration (RMSEC). Since different models could require different numbers of significant latent variables, the final number of latent variables (n) was set to the minimum among the 16 models, opting for a parsimonious approach to avoid potential overfitting. Finally, the scores on the first n LVs for each of the 14 sampling times for each subject were linearly concatenated, thereby producing a new signal comprising n × 14 variables. For clarity, the feature extraction process is schematically illustrated in **Figure 2.19**. The final data matrix for each instrument comprised 32 rows (16 conditions × 2 subjects) and was subsequently employed for all further data analysis.

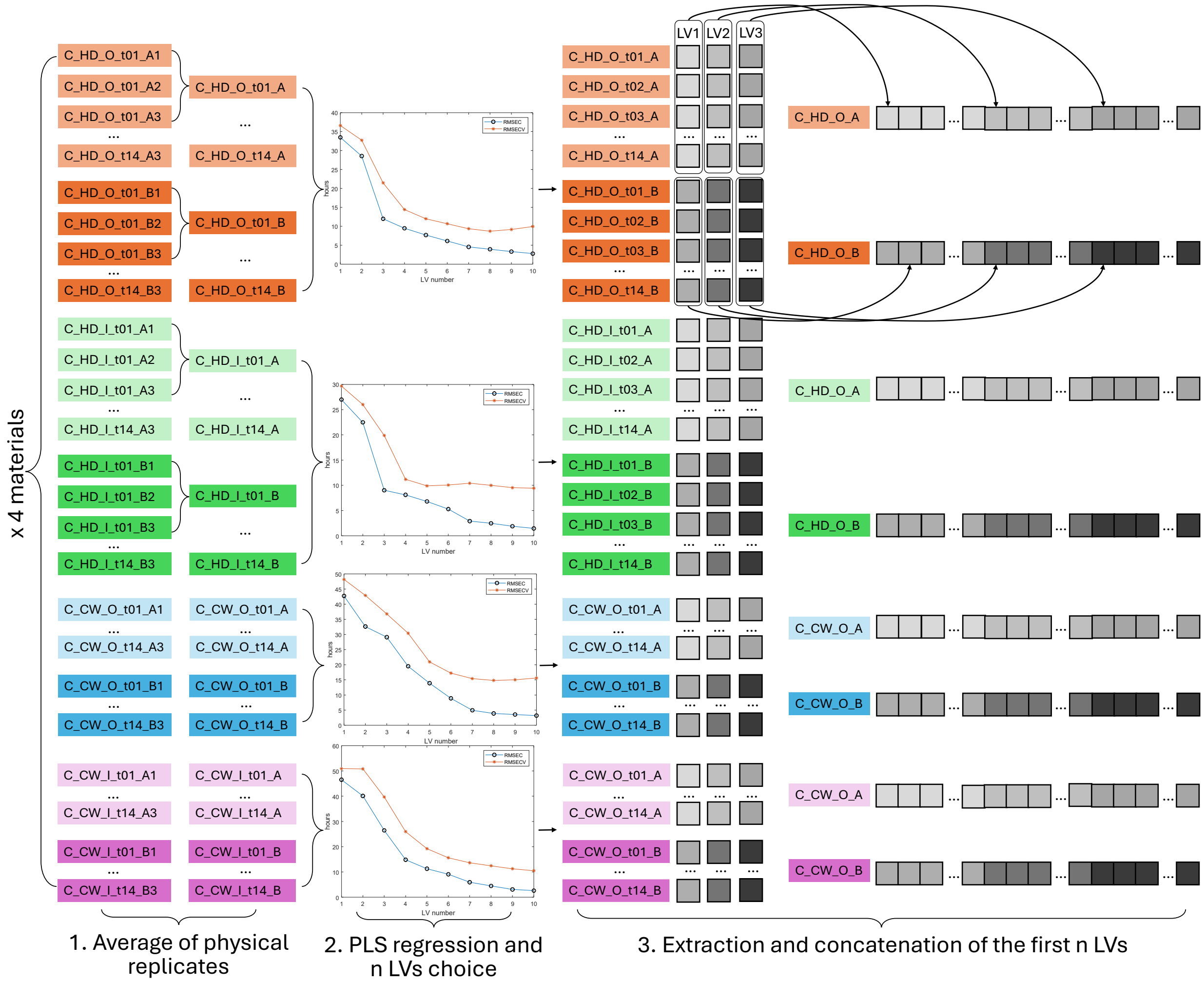

***Figure 2.19**: Schematic representation of the features extraction process, exemplified on substrate = cotton. The same scheme was repeated for all four materials and for both instruments.*

To ensure the robustness of the approach, *i.e.,* to verify that all the significant information was indeed captured in the first n LVs, the procedure was repeated three times, incrementing n by one in each iteration.

2.2.3.2.3 Application of RMANOVA

The data matrix was subsequently subjected to RMANOVA.

In this study, RMANOVA was applied to the data matrix to evaluate the statistical significance of the factors and their binary interactions. Statistical significance was calculated and tested using the Wilk's lambda distribution [170,171], whose theoretical shape was obtained through a permutation test with 10,000 permutations. P-values between 0.01 and 0.05 were regarded as slightly significant. Final p-values were adjusted using Bonferroni multiple testing correction [172].

Moreover, a factor was deemed statistically significant only if its p-value was lower than that of the subject, both taken individually and in combination with other factors. With this approach, the subject was treated as a "dummy factor", meaning that every other factor needed to be more significant than it to be considered in the analysis. This ensured that the controllable conditions, *i.e.* T&RH, illumination, and substrate, had an effect even when the original blood donor was different than that used to produce the dating model. Therefore, factors were finally considered significant if $p < 0.01$ and $p < p_{dummy}$. In addition, the percentage effect of factors was calculated based on the proportion of variance explained by the factor itself.

2.2.4 Conclusions

The present study demonstrated that substrate of deposition and environmental conditions, in the form of temperature, humidity and illumination, influenced bloodstain ageing kinetics. These results were obtained by applying a systematic DoE approach and multivariate variance deconvolution strategies, thereby facilitating a comprehensive understanding of factors significance.

More specifically, the central role of the substrate of deposition highlighted the imperative of producing forensic blood dating models that employ the same background as that on which the collected evidence is found. This would be necessary to achieve satisfactory and reliable dating performances, and the finding serves as a cautionary note for forensic partitioners, who should be advised to always sample bloodstains together with their background, without removing them.

Moreover, the significance of temperature, humidity and illumination was shown to be noteworthy, confirming previous, more qualitative observations from other studies [113,141,142]. The potential bias arising from environmental conditions underscores once again the need for forensic researchers to move towards the development of tailored models, elaborated under conditions that accurately replicate the environment in which real bloodstain samples had been exposed from the time of their deposition to the commencement of spectroscopic measurements.

Even though only two blood donors were considered in the present study, the results suggested that, if the factors were properly accounted for, the production of reliable dating models would still be feasible. Tailored models could therefore be developed using donors different from the subject under investigation. Of course, this evidence requires substantiation through a more systematic study of subject variability, but it may be regarded as an encouraging indication.

This study also highlighted another noteworthy aspect, namely the instrument specificity of certain factors. This indicates that the choice of spectroscopic technique should also be guided by the conditions under which the samples were collected. For instance, NIR appeared to be more suitable for the analysis of blood deposited on absorbing substrates, whereas performance differences on non-absorbing substrates require further data to substantiate this observation. Conversely, NIR seemed more susceptible to illumination effects, implying that the use of this technique should be combined with precise control of lighting during experimentation.

For the first time, it was possible to quantify the effect of environmental conditions on blood degradation and to statistically compare their significance, while also accounting for subject variability. In light of these results, the development customised models tailored to the characteristics of individual crime scenes becomes increasingly valuable and opens new frontiers in forensics science.

2.3 GOOD LABORATORY PRACTICE IN BLOODSTAINS DATING

The two stages of the research presented in this chapter clearly illustrate the intrinsic challenges associated with bloodstain dating in forensic practice, namely the huge variety of factors that intervene both in the blood ageing process and in the measurement setup, and that influence the accuracy, precision and predictive capability of laboratory-scale models. To account for instrumental differences and complementary features, the simultaneous use of more than one spectroscopic technique should always be recommended, as demonstrated by the improved performance of the models developed through data fusion, as demonstrated in Section 2.1. Moreover, instrument specificities may be encountered, as suggested in Section 2.2, rendering one instrument preferable over the other in specific situations, which should be considered when simultaneous application of several spectroscopic methods is not feasible in real-case scenarios.

Given the high number of factors identified throughout this chapter, and their substantial impact on bloodstain ageing, and consequently on dating performances, this subsection aims to propose a recommended procedure for bloodstain dating that can be applied by forensic practitioners in real-case scenarios, encompassing the process for sample collection at the crime scene to the selection of the analytical methods and the generation of results. This section is hoped to serve as a foundation for the development of internationally recognised forensic guidelines, promoting the adoption of validated bloodstain dating approaches in actual forensic casework. Ultimately, integrating this analytical strategy among the standard tools available to courts would represent a meaningful advancement for forensic science. It is my strong belief that such progress would significantly enhance both the accuracy and the scientific rigor of forensic investigations.

2.3.1 Evidence discovery

The very first step upon arrival at the crime scene should be the documentation of the environmental conditions of the location, ensuring that the ambient conditions in which the samples were preserved from deposition to discovery are accurately recorded. This proposal represents an innovation compared to current standard procedures, which typically begin with the documentation of bloodstains through photography and visual description. The present proposal aims to minimise the risk of environmental alteration prior to measurement. Indeed, the movement of practitioners within the area, resulting in the formation of air currents and disturbance of the internal environment, may cause significant modifications by opening a previously isolated system.

It is important to note that temperature and humidity can be measured with simple probes, without requiring movement through the room. For this reason, performing the measurements before sample documentation does not compromise the latter, while ensuring greater precision in monitoring environmental conditions.

According to this proposal, in indoor crime scenes, temperature and humidity should be measured immediately. As an additional precaution, if the crime scene allows it, *i.e.* no toxic molecules nor fire or explosion risks are evidenced, air currents should be kept to a minimum, to maintain conditions as close as possible to those existing prior to discovery. Under these circumstances, continuous monitoring of temperature and humidity should be conducted for at least 24 hours, and preferably for 24-72 hours. Recording these fluctuations over a daily cycle would later facilitate supervised aging procedure in the laboratory [98]. It is reasonable to assume that a closed indoor environment exhibits relatively consistent daily patterns in temperature and humidity, and that a precise record of these variations enables a close laboratory simulation of the sample's pre-discovery storage conditions. A proof of concept for this procedure has been simulated along in Section 2.2.

Conversely, in outdoor scenarios, this protocol is less critical, as the presence of forensic practitioners is expected to have minimal impact on open environments. However, environmental conditions at the time of discovery should still be recorded, and when possible, meteorological data from the days preceding discovery should be retrieved from local weather stations or services. Continuous recording of environmental daily cycles remains beneficial, as it provides an approximation of the climatic variations affecting the sample, and is therefore strongly encouraged even in outdoor contexts.

After temperature and humidity have been recorded, the proper documentation of the evidential bloodstains, including their location, size, and morphological characteristics, should follow. Subsequently, the monitoring of environmental factors should continue with the assessment of the illumination to which the samples themselves are and have been exposed. In particular, the type of light (natural or artificial), its spectral composition, and its intensity should be measured. Preferably, these parameters should be documented over a full daily cycle, noting any changes in light exposure throughout the day, and recording both the hours of illumination and darkness for each sample. This information will be invaluable for the development of tailored supervised ageing models.

2.3.2 Evidence collection

Regardless of the nature of the substrate on which a sample is found, whether absorbent or non-absorbent, it is advisable to secure the entire piece of evidence whenever possible, especially when it constitutes a small or movable object. If the whole object cannot be taken to the laboratory, it is recommended to isolate or cut the bloodstain along with a portion of the underlying substrate. If this is not feasible and the bloodstain is not at risk of alteration, destruction or loss if left in place, it should remain in its original position at the crime scene. In such cases, the use of portable spectrophotometers should be considered as a first choice for the analysis.

Only after on-site analysis using portable spectrometers should the entire trace be secured by isolating it from the substrate, taking care to avoid disintegration of the evidence. A clean (*i.e.*, DNA-free) and dry collection tool should be used to gather blood samples, avoiding contamination. The use of moist cotton swabs or solvents such as water, alcohol, or any other liquid must be strictly avoided, as these may both induce protein denaturation and reverse certain ageing processes connected to desiccation, compromising further analysis.

In all situations, it is essential to collect additional samples of the background material that do not contain any blood traces. These substrate samples will subsequently serve as references for the development of tailored laboratory-scale models.

2.3.3 Evidence securing and storing

Collected bloodstains should be stored in airtight, light-resistant containers once they are completely dried. The use of adhesive films (*e.g.*, those designed for securing microtraces) must be strictly avoided, as the adhesive layer may contaminate the blood sample. Consistent temperature and humidity must be maintained during storage, and both should be as low as possible, to slow further degradation processes prior to instrumental analysis. Exposure of samples to sunlight or artificial light sources must always be prevented. All data and metadata collected during the analytical process should be traceable and recorded in compliance with ISO 21043-2 requirements, ensuring the chain of custody and admissibility of results in judicial contexts.

Under no circumstances should samples be stored for an extended period after discovery. Instead, bloodstains should be analysed as soon as possible following their delivery to the laboratory. Given that the age of a bloodstain may prove important during the investigation, it is necessary to act quickly in cooperation with forensic genetics experts and

BPA specialists. Close collaboration between law enforcement and forensic laboratory personnel is therefore essential to ensure timely transfer of evidence and to raise awareness of the importance of rapid processing for accurate bloodstain dating.

2.3.4 Selection of spectroscopic method

Whenever feasible, all three spectroscopic techniques described in this chapter, *i.e.,* UV-Vis, Raman and NIR spectroscopies, should be employed. This approach is expected not only to improve the accuracy of bloodstain age estimation through data fusion, as demonstrated in Section 2.1, but also to provide a cross-verification tool for the validating the consistency of results. However, in practice, it may not always be possible to analyse each sample using all three techniques, either because a particular instrument is not available in the laboratory or because the substrate is unsuitable for certain methods. For this reason, a few general guidelines for selecting the most appropriate technique in specific situations are outlined below.

Considering background colour, when it is very dark the use of UV-Vis spectroscopy may prove less effective due to the high interferences. For this reason, NIR spectroscopy in reflection mode or Raman spectroscopy should be preferred in such cases. Conversely, when the substrate is light coloured, all three techniques are suitable, and NIR and UV-Vis spectroscopies may be applied in transmission or reflection modes.

If the bloodstain is deposited on an absorbent substrate, NIR or UV-Vis spectroscopies should be preferred; if the substrate is non-absorbent, Raman or UV-Vis spectroscopies are generally more suitable. Raman spectroscopy is particularly advantageous when the non-absorbing substrate is also flat, while UV-Vis spectroscopy coupled with an integrating sphere should is preferable for uneven non-absorbing surfaces.

As a rule, samples should not be extracted from the substrate. However, if it is necessary to perform both genetic analysis and bloodstain dating on the same small sample, the stain must be divided, one part extracted for genetic testing, and the remaining fragment used for age determination. If this is not possible, dating should be performed first.

Standard procedures for spectroscopic data acquisition should be followed in accordance with the instrumentation available in the forensic laboratory, adjusting parameters such as acquisition time, integration time, and the number of collected spectra according to the characteristics of the trace. These parameters, in fact, may need to be increased when the bloodstain is small or appears diluted.

It is also advisable to record the spectrum of the clean substrate, *i.e.* without blood, to identify the spectral signature of the background material and to facilitate spectral deconvolution when interference is significant.

Each spectrum should be recorded at least in triplicate. When using a microscope-coupled instrument, the three spectra should be collected from different regions of the stains to account for sample inhomogeneity. In this case, the use of a rotating stage to obtain a representative average spectrum may also be considered. When the instrument is not microscope-coupled and the probe covers most of the sample in a single scan, the sample should still be moved or rotated between acquisitions to account for spatial variability.

2.3.5 Model development

As demonstrated in Section 2.2, the use of a single universal regression model for dating blood traces is unlikely to be effective. Therefore, the creation of general-purpose models under laboratory conditions to be kept “ready-to-use” for any blood trace should be regarded as an outdated and unsuitable approach. Instead, the dating methodology must be tailored to each individual case, explicitly considering the specific conditions under which the bloodstain has undergone degradation. A new model should be prepared for each real-case scenario.

In particular, the same substrate on which the evidential samples were found should be obtained, either by collecting spare blank substrate form the crime scene or, if unavailable, by purchasing it commercially. Once the substrate is available, a cohort of diverse donors should be selected, ideally varying in age, sex, health status, and geographical origin. If the source of the discovered bloodstain is known and accessible, a fresh blood sample form that individual should be also collected. When the original donor is known but unavailable, individuals with similar biological and demographic characteristics, *i.e.*, age, sex, health condition, physiognomy, and geographical origin, should be included in the cohort to serve as substitutes.

Blood samples should be collected from all selected donors without the use of anticoagulants and deposited on the obtained substrate, ensuring that the volume of blood is as similar as possible to that of the evidential stain. The approximate amount of blood can be estimated using bloodstain pattern analysis techniques, considering the shape, appearance, and substrate of the bloodstain. Using the same substrate is also advantageous in this respect, since blood from different individuals is expected to interact similarly with the same material. Once the target volume is determined, blood samples should be collected in triplicates from each subject and immediately deposited on the blank substrate.

Right after deposition, the samples should be stored in a programmable climatic chamber designed to reproduce the environmental conditions measured at the time of discovery. The chamber should allow simulation of day-night alternation and gradual changes in temperature and humidity, following the recorded daily trends. It should also be equipped with an adjustable light source capable of reproducing both the type and the intensity of illumination to which the samples were exposed between formation and discovery.

When it is possible to formulate a hypothesis about the age of the bloodstain, which is usually the case when dating is required, artificial ageing should be carried out for a period corresponding to this hypothesis. When two contrasting hypotheses are available, the artificial dating should be carried out to a period corresponding to the longer hypothesis. Then, the correctness of the hypothesis should be checked with a likelihood ratio approach If no preliminary hypothesis is available, the ageing of the samples should be monitored for a minimum of 14 days. Whatever the timeframe selected, daily spectroscopic measurements using all selected techniques should be carried out. After this period, a multivariate regression model, such as PLS regression, should be calibrated from the collected data and prediction of the unknown sample's age should be attempted. The likelihood ratio between the evidential sample and the laboratory samples should also be calculated. If the likelihood ratio is unacceptable and/or the PLS model suggests that the evidential sample is older than the considered timeframe, *i.e.* when the prediction is extrapolated beyond the calibration range or lies at its upper limit, daily measurement should continue. A new likelihood ration and PLS model should be produced each day until both yield acceptable and consistent results.

To facilitate this process, the development of user-friendly algorithms and software capable of performing model calibration and likelihood ratio calculation would be highly beneficial. Such tools would make the dating procedure more accessible to non-specialised personnel, thereby enhancing its applicability in routine forensic laboratories. This is a direction in which further research work should be advisable.

If more than one spectroscopic technique is used during analysis, separate dating models and likelihood ratio calculations should be generated for each technique. The performance of the regression models should then be evaluated, for example through the RMSECV, to determine whether one technique outperforms the others in terms of precision and accuracy in the given scenario. When multiple techniques yield comparably precise and accurate predictions on the calibration set, *i.e.* on the samples collected and stored in the camera, their concordance should be assessed. A mid-level data fusion approach should then be implemented to confirm model robustness and improve result reliability.

While this approach is surely deemed to be more time consuming than having a global model available, it does not, anyway, defeat the purpose of timely analysis presented in Section 2.3.3. In fact, once the specimen is collected and measured, it may proceed to the subsequent steps of forensic analysis, *e.g.* DNA identification, which are needed for timely suspect identification and securing. Conversely, the calculation of TSD of bloodstains is usually a less urgent one, and therefore the time required to produce a tailored model will normally be compatible with the timeframe intercurrent between the discovery of the crime and trial, when information on TSD becomes crucial.

2.3.6 Validation and reporting

The age prediction results obtained from the developed models should always be accompanied by an explicit measure of uncertainty, expressed either as RMSECV or, preferably, as a confidence interval. These results must be presented to court or legal representatives together with a clear and transparent description of the analytical protocol employed, of which these guidelines can be a valid starting point.

Establishing a standardised approach for calculating and reporting uncertainty is highly desirable in this context, as it would enhance the credibility and interpretability of results for non-scientist audiences, such as judges, attorneys, and juries, who rely on expert testimony to inform judicial decisions. Developing a harmonised procedure for assessing the uncertainty of dating models, which integrates metrics such as RMSE and confidence intervals, represents a valuable avenue for further research. This should be pursued both from a chemometric standpoint and within the broader forensic context, as previously discussed in Section 2.1.2.5 of this chapter.

It is also advisable to present the obtained results within an evidence evaluation framework based on two competing hypotheses, each representing a different possible sequence of events. In this case, the two different assumptions should regard the age of bloodstains. This approach aligns with the likelihood ratio framework recommended by the European Network of Forensic Science Institutes (ENFSI) [173], which promotes probabilistic reasoning and transparency in forensic reporting.

Ultimately, the reliability and global recognition of forensic bloodstain dating depend not only on methodological rigour but also on continuous professional development and collaboration across the forensic community. Forensic practitioners and laboratory personnel should remain up to date with advancements in spectroscopic techniques and chemometric methodologies. Moreover, collaboration between scientists developing new spectroscopic tools for monitoring blood degradation and those applying the methods in practice should be actively encouraged. Such cooperation will enhance methodological consistency, improve the reliability of bloodstain dating, and promote its acceptance as a valid forensic technique.

Finally, the proposed protocol should also be further expanded to incorporate additional analytical techniques, such as fluorescence spectroscopy [82,174], FT-IR spectroscopy [114,141] and hyperspectral imaging [95], which may contribute to improving both the sensitivity and robustness of forensic bloodstain dating models.

3 ENVIRONMENTAL APPLICATIONS

3.1 NIR HYPERSPECTRAL IMAGING COMBINED WITH CHEMOMETRICS FOR MAPPING WATER PATTERNS DURING DEHYDRATION OF NONVASCULAR EPIPHYTIC COMMUNITIES

3.1.1 Introduction

In recent years, research has increasingly investigated the biological responses of species to climate change, with a particular focus on their distribution patterns and how these may shift in the future, while considering their ecological niches [175,176]. In this context, statistical analyses are being widely employed to interpret biotic interactions between co-occurring species, usually at the medium or large spatial scales [177]. Conversely, focusing studies on the microclimate in which a given organism lives could lead to more accurate and realistic insights [178,179]. Indeed, microclimate has been shown to exert a strong influence on the physiological activity of organisms, while also affecting the structure, composition and functioning of ecosystems at smaller scale [180,181]. Therefore, studying organisms within their specific microclimates could reasonably improve the prediction of the biotic response to climate change. In this framework, spectroscopic and chemometric approaches represent powerful tools for exploring biological processes non-invasively, enabling quantitative assessment of physiological and environmental parameters with high spatial and temporal resolution.

Within this context, the study of nonvascular poikilohydric organisms, such as bryophytes and lichens, is particularly relevant. These organisms, lacking organs for active water uptake (*e.g.* roots), equilibrate their moisture content according to the atmospheric water availability [182]. Specifically, lichens and bryophytes absorb water, nutrients, and gases directly from the atmosphere, and absorption occurs over their entire surface [183]. For this reason, their physiology is closely linked to both micro- and macroclimatic environmental factors, among which air humidity and rainfall are the main water sources regulating their metabolic processes [184–186]. Additionally, nonvascular epiphytic communities, consisting of single organisms or, more often, the coexistence of different types of organisms in the same space, are crucial contributors to the water balance of forest ecosystems [187]. Hence, understanding their water management under conditions of climatic stress is increasingly important [188]. Moreover, beyond their intrinsic physiological interest, these organisms play essential ecological roles as early colonisers and bioindicators of environmental change, owing to their direct dependence on atmospheric conditions [189].

In an ideal climate, continuous humidity due to prolonged or frequent precipitation (including fog) and slow evaporation enhance the photosynthetic activity of nonvascular organisms and reduce the occurrence of desiccation [190], which causes a halt in biologic activity. However, nonvascular epiphytes have, to some extent, adapted to the discontinuity of water availability through a variety of structural and physiological strategies. Additionally, adaptations also aim to collect, store, and retaining water, thus improving desiccation tolerance [191]. In general, the mechanisms through which nonvascular epiphytes and their photobionts tolerate desiccation remain only partially understood [192].

To address this gap, imaging represents an interesting tool for obtaining a better understanding of the processes occurring during desiccation in a non-invasive manner, while providing fine spatial detail consistent with the biological scale of the organisms under study. Optical imaging techniques collect large amounts of information and generate detailed spatial maps, which can be exploited to visualise and analyse sample features. When digital imaging is combined with spectroscopy to obtain hyperspectral imaging (HSI), both spectral (characterisation) and spatial (localisation) information can be obtained from the samples. This combination makes HSI an appealing technique for environmental monitoring [193,194].

HSI has already been used to study nonvascular communities, even though the focus was mainly on analysing species coverage. Visible-short wave infrared (Vis-SWIR ¸ 400-2400 nm) HSI was applied in two studies, one focusing on heathland vegetation as an indicator of environmental quality [195] and the other classifying forest elements [196]. Vis-SWIR and UV-Vis-NIR (200-1100 nm) HSI have also been employed to estimate ground lichen cover in boreal forest stands [197]. Vis-NIR and Vis-SWIR HSI have in some cases been exploited as biosensors for biocrust localisation and monitoring [197,198], and to predict lichen species abundance and community composition, with the final goal of identifying suitable habitats for lichens [199].

At the same time, point spectroscopy in the NIR region (800-2500 nm) has been used to investigate hydration and dehydration cycles in lichens. Water, in fact, is a strong absorber in the NIR region of the electromagnetic spectrum, and particularly the first overtone of the O-H covalent bond stretching (1300 – 1600 nm) is recognised as an excellent feature for studying water dynamics [200]. Among others, a recent study used Vis and NIR lichen signatures to calculate indices and assess the possibility of estimating the water content with a species-specific approach [201]. In another study, both spectral indices and photosynthetic activity were correlated with hydration conditions, again revealing differences among lichen species [202]. Milos *et al.* used NIR spectroscopy to study the hydration-dehydration cycles of lichens with the aim of investigating desiccation-induced reductions in photosynthesis and identifying thallus optical properties. In particular, they focused on thallus colour change between wet and dry states, and on the spectral reflectance indices showing the greatest differences between these conditions, again emphasising species-specific behaviour [203].

To date, no study has ever combined NIR-HSI with the evaluation of hydration and dehydration in nonvascular epiphytic communities, although the approach has proven valuable for nonvascular terricolous communities. In particular, Granlund et al [204] used HSI across a wide wavelength range to extract two indices from their specimens and correlate them with the water content in different lichen species, assessing species specificity. They also constructed heat maps, correlated with water content. However, like most of the studies mentioned above, their work focused on single-species responses, identifying differences and similarities without accounting for the interactions that occur naturally in mixed communities.

Finally, no previous study combining NIR spectroscopy (either imaging or point analysis) for the study of nonvascular communities and their relationship with water has exploited the entire spectrum, for instance by constructing multivariate models and water maps. The possibility of taking into account the entire spectral signature of a sample would however allow correlations among variables to be accounted for. Therefore, the use of chemometrics is considered invaluable in this context. However, published studies have mostly focused on the extraction of indices, with few or no applications of chemometric techniques.

Indeed, several studies have already demonstrated that combining HSI and chemometrics can provide valuable information on sample dehydration, as this approach has been successfully applied in other fields of research. For instance, in the environmental field, Stefansson *et al.* [205] developed a method for the spatial and temporal estimation of moisture content in thermally modified Scots pine over a 20-hour period. In food research, the dehydration of various meats has been investigated in two different studies using time-series HSI, yielding moisture content maps as final outputs [206,207], and the same goal has been achieved for cheese during ripening [208], tea buds during dehydration [209], and ginger slices during hot-air drying [210]. All these studies collectively demonstrate the potential of NIR imaging combined with chemometrics for dehydration monitoring, making it a technique worthy of investigation for nonvascular epiphytic communities as well. The present work therefore introduces, for the first time, an integrated approach that combines NIR-HSI, chemometric modelling, and quantitative dehydration monitoring to obtain simultaneous spatial and compositional insights into nonvascular epiphytic communities.

In light of these considerations, the aim of the present study is to develop an analytical strategy based on NIR-HSI to map water distribution during the dehydration of complex nonvascular epiphytic communities. For the first time, with the aid of chemometrics, water content maps are developed at a microscale in this microenvironment. Through the visual monitoring of the communities under stress conditions, such as water management, the response of individual life forms is evaluated, with the aim of understanding the facilitation or competition schemes undergoing that depend on community composition.

To achieve this goal, hyperspectral images and the weights of samples colonised by different compositions of nonvascular epiphytic communities (distinguished as bryophytes, foliose lichens, and crustose lichens), were monitored over time (18 sampling points). The resulting images were first used to construct principal component (PC) maps to explore the similarities and differences between organisms. Then, a partial least squares (PLS) regression model was trained and used to estimate water content at the pixel level. The chemometric strategy was applied both at the pixel and image levels to investigate the consistency between the two, and the complementarity of the information that can be extracted depending on the level of data processing.

3.1.2 Results and discussion

3.1.2.1 Experimental protocol

For this study, nonvascular epiphytic communities were taken into account. The organisms considered were bryophytes (referred to in the text as BRYO), foliose lichens, and crustose lichens (LIFO and LICR, respectively). In this context, bryophytes were not distinguished between mosses and liverworts but were considered as co-occurring components present to varying extents [211]. Foliose lichens exhibited thalli of individual leaf-like lobes exhibiting radial growth and periodically branched and divided, as is typical of this type of lichen [212]. Crustose lichens, lacking a lower cortex layer, were intimately associated with the substratum and not readily detachable from the surface [213].

Since these organisms, *i.e.,* bryophytes, crustose lichens, and foliose lichens, usually spatially coexist in different proportions on the same tree, ternary-mixtures experimental design [214] was used as an inspiration for the sampling scheme. Specimens composed only of bryophytes, crustose lichens, or foliose lichens were referred to in the text as pure communities to underline that they contain a single life form type. Specimens containing two or three different life forms were sampled as well; for clarity, these are referred to as binary or ternary composites in the text. All samples were chosen to be naturally supported by chestnut bark since bark water is relevant for the growth of the studied organisms [215]. For this reason, samples of whole bark (WOBA hereafter) were collected for analysis as well.

As can be observed in **Figure 3.1**, three different binary composites were considered:

- BRCR: samples containing both bryophytes and crustose lichens;
- BRFO: samples containing both bryophytes and foliose lichens;
- CRFO: samples containing both crustose and foliose lichens.

Moreover, the ternary composite BRCF, containing bryophytes, crustose and foliose lichens all together on the same sample, was considered as well.

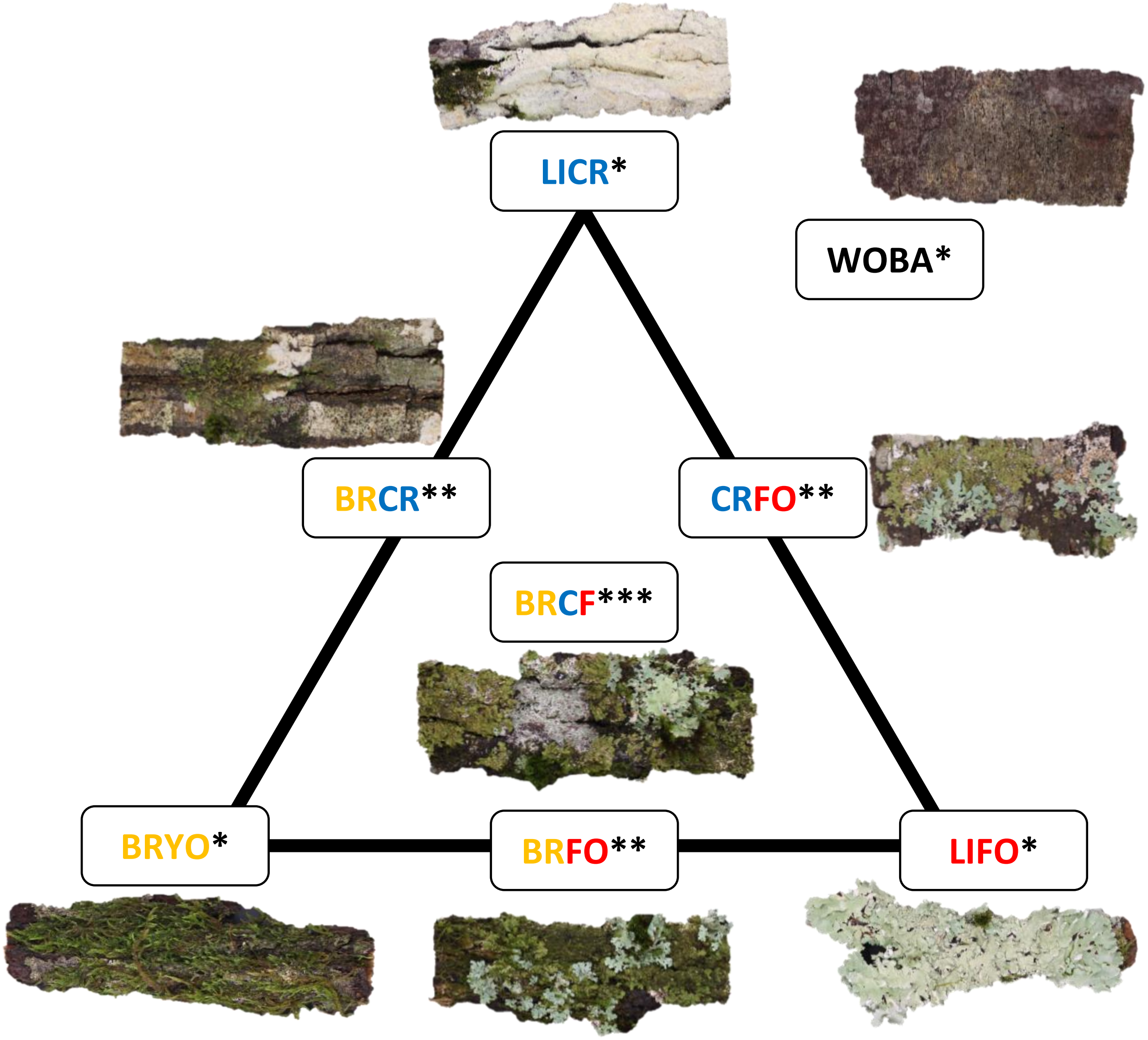

Figure 3.1: *Graphical representation of sampling scheme with labels indicating the coded names for the specific samples. A colour coding has been used to visually differentiate between pure communities, binary composites and the ternary composite.*

Thus, a total of eight different types of samples were considered in the study. Moreover, to account for biological variability, four independent physical replicates, *i.e.,* coming from different threes but with the same macroscopic composition in terms of communities present, were collected for each class, making a total of 32 samples available for subsequent analysis. Samples were chosen to be as similar as possible in terms of bark coverage and size, with an average of 15x5 cm.

After collection, samples were sprinkled with water until complete hydration was achieved and were then left to dry at room temperature and humidity. The weight of the samples was monitored over 18 sampling points until complete dehydration was achieved, and SWIR-HSI images were taken at each sampling point immediately after weighing. Details of the measurement pipeline can be found in the Materials and methods section. The weight at each sampling point was used to calculate the percentage water content (WC%) of the sample at that moment.

3.1.2.2 Dehydration curves and spectral visualisation

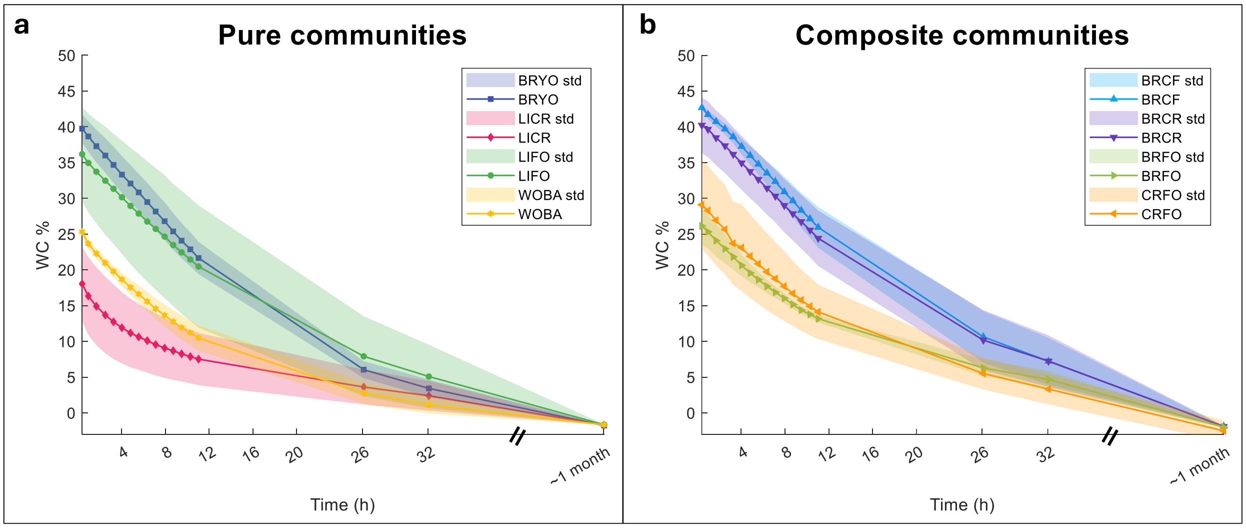

Figure 3.2: *Average water content and its associated standard deviation (shaded area), calculated on the four physical replicates, for each of the eight sample types along time. A: Pure communities. B: Composites.*

As a first step in data analysis, the evolution of WC% over time was evaluated to identify general community-related trends. In particular, **Figure 3.2** illustrates the dehydration trends for pure communities and composites, reporting the average water content with its associated standard deviation for each sample type. As demonstrated in **Figure 3.2A**, the pairs LIFO-BRYO and LICR-WOBA showed very similar water contents and dehydration patterns. This observation suggested that the rate of thallus desiccation is strongly influenced by the morphology and anatomy of the nonvascular epiphytic organisms that colonise the bark. Indeed, BRYO and LIFO share a broadly similar morphology, with leaf-like formations and a vertical extension of at least a couple of mm. These two types of communities, however, markedly differ from LICR, which lies flat on the bark and has a more homogeneous appearance.

Crustose lichens (LICR) appeared to dry faster than any other sample type during the first 15 sampling points (~12 hours), with a steep decrease at the beginning of the process, followed by rapid stabilisation. This result could be related to the strategy adopted by many crustose lichens to limit the formation of water films on the upper cortex through hydrophobic proteins that restrict the penetration of free water [216]. These morphological differences account for the dehydration patterns observed in **Figure 3.2**.

Another interesting observation was that the standard deviation differed among classes, with foliose lichens having the largest standard deviation, followed by crustose lichens, bryophytes, and bark, which presented the smallest standard deviation. This reflects the fact that the internal anatomy of lichen medulla, which may be variably thick and porous, can also be highly variable within both foliose and crustose lichen groups [217], thus explaining the increased standard deviation observed for them.

Figure 3.2B, which represents the average moisture content for composites together with the respective standard deviation, showed that the water content range was comparable between these samples and the pure communities. Moreover, samples containing a high percentage of foliose lichens displayed the highest standard deviation, thus confirming the previous observation that the presence of these nonvascular organisms introduces greater variability into the system.

The next step was to evaluate the spectral signature of pure communities, in order to visually confirm whether the trends observed in the WC% were mirrored in the spectral information. Therefore, **Figure 3.3** presents the spectral profiles of pure communities across the dehydration timeline, illustrating the relationship between water loss and spectral changes in the NIR region. The spectra displayed all the key water-related bands, in particular the combination band of O–H stretching and bending (1800-2000 nm) and the 1st overtone of the O–H stretching (1300-1600 nm) [200], both of which exhibited decreasing intensity over time, as dehydration progressed. This progressive reduction in pseudo-absorbance mirrored a reflectance increase associated with the drying process. This behaviour is in accordance with previous literature reports [197,202,203]. Moreover, when comparing the response of different communities, BRYO (**Figure 3.3A**) and LIFO (**Figure 3.3C**) were characterised by a continuous and regular dehydration pattern, presenting a slow and constant decrease of pseudo-absorbance along the entire temporal trajectory. Conversely, LICR (**Figure 3.3B**) and WOBA (**Figure 3.3D**) presented a steep decrease from sampling time 1 to 3, followed by rapid stabilisation of the spectrum. This behaviour mirrored the pattern observed in the water content trend (**Figure 3.2**), and confirmed the suitability of SWIR spectroscopy for dehydration process monitoring.

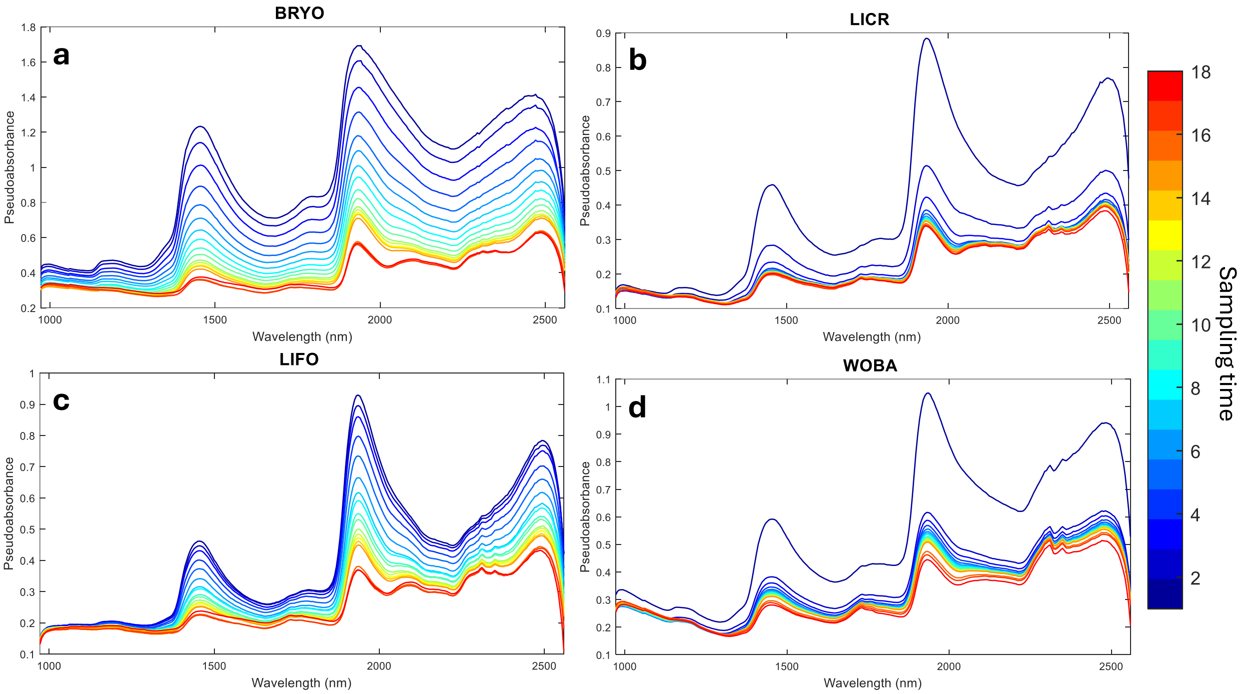

Figure 3.3: *Mean spectra for each pure community (respectively: A = BRYO; B = LICR; C = LIFO; D = WOBA), obtained with the image-based approach followed by averaging the four spectra representing each physical replicate at a specific time. Spectra are colour-coded according to the sampling order from the first (time 1 in dark blue) to the last (time 18 in dark red), see colour bar.*

Interestingly, time 18, which was recorded one month apart from time 17, does not significantly differ from the previous sampling point from a spectral perspective in any of the observed classes. This feature confirmed that at time 17 a complete drying had nearly been achieved. Having established how dehydration affects spectral profiles, the next step was to investigate whether these changes could be captured and visualised in a multivariate space through PCA.

3.1.2.3 Principal Component Analysis

3.1.2.3.1 Image-based approach

Chemometric exploratory analysis of data was the conducted to understand whether macroscopic differences in the form of grouping could be observed, to differentiate between community types, and to verify the presence of a time trend. To achieve this, spectral data underwent row pre-processing by means of first derivative followed by data normalisation to unit area, aimed at removing unwanted spectral variability. The pre-processed data then underwent chemometric exploratory analysis by means of PCA.

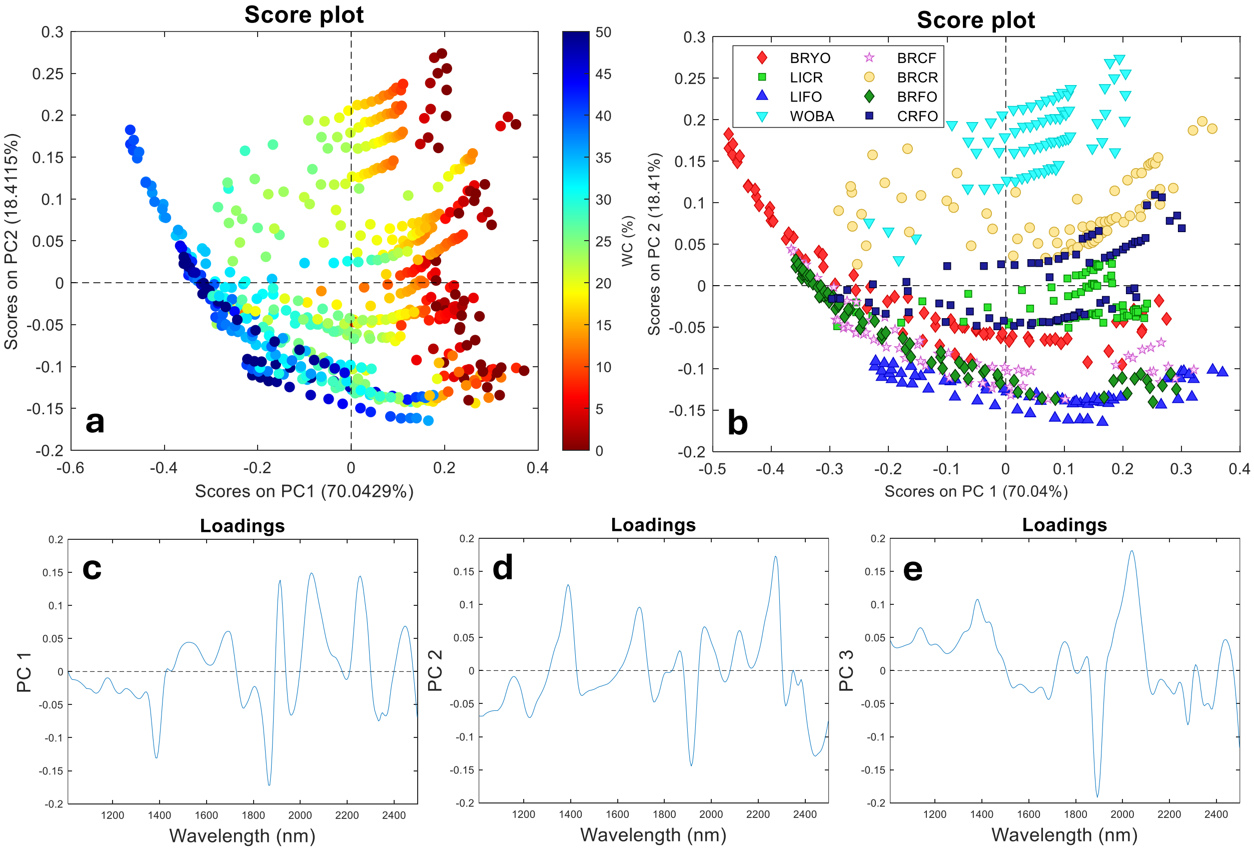

Figure 3.4: *Results of PCA with the image-based approach. A: score scatter plot coloured according to WC%; B: score scatter plot coloured according to sample type; C-E: Loading profiles on PC1-3, respectively.*

PCA was first applied with an image-based approach (as detailed in the Materials and methods section). The resulting score and loading plots are reported in **Figure 3.4**. In particular, in **Figure 3.4A** each point represents a physical replicate at a specific sampling point, and the colour represents the corresponding WC%. PC1, explaining 70% of the total variability, captured the dominant variation associated with the drying process. In particular, low PC1 scores corresponded to samples analysed at the beginning of the dehydration process, and therefore with higher water content (coloured in blue), while samples in the later stages of the process, and thus drier, were located at higher PC1 values (coloured in red). This gradient confirmed that the dehydration trajectory was clearly observable along PC1.

In addition, PC2, explaining 18% of the total variance, described the differences in sample composition, as illustrated in **Figure 3.4B**, where the points are coloured according to sample type. In the score plot, specimens of the same type clustered in proximal areas of the PC space, with the bark (WOBA, light blue inverted triangles) being the most isolated and positioned in the upper-central region of the score space. Notably, different replicates of the same type tended to fall closer to each other than to samples from other types, confirming that, for the samples under study, intraspecific variability was minimised allowing the analysis to focus on interspecific variability. Interestingly, LIFO (dark blue triangles) and LICR (green squares) lied quite far from each other, with BRYO (red diamonds) occupying an intermediate position. This observation is in line with what had already emerged from the WC% evaluation, *i.e.* that water management is largely determined by the morphological traits of nonvascular epiphytic communities.

PCA loadings are represented in **Figure 3.4C**, **3.4D** and **3.4E** for PC1, PC2 and PC3, respectively. Although it is important to keep in mind that band attribution should preferably be done on raw data rather than on pre-processed spectra, since pre-processing may lead to misinterpretation [131], it is still possible to draw general conclusions from the loadings. In this case, PC1 showed high negative loadings for spectral regions associated with water, in particular corresponding to the first overtone of the O–H stretching (1300-1400 nm) and to the combination band of the O–H stretching and bending (1850-1950 nm). This indicates that samples located at negative scores on this component had higher water content compared to samples at positive scores. This outcome confirmed that the trend observed in the score plot was driven by water loss.

Complementarily, PC2 and PC3 displayed higher loadings in regions not attributed to water, namely around 1700 nm and after 2000 nm. These spectral regions are typically assigned to cellulose and lignin instead [218]. When the loading profiles were compared with raw spectra (**Figure 3.3**), it became evident that the regions around 1700 nm and after 2000 nm were those showing the highest variability between pure communities. Therefore, this confirmed that PC2 and PC3 captured the variability due to chemical differences among communities, as already suggested by qualitative analysis of the score plots.

3.1.2.3.2 Pixel-based approach

Afterwards, a pixel-based approach was adopted to describe the samples in a spatially resolved way. For this purpose, 500 random pixels were selected from each image of the pure communities (4 replicates × 18 sampling times), and the obtained matrix was pre-processed as previously described and used to train a PCA model. Score and loading plots of the pixel-based model were compared to those presented in **Figure 3.4** from the image level model, and the results were confirmed to be consistent (data not shown).

Then, the model was stored by retaining the first three principal components, to be used for prediction. The three selected components explained 43%, 22% and 7% of the total variance, respectively, accounting for 72% overall. This step was aimed at exploiting the information extracted from the reduced, randomly selected dataset to describe the entire images, with the final goal of providing multivariate maps of the samples. Consequently, in the subsequent step, all pixels of the pure community images (BRYO, LICR, LIFO and WOBA) were projected into the PCA space. Predicted score values were calculated for each pixel and used to produce false-colour RGB score maps, assigning the first three PCs to the three RGB channels: PC1 to red, PC2 to green and PC3 to blue.

To enable an easier interpretation of false-colour RGB score maps, a customised colour scale was developed, as shown in **Figure 3.5**. To construct it, pure community score values at each sampling time were averaged across physical replicates. For instance, all pixels of BRYO replicate 1 at time 1, BRYO replicate 2 at time 1, BRYO replicate 3 at time 1 and BRYO replicate 4 at time 1 were averaged, yielding a single average value for PC1, PC2 and PC3 representing the BRYO sample at time 1. The three average score values obtained were then attributed to the red channel (PC1), green channel (PC2) and blue channel (PC3), generating a specific colour used as a discrete descriptor of the status of that community (in our example, BRYO) at that specific dehydration level (in our example, fully hydrated – time 1). The process was repeated across all pure communities and sampling times, and the concatenation of the average colours systematically generated a customised colour scale (**Figure 3.5C**), summarising the changes experienced by each pure community along the entire dehydration process.

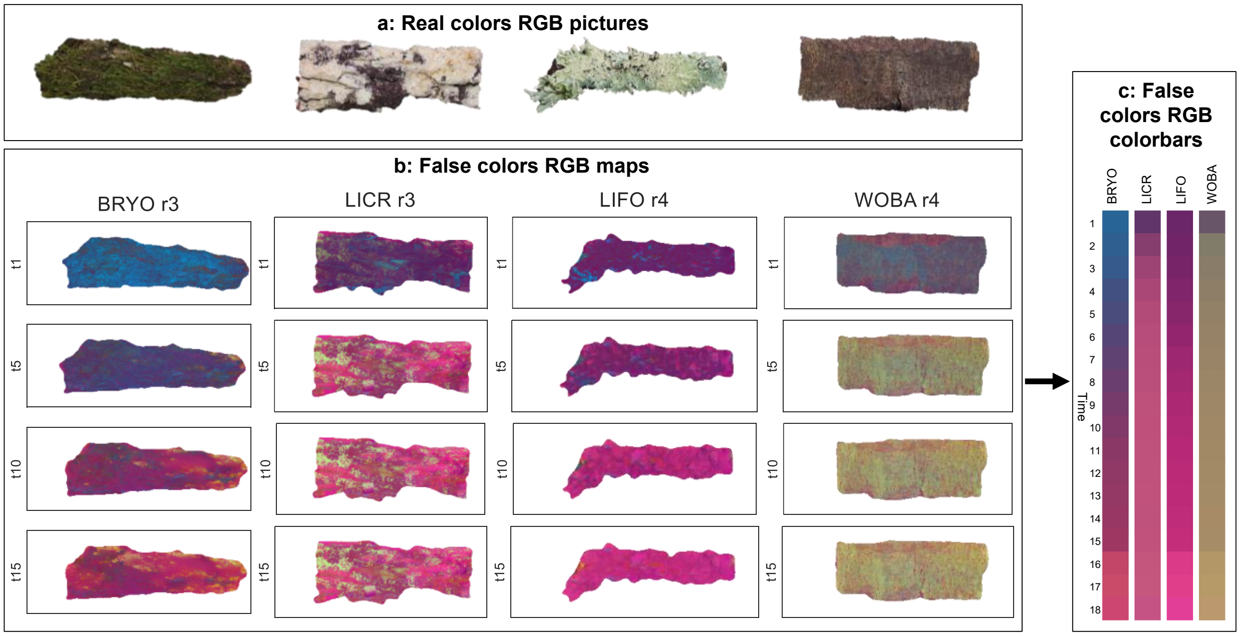

***Figure 3.5**: Summary of the colourbar generation process. A: Photograph of the sample at time 1; B: Projection of pure communities at times 1, 5, 10 and 15 in the PCA space. The samples used are r3 for BRYO and LICR, r4 for LIFO and WOBA; C: False-colour RGB colourbars obtained for each class of pure community. Each coloured rectangle represents the mean RGB triplet of all physical replicates at the indicated time for the specific sample type.*

False-colour RGB score maps were then plotted for the pure communities. A summarised version of the resulting maps, showing one of the replicates for each pure community at every other sampling time, is shown in **Figure 3.6**. The complete results are reported in Appendix A, at the end of the current chapter.

Observation of these RGB score maps highlighted both a change of colour within each sample type over time, reflecting the time trend, and a change of colour between pure communities at the same sampling point. For instance, when comparing the BRYO samples from time 1 to time 18, a clear colour change from blue to pink was observed, demonstrating a change between the images correlated to the hydration state. Concurrently, a comparison between, for instance, BRYO and LICR at time 1 further emphasises a clear difference in colour, with the former appearing dark blue and the latter dark violet. These illustrative observations, which can be repeated across other communities, confirmed that PCA captured the information referred both to the dehydration process – as a general change in the colour of the images over time – and to the chemical differences among communities –

as distinctive colour patterns within an image and between images from different community types.

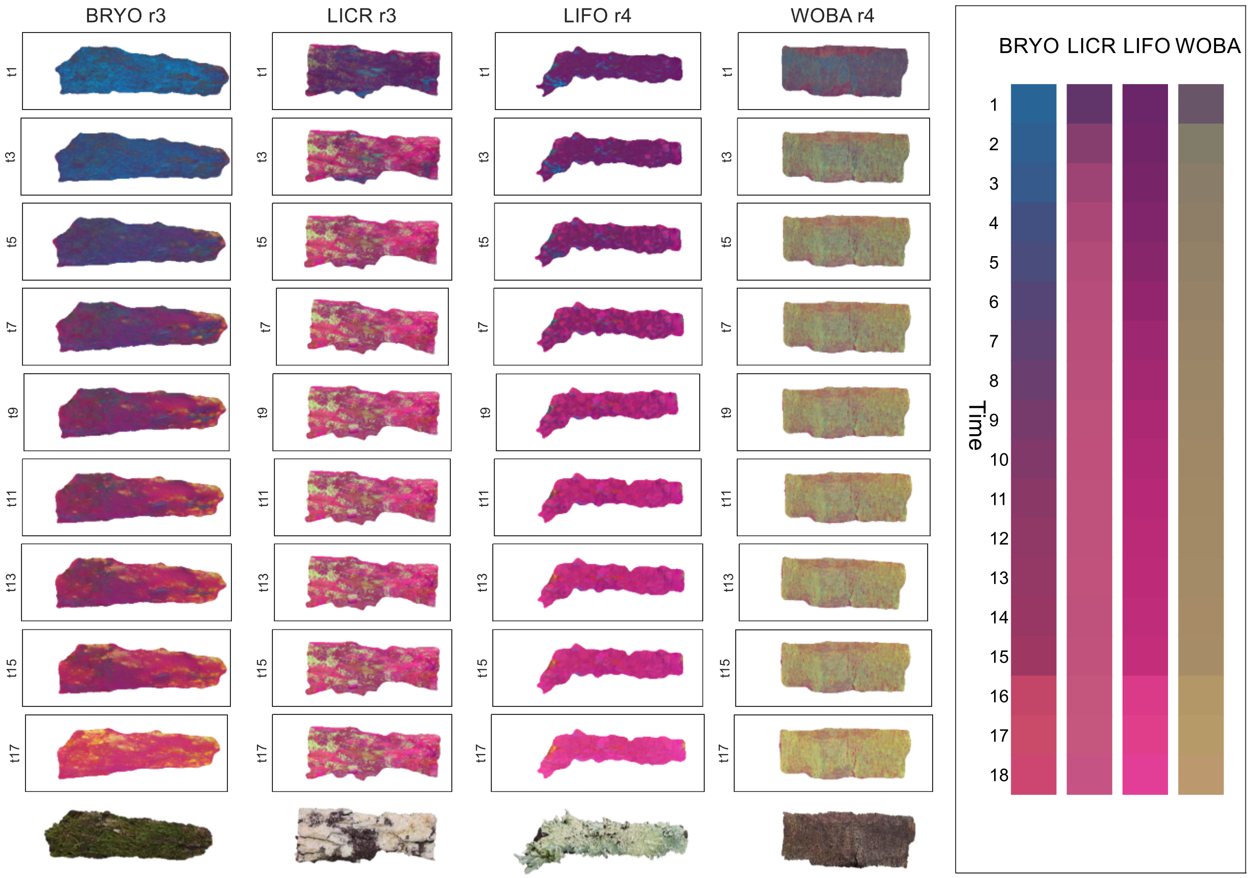

Figure 3.6*: False-colour RGB score maps of one physical replicate for each pure community (BRYO r3, LICR r3, LIFO r4, WOBA r4) at times 1, 3, 5, 7, 9, 11, 13, 15 and 17. Underneath each map is the picture of the sample at time 1. On the right pane, four false-colour RGB colourbars are displayed.*

Subsequently, the PCA model was applied on composites as well. For this purpose, the images of binary and ternary composites were projected into the PCA space, and PC1, PC2 and PC3 scores were calculated for each pixel of each image. The obtained scores were used to produce false-colour RGB score maps for all samples and time points. A summarised version of these maps, showing one replicate for each composite at every other sampling time, is shown in **Figure 3.7**. The complete results are reported in Appendix A, at the end of the current chapter.

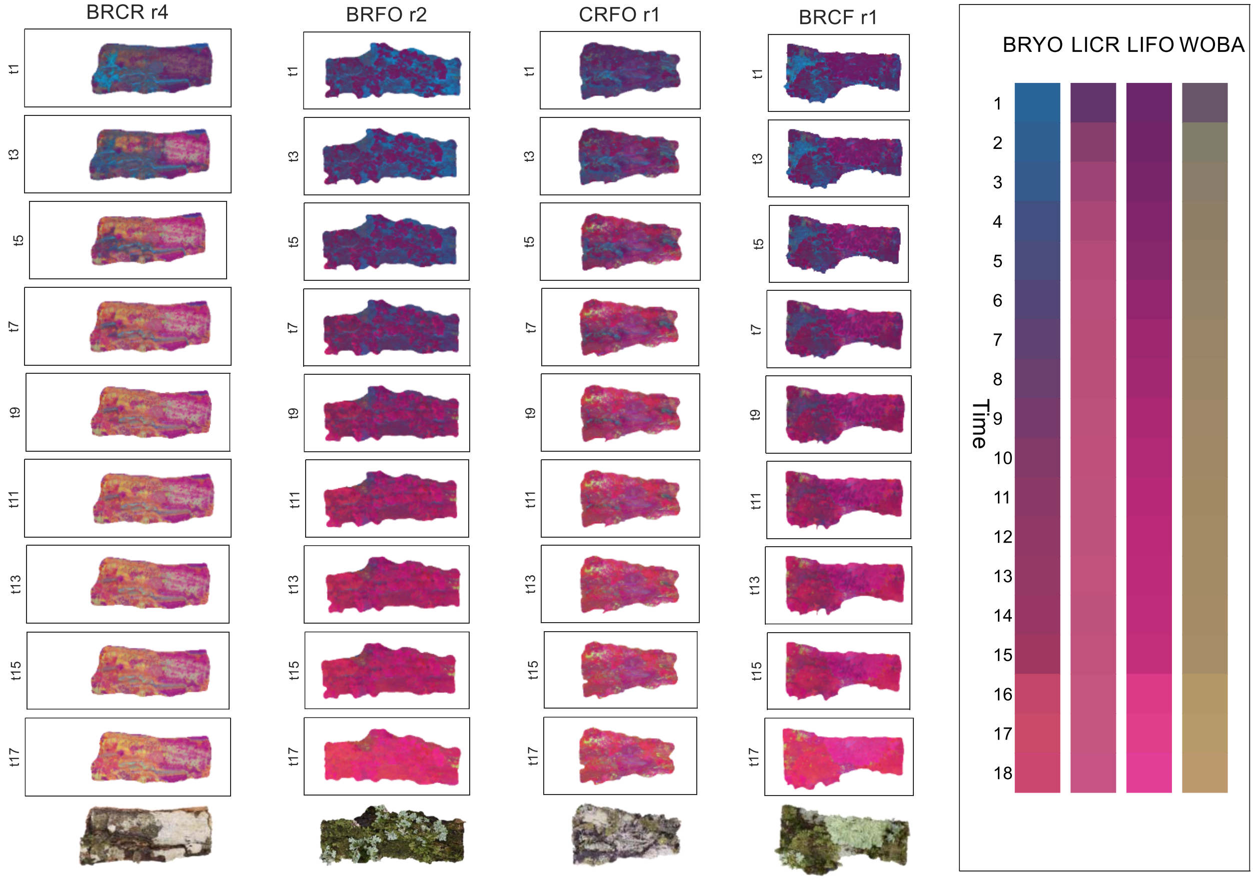

Figure 3.7*: False-colour RGB score maps of one physical replicate for each composite (BRFO r4, BRCR r2, CRFO r1, BRCF r1) at times 1, 3, 5, 7, 9, 11, 13, 15 and 17. Underneath each column is the picture of the corresponding sample at time 1. On the right pane, four false-colour RGB colourbars are displayed.*

Observing **Figure 3.7**, it was possible to draw some initial conclusions regarding the response of life forms when they interacted with each other. For instance, when comparing the bryophytes present in the BRFO sample with the colourbar, a slower change of the blue colour toward violet could be observed compared to the same community when present alone on the bark. Specifically, the colour for bryophytes at time 7 in **Figure 3.7** closely resembled BRYO at time 4 on the colourbar. This trend, also confirmed in other regions of the samples, reflected a slower water loss for bryophytes in the presence of foliose lichens.

On the other hand, when bryophytes are found together with crustose lichens, their water loss occurred more rapidly. In particular, increased water loss could be observed in the areas adjacent to the lichens themselves. Indeed, in the BRCR sample, the bluish colour typical of wet bryophytes disappeared quickly, replaced by the violet/pink colour typical of dry bryophytes. These two complimentary effects were mutually attenuated in BRCF samples, where both crustose and foliose lichens were present. In fact, in BRCF samples, the dehydration rate of bryophytes resulted similar to what observed in the BRYO samples.

Similar observations could be made for all life forms considered in this study. However, it was clear that visual interpretation of false-colour RGB score maps, even with the aid of the custom colourbars, may be subjective and influenced by the colour perception of the analyst. Indeed, while this strategy was powerful and provided biologically interesting insight, it could not be considered unambiguous for understanding of the water management in the communities. Consequently, a regression model was required to estimate pixel-based water content.

3.1.2.4 Partial Least Squares Regression

Keeping in mind the final goal of this study, namely predicting the WC% of different communities even when co-occurring in nature, a single model was trained for all types of samples. As a first step, the samples were divided into a training set and a test set. The training set contained all replicates and sampling points of the pure communities, as well as three replicates of each composite type. The test set contained one randomly selected physical replicate for each composite type. Details of the samples selected for each set can be found in the Materials and methods section.

The choice to include composites in the training set reflected the need for a training set that represented all possible sources of variability. In particular, using only pure communities as a training set would have exclude variability associated with the overlap of different life forms, which was a common scenario in composites. Moreover, relying solely on pure communities would also have left a gap in the WC% coverage along the calibration range, with LICR and WOBA covering the lower range and BRYO and LIFO covering the upper range, leaving a gap in between. Including some replicates of the composites ensured an even coverage of the full WC% range.

After assigning samples to either the training or test set, the data were pre-processed using the first derivative followed by normalisation to unit area. Subsequently, a regression model was developed with the image-based approach. The obtained model retained eight significant latent variables, with a RMSECV of 5.0%. When applied to the test set, the model yielded a RMSEP of 3.1%. These error rates were deemed satisfactory, representing approximately 10% and 6% of the total WC% range, respectively.

Observation of the predicted versus measured space (**Figure 3.8**), however, highlighted some degree of non-linearity in the response. In particular, communities containing crustose lichens displayed an “S”-shaped behaviour. This outcome suggested that the PLS regression model was better suited for communities that exhibited a continuous change in WC% over time, such as BRYO and LIFO. This finding is not surprising, as PLS regression is a linear multivariate regression technique and is therefore more appropriate for describing gradual, regular changes rather than discontinuous ones.

Subsequently, a PLS regression model was developed under the same conditions using the pixel-based approach. The model retained eight latent variables, with an associated RMSECV of 6.8%. The slightly higher RMSECV compared to the image-based model reflected the greater variability captured when describing a sample with multiple pixels rather than a single global average signal. Moreover, in the pixel-based approach, all 500 pixels from a single image were associated with same WC% value. This increased the internal variability of the dataset, because the actual WC% of individual pixels is unlikely to be identical. This limitation, common to pixel-based regression, arises from the fact that reference measurements, in this case WC%, are unique for an image and represent an average value. Consequently, the assumption that each pixel from the same image shares the same Y value, though necessary for building the regression model with this approach, is not strictly correct, leading to an increase in CV error, as observed in the results.

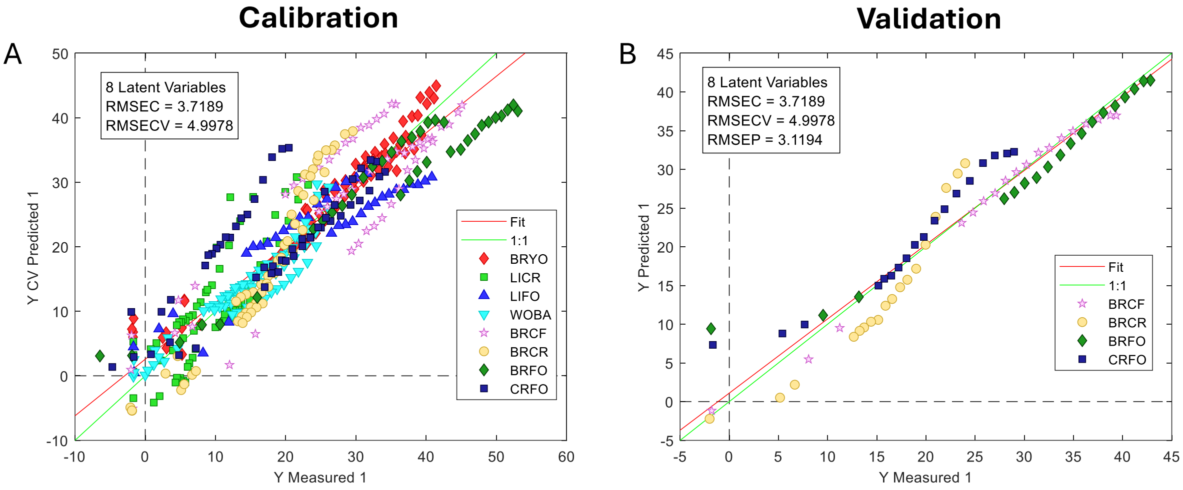

Figure 3.8: *PLS predicted vs measured WC% using the image-based approach. A: Training set (cross-validation); B: Test set.*

Afterwards, all pixels from all images in the training and test sets were projected into the PLS space of both models, and a WC% value was predicted for each pixel. To compare the prediction results obtained with the two approaches, an average predicted WC% value and its standard deviation were calculated for each image. A visual representation of this procedure for BRCF is shown in **Figure 3.9**, and comparable results were obtained for all other communities (data not shown).

From **Figure 3.9**, it was evident that the image-base and pixel-based average predicted values were close to each other and to the expected WC%, demonstrating good agreement between the two approaches. However, the image-based model consistently produced a larger standard deviation, indicating that WC% values predicted within the same image varied more widely with this approach. This higher prediction variability is not surprising. By design, the image-based model minimised the variability by describing each training sample using its average spectrum. As a result, when used in pixel level prediction, extreme pixels were not accurately described, since they were not represented in the training set, leading to an increase in standard deviation.

Conversely, the pixel-based model, trained using 500 randomly selected per image, likely included some extreme pixels in the training set. This made the model better suited to predict such pixels accurately. These conclusions were supported by the evaluation of T^2 and Q diagnostic statistics: while approximately 5% of the predicted pixels were considered extreme in the pixel-based model, more than 15% of pixels were classified as extreme in the image-based model, demonstrating lower robustness of the latter.

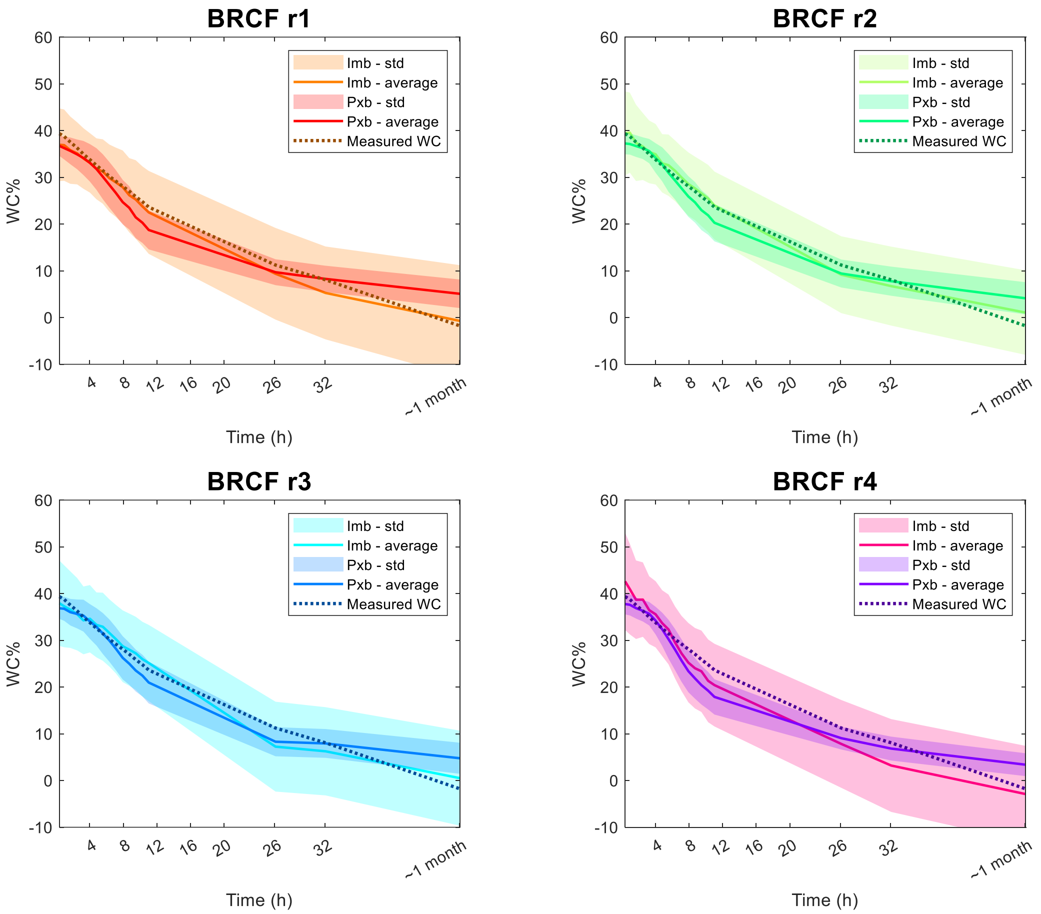

__Figure 3.9:__ Expected value (WC, dotted line), average predicted value with the pixel-based model (pxb, solid line), average predicted value with the image-based model (imb, solid line), and ±standard deviation of the prediction (shaded area, both for pxb and imb), for each physical replicate of the ternary composite BRCF.

Combining the previous observations, it appeared that the image-based model was more strictly correct, since it associated each spectrum to a unique y value. Moreover, the results provided by this model were more easily interpretable, enabling visualisation of the predicted versus measured space and allowing conclusions to be drawn on the behaviour of different classes. Conversely, pixel-level prediction obtained from the pixel-based model demonstrated superior performance in terms of robustness, providing lower standard deviations and a more accurate description of the sample. This was further supported by the lower number of extreme pixels revealed by T and Q^2 statistics. At the same time, both models showed high concordance between the average predicted values and the expected WC%.

From this perspective, the results suggested that the two approaches provide complementary insights: the pixel-based model is more suitable for pixel-level predictions, while the image-level model is superior for interpretability and visual analysis.

The final step of the regression pipeline was the production of water content maps for the test set samples. These maps were single-layer images in which each pixel was coloured according to its estimated water content, with the colour scale normalised between the minimum (0%) and the maximum (45%) WC% recorded across the entire dataset. This approach provided a visual representation of moisture content along the dehydration process in a fully non-destructive manner, preserving spatial information. Following the considerations above, the water content maps were calculated using the pixel-based model. The resulting maps for times 1 (0 h), 3 (1.5 h), 5 (3 h), 7 (4.5 h), 9 (6 h), 11 (7.5 h), 13 (9 h), 15 (10.5 h) and 17 (32 h) for the four test set samples are shown in **Figure 3.10**. Water maps for all samples (training and test set) at all sampling times are reported in Appendix B, at the end of the current chapter.

When observing **Figure 3.10**, a clear drying trend could be identified in the maps, with a global colour change over time as well as finer local variations within the samples. Compared to the PCA score maps, it was now easier to interpret the information related to moisture content, although distinguishing different life forms within the communities was more challenging, since each pixel was coloured according to WC% rather than life form. However, this information could be inferred by comparing the water content maps with photographs of the samples (**Figure 3.10**, bottom). Within each sample, colour variations could be observed even at the same sampling point, and these differences generally corresponded to different adjacent life forms, confirming local differences in water behaviour related to community composition.

It was also noteworthy that drying did not proceed from the borders to the centre of the sample, contrarily to what is commonly observed for non-living specimens [208]. In non-living samples, passive drying typically results in a radial moisture gradient. The absence of this feature in lichens and bryophytes suggested an “active drying” process. This implies an active role of nonvascular epiphytic communities in water retention and release, potentially linked to metabolic activity involved in respiration and photosynthesis [219,220].

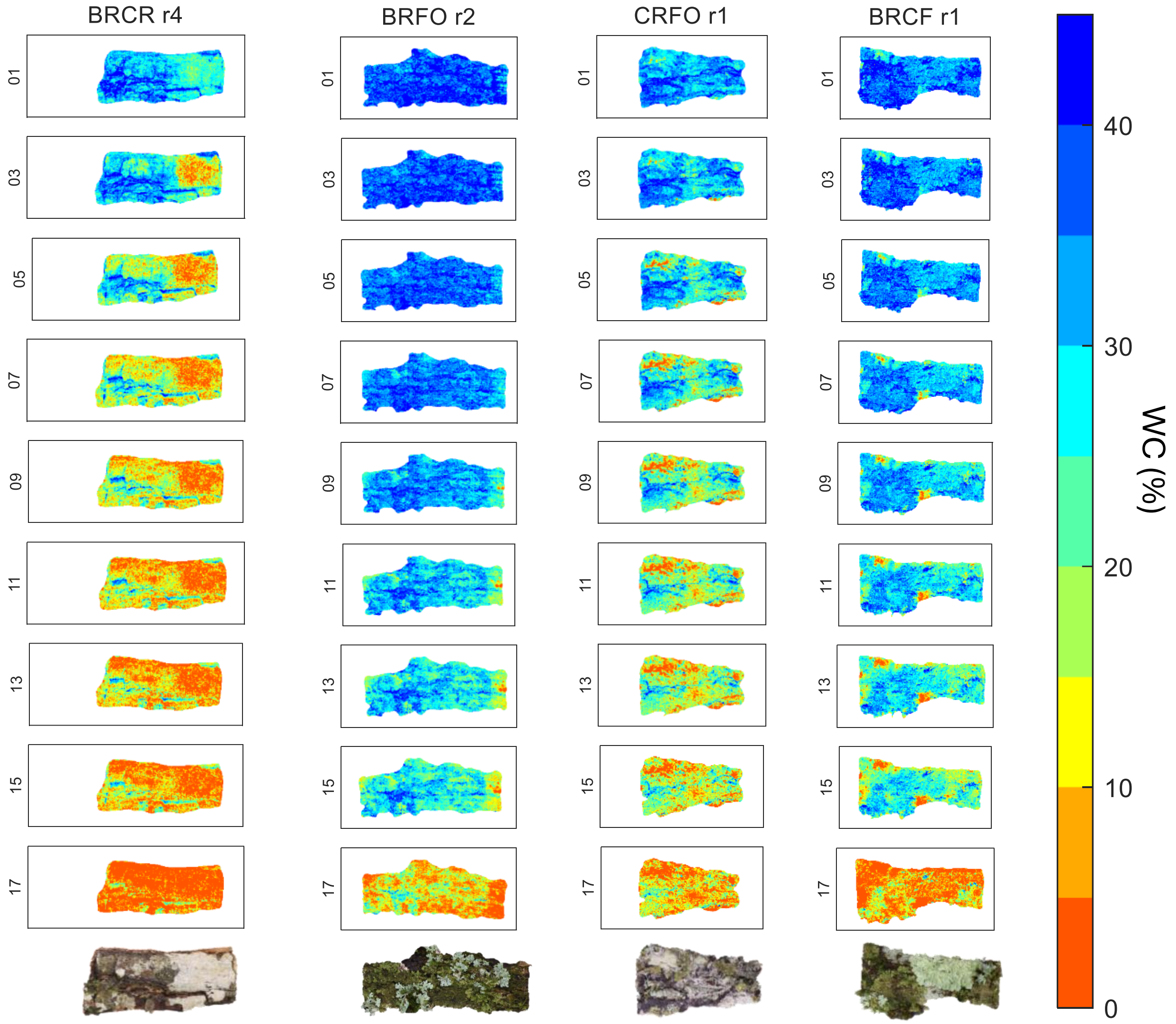

__Figure 3.10:__ Water content maps for the test set samples (BRFO r4, BRCR r2, CRFO r1, BRCF r1) at times 1, 3, 5, 7, 9, 11, 13, 15 and 17. Underneath each column is the picture of the corresponding sample at time 1.

Thanks to the water maps, it was possible to compare the response of each life form when present alone with their behaviour when multiple life forms coexisted on the same substrate (*e.g.* on the same piece of bark). To facilitate in this comparison, water content maps for one replicate of each pure community at every other sampling time are displayed in **Figure 3.11**, providing an example of the response of the life forms when present alone on the substate. The complete set of maps of all pure communities at all sampling points is reported in Appendix B, at the end of the chapter.

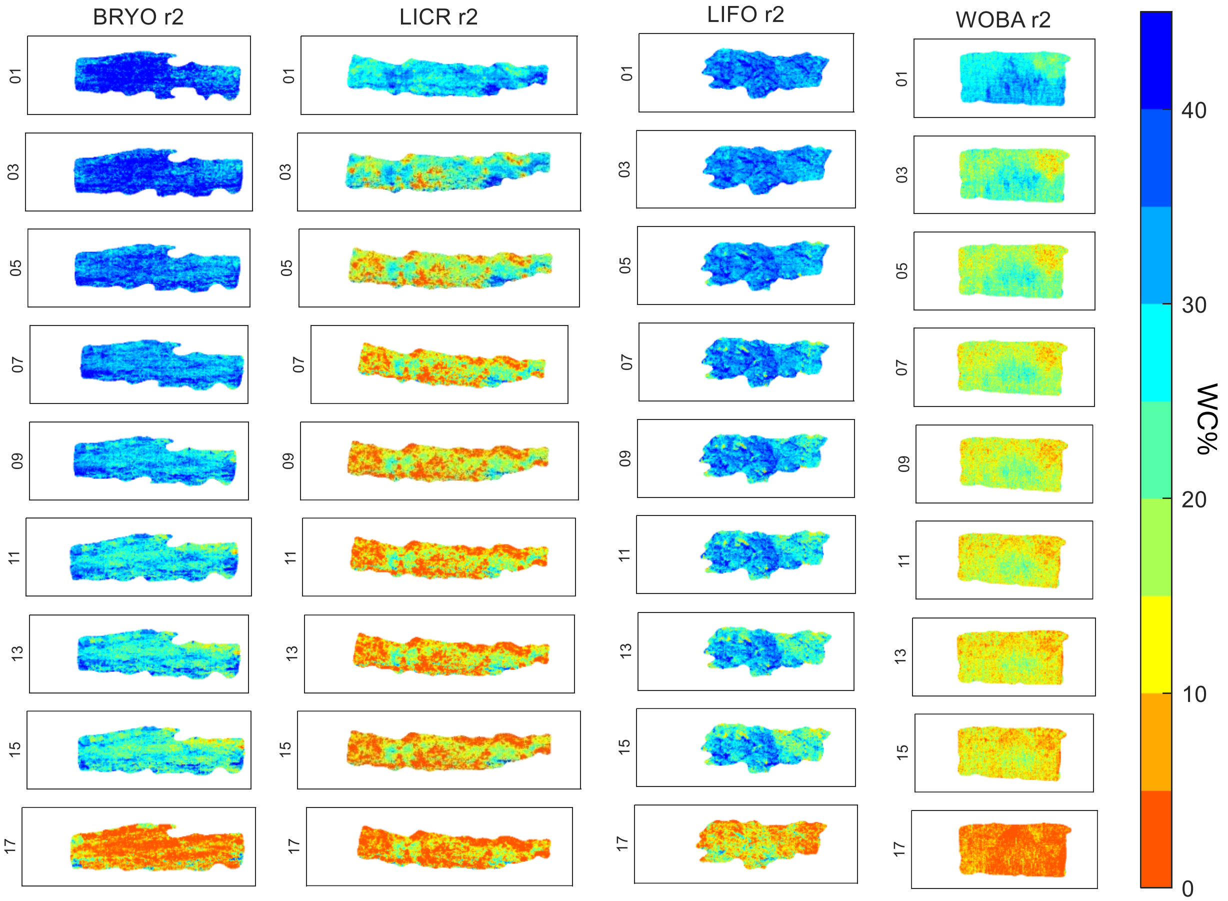

__Figure 3.11__: Water content maps for replicate 2 for each pure community at times 1, 3, 5, 7, 9, 11, 13, 15 and 17.

Starting with bryophytes, it could be observed that, when present with foliose lichens (BRFO), their drying process was very similar to that observed when this life form was present alone. In contrast, the contiguous presence of crustose lichens and bryophytes (BRCR) promoted faster dehydration of the bryophytes. A similar trend could be observed for foliose lichens: their dehydration dynamics appeared unaffected when adjacent to bryophytes (BRFO) but was accelerated when they coexisted with crustose lichens (CRFO). A different pattern emerged for crustose lichens: their drying process seemed enhanced when next to bryophytes (BRCR), while it appeared unaffected or slightly slowed down when sharing the community with foliose lichens (CRFO).

An even more complex scenario arose when all three life forms coexisted within the same region, as seen in the BRCF sample. In this specimen, bryophytes, crustose lichens, and foliose lichens occupied overlapping spaces, allowing direct interactions among them. In particular, it could be observed that the two crustose lichens thalli (top-left and bottom-centre of the BRCF sample; see real colour RGB picture in **Figure 3.10**) dried more slowly compared to when this life form was present alone. Specifically, the red colour, representing WC% < 5%, appears only at time 7 in crustose lichens spots in the BRCF sample, whereas in the crustose lichens-only community this colour was already present at time 3. Meanwhile, foliose lichens appeared to dry slightly faster that when present alone. In the composite, light blue regions (25% < WC% < 30%) were already visible around time 5-7, compared to time 9-11 for the pure foliose lichen community. Conversely, the desiccation of bryophytes desiccation seemed largely unaffected by the presence of other life forms.

3.1.2.5 Biological discussion and process interpretation

Considering the presented results, it is possible to outline some general considerations for understanding their impact in the biological context.

Nonvascular epiphytic communities shape water-related ecological processes. Through their morphological and anatomical traits, they directly influence the dynamics of hydration/dehydration cycles of the ecosystems, both at a micro- and macroscale [188]. In more detail, communities consisting of a single life form showed characteristic desiccation patterns. In particular, samples mainly consisting of bryophytes or foliose lichens showed slower desiccation in respects to community dominated by crustose lichens. This characteristic behaviour can be ascribable to morphological traits. Indeed, in the case of bryophytes, their very complex architecture and structure with different growth forms (*e.g.*, mats, cushions, turfs, or wefts) enhance their water holding capacity [221,222]. Moving to the inner structure of the thalli, bryophytes have a distinct water transport mechanism, as they prioritise the water movement through external pathways and capillary spaces [220,223]. Coming to lichens, both foliose and crustose varieties adopt their own water management strategies as well [224]. Considering the inner structure of the thalli, in fact, foliose lichens have a porous internal anatomy that retains more water to prevent rapid desiccation of the thallus. This makes them more similar to bryophytes in terms of water management. Conversely, many crustose lichens avoid the formation of water films on their upper surface, thus limiting their water uptake and reducing the risk of water supra-saturation.

The described water uptake strategies, characteristic for each growth form, are the result of adaptations to compensate for the water saturation, while facilitating the photosynthetic activity.

When moving to composites, typical of natural environments, the functional composition of the community is the decisive factor in determining how the epiphytic community manages water and how it contributes to the water balance at the ecosystem level. Although complex, by analysing communities composed of several organisms, it is possible to figure out mechanisms of competition or facilitation for the water resource within the community. Organisms that adopt similar uptake strategies, such as bryophytes and foliose lichens, do not differ in the water management, suggesting mechanisms of favouritism toward the water resource. In contrast, if crustose lichens are present along with bryophytes and/or foliose lichens, water loss is faster for the thalli of bryophytes and foliose lichens, while it is slower for the thalli of crustose lichens, suggesting mechanisms of competition for water resources. These results are in accordance with the hypothesis presented by Bowker *et al.*, who suggested that facilitation and competition mechanisms are a response of species to stress [225].

3.1.3 Materials and methods

Samples were collected using a chisel on chestnut (Castanea sativa Mill.) bark in a remote area of the Ligurian Apennines (N-Italy) and kept in paper bags until return to the laboratory. Here, all samples were left at room temperature and humidity (18°C and 40% relative humidity) for one week. During the week the weights of all samples were monitored until weight stabilisation and then natural dry weight was measured and stored as DW (Dry Weight).

The day before the analysis samples were sprayed every three hours with water until the saturation point was reached. During the day of analysis, just before the analysis started, samples were treated according to Longinotti *et al.* [226]: the upper surface of the samples was sprayed with water until complete hydration was achieved, *i.e.* continued spraying would not induce an increase in wet mass. The samples were then shaken to remove the external water and, finally, their surface was quickly blotted with paper towel to avoid the presence of waterdrops. The weight after blotting was measured and stored as WW (Wet Weight).

Immediately after weighing, samples underwent NIR hyperspectral analysis. The samples were divided into 8 different trays to facilitate HSI analysis, each tray containing the four physical replicates of one of the sample types. The process of weighing and taking hyperspectral images was repeated every 45 minutes for each tray, analysing the trays in a fixed order to ensure consistency in the time gap between analysis. The weight measured each time before taking the images was stored as CW (Current Weight). Between one set of measurements and the following, the samples were kept in fixed laboratory conditions. The temperature and relative humidity of the laboratory was monitored using a data logger (Onset HOBO MX2304 Weatherproof Bluetooth Temperature Data Logger with External Sensor) that recorded data every minute, and both resulted to be stable, with mean values respectively 19.7°C and 40.5%.

In total, the analytical procedure was repeated every 45 minutes for 15 times (t01-t15), covering a total of 630 minutes (= 10h 30’). Two other measurements were taken the following day, one at 26 h (t16) and one at 32 h (t17) from the first measurement, with the aim of including in the study also the following steps of the drying process. Finally, the pipeline was repeated one last time around one month after the end of the experiment (t18) to ensure that the samples had completely dried and that they had gotten to stable conditions. Complete drying was considered achieved when the weight of samples was not significantly changing overtime for at least 3 days.

3.1.3.1 Water content

To evaluate the amount of water present in the samples at every stage of the drying process, an index was calculated, according to **Equation 3.1**:

$$WC\% = \frac{CW - DW}{CW} * 100\% \qquad (3.1)$$

Water content (WC%) is expressed as a percentage and indicates equivalent water per mass of the dry thallus area [186,205,226]. It is calculated by subtracting the dry weight (DW) from the current weight (CW) and then normalising the result according to the CW. Therefore, it provides an indication of the percentage of water contained in the sample with respect to the sample's weight at that specific time. It ranges from 0% when CW = DW to values always lower than 100%.

For summarising the information related to the water content, several indices were calculated alternatively combining DW, CW and WW [205]. However, all indices were confrontable and therefore the most represented in literature was chosen.

3.1.3.2 Hyperspectral imaging

NIR-HSI images were acquired for all samples using a push-broom HSI system by Specim (Spectral Imaging ltd., Oulu, Finland) composed of a short-wave infrared SWIR3 hyperspectral camera operating in the 1000–2500 nm spectral range with an OLES15 camera lens located 25 cm above the samples. The camera had a spatial resolution of 384 pixels and 288 spectral channels (FWHM = 5.6 nm). The resulting image had a pixel size of about 0.5 mm. Samples were scanned using a horizontal linear scanner (40 × 20 cm LabScanner) and were illuminated with three tungsten halogen lamps (12 V, 35 W, 430 lm, 2900 K, each) located 30 cm away from the samples and with a 45° angle. During image acquisition, the frame rate was equal to 50 Hz and the exposure time was set to 9 ms. The Lumo Scanner v. 2.6 software (Specim, Spectral Imaging ltd., Oulu, Finland) was used to control the system. Dark (closed shutter) and white (20 × 200 mm plate, 99% reflectance Spectralon®) reference images were automatically recorded and stored before analysis of each tray of samples. The dark image was subtracted from sample and the white reference images. After this, reflectance (R) was computed dividing the sample image by the white reference in a wavelength and pixel-resolved way. A total of 144 (8 sample trays × 18 times) images were recorded during the experiment.

3.1.3.3 Data treatment

The data treatment consisted of the following steps: a) images processing, aimed at preparing the collected HSI data and b) multivariate analysis of the pre-processed data to explore the sources of variation and developing calibration models for the assessment of WC% during the dehydration of epiphytic communities. These steps are summarised in **Figure 3.12** and detailed below.

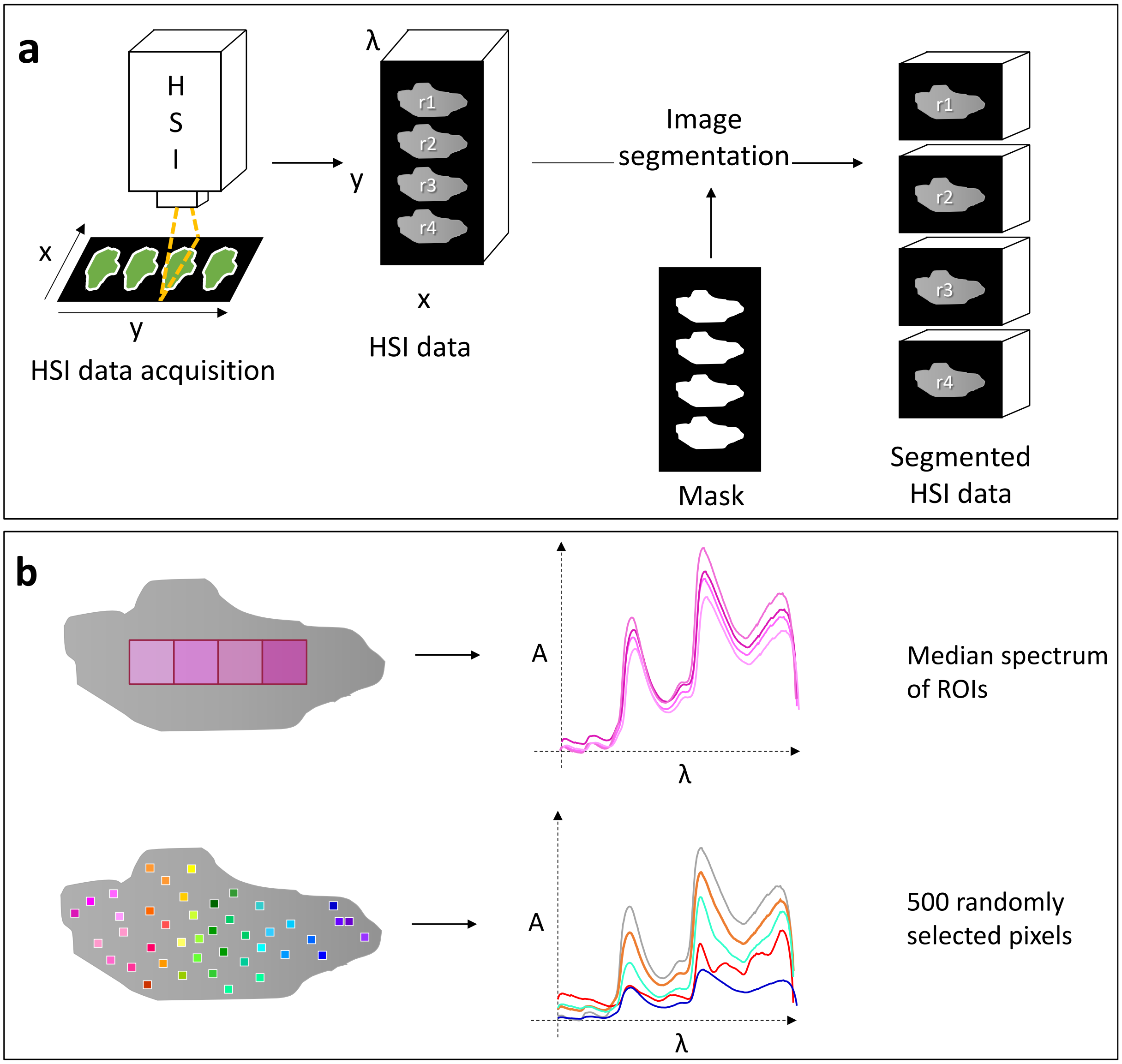

***Figure 3.12**: Data processing pipeline. A: Image acquisition, masking and segmenting; B: Visual schematisation of data selection with image-based (top) and pixel-based (bottom) approaches.*

3.1.3.3.1Image processing

All data pre-processing, processing and chemometrics analysis were carried out using in-house developed scripts in the MATLAB® environment, version R2023a (The MathWorks, Natick, MA, USA) and the PLS-Toolbox 9.2 software (Eigenvector Research Inc., Manson, WA, USA).

Each captured hyperspectral image was stored in a three-dimensional data array, wherein the first two dimensions represented the length and width in pixels, respectively, while the third dimension corresponded to the 288 wavelength channels. The initial step in data treatment involved masking the background using a total intensity threshold, and it was followed by image segmentation, used to separate the four physical replicates measured simultaneously. This step involved the detection and extraction of each sample from the original image, as shown in **Figure 3.12A**. This segmentation process was automated across all collected images, thereby storing a total of 576 (8 sample trays × 4 replicates in each tray × 18 times) segmented images and their associated masks.

Before conducting multivariate analysis, the reflectance spectra were transformed into pseudo-absorbance, *i.e.* $-log_{10}(\mathrm{R})$ was calculated and then pre-processed. The pre-processing involved applying a Savitzky-Golay first derivative (second order polynomial and window size of 11 points) [132] followed by normalisation to unit length obtained by computing the square root of the sum of the squared value of all selected variables for the given sample, returning a vector of length equal to 1.

3.1.3.3.2 Multivariate analysis

Multivariate analysis was carried out for data exploration and building calibration models to predict water content. However, given the high amount of data to be handled, before multivariate analysis information was extracted from each pre-processed image using two different approaches: a) image-based and b) pixel-based [58], as represented in Figure **3.12B**.

The image-based approach consisted first of individuating four adjacent 25x25 pixels regions of interest (ROIs) from the centre of each segmented image. For each of those regions, the median SWIR spectrum was calculated, and then an average of the four medians was computed, thus obtaining a single spectrum to represent the whole sample. This resulted in a total of 576 mean spectra collected in a matrix with 576 rows (samples) and 288 columns (spectral variables). Even though the proposed image-based strategy is not properly accounting for spatial variability within each sample, the presented approach was aimed at interpreting the spectral data and drawing general conclusions on macroscopic differences among the samples of different epiphytic communities during the dehydration process. Indeed, condensing the information for each sample in a single spectrum improves the readability both of score and loading plots and regression vectors.

The pixel-based approach consisted of extracting 500 random pixels from each segmented image and it allowed to take into consideration the intra-sample biological variability. In this way the models developed were more robust, in terms of representativity of the samples, though more complex for the sake of interpretation.

Both the approaches were carried out in parallel in all stages of data analysis, with the aim of checking the consistency of the two strategies but also for exploiting, from one side, the interpretability of a simple approach and, from the other side, the robustness of a properly trained model. The data issued from each approach were used as input for the development of multivariate analysis models, using the strategies described below.

Principal component analysis (PCA)

In this study, PCA was used for exploratory data analysis using the datasets obtained from image- and pixel-based approaches. In the first case (image-based), the data matrix with the mean spectrum from each pre-processed image was column mean centred and subjected to PCA. Score and loading plots were analysed to understand the spectral regions most significant to globally describe the dissimilarities among the distinct types of nonvascular epiphytic communities throughout the dehydration process. Systematic differences between physical replicates were also studied, to better understand the influence of inter- and intra-specific variation.

When employing the pixel-based approach, the PCA model was built using spectra exclusively from samples exhibiting a single life form, *i.e.* BRYO, LICR, LIFO and WOBA, as the training set. Given the interest of representing the samples as score maps, highlighting the distribution of different communities from a spatial perspective, prediction score maps were also obtained. To do that, all pixel spectra of the training set and test set (binary and ternary composites - BRCF, BRCR, BRFO, CRFO), were pre-processed using the same strategy used for model training and projected onto the previously obtained model, *i.e.* their spectra were multiplied to the model's loading values and score values were obtained.

False-colour RGB score maps were derived overlaying the first three principal components [227], thus having the first PC accounting for the red colour and the second and the third for green and blue, respectively. Then, to better interpret the score maps of the test set, false-colour RGB colourbars were produced from the samples of the training set. To reach this goal, scores of pure communities at each time were averaged across all four replicates, thus obtaining a PC1/PC2/PC3 triplet referring to this specific pure community at this sampling time. The triplet was translated into an RGB colour and used to describe the behaviour of the life form at the considered time. In this way, four colourbars were obtained, one for bryophytes, one for crustose lichens, one for foliose lichens and one for bark, and used together to interpret the behaviour of binary and ternary composites.

Partial least squares regression (PLS-R)

In this study, PLS regression models were built to predict the water content both at an image level and at a pixel level. Before PLS regression model training, the samples were split into independent training and test sets. The test set comprised four composites, one randomly selected from each composite type, and in particular BRCR replicate 4, BRFO replicate 2, CRFO replicate 1 and BRCF replicate 1. The training set comprised all pure communities (BRYO, LICR, LIFO and WOBA) and the remaining three physical replicates from each composite type, amounting to 28 samples.

To build the PLS regression model, both the matrix with pre-processed spectral data and the vector with reference water content were column mean centred. To determine the number of significant PLS latent variables, a leave-one-sample-out cross validation method was used. In more detail, at each cross-validation iteration, a physical replicate at all sampling times was kept out, thus at each iteration of the cross-validation the model was built on 27 out of the 28 samples of the training set and tested on all 18 times of the left out sample. This approach ensures a minimisation of overfitting [96], ensuring that the model is being evaluated on samples independent from those used for model calibration. The final RMSECV was calculated as an average of the RMSECV obtained at each iteration.

Figures of merit for multivariate calibration were calculated to evaluate the performances of model training and test [228]. In particular, the best model was chosen minimising the root mean square error in cross validation (RMSECV).

After building the PLS regression models, they were employed to predict the WC% of samples within the test set. Both the image-based and the pixel-based approaches were used in prediction, and the outcomes were compared. The final result was a water content for each pixel of the image, enabling the visualisation of a sample water map for each time of the dehydration process. To ensure that a specific colour represented the same water content in all images, facilitating the comparison between both different samples at the same time and the same sample at different times, the colour scale used for the images was kept constant and was scaled between the minimum and the maximum water contents identified in the dataset, *i.e.* between 0% to 45%.

3.1.4 Conclusions

Using NIR-HSI and multivariate methods, the present study enabled the detailed visualisation of water content maps during the dehydration process of nonvascular epiphytic communities, revealing patterns of water management that highlight facilitation and competition mechanisms between different life forms. The present research has underscored the importance of studying the dynamic processes of resource management between species with different morphologies and anatomies through a spatially-resolved approach, a topic considered particularly challenging by the scientific community.

For the first time, an analytical strategy based on HSI was established to map the water content of nonvascular epiphytic communities during a desiccation process while explicitly accounting for interactions among different life forms. In particular, exploratory analysis of the data by means of PCA demonstrated that the highest source of variability throughout the process arises primarily from water loss, while differences among communities were also detectable. Indeed, the production of false-colour RGB score maps enabled the evaluation of different life forms' behaviour, providing an initial contribution to understanding facilitation and competition mechanisms based on community composition. Moreover, the use of multivariate regression by means of PLS to predict water content at the pixel level led to the construction of single layer maps representing the actual humidity of each pixel composing the sample, thus permitting the evaluation of communities' behaviour at a fine-scale. Importantly, all result obtained from the analysis of raw spectra, PCA, and regression were mutually consistent and accurately reflected what was observed by weight loss monitoring, thereby providing a valuable method for recovering spatial information while monitoring dehydration.

The analytical impact and novelty of the approach were further supported by the consistency of results obtained when developing the model with two different strategies, namely image-based and pixel-based, and by the complementarity of the information derived from each strategy. This result suggests the advantage of not prioritising one strategy over the other, highlighting instead the importance of applying both to gain a deeper understanding of the topic under study.

The analytical strategy developed in this work has the potential to exert substantial impact in this context, enabling real time, non-destructive monitoring of water management for lichens and bryophytes, and demonstrating the viability of NIR-HSI as a tool for following dehydration processes in living organisms. In particular, the possibility of monitoring the process without interfering with community water management could lead to an enhanced understanding of potential ecosystem functions for other organisms associated with the same environment as the monitored one.

However, it is important to consider that photosynthetic activity is strongly associated with water management. Therefore, contextual monitoring of metabolic activity and moisture content of communities might be relevant in further work. Indeed, mechanisms of facilitation and competition in water management could mirror those of photosynthesis, and such insight might ultimately increase the relevance of the conclusions.

Appendix A


BRYO
r1
r2
r3
r4
t1
t2
t3
t4
t5
t6
t7
t8
t9
t10
t11
t12
t13
t14
t15
t16
t17
t18
Sampling point
1
2
3
4
5
6
7
8
9
10
11
12
13
14
15
16
17
18

LICR

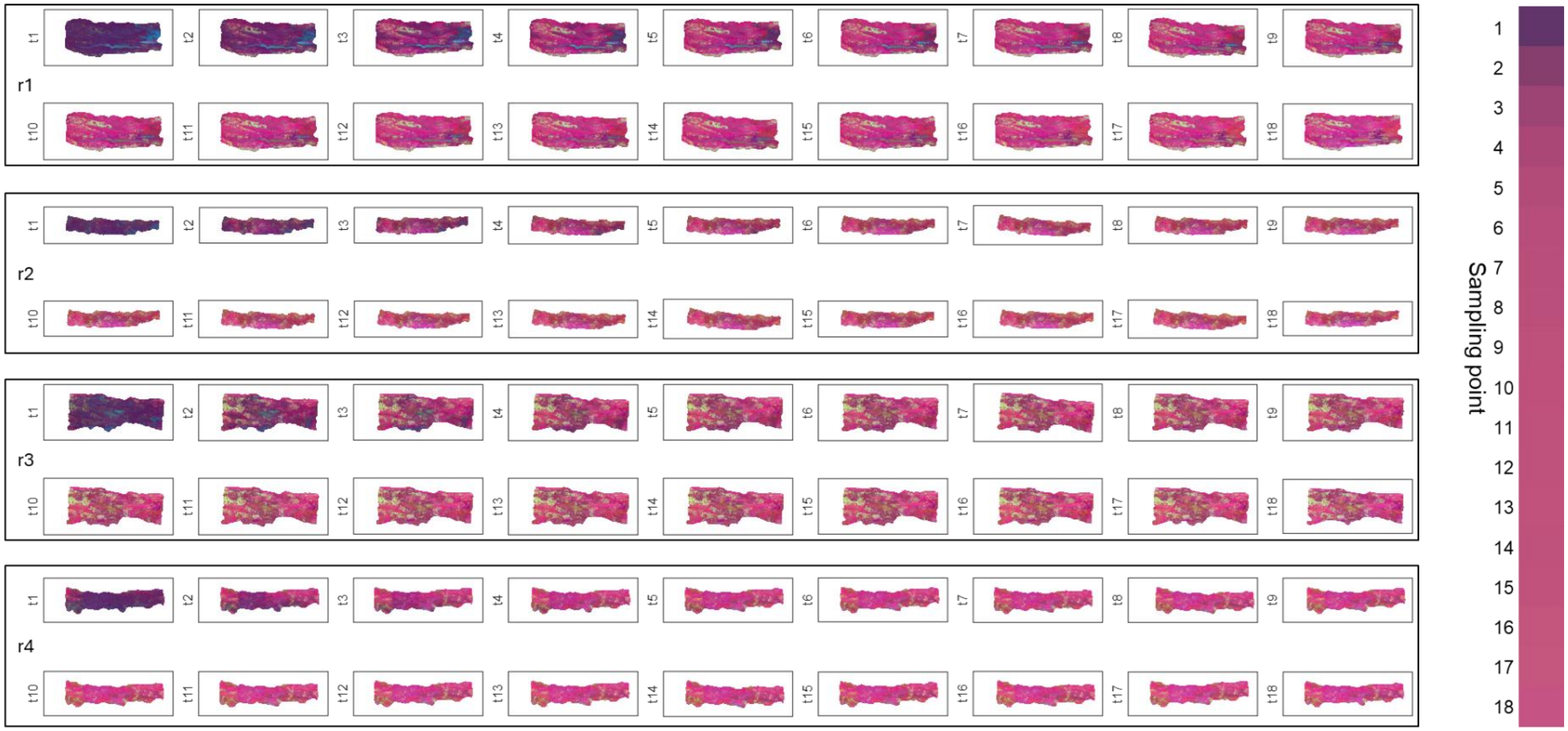
r1
r2
r3
r4
t1
t2
t3
t4
t5
t6
t7
t8
t9
t10
t11
t12
t13
t14
t15
t16
t17
t18
Sampling point
1
2
3
4
5
6
7
8
9
10
11
12
13
14
15
16
17
18

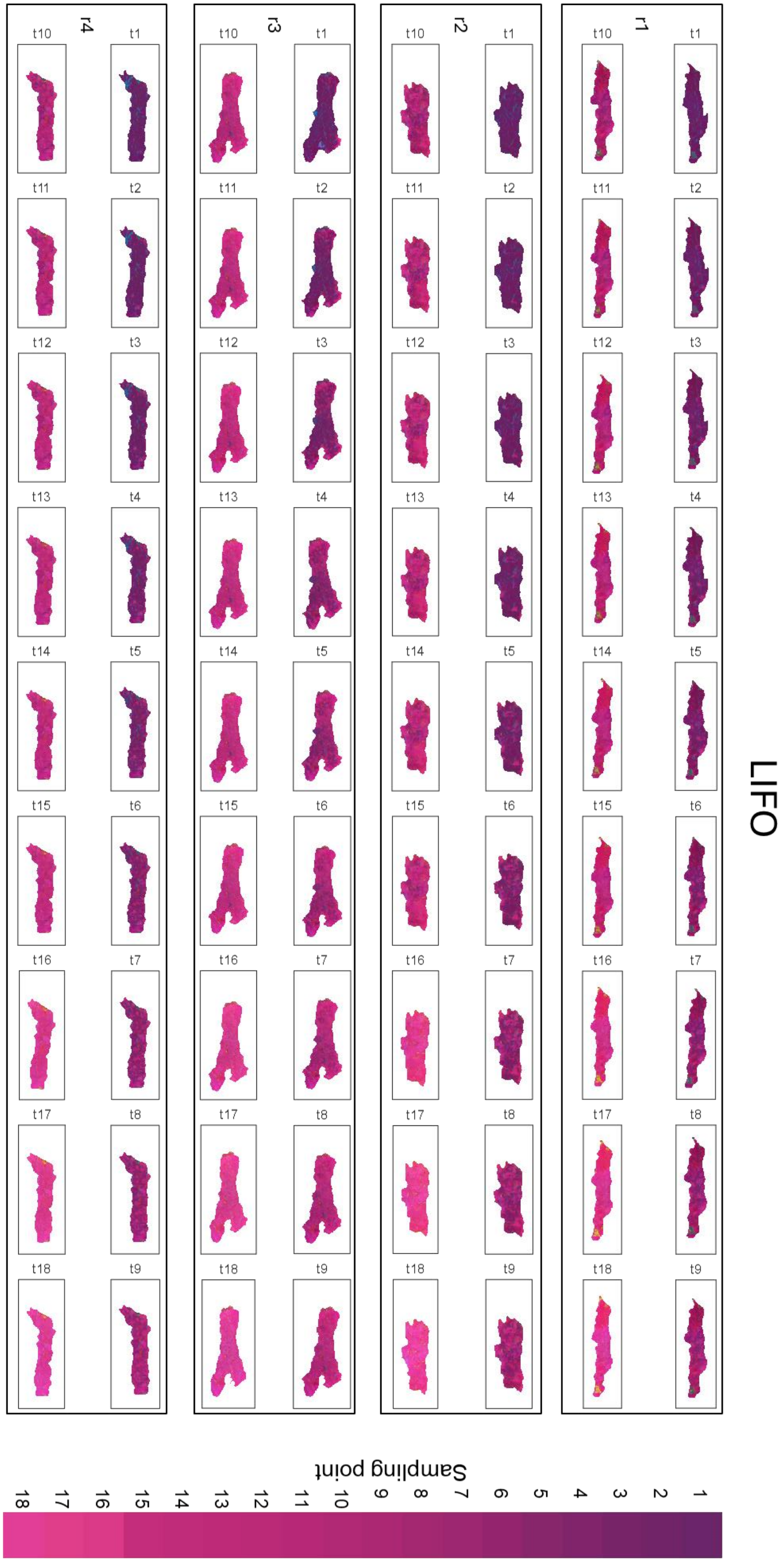
LIFO
r1
r2
r3
r4
t1
t2
t3
t4
t5
t6
t7
t8
t9
t10
t11
t12
t13
t14
t15
t16
t17
t18
Sampling point
1
2
3
4
5
6
7
8
9
10
11
12
13
14
15
16
17
18

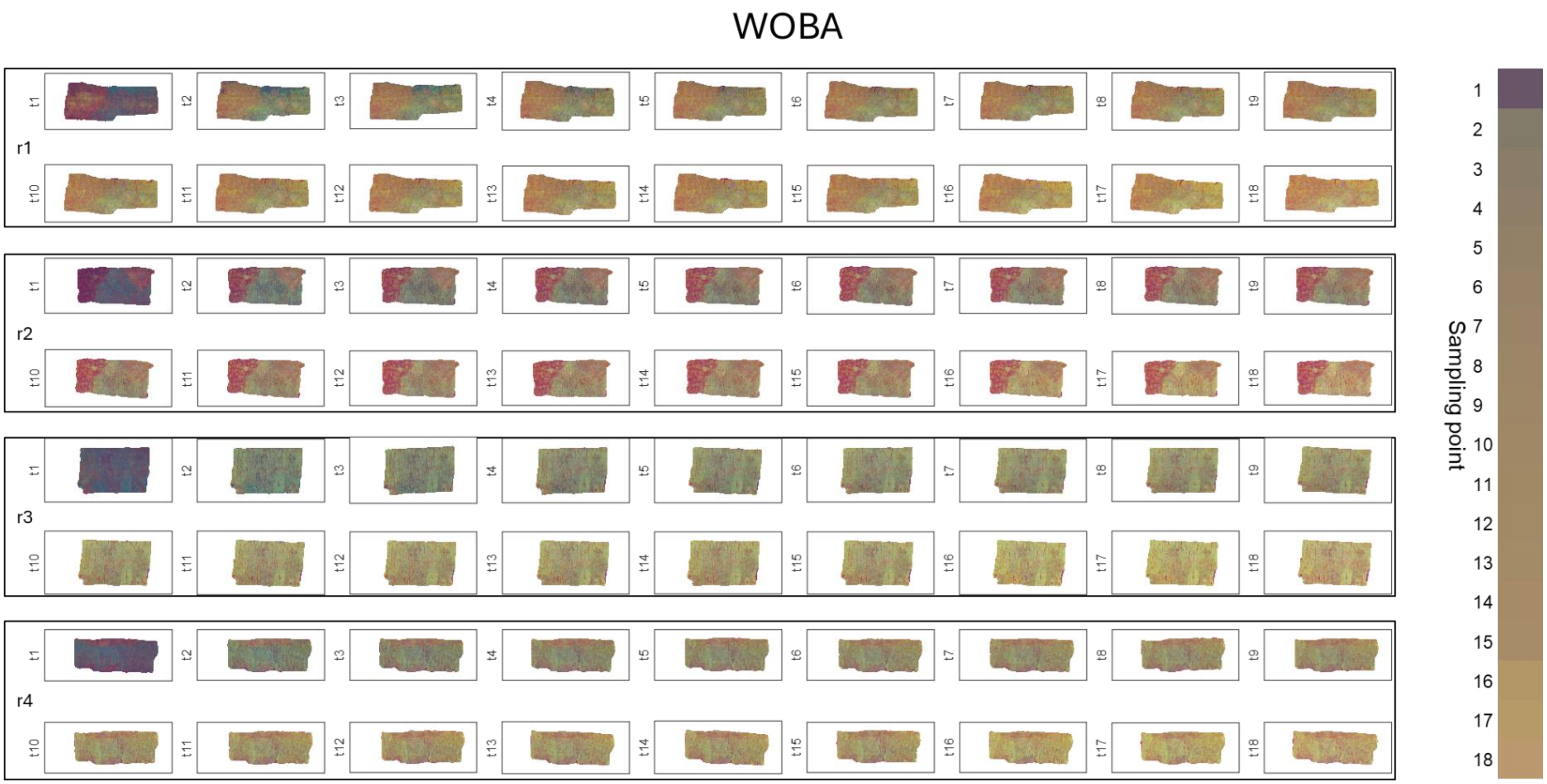
WOBA
r1
r2
r3
r4
t1
t2
t3
t4
t5
t6
t7
t8
t9
t10
t11
t12
t13
t14
t15
t16
t17
t18
Sampling point
1
2
3
4
5
6
7
8
9
10
11
12
13
14
15
16
17
18

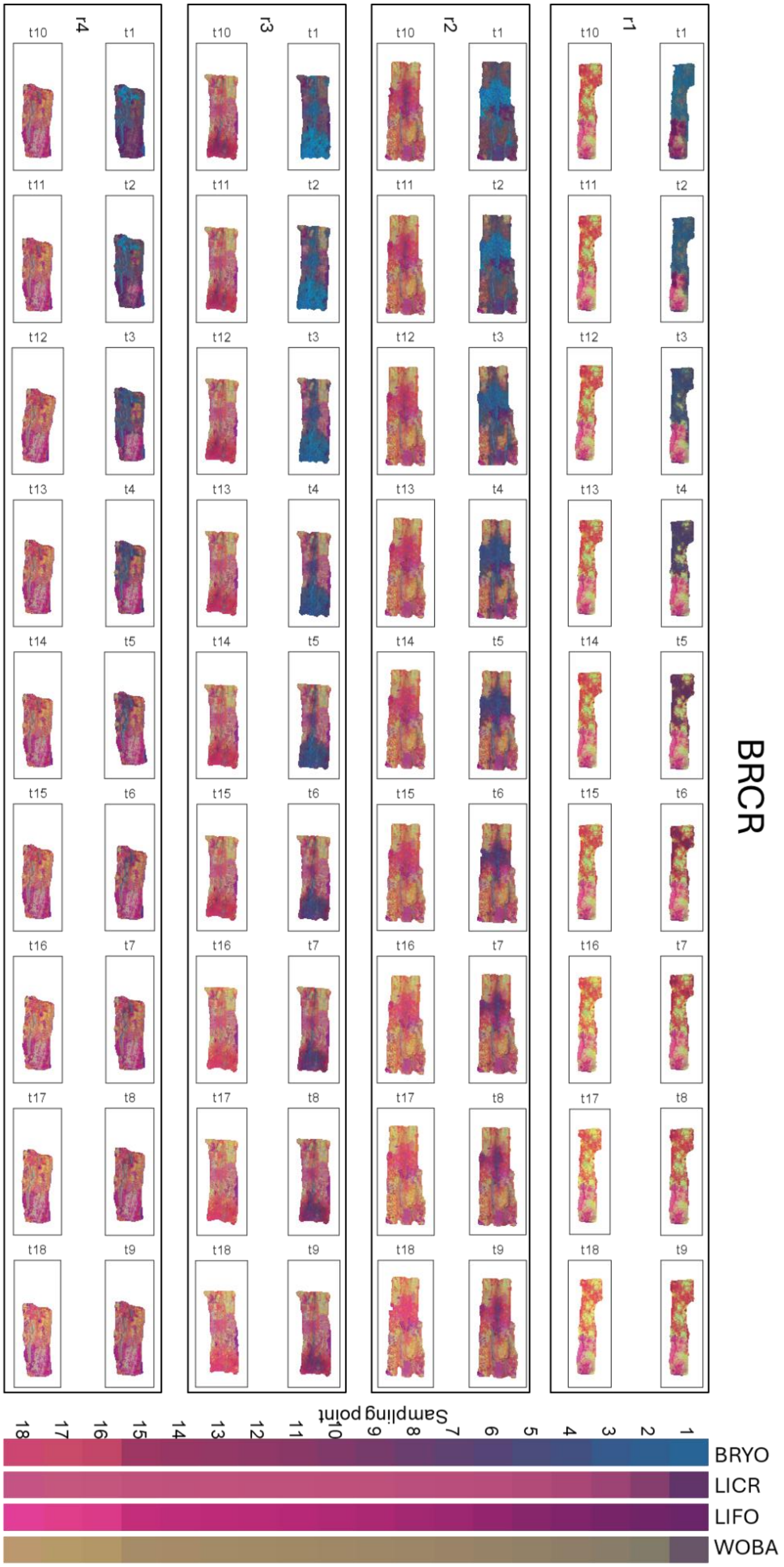
BRCR
r1
r2
r3
r4
t1
t2
t3
t4
t5
t6
t7
t8
t9
t10
t11
t12
t13
t14
t15
t16
t17
t18
Sampling point
1
2
3
4
5
6
7
8
9
10
11
12
13
14
15
16
17
18
BRYO
LICR
LIFO
WOBA


BRFO
r1
r2
r3
r4
t1
t2
t3
t4
t5
t6
t7
t8
t9
t10
t11
t12
t13
t14
t15
t16
t17
t18
Sampling point
1
2
3
4
5
6
7
8
9
10
11
12
13
14
15
16
17
18
BRYO
LICR
LIFO
WOBA


CRFO
r1
r2
r3
r4
t1
t2
t3
t4
t5
t6
t7
t8
t9
t10
t11
t12
t13
t14
t15
t16
t17
t18
Sampling point
1
2
3
4
5
6
7
8
9
10
11
12
13
14
15
16
17
18
BRYO
LICR
LIFO
WOBA

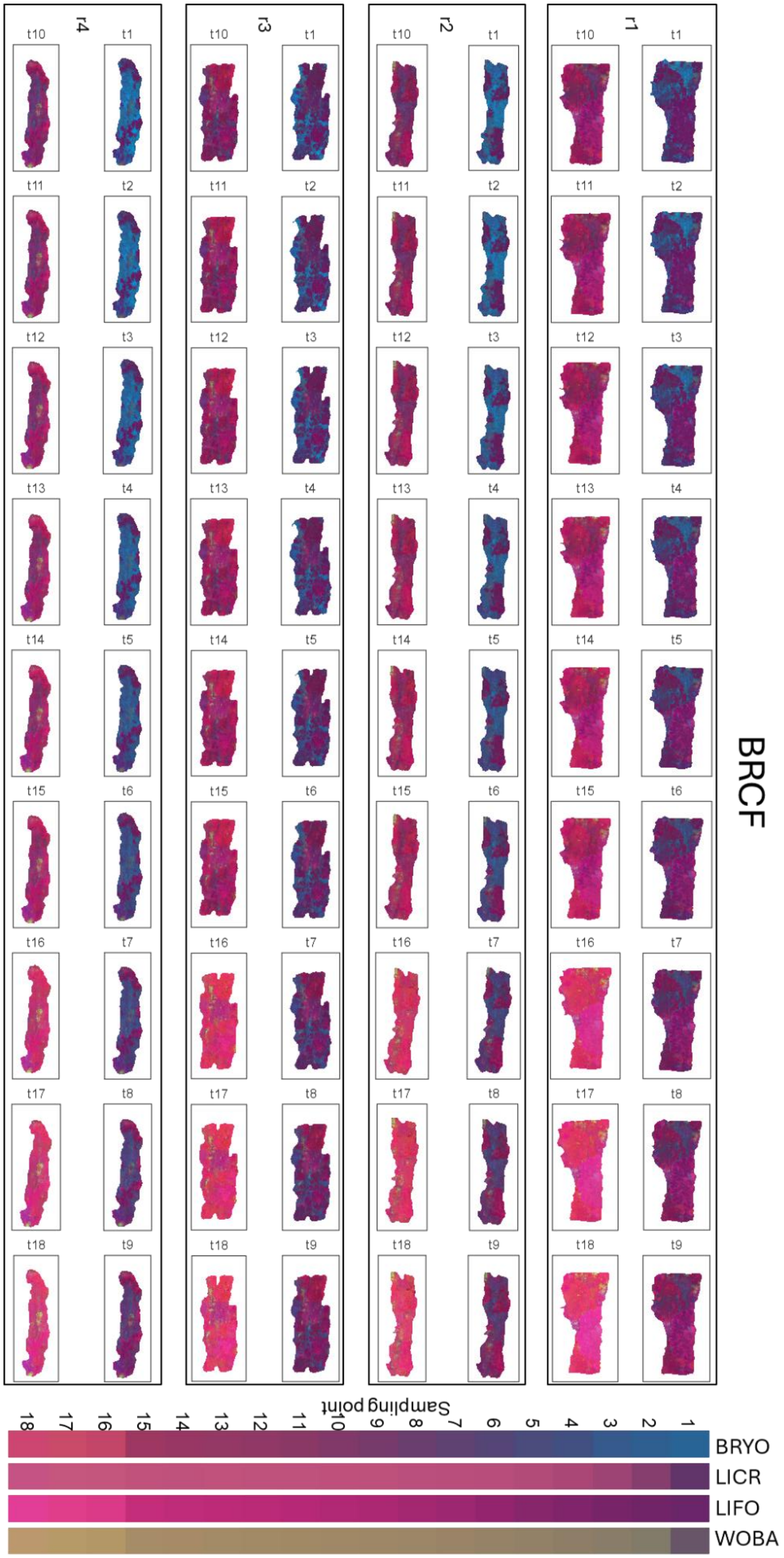
BRCF
r1
r2
r3
r4
t1
t2
t3
t4
t5
t6
t7
t8
t9
t10
t11
t12
t13
t14
t15
t16
t17
t18
Sampling point
1
2
3
4
5
6
7
8
9
10
11
12
13
14
15
16
17
18
BRYO
LICR
LIFO
WOBA

Appendix B

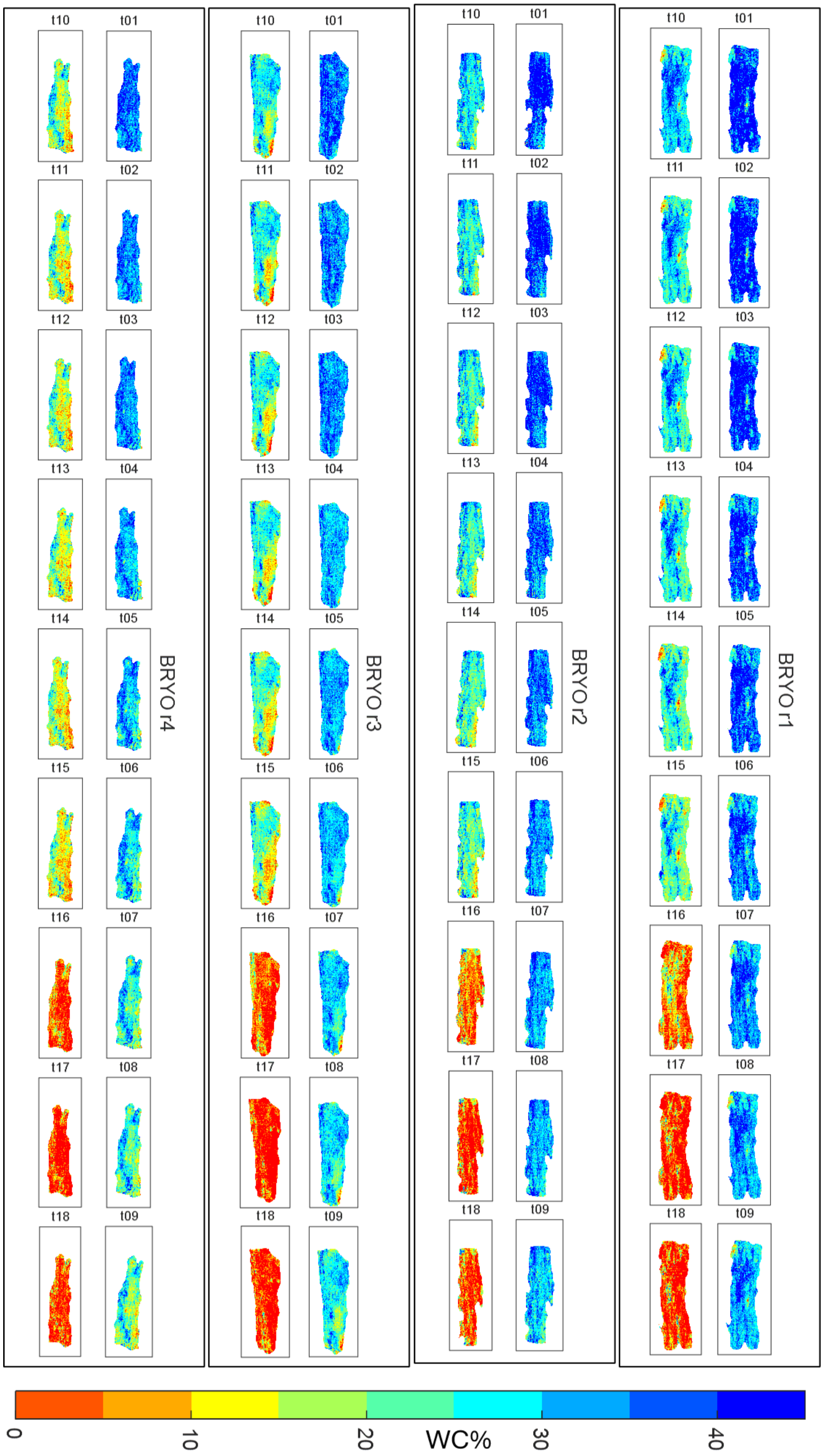
BRYO r4
BRYO r3
BRYO r2
BRYO r1
t01
t02
t03
t04
t05
t06
t07
t08
t09
t10
t11
t12
t13
t14
t15
t16
t17
t18
0
10
20
WC%
30
40

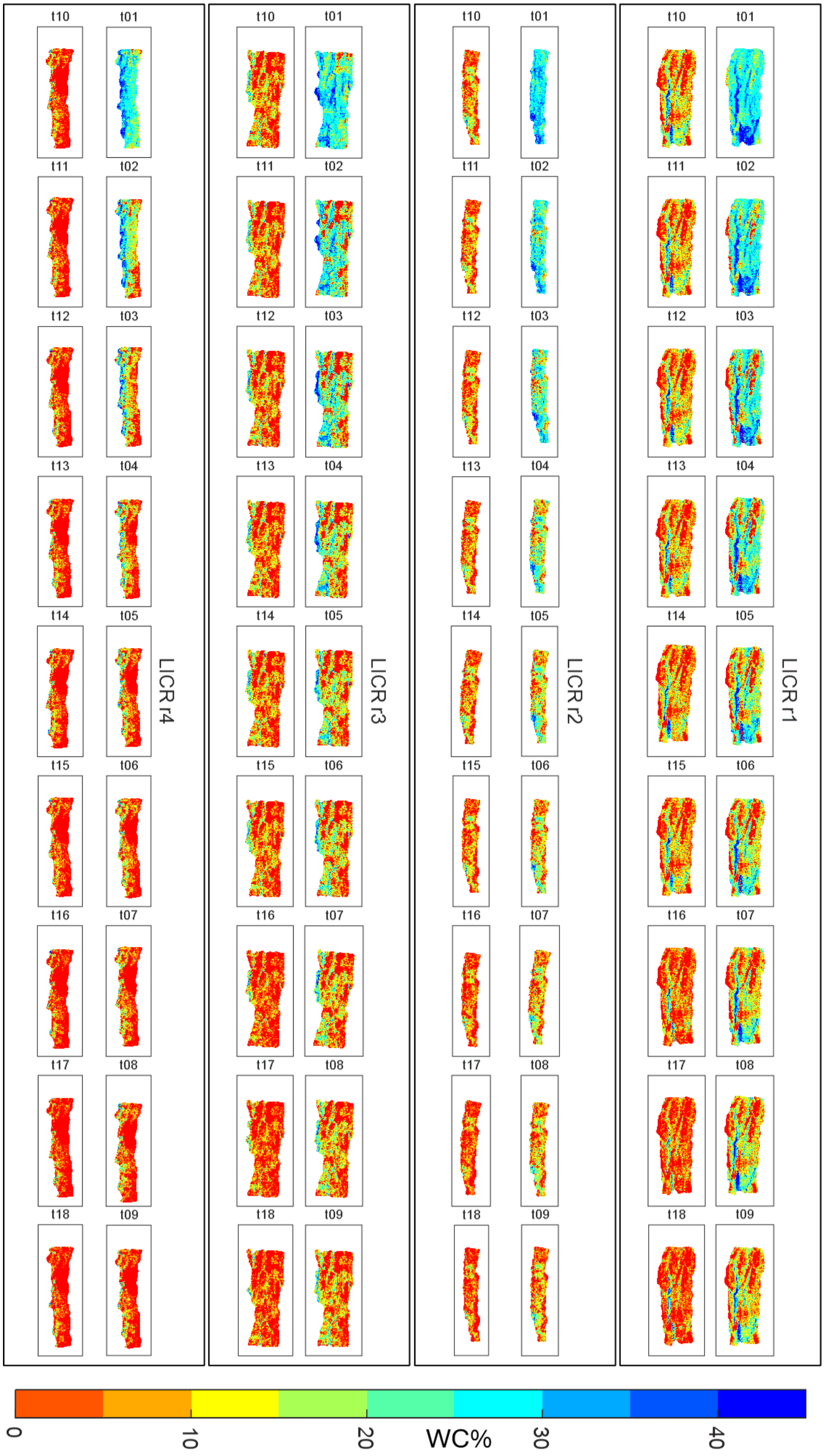
LICR r1
LICR r2
LICR r3
LICR r4
t01
t02
t03
t04
t05
t06
t07
t08
t09
t10
t11
t12
t13
t14
t15
t16
t17
t18
0
10
20
WC%
30
40

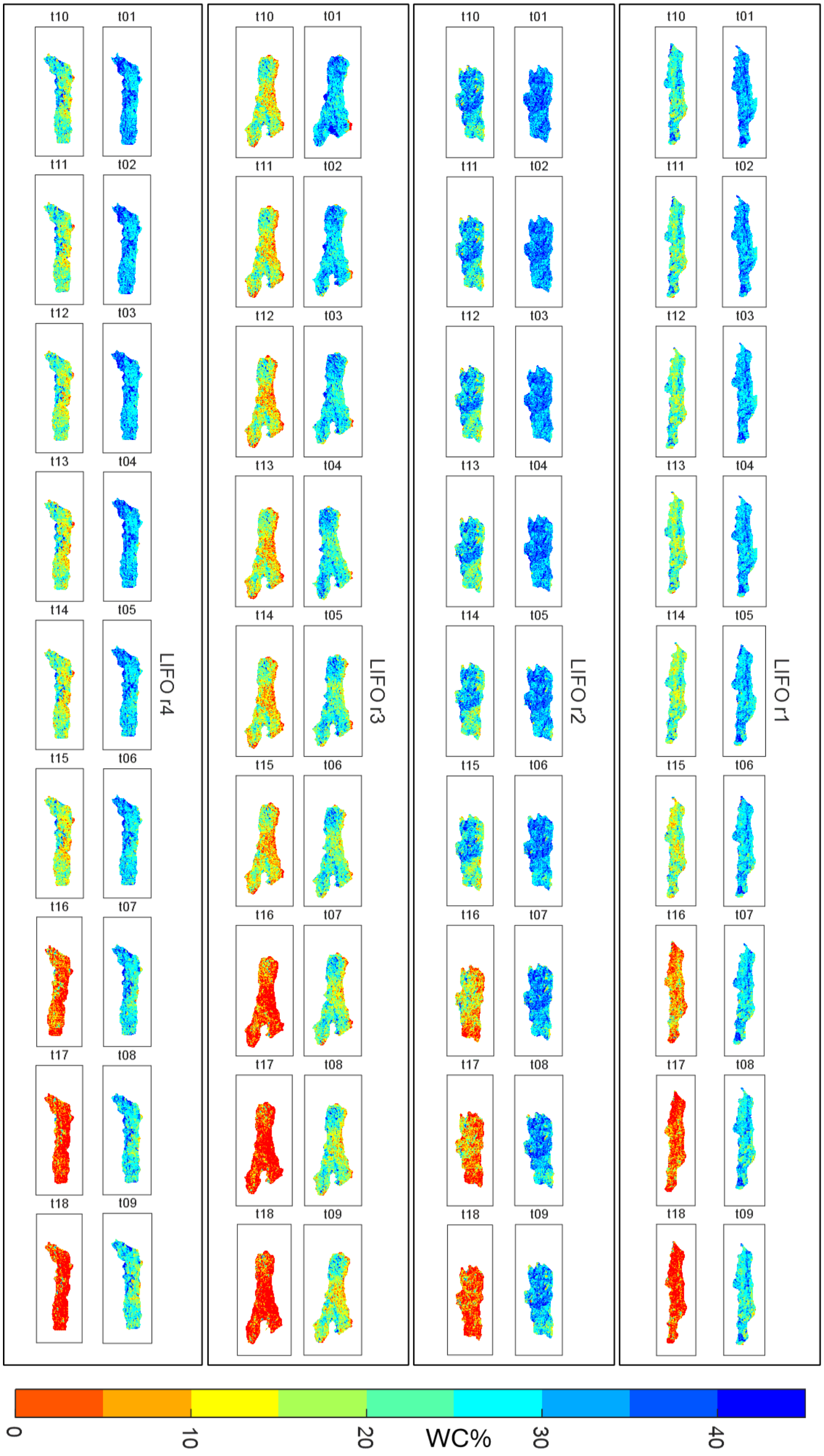

LIFO r4
LIFO r3
LIFO r2
LIFO r1
t01
t02
t03
t04
t05
t06
t07
t08
t09
t10
t11
t12
t13
t14
t15
t16
t17
t18
0
10
20
WC%
30
40

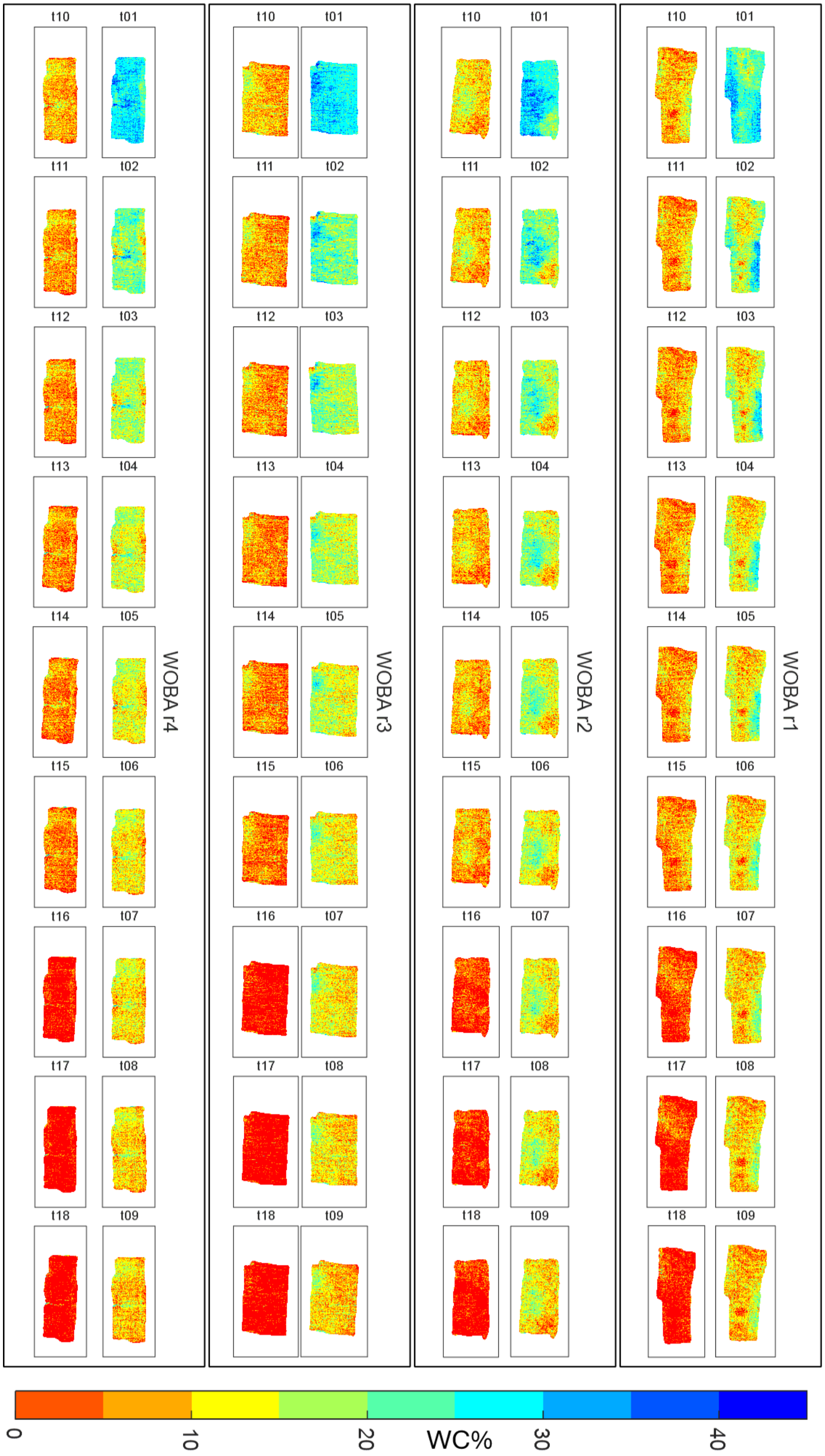
WOBA r4
WOBA r3
WOBA r2
WOBA r1
t01
t02
t03
t04
t05
t06
t07
t08
t09
t10
t11
t12
t13
t14
t15
t16
t17
t18
0
10
20
WC%
30
40

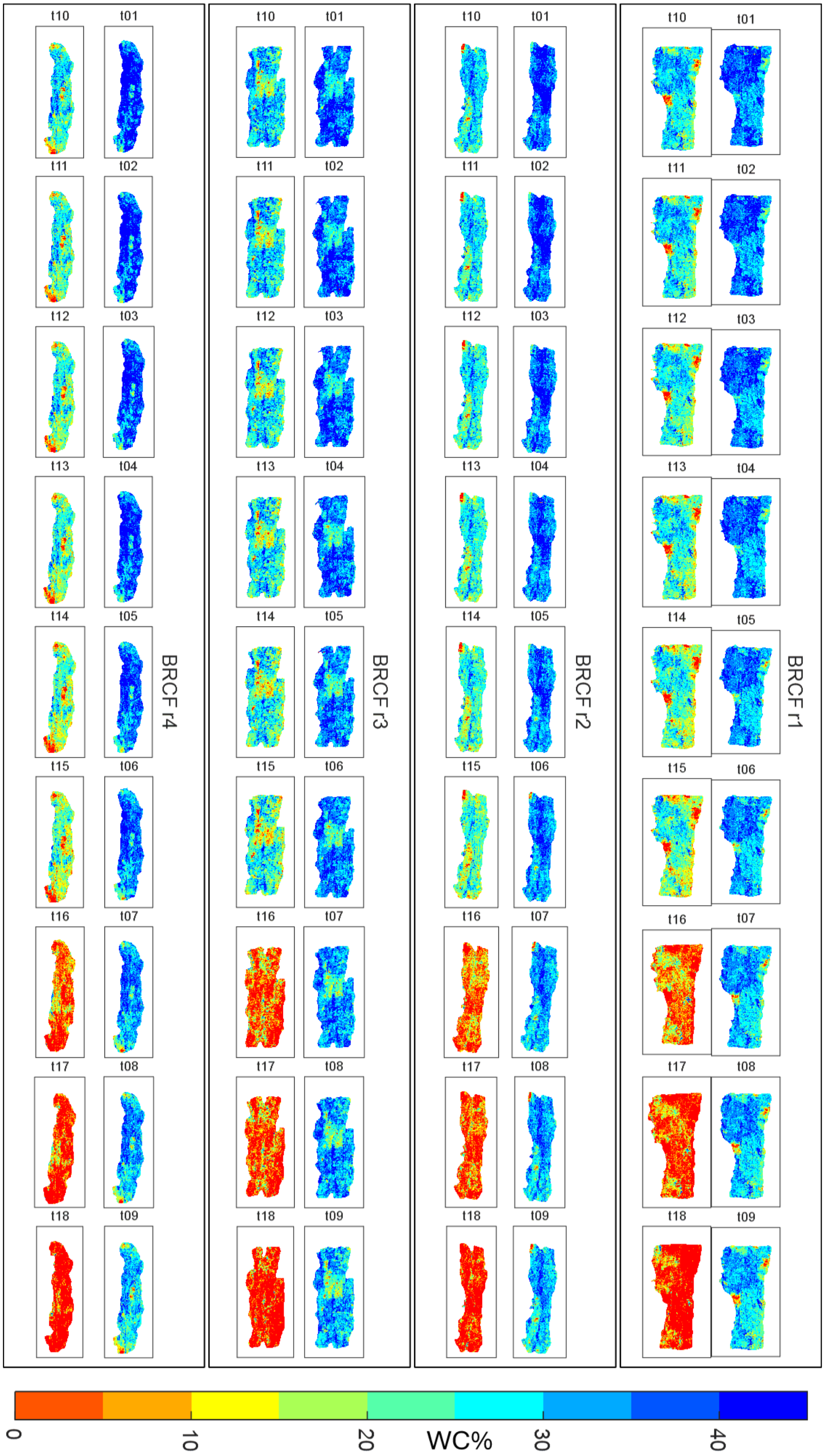
BRCF r1
BRCF r2
BRCF r3
BRCF r4
t01
t02
t03
t04
t05
t06
t07
t08
t09
t10
t11
t12
t13
t14
t15
t16
t17
t18
0
10
20
WC%
30
40

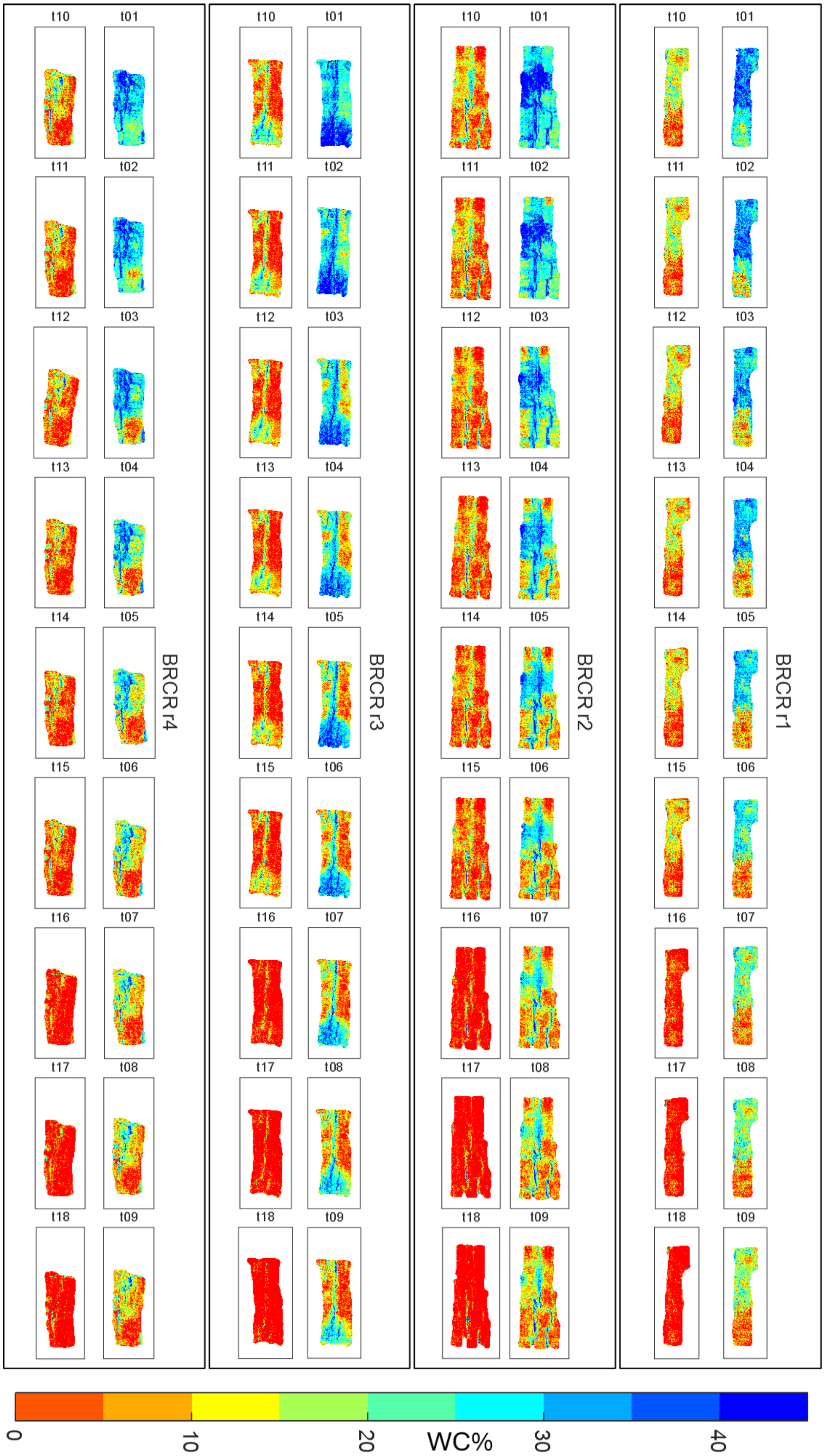
BRCR r1
BRCR r2
BRCR r3
BRCR r4
t01
t02
t03
t04
t05
t06
t07
t08
t09
t10
t11
t12
t13
t14
t15
t16
t17
t18
0
10
20
WC%
30
40

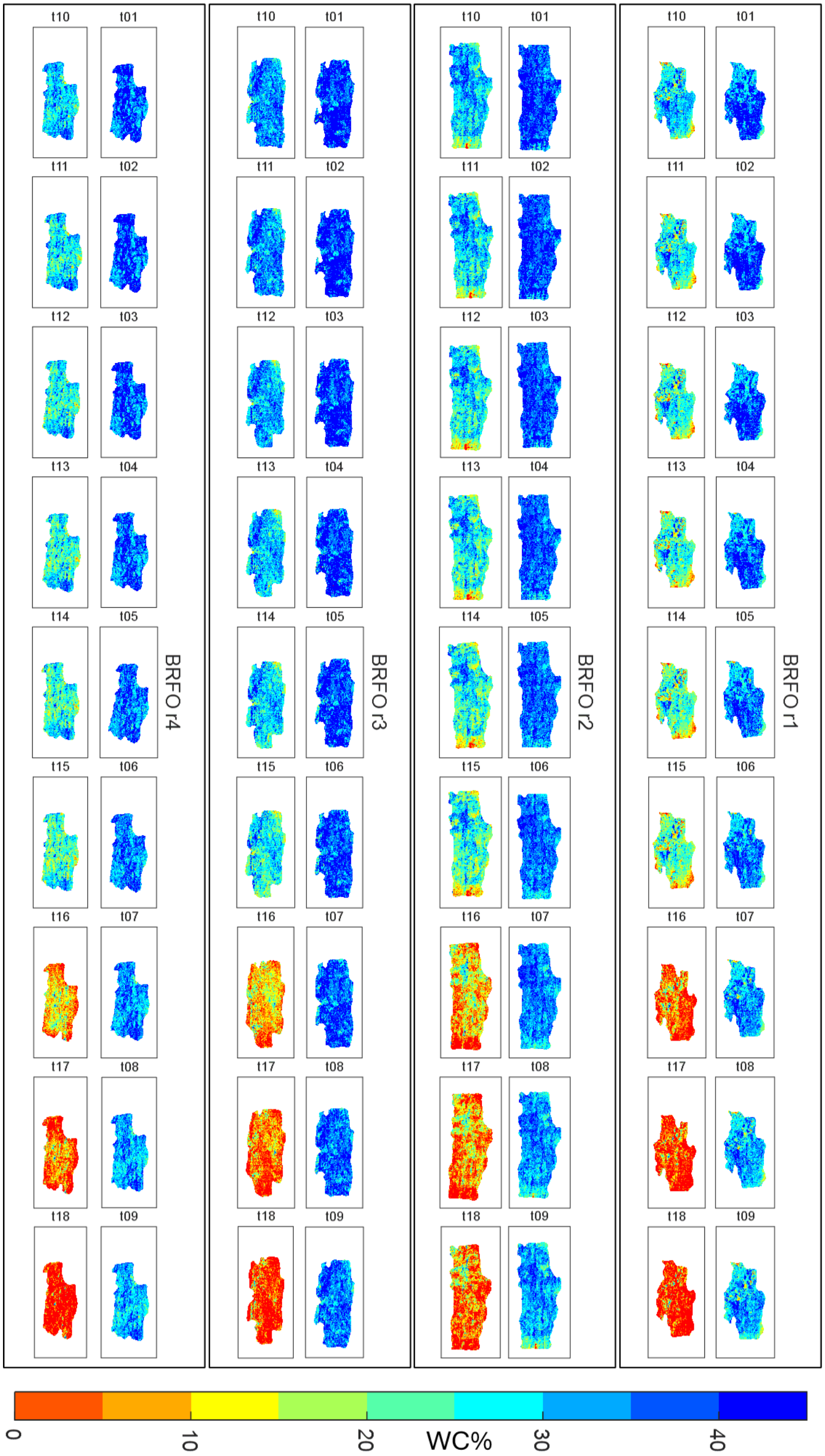
BRFO r4
BRFO r3
BRFO r2
BRFO r1
t01
t02
t03
t04
t05
t06
t07
t08
t09
t10
t11
t12
t13
t14
t15
t16
t17
t18
0
10
20
WC%
30
40

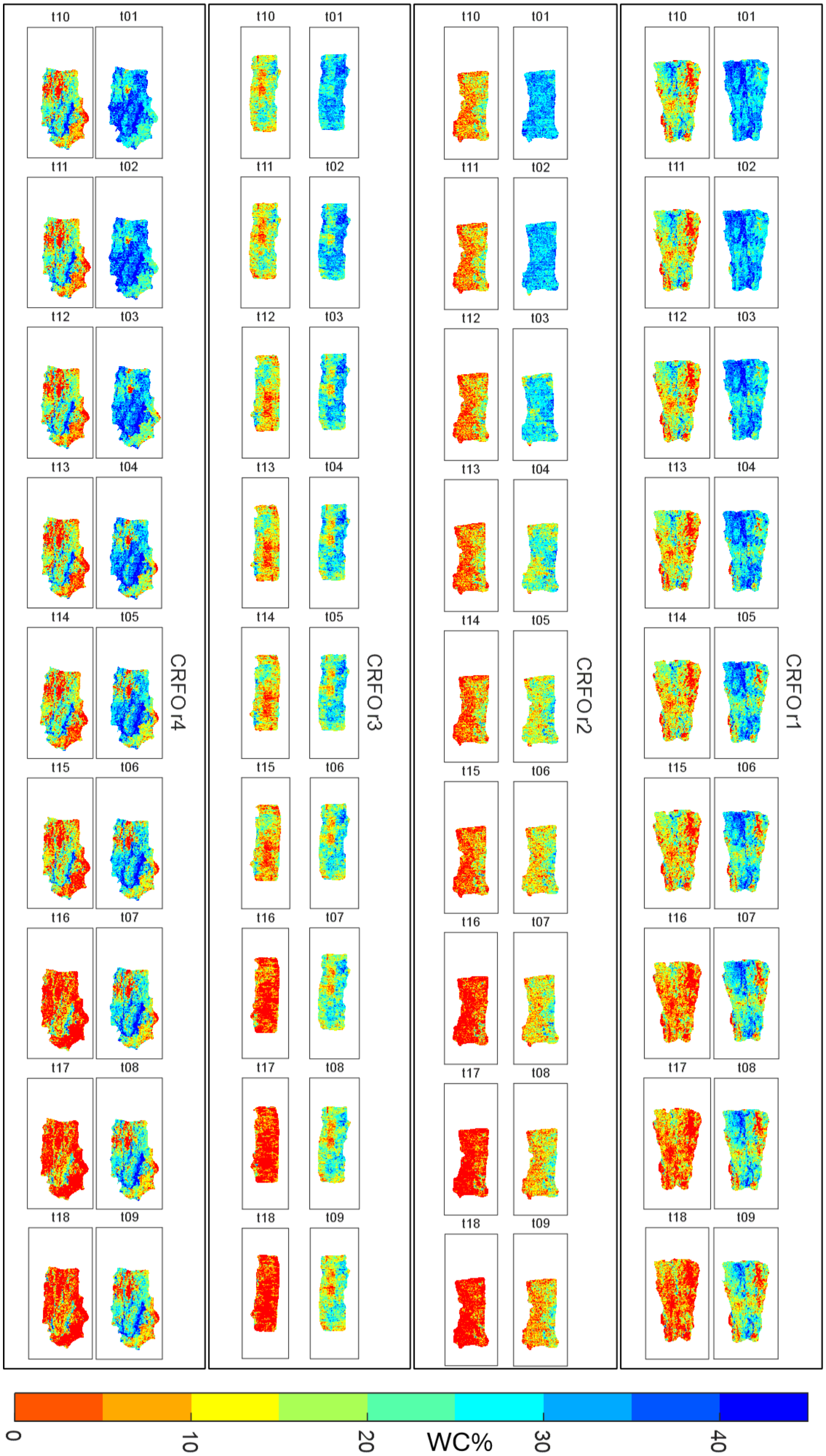
CRFO r1
CRFO r2
CRFO r3
CRFO r4
t01
t02
t03
t04
t05
t06
t07
t08
t09
t10
t11
t12
t13
t14
t15
t16
t17
t18
0
10
20
WC%
30
40

4 MATERIAL SCIENCES

4.1 INVESTIGATING THE PENETRATION DEPTH OF SWIR RADIATION THROUGH HYPERSPECTRAL IMAGING

4.1.1 Introduction

The fundamental objective of imaging techniques is to acquire a surface or a scene and represent the associated information [229]. In the context of spectral imaging, this objective is broadened to encompass the simultaneous acquisition of spatial and spectral information, thereby generating a complete spectral profile at each individual pixel. Instruments employed for this purpose are based on most of the primary spectroscopic techniques of analytical relevance, such as ultraviolet–visible (UV-Vis), fluorescence, near-infrared (NIR), mid-infrared (MIR), Raman and X-ray fluorescence (XRF) [52]. Collectively, these methodologies fall under the broad classification of hyperspectral imaging (HSI) techniques, which are typically non-destructive and contactless analytical methods particularly suitable for the study of delicate or high-value specimens.

Conventionally, HSI entails the acquisition of two spatial dimensions (x, y) in conjunction with a spectral dimension (λ). However, although hyperspectral datasets are primarily interpreted as surface information, they may also contain subsurface contributions, as radiation at certain wavelengths can penetrate below the surface. Within the spectral regions employed in analytical spectroscopy, NIR radiation has been shown to exhibit notable penetration capabilities [230].

NIR spectroscopy is a rapid, non-invasive and non-destructive analytical technique with broad applicability across diverse domains, including medical diagnostics, food quality assessment, forensic analysis, and cultural heritage investigations [24]. It operates within the electromagnetic spectrum range of 780 to 2500 nm (12,820 to 4000 cm^{-1}), where absorption of radiation arises overtone and combination transitions of molecular vibrations. The relatively low energy of NIR photons means that they seldom correspond to strong electronic transitions, resulting in fewer absorption events [24] and consequently allowing for deeper radiation penetration through materials. The effective penetration depth of NIR radiation is, however, influenced by multiple factors beyond chemical composition, including scattering, sample geometry, radiation intensity and incidence angle, and the specific wavelengths employed as well [230,231]. A comprehensive understanding of these parameters is essential for optimising the application of NIR spectroscopy across various scientific and technological fields.

Some studies have explored the penetration depth of NIR radiation in biomedical, pharmaceutical, cultural heritage, and food science applications. For instance, brain imaging research demonstrated that NIR penetration is deeper in neonates than adults due to tissue composition differences [232], reporting depths up to 2–3 cm in adults, with superficial layers absorbing most of the energy [233]. On the other hand, when studying non-invasive glucose monitoring, effective penetration was limited to a few millimetres, reportedly due to high water content in skin tissues [234]. Cartilage analysis pointed out a wavelength-dependent behaviour of penetration, which was up to 5 mm at 1110–1430 nm and decreased at longer wavelengths [235]. Wavelength dependence of penetration was also confirmed in pharmaceutical studies. Among others, Clarke *et al.* found penetration depths ranging from ~0.1 mm at 2500 nm to ~0.8 mm at 1100 nm in cellulose-based materials [236], while Yang *et al.* observed penetration up to 2 mm in tablets [237], influenced by formulation and wavelength selection. In cultural heritage analysis, Longoni *et al.* indirectly estimated penetration depths of 60–100 μm using FT-NIR (7500–4000 cm^{-1}) in multilayered paintings [238], while Cucci *et al.* and Catelli *et al.* extended NIR-HSI (750–2500 nm) for stratigraphic imaging, demonstrating enhanced subsurface visualisation capabilities [239,240]. In the food sector, NIR radiation was shown to penetrate 9–15 mm in watermelon, depending on sample configuration [241,242], and up to 1.8 mm in powdered products like wheat flour [243]. Moisture content emerged as a key factor, reducing penetration in high-moisture samples such as raw potato (1 mm) versus ham (2.4 mm) [244,245].

While these studies provide valuable application-specific insights, to date, only a limited number of studies have attempted to characterise NIR penetration depth in a systematic and quantitative manner. Among them, Pomerantsev *et al.* [246,247] proposed a deconvolution strategy to separate transmittance, scattering, and absorbance contributions, but their work primarily aimed at identifying the spectral signature of subsurface targets rather than elucidating the physical mechanisms of penetration. Moreover, most studies employed point-based NIR spectroscopy rather than hyperspectral imaging, thus neglecting the potential of spatially resolved data for investigating penetration phenomena. In fact, despite the increasing adoption of NIR-HSI, a comprehensive, physically grounded understanding of how deeply NIR radiation penetrates in stratified materials, and of the physical factors governing this process, remain elusive. The absence of such understanding represents a major limitation, as it constrains the interpretability of NIR-HSI data and hampers its extension beyond traditional surface analysis.

Within this context, the present study addresses this critical gap. The project aims to revolutionise the conventional concept of HSI by evolving it from a surface analytical technique into a depth-resolved, three-dimensional spectral tomography. Specifically, this work provides the first systematic and quantitative investigation of NIR radiation penetration in a controlled HSI configuration, using stratified polymeric samples with known stratigraphy and composition produced via 3D printing. The penetration behaviour was examined using complementary chemometric strategies, including exploratory (principal component analysis – PCA), unmixing (classical least squares – CLS), and both linear (partial least squares – PLS) and non-linear (convolutional neural networks - CNN) regression approaches. To verify the consistency of the outcome, analyses were carried out in parallel with two different NIR-HSI instruments.

The present work therefore represents the first systematic attempt to quantify NIR-HSI penetration, using well-defined model systems. This integrated approach bridges the gap between qualitative visualisation and quantitative modelling of penetration phenomena, establishing a reproducible framework to assess and predict NIR-HSI penetration depth. By doing so, it challenges the conventional interpretation of NIR-HSI as a purely surface-sensitive method and lays the groundwork for a deeper understanding of NIR radiation penetration, opening the way for the future development of the technique into a true 3D spectral imaging tool.

4.1.2 Results and discussion

4.1.2.1 Experimental protocol

Multi-material stratified samples were produced by means of a 3D printer using two different transparent polymers: polylactic acid (PLA) and polyethylene terephthalate glycol (PETG). Twenty-one samples were produced in the form of 1 cm cubes. The first cube was made entirely of PLA, then strata were prepared, increasing the height of PETG by 0.5 mm and consequently decreasing the height of PLA by the same amount (or “pace”) for each sample until the last cube, which was made entirely of PETG. **Figure 4.1A** shows a schematic representation of the series. The cubes were made as solid samples, *i.e.*, without empty space within the structure (fill density = 100%), and subsequent layers were printed with a linear fill pattern, as represented in **Figure 4.1D**.

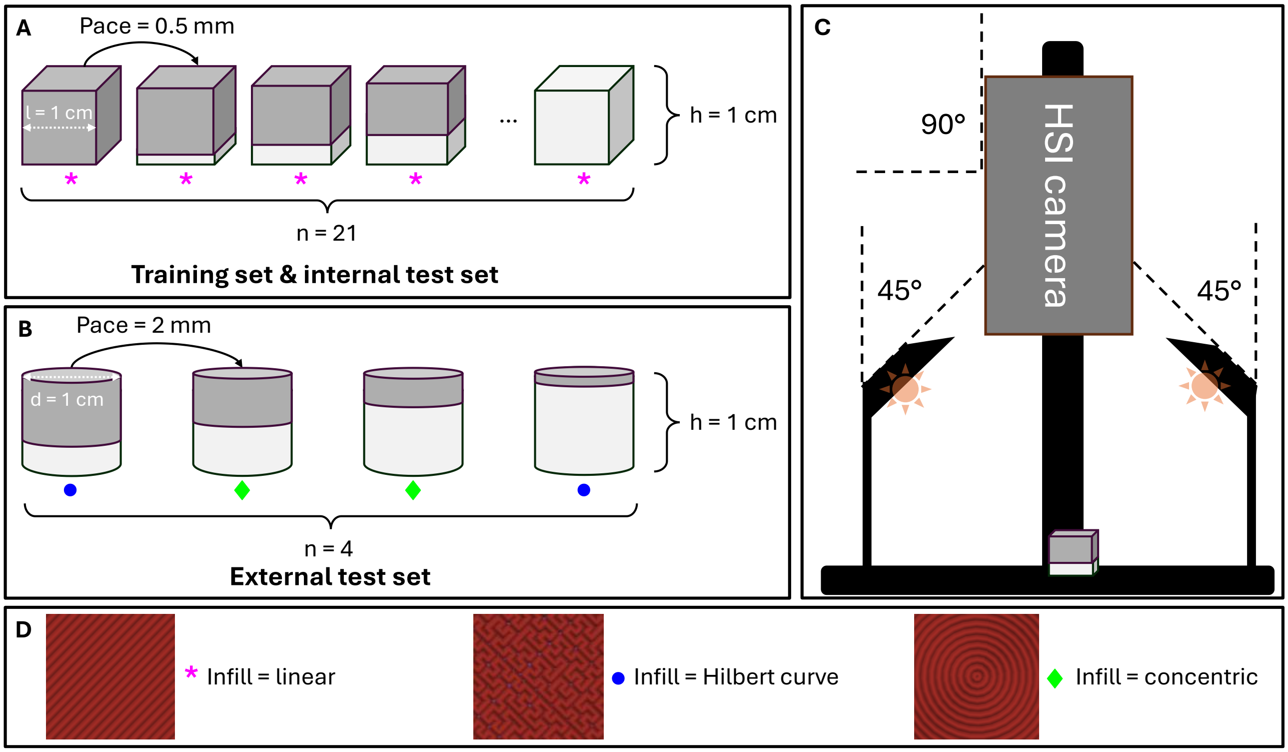

Figure 4.1: Schematic representation of the samples, their printing pattern and the instrumental configuration. A: Cubic samples, showing the increase of PETG (light grey) of 0.5 mm and consequent decrease of PLA (dark grey) along the series, keeping the total height constant (1 cm); B: Same but for cylindrical samples; C: Schematic representation of the HSI acquisition setup; D: Detail of the fill patterns used for sample infill.

Furthermore, four additional stratified samples were printed in the shape of cylinders with a 1 cm base diameter and a total height of 1 cm, with a pace of 2 mm (**Figure 4.1B**). They were all printed with a 100% fill density, but the fill patterns utilised differed from those employed in the cubes. Specifically, the cylinders with 2 and 8 mm of PLA employed the Hilbert curve fill pattern, while the cylinders with 4 and 6 mm of PLA used the concentric fill pattern. Both patterns are represented in **Figure 4.1D**. This further set was produced with the idea that the printing pattern, affecting the physical properties of the material, might have an effect on how it interacts with the radiation, conditioning scattering effects. Therefore, the production of new samples with the same fill density but different shape and printing patterns ensured the presence of a truly independent set of samples to be used for model validation.

After production, samples underwent HSI analysis. In particular, samples were located under the detector and images were captured from above. The images were captured with two different cameras, one by Specim and one by HySpex (details in Materials and methods section), and they were registered either with the PETG layer facing the detector (PETG-UP) or with the PLA layer facing the detector (PLA-UP).

4.1.2.2 Spectral analysis

Initially, HSI images of the training set samples were segmented and regions of interest (ROIs) were extracted from each cubic sample. Then all pixel spectra of each ROI were averaged, obtaining a single spectrum representing each sample. These spectra were then plotted in order to interpret the spectral signatures of the two polymers, PETG and PLA, and to identify trends related to polymer height, as illustrated in **Figure 4.2**.

The NIR spectra of the two polymers exhibited pronounced characteristic absorptions within the 1100-1250 nm region. These absorptions were attributed to the second overtone of the carbon-hydrogen (C–H) bond. This region corresponds both to the antisymmetric methyl and methylene stretching [218], which is indicative of the presence of the CH_2 and CH_3 groups, and to aromatic C–H stretching. In this region, PLA exhibited a single band, likely attributable to the exclusive presence of aliphatic C–H bonds. Conversely, PETG, which presented both aromatic and aliphatic bonds, displayed two bands. A strong band pertaining to the combination band of stretching and bending ($2\nu+\delta$) [248] of methyl and methylene groups was discernible at approximately 1400 nm, overlapping with the first overtone of the oxygen-hydrogen bond (O–H) stretching vibration. This band was connected both to the glycol group of PETG and to water in PLA, the latter being a hygroscopic polymer [249]. In particular, the humidity contribution for PLA probably outweighed the O–H contribution for PETG, thus rendering PLA absorption more pronounced in this region.

Subsequently, from 1600 nm to approximately 2250 nm, the spectra exhibited multiple overlapped absorption bands, whose precise attribution resulted challenging. However, this region could be generally regarded as a fingerprint related to C–H, O–H, C=O and C–O bond vibrations. Conversely, the region of the spectrum after 2250 resulted quite flat, exhibiting minimal diagnostic capability to differentiate between the two polymers.

Upon examination of the raw spectra, depicted in **Figures 4.2A-B-E-F**, the presence of a total intensity effect emerges. This trend is at least slightly related to the increase in thickness of PLA and to the simultaneous reduction of PETG, with samples with more PLA presenting lower reflectance. This outcome partly confirms what was evidenced by Pomerantsev et al [246,247], who demonstrated that a reflectance increase can be expected when polyethylene thickness increases. In the case of this study, however, the correlation between increased reflectance and polymer height was not perfect, therefore this effect can be effectively removed by applying the SNV transform, as illustrated in **Figures 4.2C-D-G-H**.

Following the pre-processing stage, a trend related to the height of the polymer facing the detector could be readily discerned in the figure. The region between 1100-1500 nm showed the greatest diagnostic potential, with bands indicative of PLA and PETG gradually increasing and decreasing in intensity. A continuous change in these bands was evident for the first half of the samples, where the bands representative of top polymer gradually increased in intensity when the polymer height varied from 0 to approximately 5 mm (from blue to aquamarine in the figure). In the second half, for the height going from 5 to 10 mm (from aquamarine to red in the figure), the spectra of subsequent ROIs became visually indistinguishable as they overlapped significantly. The region between 2100-2250 nm was of particular interest, as it allowed to distinguish which of the two polymers was facing the detector. Indeed, in the PETG-UP configuration, this region maintained a more defined shape, characterised by three narrow, consecutive bands. On the contrary, in PLA-UP the considered region kept a broader and rounder shape, with the distinct bands being discernible only at very low heights of PLA.

The analysis of both raw and pre-processed spectra demonstrated a consistent behaviour of the two instruments used, with spectral signatures for HySpex and Specim exhibiting an almost perfect overlap.

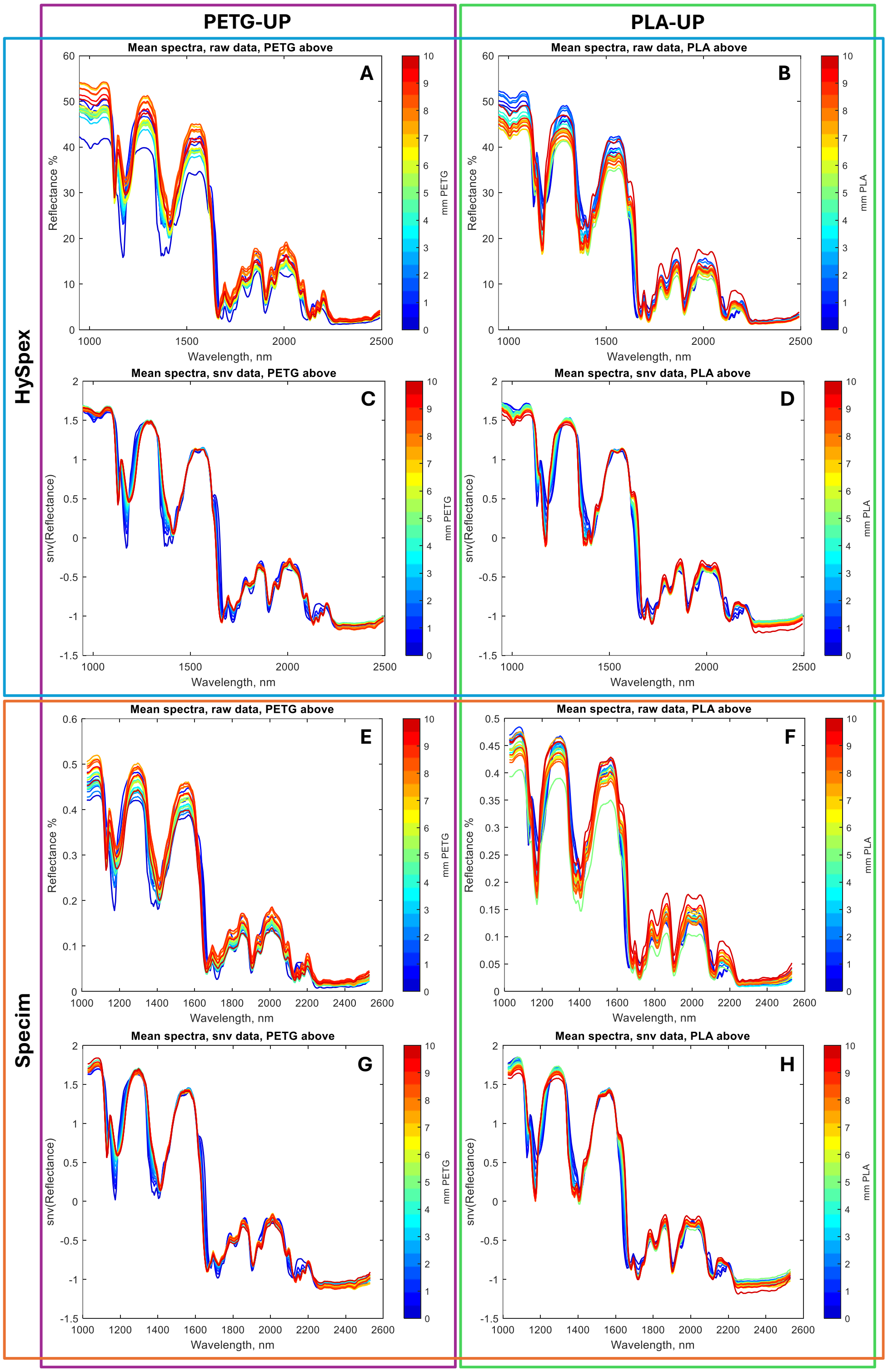

Figure 4.2: *Average (object-based) spectra for HySpex (from A to D) and Specim (from E to H) analysis, coloured according to the height of the polymer facing the detector. The spectra appear either in their raw (A, B, E, F) or SNV transformed (C, D, G, H) form, and the results are reported both for PETG-UP (A, C, E, G) and PLA-UP (B, D, F, H).*

4.1.2.3 PCA

Subsequently, pixel-based exploratory analysis was carried out utilising PCA, the results of which are illustrated in **Figure 4.3**. The application of Savitzky-Golay first derivative followed by SNV transform ensured that the highest source of variability, condensed in PC1, was connected to the information of interest, *i.e.*, polymer height, having minimised the extent of unwanted systematic variations thanks to the pre-processing applied. Indeed, when analysing the trend of PC1 score values with respect to the height of the polymer facing the detector, it was possible to observe an increasing trend for PETG-UP (**Figure 4.3A** and **4.3H**) and a decreasing trend for PLA-UP (**Figure 4.3F** and **4.3P**). However, the observed trend exhibited a non-linear behaviour. For PETG-UP, a pronounced change was evident at the beginning of the trend, with substantial variations between successive samples when the height of the polymer facing the objective changed from 0 to approximately 3 mm, diminished variations in the range of 3 to 6.5 mm, and a rapid stabilisation of score values subsequently. In a similar manner, PLA-UP scores demonstrated significant alterations from 0 to approximately 6 mm, with a rapid stabilisation of score values thereafter. This trend was visually confirmed by the score maps of the training set for both PETG-UP (**Figures 4.3C** and **4.3M**) and PLA-UP (**Figures 4.3H** and **4.3R**). While the first seven ROIs rapidly changed colour from blue to red or vice-versa, the remaining 14 samples slowly became darker, with the last ROIs being almost indiscernible from one another.

The chemical nature of the information retained in PC1 was confirmed by the loading plots (**Figures 4.3B-G-L-Q**), which presented high values in the 1100-1250 nm region. This region corresponds to the second overtone of C–H vibration, as previously identified in section 4.1.2.2. The fact that the region exhibiting the most significant variations in the spectra corresponded to the area of greatest importance in the loadings, gave further support to the hypothesis that alterations in polymer height were indeed the variable captured by PC1. However, another region which showed almost equivalent importance in terms of loading absolute values was located between 1600 and 1700 nm, a region which was not visually identified as significant in the spectral interpretation. Though it is imperative to exercise caution when evaluating band attribution in pre-processed data [131], a re-examination of the raw data profiles (**Figures 4.2A-B-E-F**) revealed that the main difference between the two polymers in this region could be ascribed to a shoulder feature that was characteristic of PLA. This was likely attributable to the C–H first-overtone (2ν) [248] contribution from the stretching of the methyl group in the PLA backbone. Indeed, PLA structure presents a pendant –CH_3 group, a feature absent in the structure of PETG. A shoulder could be indicative of overlapping C–H bands from different chemical environments. The presence of a chiral backbone in PLA engenders a distinct C–H environment compared to that observed in PETG's glycol/ethylene units, which likely results in the formation of this highly diagnostic extra shoulder in PLA.

Additionally, the analysis of loadings demonstrated a high degree of similarity across the various models, irrespective of the polymer facing the detector. This finding serves to emphasise the efficacy of PCA in discerning chemical information from the samples without being confounded by their orientation. This finding also explains the opposite trends exhibited by the score values of PETG-UP and PLA-UP.

Finally, the pixel spectra from the internal and external test sets were projected in the PC space of the respective training set, and the resulting PC1 score maps were analysed. The results for the internal test set (**Figure 4.3D-I-N-S**) exhibited substantial overlap with those obtained from the training set, characterised by comparable noise levels, consistency of the colour associated to the specific height, and evident flattening at elevated top-polymer height. However, subsequent analysis of the external test set score maps (**Figure 4.3 E-J-O-T**) revealed discrepancies when compared to the training set. Increased noise was detected, attributable to the use of an alternative fill pattern during the production of the specimens, which could be readily distinguished by visual inspection. In particular, when observing the HySpex results for the samples using the Hilbert Curve fill pattern (**Figure 4.3E** and **4.3J**, first and last of the series), the pattern shape could clearly be identified. Indeed, the pattern used for the external test set could not be explained by the model of the training set, which used a linear pattern, and therefore this source of variability reappears in the scores of the test set. Furthermore, an analysis of the external test set samples revealed colour differences when moving from 6 to 8 mm of the top-polymer, which were indiscernible in the training set. This result suggests that the fill pattern, by modifying the internal structure of the sample, influences the penetration depth of the NIR radiation, indicating that the process may be strongly conditioned by the physical properties of the sample.

When the results from HySpex (**Figure 4.3**, from **A** to **J**) and Specim (**Figure 4.4**, from **K** to **T**) were compared, they were once again found to be highly overlapped, with score maps that were almost identical and comparable amount of explained variance in the first component. However, in the Specim scores the printing pattern in the external test set was less evident, probably due to the instrumental setup, which caused a lower spatial resolution and consequent higher pixel size.

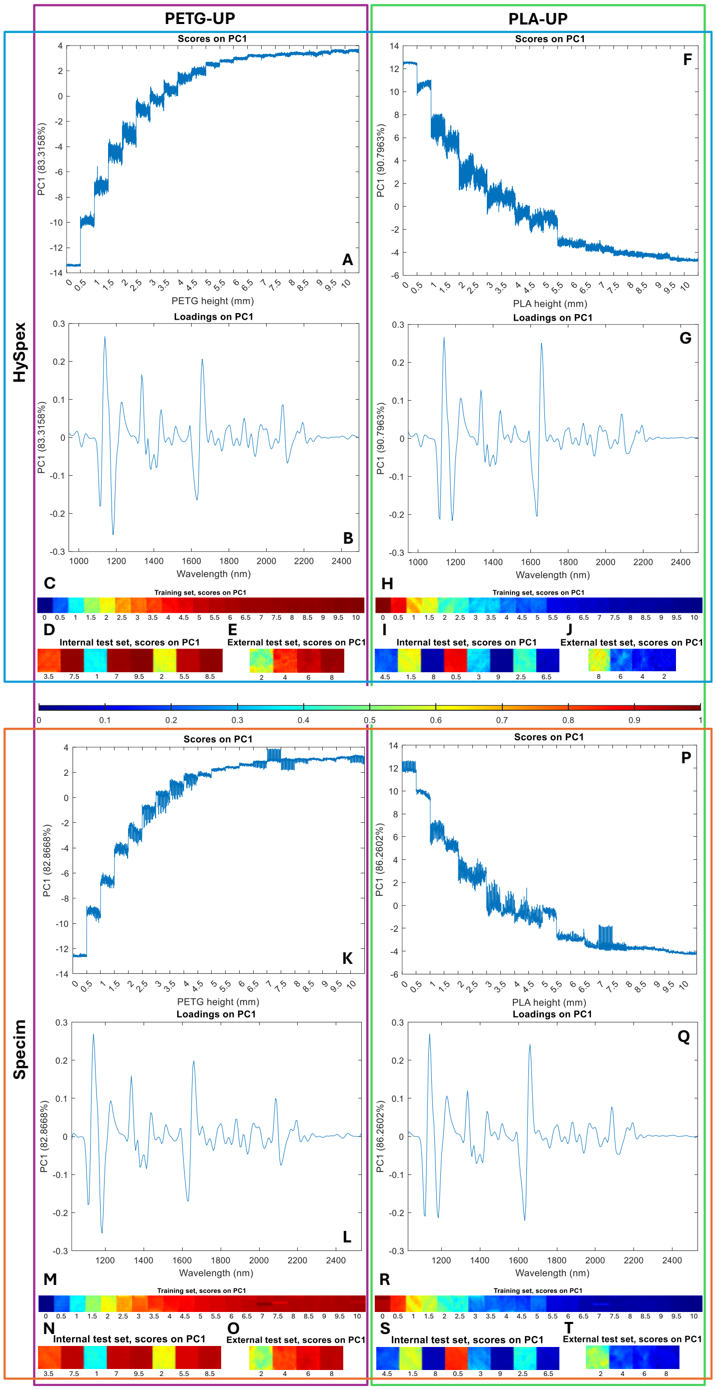

***Figure 4.3**: PCA results for HySpex (from A to J) and Specim (from K to T) data for PETG-UP (from A to E and from K to O) and PLA-UP (from F to J and from P to T) configurations. Score value for PC1 against height of the polymer facing the detector (A, F, K, P), loading line plots (B, G, L, Q), score maps of the training set (C, H, M, R), score maps of the internal test set (D, I, N, S) and score maps of the external test set (E, J, O, T) are reported. Numbers under the score maps report the height in mm of the polymer-up associated with the corresponding ROI.*

In summary, PCA results were valuable in partially confirming the penetration capability of NIR-HSI into the material, showcasing a correlation between the score values and the top polymer height. However, the identification of a penetration limit proved to be quite challenging. In fact, the non-linear behaviour observed in the scores may be attributable to a reduced penetration in the deeper layers, but increased scattering effects in these layers may also be responsible for the observed trend. The mentioned phenomena may confound the chemical information, thereby reducing the macroscopic differences between consecutive samples, even if the penetration remains effective. Consequently, further chemometric analysis is required to explore this topic more thoroughly. In particular, while PCA provided an overview of the main sources of spectral variance and suggested potential correlations with polymer thickness, a more quantitative approach was required to decompose the spectra into contributions from individual polymer components. To this end, CLS was applied to directly assess the relative contributions of the top and bottom layers.

4.1.2.4 CLS

CLS was therefore employed as a signal deconvolution technique to derive a pixel-based predicted height of the two polymers by means of the spectral signature of the pure components. The results of the deconvolution process are presented in **Figure 4.4**. As demonstrated in the predicted versus measured plot, displayed in the object-based approach for the purpose of visualisation, both the training set (**Figure 4.4A-G-M-S**), the internal test set (**Figure 4.4B-H-N-T**) and external test set (**Figure 4.4C-I-O-U**) exhibited a trend that was in alignment with the observations made from the scores of PC1 during PCA. Indeed, a non-linear trend was evident in all sets, none of which could be adequately described by the results of the deconvolution.

However, some discrepancies could be observed between the two materials, which could not be evidenced in PCA. In particular, when the PLA-UP configuration was considered, though its RMSE was still unacceptable from a modelling purpose, it was lower than that of the PETG-UP configuration, with an average discrepancy of approximately 0.6 mm. This may indicate that the penetration of NIR radiation in PLA is superior to PETG. Indeed, in the PLA-UP configuration, despite the persistence of the flattening phenomenon, samples in the range of 6-10 mm of height still present an increasing trend, though with lower steepness, a feature that is not observed in PETG. This finding aligns with the established literature on the subject, which posits a correlation between penetration and chemical properties of the material [230].

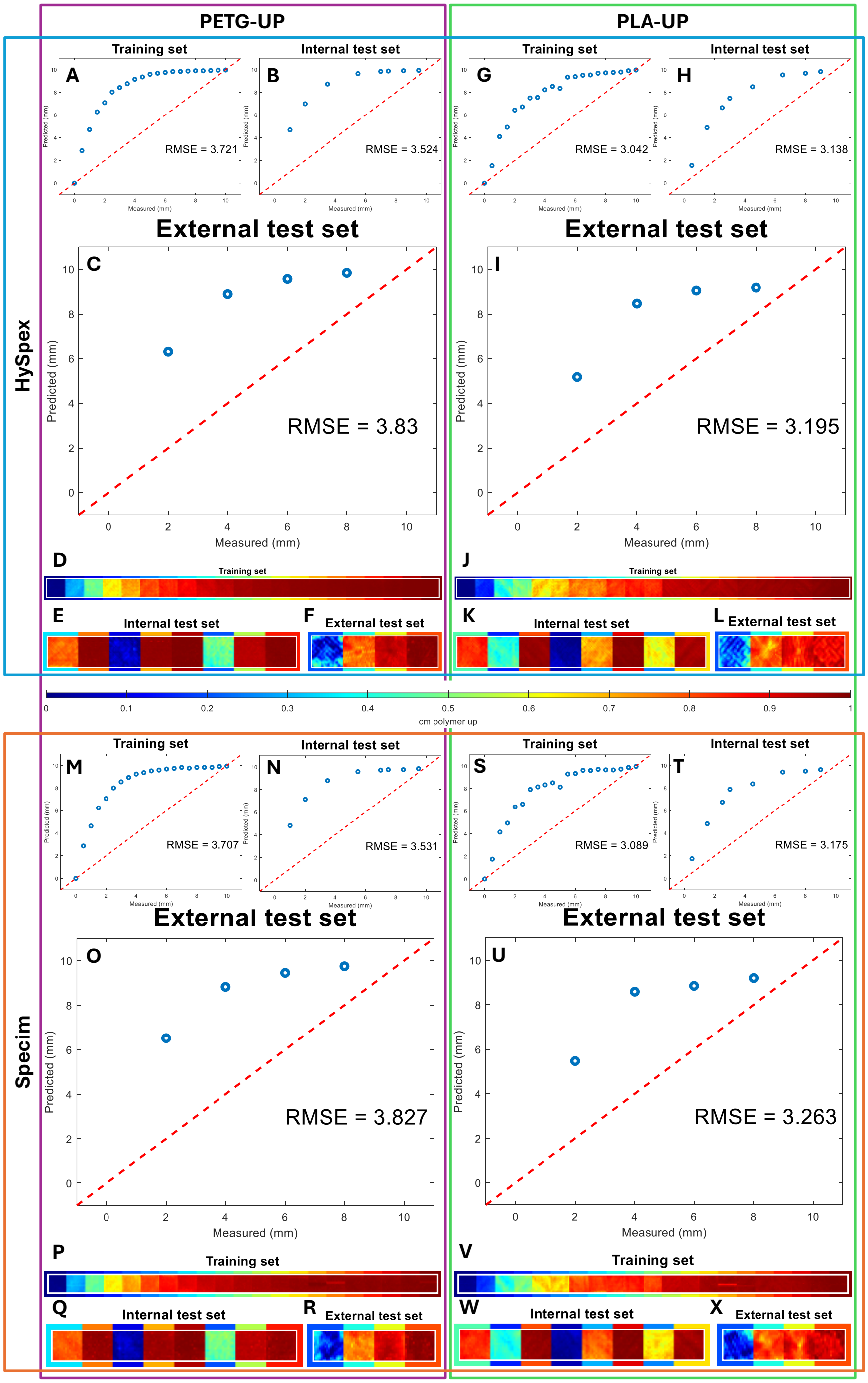

***Figure 4.4**: CLS results for HySpex (from A to L) and Specim (from M to X) data for PETG-UP (from A to F and from M to R) or PLA-UP (from G to L and from S to X) configuration. Predicted versus measured plots for the training set (A, G, M, S), for the internal test set (B, H, N, T), and for the external test set (C, I, O, U) are reported, followed by prediction maps for the training set (D, J, P, V), for the internal test set (E, K, Q, W), and for the external test set (F, L, R, X). Each prediction map is reported with a border which represents the colour the corresponding ROI should have if its prediction error was null.*

Afterwards, pixel-based height prediction of the top-polymer was employed to generate prediction maps for all sets (**Figures 4.4D-E-F-J-K-L-P-Q-R-V-W-X**). In the present paper, prediction maps are presented associated with a border indicating the colour corresponding to the expected values, *i.e.*, the colour that the ROI should have if the prediction had no error. This visualisation is aimed at facilitating map interpretation, making it intuitive. Specifically, the more the inner colour matches the border, the more accurate the prediction is; conversely, when the map colour does not match the border, it reflects poor prediction performances of the model. In the case of the CLS model, a comparison of the colour of each ROI with its border indicates that the height of the polymer facing the detector is overestimated across the entire range. Furthermore, an increased level of noise is evident in the external test set samples, attributable to the different printing pattern. This observation confirms the findings reported in PCA. Moreover, also in this case the results obtained with the two instruments are found to be highly similar, thereby confirming the robustness and reproducibility of the approach.

The use of CLS for deconvolution serves to substantiate the notion that NIR radiation is indeed capable of penetrating the matter, as already underlined by means of PCA. It is also noteworthy that the penetration of NIR-HSI is characterised by a non-linear behaviour in relation to component height, a phenomenon that cannot be accurately accounted for by unsupervised chemometric strategies, which do not consider this additional information during the process of model calibration. Consequently, the subsequent step was to implement supervised regression approaches in order to enhance the understanding of radiation penetration.

4.1.2.5 Regression

Regression was employed to determine whether the flattening tendency observed in PCA and PLS could be attributed to a lack of penetration after approximately 6 mm, or rather if, directing the model toward the desired information by means of a response variable, scattering and other confounding effects could be successfully neglected, enhancing the chemical information derived from the deepest layers. It is important to note that, in this case study, regression techniques were not utilised to obtain a robust prediction model to be applied in real case scenarios. Instead, these techniques were here exploited to ascertain whether precise and accurate predictions could be made, with the understanding that an ability to achieve both precise and accurate predictions must be the consequence of NIR radiation penetration to the considered depth.

4.1.2.5.1 PLS

First, a PLS regression model was calibrated on the training set with the pixel-based approach, and the results are presented in **Figure 4.5**. The number of latent variables for each model was selected based on the RMSECV, with the number of latent variables corresponding to a local minimum or, if the minimum was not present, to the point where RMSECV stabilised, as can be visually observed in **Figure 4.5A, E, I** and **M**. The number of selected latent variables for each model is reported in **Table 4.1**.

Model training produced slightly better results for the PLA-UP configuration than the PETG-UP one, with lower RMSECV, as can be observed from the predicted versus measured plot in **Figure 4.5B**, **F**, **J**, and **N**. This finding corroborates the earlier hypothesis of a deeper penetration in PLA compared to PETG, thereby sustaining the theory that NIR radiation penetration is material-dependent. Furthermore, while the PLA-UP model exhibited a satisfactory linear trend along the whole calibration range (**Figure 4.5B** and **F**), PETG-UP presented a slight flattening when the polymer height exceeded 7 mm. This trend, though less pronounced, confirms the findings of PCA and CLS, thereby suggesting that, in PETG, penetration may indeed be limited at approximately 7 mm. In contrast, PLS regression could extract information from the deepest layers for the samples in the PLA-UP configuration. This finding provides support for the hypothesis that at least some component of the non-linearity observed with the unsupervised methods was resulting from scattering phenomena. The improvement in model performances provided by the use of PLS regression can be confirmed observing the prediction maps of the training set, in **Figure 4.5D**, **H**, **L** and **P**. Indeed, when comparing the ROIs colour to the border, good match could be observed along most of the training set. This demonstrates that the use of supervised regression was indeed able to account for most of the non-linear behaviour observed with unsupervised strategies.

When examining the VIP scores derived from the PLS regression, it was possible to individuate some discrepancies between the descriptors involved in the model for PETG-UP (**Figure 4.5C** and **K**) when compared to the ones for PLA-UP (**Figure 4.5G** and **O**). This finding disagrees with what commented from the PCA loadings, which exhibited nearly identical shapes for the two configurations. In particular, a region around 1350 nm showed higher VIP scores in the PETG-UP configuration, while the 1600-1700 nm range had a slightly higher weight in the PLA-UP model. Additionally, a contribution from the 2050-2150 nm range, slightly more significant for PETG-UP, could be identified. These observations were strongly consistent between instruments, with the VIPs obtained from the HySpex and Specim apparatuses being indiscernible and supporting the robustness of the conclusions. These slight differences between VIP scores, therefore, demonstrate the superiority of the regression approach in identifying slight differences between configurations, thus better describing the samples.

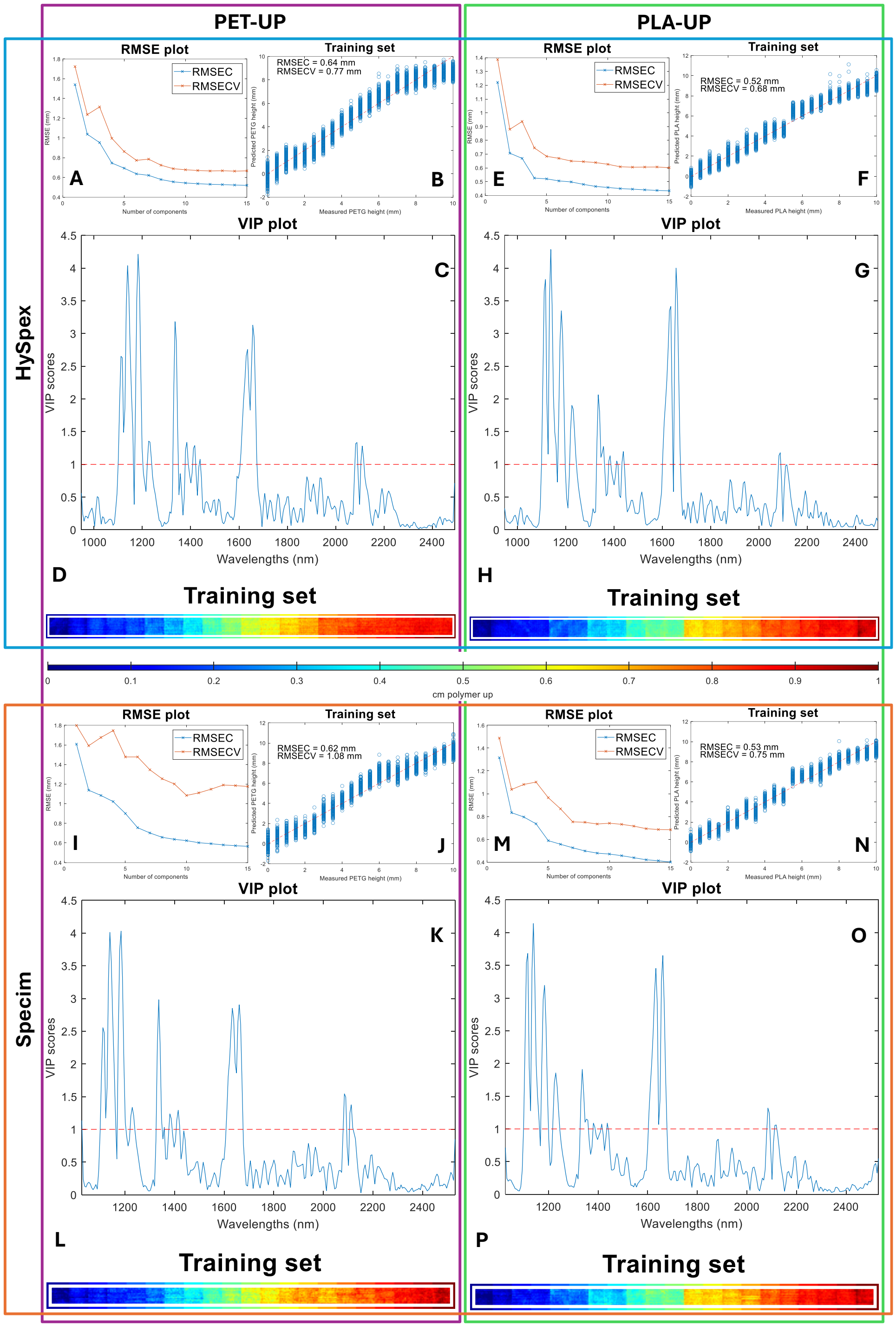

***Figure 4.5**: PLS regression results for HySpex (from A to H) and Specim (form I to P) data for PETG-UP (from A to D and form I to L) or PLA-UP (from E to H and from M to P). RMSEC and RMSECV plotted against number of latent variables (A, E, I, M), predicted versus measured plots for the training set (B, F, J, N), VIP profiles (C, G, K, O), and prediction maps for the training set (D, H, L, P) are reported. Each prediction map is reported with a border which represents the colour the corresponding ROI should have if its prediction error was null.*

The findings pertaining to the training set were subsequently corroborated when the internal and external test sets were projected in the calibration space. The prediction results are displayed in **Figure 4.6**.

In particular, when the predicted versus measured plot for the internal test set is considered (**Figure 4.6A, D, G, J**), the expected flattening could be observed for PETG-UP, while this was not evident for PLA-UP. In general, predictions for both the test sets could be regarded as satisfactory (RMSE < 10% range), as sustained both by the visual indication provided by the prediction maps (**Figure 4.6 B, C, E, F, H, I, K, L**) and by RMSEPs reported in **Table 4.1**. The internal test set presented lower noise in comparison to the external test set, as visually illustrated from the prediction maps.

However, the RMSEP behaviour exhibited differences between PETG-UP and PLA-UP. In the case of PETG-UP, RMSEP was higher for the internal test set compared to the external test set, while this behaviour was reversed for PLA. This finding may be connected to a higher penetration through the external test set samples, as previously hypothesised from CLS results. Indeed, in the case of PETG-UP, the higher penetration of radiation through the external test set samples may have corrected for the flattening observed in the training and internal sets, thus improving the prediction. Conversely, for PLA-UP the heightened penetration of NIR radiation through the printing pattern of the external test set samples became inconsequential, as this polymer presented good penetration capabilities, *i.e.*, linearity, along the whole range. In this instance, the different printing pattern of the external test set may have been responsible for the increased noise, without gaining much in terms of penetration and linear fitting, thus increasing the prediction error. These observations provided further evidence for the hypothesis that NIR radiation penetration is dependent on complex physical phenomena in addition to chemical information.

Additionally, some discrepancies between the results obtained from Specim and HySpex, which were not identified through the chemometric treatments applied before, were revealed in PLS. While the aforementioned similarities and differences remained constant, thereby maintaining the provided interpretation, the values of RMSE proved to be more satisfactory for the HySpex models in comparison to the Specim ones, as evidenced in **Table 4.1**. Furthermore, Specim models were characterised by increased levels of complexity. However, these different performances were likely not attributable to an instrumental disparity, but rather to the different lamp intensity levels employed in the two instrumental setups. Indeed, the lamps coupled to the HySpex apparatus presented higher power compared to the ones coupled to the Specim one, suggesting that the stronger illumination may be the cause for the increased penetration evidenced by the improved performances of the models.

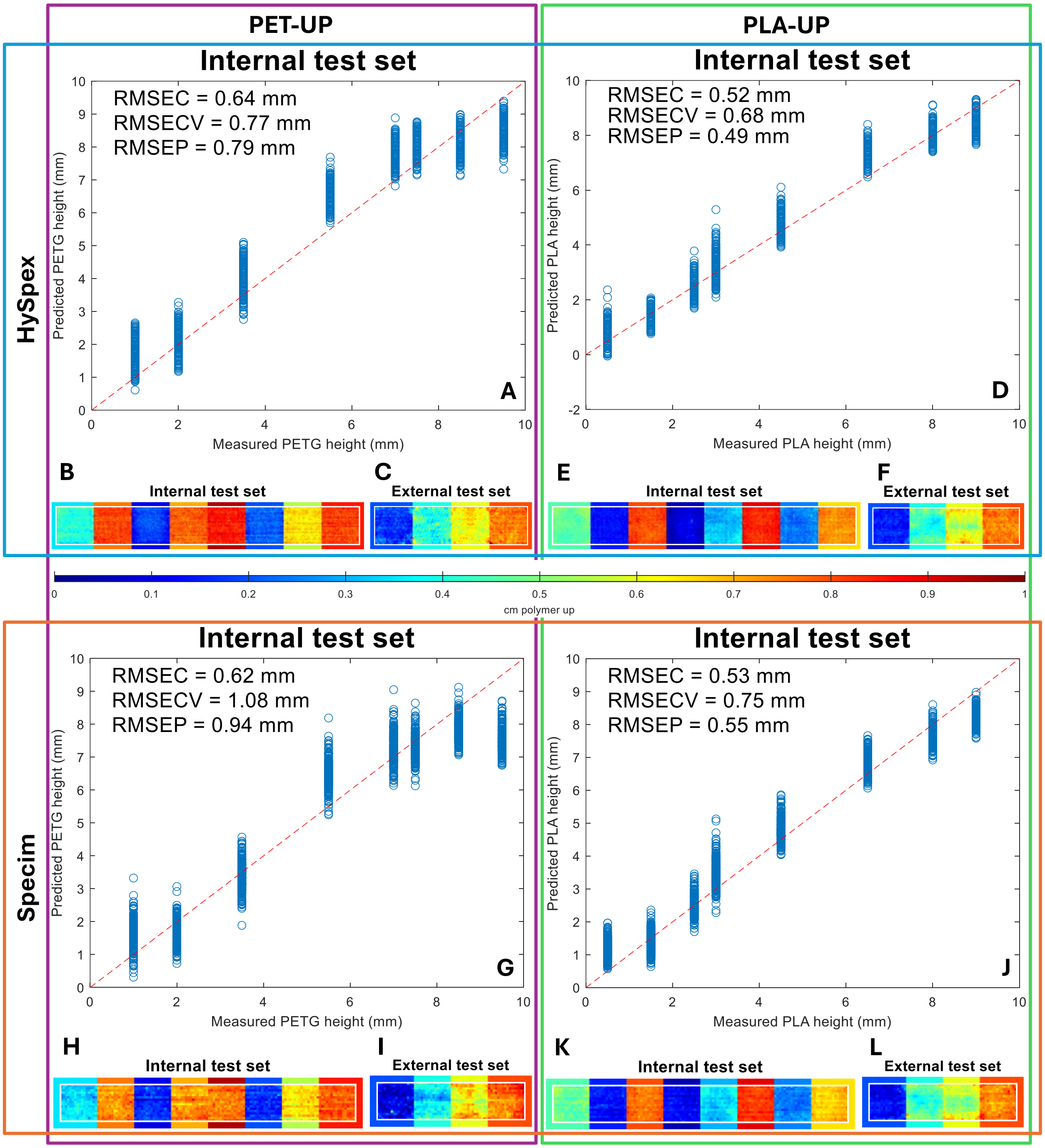

Figure 4.6: *Prediction results for HySpex (from A to F) and Specim (form G to L) data for PETG-UP (A, B, C, G, H, I) or PLA-UP (D, E, F, J, K, L). Predicted versus measured plots for the internal test set (A, D, G, J), prediction maps for the internal test set (B, E, H, K), and prediction maps for the external test set (C, F, I, L) are reported. Each prediction map is reported with a border which represents the colour the corresponding ROI should have if its prediction error was null.*

***Table 4.1**: Summary of the statistics calculated for the PLS and CNN models for training set, cross- validation, internal test set and external test set. The models for either PETG-UP or PLA-UP are reported.*

			PETG-up				**PLA-up**			
			Training set	*Cross-validation*	*Internal test set*	*External test set*	*Training set*	*Cross-validation*	*Internal test set*	*External test set*
HySpex	**PLS**	*RMSE*	0.64	0.77	0.79	0.56	0.52	0.68	0.49	0.56
		Bias	0	0.02	0.31	-0.05	0	0.004	0.10	-0.16
		LVs	6	-	-	-	5	-	-	-
	CNN	*RMSE*	0.18	-	0.24	0.72	0.14	-	0.16	0.70
		Bias	0.002	-	0.01	-0.58	-0.01	-	0.01	-0.52
Specim	**PLS**	*RMSE*	0.62	1.08	0.94	0.84	0.53	0.75	0.55	0.76
		Bias	0	-0.10	-0.16	-0.30	0	0.02	0.07	-0.26
		LVs	10	-	-	-	7	-	-	-
	CNN	*RMSE*	0.16	-	0.73	0.50	0.12	-	0.60	1.04
		Bias	0.007	-	-0.56	-0.20	0	-	-0.35	-0.78

However, PLS regression was deemed insufficient to completely rule out the possibility that NIR radiation was penetrating also through PETG along the entire range. Indeed, as PLS regression is a linear method, it is possible that it is unable to account completely for non-linear behaviours in the data. The use of a suitable nonlinear regression technique is therefore warranted to determine whether penetration through PETG occurs. Consequently, CNN were implemented to capture complex spectral-structural interactions and to further improve predictive accuracy.

4.1.2.5.2 CNN

Finally, a CNN model was calibrated on the training set pixel spectra, and the results are reported in **Figure 4.7** and in **Table 4.1**. When the predicted versus measured plots of the models referred to PETG-UP (**Figure 4.7A** and **E**) were considered, the flattening trend previously observed was no longer evident. Training performances for the two polymers were indeed comparable, thus suggesting that CNN, given its capability to deal with non-linearity, was able to adequately describe penetration in both materials. The goodness of the training process could also be substantiated by the prediction maps (**Figure 4.7B, D, F, H**), which demonstrated an almost perfect congruence between the ROIs predicted colour and the expected value, as represented by the border.

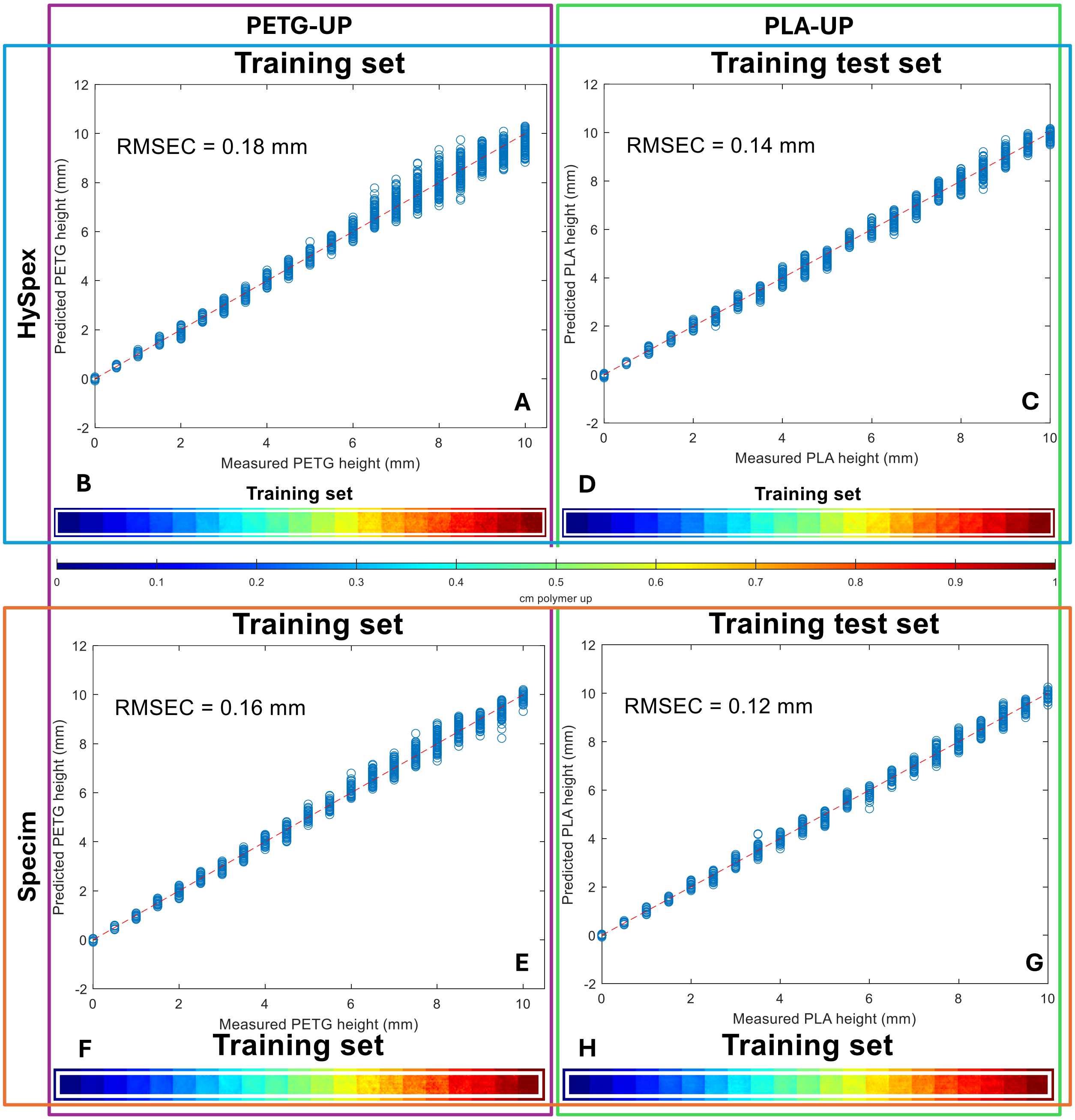

Figure 4.7: *CNN regression results for the training set obtained from HySpex (A, B, C, D) and Specim (E, F, G, H) data for PETG-UP (A, B, E, F) and PLA-UP (C, D, F, H) configurations. Predicted versus measured plot (A, C, E, G) and prediction maps (B, D, F, H) are reported. Each prediction map is reported with a border which represents the colour the corresponding ROI should have if its prediction error was null.*

Afterwards, the pixel images of the internal and external test sets were predicted with the developed model, and the results are displayed in **Figure 4.8**. The prediction outcomes corroborated what already observed in the training set. Indeed, both the internal and external test sets showed a satisfactory alignment with the regression line, without discernible flattening. Moreover, from **Table 4.1** it was possible to observe that the internal test set consistently exhibited superior performances if compared to the external test set. This suggests that the differences in printing patterns played a substantial role in the prediction process.

Furthermore, the models also demonstrated a moderate degree of overfitting, with RMSEC almost 4 times lower that the $RMSEP_{EXT}$. This observation highlights the model's efficacy in describing samples similar to the training set, such as those from the internal test set, while its limitations become evident when attempting to describe samples that exhibit distinct physical characteristics, such as those from the external test set. This outcome may be at least in part connected to the use of the pixel-based approach, which considers all pixels as individual samples, for model training. Indeed, while this approach is mandatory for CNN training, which requires a high amount of data to be robustly calibrated, it may introduce a certain degree of overfitting in the resulting models. An analysis of the predicted versus measured plots of the external test set (**Figure 4.8B, F, J, N**) revealed a systematic underestimation of top-polymer height by the model. This feature may be connected to the heightened penetration in this type of samples, as previously suggested on several occasions in the text. Indeed, higher penetration would lead to an increased presence of the signature of the polymer at the bottom, thus leading to a systematic underestimation of the polymer facing the detector.

However, a comparison between the polymers is rendered challenging by the fact that some discrepancies could in this case be observed between HySpex and Specim results. In particular, while the two instruments demonstrated comparable performances for the PETG-UP configuration, the performances for PLA-UP were significantly worse when assessed by means of the Specim apparatus. This outcome might again be ascribable to the different light intensities of the two instrumental settings; nevertheless, further research is necessary to substantiate this hypothesis.

In summary, the use of CNN was instrumental to demonstrate the capability of NIR radiation to penetrate through at least 1 cm in both the studied polymers, confirming that the phenomenon is characterised by a complex behaviour entailing a non-linear trend in the deepest layers. Indeed, the models, though slightly overfitted, enabled the resolution of the flattening individuated in all the other chemometric treatments applied, suggesting that, with the help of appropriate non-linear methods, penetration could be described even within deeper strata.

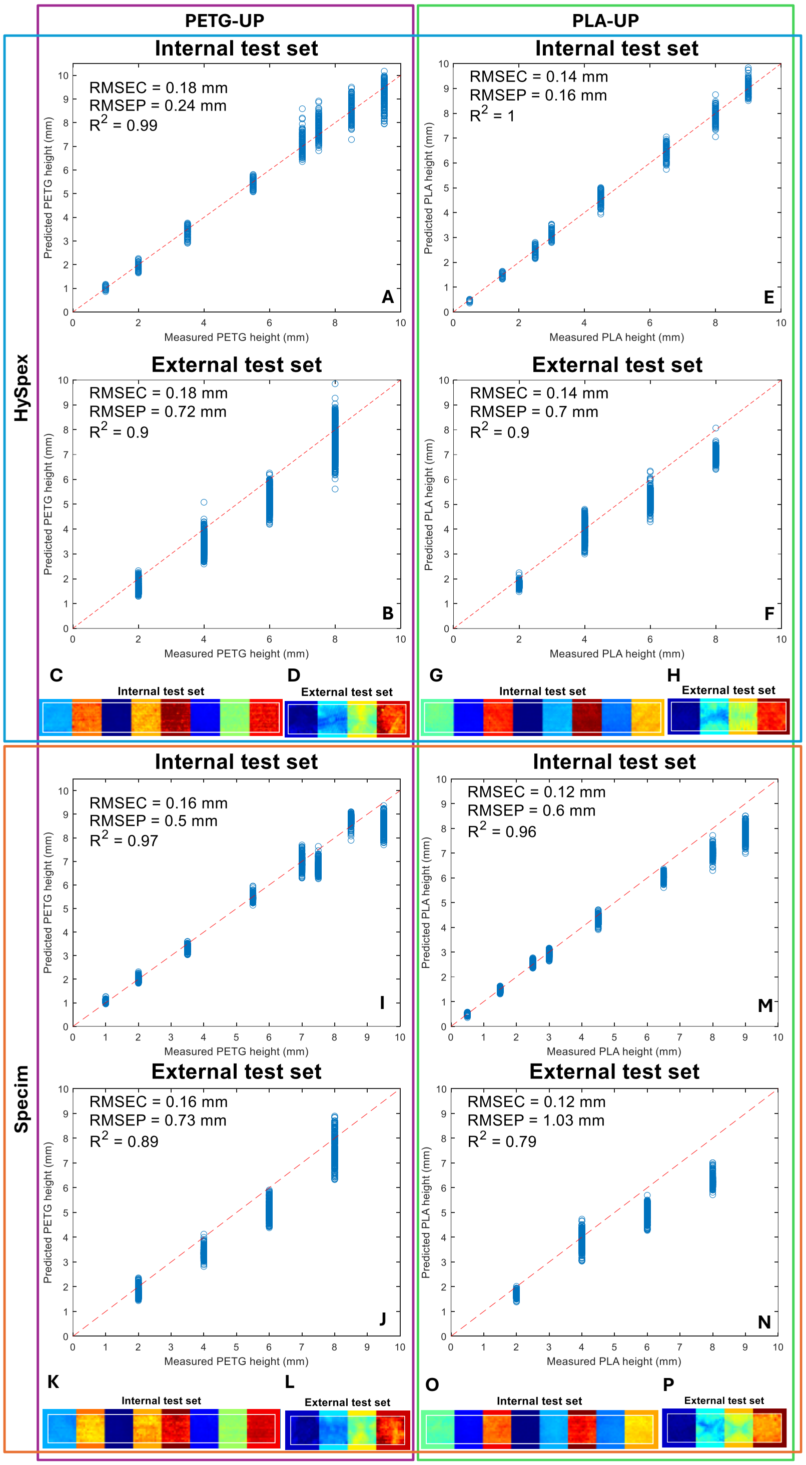

Figure 4.8: *CNN regression results for HySpex (from A to H) and Specim (from I to P) data for PETG-UP (from A to D and from I to L) or PLA-UP (from E to H and from M to P). Predicted versus measured plots for the internal test set (A, E, I, M), predicted versus measured plots for the external test set (B, F, J, N), prediction maps for the internal test set (C, G, K, O), and prediction maps for the external test set (D, H, L, P).*

4.1.3 Materials and methods

4.1.3.1 Samples production

In-house stratified samples were printed using an Original Prusa i3 MK3S + MMU3 3D printer (Prusa Research a.s., Prague, Czech Republic), coupled with the PrusaSlicer-2.9.2 software for slicing and assembling the samples. All projects were realised in the OpenSCAD 2021.01 environment.

The printing materials (Prusament by Prusa Research a.s., Prague, Czech Republic) were acquired as spools with a filament diameter of 1.75 ± 0.02 mm. Two different polymers were used to produce the samples: polylactic acid (PLA Transparent, 1 kg spool) and polyethylene terephthalate glycol (Transparent PETG Clear, 1.038 kg spool). These two polymers were chosen after preliminary spectral analysis on all the available options for their ease in printing and for their distinct spectral signatures in the NIR range.

4.1.3.2 Samples acquisition

NIR-HSI images were acquired using two different push-broom short-wave infrared hyperspectral imaging systems, which exhibited similar configurations (see **Figure 4.1C**).

In particular, the first instrument utilised was a SWIR3 hyperspectral camera from Specim (Spectral Imaging Ltd., Oulu, Finland), while the second was a SWIR-384 hyperspectral camera from HySpex (NEO HySpex, Oslo, Norway). Both instruments operated within the 960-2500 nm spectral range and were equipped with the same MCT (mercury-cadmium-tellurium) sensor with cooling down to 150 K, characterised by 384 spatial pixels (horizontal line array) and 288 spectral channels (FWHM = 5.5 nm). The first camera mounted an OLES15 lens, while the second camera mounted a SWIR-320/384 close-up 30cm lens assembly, positioned at a distance of 20.0 and 17.6 cm from the samples, respectively. The samples were illuminated with six tungsten halogen lamps (Osram, Styria, Austria) (12 V, 35 W, 2900 K, 430 Lm) in the first instrument, while the second instrument was equipped with four tungsten halogen lamps cover the spectral range 400 nm to 2500 nm (12 V, 150 W, 3100 K, 600 Lm), custom-made at HySpex (NEO HySpex, Oslo, Norway). In both cases, the lamps were positioned at a 45° angle, approximately 25 cm from the samples, with half of the lamps situated in front and the other half situated behind the samples. The image acquisition parameters in the Specim system were configured as follows: exposure time of 6 ms, frame rate of 70 Hz, scanning speed of 28.2 mm/s. Conversely, in the HySpex configuration, the exposure time was fixed at 4.8 ms, while the frame rate and a scanning speed were set to 185 Hz and 728 mm/s, respectively. Exposure times and frame rates were set for both instruments with the goal of maximising signal intensity while avoiding pixel saturation. The differences in the resulting exposure times and frame rates are connected to differences in lens' field of view (50 mm for Specim, 30 mm for HySpex), with consequent differences in magnification, and to the discrepancies in lamp intensities. With the described conditions, the resulting pixel sizes were approximately 0.4 and 0.2 mm for the Specim and HySpex spectrometers, respectively; the Lumo Scanner V. 2.6 software (Specim, Spectral Imaging Ltd., Oulu, Finland) and HySpex Ground Software v4.9.3.8 (NEO HySpex, Oslo, Norway), respectively, were utilised to regulate the system.

Prior to the acquisition of sample images, both instruments acquired a white reference image (W) (99% reflectance Spectralon®). Additionally, the Specim instrument captured a dark image (D) (closed shutter), while the HySpex instrument automatically subtracted a dark signal from all images. Accordingly, the reflectance of each pixel was computed as delineated in **Equation 4.1** and **Equation 4.2** for the Specim and HySpex data sets, respectively.

$$R_{\lambda_{Sp}} = \frac{I_{\lambda_{Sample}} - I_{\lambda_D}}{I_{\lambda_W} - I_{\lambda_D}} \qquad (4.1)$$

$$R_{\lambda_{HS}} = \frac{I_{\lambda_{Sample}}}{I_{\lambda_W}} \qquad (4.2)$$

where $R_{\lambda_{Sp}}$ and $R_{\lambda_{HS}}$ are the reflectance values calculated for each wavelength for the Specim and HySpex instruments, respectively, $I_{\lambda_{Sample}}$ is the intensity for each wavelength of the profile recorder for the sample, I_{λ_D} is the intensity for each wavelength of the profile recorded with the closed shutter, and I_{λ_W} is the intensity for each wavelength of the profile recorded for the white Spectralon reference.

For data acquisition, samples were located on the instruments' moving stage with the PETG surface oriented towards the detector. This configuration is referred to as PETG-UP throughout the text. Subsequently, the samples were upturned, and the data acquisition was repeated, with the PLA surface facing the detector. This configuration will be referred to as PLA-UP in the text.

The focal point of the instrument was recalibrated to align with the lowermost layer of the samples. However, the field of view of the two instruments was sufficiently broad to ensure good focus on the uppermost portion of the samples as well. Initially, images were acquired for the set comprising the twenty-one cubes, which were analysed subsequently in accordance with the increasing height of the polymer facing the detector. This set of images is referred to as the "training set" throughout the text. In the subsequent phase, eight randomly selected cubes were subjected to imaging, with the images being captured in random order. This set of images is referred to as the "internal test set" throughout the text.

Finally, the set containing the four cylindric samples was analysed, again following the order of increasing top-polymer height. This set of images is referred to as the "external test set" in the text. The polymers' height in the samples of each set is detailed in **Table 4.2.**

This acquisition protocol ensured the production of three independent sets of images with defined roles in the subsequent chemometric treatment. In particular, the training set image will be used in all model development steps. The two test images will instead be used in model validation. In particular, the internal test set, including a subset of the samples of the training samples but in random order, serves as a first check for model adequacy, while the external test set, being composed of new samples in terms of printing properties and shapes, represents a true independent set to be used for overfitting evaluation and general performance testing, with the additional goal of evaluating the effect of physical properties on NIR radiation penetration depth.

Table 4.2: *Details of sample types, sample numbers, polymer layer heights, ROI size and matrix dimension for training set, internal test set and external test set.*

	Sample type	**Number of samples**	**Sample layer height (PLA-PETG, mm)**	**ROI size (pixel)**		**Total number of pixels**	
				Specim	**HySpex**	**Specim**	**HySpex**
Training set	Cubes	21	0-10, 0.5-9.5, 1-9, 1.5-8.5, 2-8, 2.5-7.5, 3-7, 3.5-6.5, 4-6, 4.5-5.5, 5-5, 5.5-4.5, 6-4, 6.5-3.5, 7-3, 7.5-2.5, 8-2, 8.5-1.5, 9-1, 9.5-0.5, 10-0	16×16	26×26	5376	14196
Internal test set	Cubes	8	4.5-5.5, 1.5-8.5, 8-2, 0.5-9.5, 3-7, 9-1, 2.5-7.5, 6.5-3.5	16×16	26×26	2048	5408
External test set	Cylinders	4	2-8, 4-6, 6-4, 8-2	16×16	22×22	1024	1936

4.1.3.3 Data processing

All data pre-processing and chemometric analyses were carried out using the PLS_Toolbox 9.5 software (Eigenvector Research Inc., Manson, WA, USA) and in-house scripts developed either under the MATLAB® environment, version R2024b (The MathWorks, Natick, MA, USA) and under the Python environment, version 3.12.7 (Python Software

Foundation, Wilmington, DE, USA). All the steps detailed in the following sections were performed in parallel for both instruments and for the two configurations PETG-UP and PLA-UP.

4.1.3.3.1 Masking and segmenting

The first step of image processing consisted in sample masking and background removal. To this aim, a PCA model was calculated on each image, using mean centering as the pre-processing method. All the pixels with principal component two (PC2) score values below 1 were removed, since they were attributable to the tray on which the samples were placed during analysis. This process was automated and repeated across all images.

Afterwards, smaller regions of interest (ROIs) were selected on each sample, to remove the effect of sample borders, which suffer from high scattering and are characterised by a different printing pattern. In particular, square 16×16 pixels ROIs were extracted from each sample for Specim data and 26×26 ROIs were extracted for the training and internal test sets for HySpex data, while 22×22 pixels ROIs were extracted for the external test set. The obtained regions of interest were then concatenated to obtain a separate matrix containing all samples for each of the sets. Details on the dimensions of each matrix can be found in **Table 4.2**.

The data processing pipeline is reported in **Figure 4.9**.

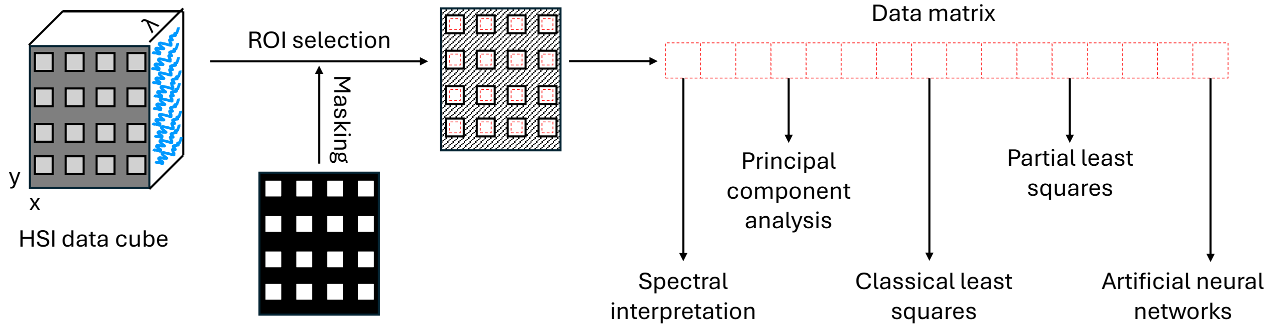

Figure 4.9*: Schematic representation of the data processing pipeline.*

4.1.3.3.2 Exploratory analysis

Initially, pixel spectra from each ROI were averaged, and an average signal representing each sample was obtained. This was done following an object-based approach [58], with the objective of enhancing graph readability and data interpretability. The obtained spectra were plotted in their raw form or pre-processed by means of SNV transformation [120]. The evolution of spectral signatures in relation to polymer height was evaluated.

Subsequently, all pixels from the ROIs were submitted to further data analysis, employing a pixel-based approach [58,250]. In this case study, the pixel-based approach was preferred since the samples were produced with an accurate 3D printing technique that guaranteed uniform polymer height across the sample section (uncertainty = ±0.1 mm). Each pixel could thus be regarded as an independent sample. Consequently, the use of the pixel-based approach was adopted to increase the sampling size.

The training set was then subjected to PCA [66]. In this step, different pre-processing techniques were employed to minimise unwanted scattering effects while enhancing the information regarding polymer height. The selected pre-processing scheme entailed a combination of Savitzky-Golay first-order differentiation (third-order polynomial, window size of 9 points) [132] followed by SNV transform. This pre-processing was applied in all subsequent processing steps. After pre-processing selection, the scores from PC1 were utilised to reconstruct the sample image, thereby yielding a single layer score image with pixel colour representing its score value. The score image was instrumental to identify the main sources of variability and to provide insights into the relationship between score values and polymer height. Furthermore, loading plots were extracted and compared to what observed in the object-based spectra. Afterwards, the internal and external test sets were projected into the training set's principal components space, and score images were obtained and analysed for those sets as well. The projection was carried out by subtracting from the test set data the training set average signal, *i.e.* centering the test set data according to the training set, and then by multiplying the training loading values to the spectra of the test sets, thus obtaining score values for the test sets. Score images were then produced for the test sets data as well.

4.1.3.3.3 Quantitative analysis

Next, the pre-processed spectra from all sets underwent classical least squares (CLS) [251,252] analysis, also known as ordinary least squares (OLS), for spectral linear unmixing. In particular, the CLS technique was employed to extract a predicted height of the two polymers by multiplying the spectra matrix with the Moore–Penrose pseudoinverse of the pure-component spectra [253,254]. The pure-components were represented by the mean spectrum of the two single-material cubes. The predicted height of the polymer facing the detector for each pixel was compared with the known polymer height in the considered sample, and the deviation from the real value was calculated in terms of root mean square error (RMSE). Then, the polymer height estimated by the model was encoded with a colour scale from blue to red, and used to reconstruct the image, obtaining a prediction image. In order to facilitate the comparison of the prediction image with the expected value, each ROI image was represented with a border representing the colour the ROI should have if the prediction had an RMSE of 0. In other words, the more the inner colour visually matches the border colour, the more precise the prediction is.

Subsequently, two regression models were fit on the training set to obtain a model capable of predicting the height in millimetres of the polymer facing the detector. In this case, the X data matrix was represented by the pixel spectra, while the Y data matrix, which served as a reference for the regression calculation, corresponded to the top-polymer height in millimetres.

The first of the two applied techniques was a linear regression approach, *i.e.* PLS [65,135]. The model was cross-validated using a leave-one-level-out approach [96,250], *i.e.*, the cross-validation scheme was designed in order to remove from each iteration one entire ROI representing a specific Y value and use it for prediction. This strategy circumvents the potential issue of duplicate samples in the calibration and cross-validation sets, thereby ensuring a more reliable estimate of prediction error (RMSEP) through RMSE in cross-validation (RMSECV). The number of significant latent variables (LVs) was determined based on RMSECV, and the associated regression vectors and variable importance in projection (VIPs) were considered for spectral interpretation. To assess the model's performance, additional quality parameters, namely bias, were computed. After model training, the internal and external test sets were projected into the PLS space, and a predicted height was stored for each pixel. This predicted height was then used to plot single-layer images representing the predicted polymer height for each pixel. As previously detailed for the CLS approach, prediction maps were represented with a border showcasing the colour the ROI should present if the prediction error was null.

The second regression approach employed was non-linear, namely CNN [255,256]. In this case, data were pre-processed by SNV transform only prior to model training, since most of the pre-processing steps can be dealt with by convolutional layers themselves [257,258]. The network structure was optimised to guarantee robustness and repeatability, and it consisted of three convolutional layers followed by three fully connected layers. The connection between subsequent layers was regulated by the ReLU function [259], and the Adam optimiser [260] from the Python Torch library was chosen for backpropagation and weight optimisation, with mean squared error (MSE) as loss function. Validation along model training was done on a random subset selected from the training set by means of the

DataLoader function from the Torch library and a batch size of 200. The number of epochs was set to 70, and the learning rate was gradually adjusted during the training process by means of a scheduler function. This allows to start with a higher learning rate, in this case 0.001, which was then reduced while the model gets fine-tuned, allowing a drastic reduction in the number of epochs needed for model training, and subsequently reducing the computational burden, while increasing robustness. The amount of learning rate adjustment is regulated by a factor, gamma, that may range from 0 to 1 and was set to 0.6 in this case. To account for randomness in CNN training [258], where the final model depends on a random seed and therefore provides slightly different performances each time a new model is trained, five models were trained consecutively for each configuration and then tested on an optimisation set, consisting of a replicate of the training set image with polymer height ranging from 0.5 to 9.5 mm, *i.e.* excluding the pure samples. The model yielding the best prediction results on the optimisation set was then selected and used in the subsequent prediction steps.

After training, the regression models were used to predict the height of the polymer facing the detector for the internal and external test sets. The predicted heights were used to generate prediction maps, where the border delineated the actual sample height, as previously illustrated for the CLS approach.

4.1.4 Conclusions

This study establishes a comprehensive framework for the quantitative assessment of NIR radiation penetration in hyperspectral imaging, thanks to the implementation of appropriate chemometric approaches to disentangle and model subsurface information. By integrating PCA, CLS, and PLS regression with CNN, the research demonstrates that spectral signals can be detected from layers located up to approximately 1 cm beneath the surface in both PETG and PLA. Importantly, penetration depth was shown to strongly depend on the interplay between material-specific optical properties (chemical composition, morphology, printing pattern) and instrumental parameters (illumination intensity, configuration), rather than being a fixed characteristic. CNN-based models, in particular, revealed non-linear penetration behaviour, confirming and extending the information derived from linear methods, thanks to their data-driven and versatile nature.

Rather than defining a fixed penetration limit, the present framework provides a quantitative methodology for assessing how NIR radiation interacts with stratified media. The results highlight that NIR-HSI spectra may include contributions from layers significantly deeper than usually assumed, possibly exceeding 1 cm, emphasising the need for careful data interpretation and spectral unmixing in real-world applications.

Looking ahead, applying this framework to thicker and more complex multicomponent samples will be essential to delineate the ultimate boundaries of NIR-HSI penetration and to further explore the non-linear interplay between optical, structural, and instrumental variables. Additionally, a systematic evaluation of wavelength-dependent effects will shed light on how different energy regions influence penetration and information retrieval.

Taken together, the present study redefines the conventional understanding of NIR-HSI as a surface analysis method, demonstrating its potential to evolve into a depth-resolved analytical and tomographic tool. The proposed framework for non-destructive, material-specific analysis of penetration for complex samples, paves the way for novel applications of NIR-HSI in quality control, materials design, and non-destructive testing of complex multilayer systems, thereby setting the stage for the next generation of spectral imaging methodologies.

5 GENERAL CONCLUSIONS

The present doctoral thesis is grounded in a central conviction: that the limitations traditionally attributed to near-infrared (NIR) spectroscopy are not intrinsic to the technique itself, but rather to the way its data have historically been interpreted and exploited. In a scientific and technological landscape increasingly defined by complexity, speed, and multidimensionality, spectroscopy cannot remain confined within static or reductionist interpretative frameworks. Instead, it must be approached through methods capable of embracing both its data richness and the physical phenomena underlying signal generation.

Starting from this premise, the present work investigates NIR spectroscopy not as a secondary or supporting technique, but as a versatile, information-dense analytical platform whose full potential emerges when it is integrated with advanced multivariate and data-driven approaches, and when it is applied beyond conventional domains. Through a combination of conceptual considerations, systematic experimentation, and methodological innovation, this thesis contributes to a shift in perspective: from NIR as a quick sensor to NIR as a sophisticated, multidimensional and, in some contexts, even transformative analytical tool.

One of the objectives of this work, as outlined in the introductory chapter, was to challenge the hierarchical perception that often governs the choice of spectroscopic techniques. In many applied studies, UV–Vis, Raman, and IR/NIR spectroscopy are positioned in a competitive framework, where the “best-performing” technique is selected and the others discarded. However, this mindset risks overlooking the fact that each type of spectroscopy probes matter through fundamentally different physical interactions, and therefore encodes distinct, yet complementary, layers of information.

The forensic case studies discussed in Chapter 2 provide a concrete demonstration of this principle. By directly comparing NIR with UV-Vis and Raman spectroscopies in the context of bloodstains ageing, this work showed that the techniques do not merely differ in performance, but in the way they respond to changes in sample deposition and interact with the sample matrix.

In detail, the critical comparison between NIR and UV-Vis presented in Section 2.1 demonstrated the potential of the combination of techniques through data fusion. In particular, regression results individuated UV-Vis as the technique yielding the best prediction performances, displaying lower error rates. However, while these results would have been deemed enough in most previous literature reports focused on method comparison, in this thesis the evaluation was taken forward, combining techniques by means of data fusion. The results showed an increase in prediction accuracy when NIR and

UV-Vis were combined with a mid-level fusion approach. This underscores what was suggested in Chapter 1, *i.e.,* that often choosing the “best-performing” technique for an application may not be the final answer to the performances’ optimisation problem. In fact, the results of this study demonstrate that combining two techniques, even with apparently different performances, may anyway lead to improved prediction accuracy. This suggests that integration of more spectroscopic techniques in a multiplatform approach may be beneficial in several applications, allowing a comprehensive exploitation of electromagnetic radiation-matter interaction, drawing different information from each technique.

Similarly, Section 2.2 applied NIR and Raman spectroscopies in parallel to evaluate the response of bloodstain ageing to different environmental conditions and deposition substrates. In this case, for instance, NIR proved particularly good for absorbing substrates such as cotton, while Raman performed more consistently on highly reflective or non-absorbing surfaces such as glass and metal. Rather than indicating a general superiority of one technique over the other, these results once again highlight the complementarity of their analytical spaces. At the same time, the systematic Design of Experiments (DoE) approach and the application of RMANOVA allowed an unprecedented deconvolution of the factors influencing bloodstain ageing. Substrate, temperature, humidity, and illumination were demonstrated to be statistically significant, with substrate emerging as a central, often underestimated, driver of spectral evolution. This finding carries a strong practical and conceptual implication: forensic models must be built and validated in strict coherence with the real conditions of evidence deposition. At the same time, it also reinforces a more general message of this thesis: spectroscopic data cannot be interpreted in isolation from their physical and environmental context.

The findings from Chapter 2, condensed, enabled the proposal of comprehensive practical guidelines to be proposed to forensic practitioners. This result represents a major advancement for the forensic context, where the availability of recognised guidelines is imperative for the implementation of any procedure in real-case scenarios. Section 2.3 may therefore represent a first step toward a wider application of spectroscopic bloodstains dating in court, making for a crucial progress on how this problem is dealt with by practitioners.

The second major contribution of this thesis lies in exploiting the extension of NIR spectroscopy from point-based measurements to spatially resolved analyses via HSI. In Chapter 3, NIR-HSI was applied to the study of dehydration dynamics in epiphytic communities composed of lichens and bryophytes. This research line moved NIR far beyond its traditional association with moisture determination, transforming it into a tool for visualising and quantifying biological processes in space and time. Through the generation of false-colour PCA score maps and pixel-based water content maps, the work demonstrated that HSI can capture both global temporal trends and fine local heterogeneities that would be invisible to conventional, spatially averaged spectroscopy. The results of this study are significant not only for ecological and environmental topics, but also from a conceptual standpoint. Indeed, they demonstrate that NIR-HSI, when combined with carefully designed chemometric workflows, is capable of describing dynamic, non-linear, and spatially complex biological phenomena. This shifts the role of NIR from a passive observer of bulk composition to an active tool for studying living or semi-living systems, opening new perspectives in environmental monitoring, plant science, and ecosystem research, thus fulfilling the second objective of the thesis, as previously outlined in the Introduction chapter.

Equally or even more important was the methodological contribution associated with the comparison of image-based and pixel-based approaches. The study demonstrated the superior interpretability of the image-based approach, which provides easily readable score plots, and, summarising the information into one average signature, enables spectral interpretation and therefore the description of the processes or samples being described. On the other hand, the results also pointed out that models trained with a pixel-based approach better represent the variability of the data, finally yielding more robust prediction results. Through these results, rather than advocating for a single "optimal" strategy, the thesis showed that both perspectives reveal different but equally important aspects of the system under analysis, ultimately demonstrating that a multi-level approach is potentially the most informative choice. This reinforces the broader philosophical position of the work: complex analytical reality cannot be compressed into a single representation without loss of meaning.

Finally, the most original and potentially impactful contribution of this thesis is presented in Chapter 4, which tackles the third and final objective of the thesis as outlined in the introduction by addressing one of the most underexplored questions in NIR hyperspectral imaging, and possibly in NIR research in general: how deeply does NIR radiation actually penetrate into matter, and what governs this penetration? While the literature offers scattered and often contradictory estimates of NIR penetration depth, a systematic, quantitative, and from scratch investigation had been lacking, especially in the context of HSI.

By designing custom 3D-printed stratified polymer samples with controlled thickness and composition, this work established the first structured experimental framework to study NIR-HSI penetration in a reproducible and quantitative manner. The combined use of PCA, CLS, PLS and CNN allowed the phenomenon to be approached from multiple analytical angles. Initial PCA results confirmed that spectral information from underlying layers does influence the measured signal, even when these layers are located several millimetres beneath the surface. CLS further demonstrated that conventional linear unmixing techniques are insufficient to fully disentangle the contributions of deeper strata, especially when non-linear scattering effects become dominant.

The application of regression techniques, and in particular of convolutional neural networks, proved crucial to address this topic. Unlike linear methods such as PLS regression, CNN was able to capture and model the complex, non-linear behaviour of radiation propagation in stratified materials. The results indicated that, under specific instrumental configurations, NIR radiation can penetrate up to, or even beyond, 1 cm in polymeric materials such as polylactic acid (PLA) and polyethylene terephthalate glycol (PETG). At the same time, the work clearly confirmed that penetration depth is not a universal constant but a conditional parameter, dependent on material properties, structural organisation (*e.g.* printing pattern), radiation wavelength, instrumental configuration, and source intensity, pointing out that the determination of a global penetration limit should not be the final research goal.

Rather than proposing a fixed “penetration limit”, this thesis introduces a methodological framework for assessing penetration in a material-specific and instrument-specific manner. This is perhaps its most important theoretical contribution: shifting the question from “How deep does NIR go?” to “Under which conditions, and through which mechanisms, does NIR propagate within a given system?”. This reframing has direct consequences for any application of NIR-HSI to layered, heterogeneous or stratified samples, including in food analysis, cultural heritage, polymer science, and biomedical fields.

A unifying theme across all chapters of this thesis is an ongoing dialogue between traditional chemometric philosophy and modern machine learning paradigms. Early analyses were rooted in PCA, PLS, and variance deconvolution, emphasising interpretability and physical meaning as a fundamental and indispensable aspect of any data analysis procedure in analytical chemistry. In later stages, especially in the penetration study, deep learning approaches were introduced to address non-linearity and data complexity beyond the reach of classical models. Rather than representing a rupture, this transition was deliberately conceptualised as an evolution. The strength of chemometrics, *i.e.,* its grounding in chemical understanding and model transparency, was not abandoned, but rather it was carried forward into a more data-driven domain.

In particular, the possibility of integrating “classical” chemometric approaches, such as PLS, with modern deep learning strategies, supports the idea that the two approaches are not mutually exclusive, but rather can be harmonised to extract the most from each. To give an explanatory example, in the penetration study, PLS regression enabled, through VIPs scores interpretation, to confirm a chemistry-rooted behaviour of NIR radiation penetration, while CNN accounted with higher accuracy for non-linear behaviours. Once again, this conclusion follows the *fil rouge* of the thesis, *i.e.,* that combination, rather choice of an approach over the other, might be the deal-breaker in model analytical chemistry. In this sense, the thesis proposes a view of modern analytical chemistry where interpretability and performance are not mutually exclusive, but can co-evolve through the development of hybrid approaches that respect both mathematical power and physicochemical meaning.

However, as with any scientific work, the present thesis has limitations that also represent opportunities for future research.

In the forensic case studies, the use of a limited amount of blood donors reduced the generalisability of the conclusions regarding subject variability. Expanding the dataset to include a wider population and more complex deposition scenarios would further strengthen the robustness of the proposed models.

In the environmental study, the complexity of real ecosystems was intentionally reduced to controlled communities and laboratory conditions. While this choice was necessary for methodological development, future work should explore the application of NIR-HSI in true field conditions, where additional variables such as light fluctuation, temperature gradients and background interference must be addressed.

In the penetration study, although the use of 3D-printed model systems provided exceptional control and repeatability, real-world materials are often more irregular and chemically complex. The proposed framework should therefore be extended to heterogeneous, naturally occurring multilayer systems, including biological tissues, composite foods, and historical artefacts.

From a methodological standpoint, future research could further explore the integration of physically informed models with data-driven neural networks, opening the way to a new generation of “hybrid” chemometric models, capable of both explaining and predicting complex spectroscopic phenomena.

Taken as a whole, this thesis does not simply present a collection of case studies, but proposes a coherent, alternative way of thinking about spectroscopy in the modern era. It argues that analytical power does not lie in the technique alone, but in the relationship between physics, data, and interpretation. By challenging traditional hierarchies, embracing multidimensionality, and integrating classical and modern analytical philosophies, this work contributes to redefining the role of NIR spectroscopy in contemporary science.

In doing so, it places NIR, especially when combined with hyperspectral imaging and advanced data analysis, not at the margins of analytical chemistry, but at its frontier: as a tool capable not only of measuring, but of revealing hidden structures, dynamics and interactions within complex systems.

Ultimately, the most important outcome of this thesis may not be a specific model or numerical limit, but a conceptual one: a demonstration that when complexity is approached with rigor, creativity, and interdisciplinary integration, what once appeared as a limitation can become a source of profound analytical insight.

REFERENCES

[1] N. Vervoort, K. Goossens, M. Baeten, Q. Chen, Recent advances in analytical techniques for high throughput experimentation, Analytical Science Advances 2 (2021) 109–127. https://doi.org/10.1002/ANSA.202000155.

[2] F. Adams, M. Adriaens, The metamorphosis of analytical chemistry, (n.d.). https://doi.org/10.1007/s00216-019-02313-z.

[3] Y. Feng, X. Zhang, J. Liu, Z. Yuan, S. Gao, J. Shi, Advancing food safety and quality assessment: a comprehensive review of non-destructive analytical technologies, Analytical Methods 17 (2025) 4697–4717. https://doi.org/10.1039/D5AY00647C.

[4] E. Skibsted, S.B. Engelsen, Spectroscopy for process analytical technology (PAT), Encyclopedia of Spectroscopy and Spectrometry (2017) 188–197. https://doi.org/10.1016/B978-0-12-803224-4.00026-1.

[5] M.C. Alvarado, P.D.C. Sanchez, S.G.N. Polongasa, Emerging rapid and non-destructive techniques for quality and safety evaluation of cacao: recent advances, challenges, and future trends, Food Production, Processing and Nutrition 2023 5:1 5 (2023) 40-. https://doi.org/10.1186/S43014-023-00157-W.

[6] N. Modupalli, M. Naik, C.K. Sunil, V. Natarajan, Emerging non-destructive methods for quality and safety monitoring of spices, Trends Food Sci. Technol. 108 (2021) 133–147. https://doi.org/10.1016/J.TIFS.2020.12.021.

[7] K. Hashimoto, V.R. Badarla, A. Kawai, T. Ideguchi, Complementary vibrational spectroscopy, Nature Communications 2019 10:1 10 (2019) 4411-. https://doi.org/10.1038/s41467-019-12442-9.

[8] Z. Xu, X. Li, W. Cheng, G. Zhao, L. Tang, Y. Yang, Y. Wu, P. Zhang, Q. Wang, Data fusion strategy based on ultraviolet–visible spectra and near-infrared spectra for simultaneous and accurate determination of key parameters in surface water, Spectrochim. Acta A Mol. Biomol. Spectrosc. 302 (2023) 123007. https://doi.org/10.1016/J.SAA.2023.123007.

[9] C. Farber, J. Li, E. Hager, R. Chemelewski, J. Mullet, A.Y. Rogachev, D. Kurouski, Complementarity of Raman and infrared spectroscopy for structural characterization of plant epicuticular waxes, ACS Omega 4 (2019) 3700–3707. https://doi.org/10.1021/ACSOMEGA.8B03675.

[10] J. Dai, P. Chen, X. Chu, B. Xu, S. Su, Data fusion of near infrared, Fourier Transform infrared and Raman spectroscopy for quantifying the conversion of Poly Alpha Oil (PAO), Fuel 366 (2024) 131420. https://doi.org/10.1016/J.FUEL.2024.131420.

[11] R.K.R. Ranaweera, D.L. Capone, S.E.P. Bastian, D. Cozzolino, D.W. Jeffery, A Review of wine authentication using spectroscopic approaches in combination with chemometrics, Molecules 26 (2021) 4334. https://doi.org/10.3390/MOLECULES26144334.

[12] A. Nordon, A. Mills, R.T. Burn, F.M. Cusick, D. Littlejohn, Comparison of non-invasive NIR and Raman spectrometries for determination of alcohol content of spirits, Anal. Chim. Acta 548 (2005) 148–158. https://doi.org/10.1016/J.ACA.2005.05.067.

[13] B.H. Stuart, Infrared spectroscopy: fundamentals and applications, Infrared Spectroscopy: Fundamentals and Applications (2005) 1–224. https://doi.org/10.1002/0470011149.

[14] C. Puzzarini, M.P. De Lara-Castells, M.J. Ramos, Challenges in spectroscopy: accuracy versus interpretation from isolated molecules to condensed phases, Physical Chemistry Chemical Physics 21 (2019) 3395–3396. https://doi.org/10.1039/C9CP90025J.

[15] M. Kharbach, M. Alaoui Mansouri, M. Taabouz, H. Yu, Current application of advancing spectroscopy techniques in food analysis: data handling with chemometric approaches, Foods 12 (2023). https://doi.org/10.3390/FOODS12142753.

[16] A. Biancolillo, F. Marini, Chemometric methods for spectroscopy-based pharmaceutical analysis, Front. Chem. 6 (2018) 412780. https://doi.org/10.3389/FCHEM.2018.00576.

[17] I. V. Tetko, O. Engkvist, U. Koch, J.L. Reymond, H. Chen, BIGCHEM: Challenges and opportunities for big data analysis in chemistry, Mol. Inform. 35 (2016) 615. https://doi.org/10.1002/MINF.201600073.

[18] H. Parastar, R. Tauler, Big (bio)chemical data mining using chemometric methods: A need for chemists, Angew. Chem. Int. Ed Engl. 61 (2022) e201801134. https://doi.org/10.1002/ANIE.201801134.

[19] K.B. Beć, J. Grabska, C.W. Huck, Interpretability in near-infrared (NIR) spectroscopy: Current pathways to the long-standing challenge, TrAC Trends in Analytical Chemistry 189 (2025) 118254. https://doi.org/10.1016/J.TRAC.2025.118254.

[20] K.B. Bec, C.W. Huck, Advances in near-infrared spectroscopy and related computational methods, Molecules 24 (2019) 4370. https://doi.org/10.3390/MOLECULES24234370.

[21] T. Davies, The history of near infrared spectroscopic analysis: Past, present and future - From sleeping technique to the morning star of spectroscopy, Analusis 26 (1998). https://doi.org/10.1051/ANALUSIS:199826040017.

[22] M. Manley, Near-infrared spectroscopy and hyperspectral imaging: Non-destructive analysis of biological materials, Chem. Soc. Rev. 43 (2014) 8200–8214. https://doi.org/10.1039/c4cs00062e.

[23] A. Eilert, History and theory of near-infrared spectroscopic analysis (NIRS), in: IGC Proceedings (1985-2023), 2023: p. 101. https://doi.org/10.13023/dk1w-4m49.

[24] Y. Ozaki, Near-infrared spectroscopy-its versatility in analytical chemistry, Analytical Sciences 28 (2012) 545–563. https://doi.org/10.2116/ANALSCI.28.545.

[25] G. Gullifa, L. Barone, E. Papa, A. Giuffrida, S. Materazzi, R. Risoluti, Portable NIR spectroscopy: the route to green analytical chemistry, Front. Chem. 11 (2023) 1214825. https://doi.org/10.3389/FCHEM.2023.1214825.

[26] M. Blanco, I. Villarroya, NIR spectroscopy: a rapid-response analytical tool, TrAC Trends in Analytical Chemistry 21 (2002) 240–250. https://doi.org/10.1016/S0165-9936(02)00404-1.

[27] K.B. Beć, J. Grabska, C.W. Huck, Principles and applications of miniaturized near-infrared (NIR) spectrometers, Chemistry 27 (2020) 1514. https://doi.org/10.1002/CHEM.202002838.

[28] G.W. Small, Chemometrics and near-infrared spectroscopy: Avoiding the pitfalls, TrAC Trends in Analytical Chemistry 25 (2006) 1057–1066. https://doi.org/10.1016/J.TRAC.2006.09.004.

[29] Y. Roggo, P. Chalus, L. Maurer, C. Lema-Martinez, A. Edmond, N. Jent, A review of near infrared spectroscopy and chemometrics in pharmaceutical technologies, J. Pharm. Biomed. Anal. 44 (2007) 683–700. https://doi.org/10.1016/J.JPBA.2007.03.023.

[30] K.M. Sørensen, F. Van Den Berg, S.B. Engelsen, NIR data exploration and regression by chemometrics-A primer, Near-Infrared Spectroscopy: Theory, Spectral Analysis, Instrumentation, and Applications (2020) 127–189. https://doi.org/10.1007/978-981-15-8648-4_7.

[31] D. a Skoog, F.J. Holler, T. a Nieman, Molecular spectroscopy, in: Principles of Instrumental Analysis, Belmont Calif. : Thomson, Brooks/Cole, 1998.

[32] J.B. Wiester, Investigating the similarities and differences among UV/Vis, infrared, fluorescence, and raman spectroscopies through discussion of light-matter interactions, ACS Symposium Series 1305 (2018) 13–33. https://doi.org/10.1021/BK-2018-1305.CH002.

[33] S. Svanberg, Atomic and molecular spectroscopy, Springer Berlin Heidelberg, Berlin, Heidelberg, 2001. https://doi.org/10.1007/978-3-642-98107-4.

[34] S. Sinha, C. Jeyaseelan, G. Singh, T. Munjal, D. Paul, Spectroscopy—Principle, types, and applications, Basic Biotechniques for Bioprocess and Bioentrepreneurship (2023) 145–164. https://doi.org/10.1016/B978-0-12-816109-8.00008-8.

[35] N. Nag, S. Sasidharan, P. Saudagar, T. Tripathi, Fundamentals of spectroscopy for biomolecular structure and dynamics, Advanced Spectroscopic Methods to Study Biomolecular Structure and Dynamics (2023) 1–35. https://doi.org/10.1016/B978-0-323-99127-8.00002-7.

[36] D.A. Roberts, G.L. Geoffroy, Compounds with heteronuclear bonds between transition metals, Comprehensive Organometallic Chemistry 6 (1982) 763–877. https://doi.org/10.1016/B978-008046518-0.00085-4.

[37] J.W. Farley, W.C. Brumley, D.L. Eastwood, Electronic spectroscopy, environmental applications, Encyclopedia of Spectroscopy and Spectrometry (2017) 452–458. https://doi.org/10.1016/B978-0-12-803224-4.00136-9.

[38] M. Reichenbächer, J. Popp, Electronic absorption spectroscopy, Challenges in Molecular Structure Determination (2012) 145–214. https://doi.org/10.1007/978-3-642-24390-5_3.

[39] A.S. Gilbert, R.W. Lancaster, IR and Raman spectroscopy, industrial applications, Encyclopedia of Spectroscopy and Spectrometry (2017) 394–407. https://doi.org/10.1016/B978-0-12-803224-4.00331-9.

[40] A.A. Bunaciu, H.Y. Aboul-Enein, Vibrational spectroscopy applications in drugs analysis, Encyclopedia of Spectroscopy and Spectrometry (2017) 575–581. https://doi.org/10.1016/B978-0-12-409547-2.12214-0.

[41] D.L. Andrews, Rayleigh scattering and Raman effect, theory, Encyclopedia of Spectroscopy and Spectrometry (2017) 924–930. https://doi.org/10.1016/B978-0-12-409547-2.11337-X.

[42] C. Vogt, C.S. Wondergem, B.M. Weckhuysen, Ultraviolet-Visible (UV-Vis) Spectroscopy, Springer Handbooks (2023) 237–264. https://doi.org/10.1007/978-3-031-07125-6_11.

[43] P.J. Worsfold, Spectrophotometry | Overview, Encyclopedia of Analytical Science: Second Edition (2005) 318–321. https://doi.org/10.1016/B0-12-369397-7/00714-7.

[44] N. Azad, UV-visible spectroscopy, Analytical Methods in Chemical Analysis: An Introduction (2023) 59–80. https://doi.org/10.1515/9783110794816-004.

[45] S.M. Saleem, S.A.R. Naqvi, M.R.S.A. Janjua, T.A. Sherazi, M. Saeed, S.U. Hassan, M. Imran, M. Asif, M.U. Rasheed, T. Jabbar, UV–Visible spectroscopy for quantitative analysis of biomolecules, Bioanalytical Techniques (2028) 79–117. https://doi.org/10.1002/9781394314133.CH3.

[46] Z. Yang, M. Zhu, Case Studies: Ultraviolet-Visible (UV-Vis) Spectroscopy, Springer Handbooks (2023) 265–283. https://doi.org/10.1007/978-3-031-07125-6_12.

[47] M. Hlavatsch, J. Haas, R. Stach, V. Kokoric, A. Teuber, M. Dinc, B. Mizaikoff, Infrared spectroscopy–Quo vadis?, Applied Sciences (Switzerland) 12 (2022). https://doi.org/10.3390/app12157598.

[48] F. Adar, G. LeBourdon, J. Reffner, A. Whitley, FT-IR and Raman microscopy on a united platform: A technology whose time has come, Spectroscopy (Santa Monica) (2003). https://www.scopus.com/pages/publications/4444273050?origin=resultslist (accessed November 25, 2025).

[49] Y. Ozaki, T. Genkawa, Y. Futami, Near-Infrared Spectroscopy, in: Encyclopedia of Spectroscopy and Spectrometry, Academic Press, 2017: pp. 40–49. https://doi.org/10.1016/B978-0-12-409547-2.12164-X.

[50] Y. Ozaki, C.W. Huck, K.B. Beć, Near-IR spectroscopy and its applications, in: Molecular and Laser Spectroscopy: Advances and Applications, Elsevier Inc., 2018: pp. 11–38. https://doi.org/10.1016/B978-0-12-849883-5.00002-4.

[51] Y. Ozaki, M. Ishigaki, Frontiers of NIR imaging, Spectroscopy (2023) 26–33. https://doi.org/10.56530/SPECTROSCOPY.XG9883T4.

[52] N.C. Basantia, L.M.L. Nollet, M. Kamruzzaman, Hyperspectral imaging analysis and applications for food quality, 1st ed., CRC Press, Boca Raton, 2018. https://doi.org/10.1201/9781315209203.

[53] G.J. Edelman, E. Gaston, T.G. van Leeuwen, P.J. Cullen, M.C.G. Aalders, Hyperspectral imaging for non-contact analysis of forensic traces, Forensic Sci. Int. 223 (2012). https://doi.org/10.1016/j.forsciint.2012.09.012.

[54] R. Bhargava, Infrared spectroscopic imaging: The next generation, Appl. Spectrosc. 66 (2012) 1091–1120. https://doi.org/10.1366/12-06801.

[55] S. Mukhtar, A. Arbabi, J. Viegas, Advances in spectral imaging: a review of techniques and technologies, IEEE Access 13 (2025) 35848–35902. https://doi.org/10.1109/ACCESS.2025.3544476.

[56] P. Dixon, N. Masaun, M. Evans, J. Trezza, M. Ettenberg, J. Ueng-McHale, Monolithic planar InGaAs detector arrays for uncooled high-sensitivity SWIR imaging, in: Airborne Intelligence, Surveillance, Reconnaissance (ISR) Systems and Applications VI, SPIE, 2009: pp. 39–50. https://doi.org/10.1117/12.818731.

[57] D. Cozzolino, Conventional near-infrared spectroscopy and hyperspectral imaging: similarities, differences, advantages, and limitations, Molecules 2025, Vol. 30, Page 2479 30 (2025) 2479. https://doi.org/10.3390/MOLECULES30122479.

[58] C. Malegori, P. Oliveri, Principal component analysis, in: Hyperspectral Imaging Analysis and Applications for Food Quality, CRC Press, 2018: pp. 85–107. https://doi.org/10.1201/9781315209203-6.

[59] S. Kucheryavskiy, A new approach for discrimination of objects on hyperspectral images, Chemometrics and Intelligent Laboratory Systems 120 (2013) 126–135. https://doi.org/10.1016/J.CHEMOLAB.2012.11.009.

[60] F. Filipponi, C. Iadanza, · Valerio Vivaldi, F. Zucca, C. Meisina, · Maria, F. Ferrario, A. Trigila, Hybrid pixel-based and object-based image analysis approach for landslides rapid mapping: the extreme rainfall in Emilia-Romagna (Italy) May 2023 case study, Natural Hazards 121 (2025) 22549–22580. https://doi.org/10.1007/s11069-025-07705-2.

[61] D.C. Duro, S.E. Franklin, M.G. Dubé, A comparison of pixel-based and object-based image analysis with selected machine learning algorithms for the classification of agricultural landscapes using SPOT-5 HRG imagery, Remote Sens. Environ. 118 (2012) 259–272. https://doi.org/10.1016/J.RSE.2011.11.020.

[62] R.G. Brereton, A short history of chemometrics: A personal view, J. Chemom. 28 (2014) 749–760. https://doi.org/10.1002/CEM.2633.

[63] R.G. Brereton, J. Jansen, J. Lopes, F. Marini, A. Pomerantsev, O. Rodionova, J.M. Roger, B. Walczak, R. Tauler, Chemometrics in analytical chemistry—part I: history, experimental design and data analysis tools, Analytical and Bioanalytical Chemistry 2017 409:25 409 (2017) 5891–5899. https://doi.org/10.1007/S00216-017-0517-1.

[64] S. Wold, Chemometrics; what do we mean with it, and what do we want from it?, Chemometrics and Intelligent Laboratory Systems 30 (1995) 109–115. https://doi.org/10.1016/0169-7439(95)00042-9.

[65] S. Wold, M. Sjöström, L. Eriksson, PLS-regression: A basic tool of chemometrics, Chemometrics and Intelligent Laboratory Systems 58 (2001) 109–130. https://doi.org/10.1016/S0169-7439(01)00155-1.

[66] S. Wold, K. Esbensen, P. Geladi, Principal component analysis, Chemometrics and Intelligent Laboratory Systems 2 (1987) 37–52. https://doi.org/10.1016/0169-7439(87)80084-9.

[67] K. Guo, Y. Shen, G.A. Gonzalez-Montiel, Y. Huang, Y. Zhou, M. Surve, Z. Guo, P. Das, N. V Chawla, O. Wiest, X. Zhang, Artificial intelligence in spectroscopy: advancing chemistry from prediction to generation and beyond, (2025) 10445–10454. https://doi.org/10.24963/ijcai.2025/1160.

[68] J. Workman, H. Mark, From classical regression to AI and beyond: the chronicles of calibration in spectroscopy: part I, Spectroscopy (Santa Monica) 40 (2025) 13–18. https://doi.org/10.56530/SPECTROSCOPY.PU3090T7.

[69] E. Szymańska, Modern data science for analytical chemical data – A comprehensive review, Anal. Chim. Acta 1028 (2018) 1–10. https://doi.org/10.1016/J.ACA.2018.05.038.

[70] P. Oliveri, Chemometrics: a bridge to the AI age, The Analytical Scientist (2025). https://www.theanalyticalscientist.com/issues/2025/articles/september/chemometrics-a-bridge-to-the-ai-age/ (accessed November 25, 2025).

[71] C. Roux, R. Bucht, F. Crispino, P. De Forest, C. Lennard, P. Margot, M.D. Miranda, N. NicDaeid, O. Ribaux, A. Ross, S. Willis, The Sydney declaration – Revisiting the essence of forensic science through its fundamental principles, Forensic Sci. Int. 332 (2022) 111182. https://doi.org/10.1016/j.forsciint.2022.111182.

[72] G. Sauzier, W. Van Bronswijk, S.W. Lewis, Chemometrics in forensic science: Approaches and applications, Analyst 146 (2021) 1–60. https://doi.org/10.1039/d1an00082a.

[73] C.D. Adam, Fundamental studies of bloodstain formation and characteristics, Forensic Sci. Int. 219 (2012) 76–87. https://doi.org/10.1016/J.FORSCIINT.2011.12.002.

[74] C. Weyermann, O. Ribaux, Situating forensic traces in time, Science & Justice 52 (2012) 68–75. https://doi.org/10.1016/J.SCIJUS.2011.09.003.

[75] L. Tomellini, De l’emploi d’une table chromatique pour les taches de sang (une planche hors texte), Arch. d’Antropologie Criminelle Criminol 4 (1907).

[76] S. Anderson, B. Howard, G.R. Hobbs, C.P. Bishop, A method for determining the age of a bloodstain, Forensic Sci. Int. 148 (2005) 37–45. https://doi.org/10.1016/J.FORSCIINT.2004.04.071.

[77] M. Bauer, S. Polzin, D. Patzelt, Quantification of RNA degradation by semi-quantitative duplex and competitive RT-PCR: a possible indicator of the age of bloodstains?, Forensic Sci. Int. 138 (2003) 94–103. https://doi.org/10.1016/J.FORSCIINT.2003.09.008.

[78] S. Arany, S. Ohtani, Age estimation of bloodstains: A preliminary report based on aspartic acid racemization rate, Forensic Sci. Int. 212 (2011) e36–e39. https://doi.org/10.1016/J.FORSCIINT.2011.05.015.

[79] K. Ackermann, K.N. Ballantyne, M. Kayser, Estimating trace deposition time with circadian biomarkers: A prospective and versatile tool for crime scene reconstruction, Int. J. Legal Med. 124 (2010) 387–395. https://doi.org/10.1007/S00414-010-0457-1.

[80] A. Tsutsumi, Y. Yamamoto, H. Ishizu, Determination of the age of bloodstains by enzyme activities in blood cells, Japanese Journal of Legal Medicine 37 (1983) 770–776. https://okayama.elsevierpure.com/en/publications/determination-of-the-age-of-bloodstains-by-enzyme-activities-in-b (accessed June 4, 2025).

[81] K. Guo, S. Achilefu, M.Y. Berezin, Dating bloodstains with fluorescence lifetime measurements, Chemistry 18 (2012) 1303. https://doi.org/10.1002/CHEM.201102935.

[82] S. Mc Shine, K. Suhling, A. Beavil, B. Daniel, N. Frascione, The applicability of fluorescence lifetime to determine the time since the deposition of biological stains, Analytical Methods 9 (2017) 2007–2013. https://doi.org/10.1039/C6AY03099H.

[83] H. Inoue, F. Takabe, M. Iwasa, Y. Maeno, Y. Seko, A new marker for estimation of bloodstain age by high performance liquid chromatography, Forensic Sci. Int. 57 (1992) 17–27. https://doi.org/10.1016/0379-0738(92)90041-T.

[84] J. Andrasko, The estimation of age of bloodstains by HPLC analysis, J. Forensic Sci. 42 (1997) 601–607. https://doi.org/10.1520/JFS14171J.

[85] Y. Fujita, K. Tsuchiya, S. Abe, Y. Takiguchi, S.I. Kubo, H. Sakurai, Estimation of the age of human bloodstains by electron paramagnetic resonance spectroscopy: Long-term

controlled experiment on the effects of environmental factors, Forensic Sci. Int. 152 (2005) 39–43. https://doi.org/10.1016/J.FORSCIINT.2005.02.029.

[86] K. Rajamannar, Determination of the Age of Bloodstains Using Immunoelectrophoresis, J. Forensic Sci. 22 (1977) 159–164. https://doi.org/10.1520/JFS10381J.

[87] S. Strasser, A. Zink, G. Kada, P. Hinterdorfer, O. Peschel, W.M. Heckl, A.G. Nerlich, S. Thalhammer, Age determination of blood spots in forensic medicine by force spectroscopy, Forensic Sci. Int. 170 (2007) 8–14. https://doi.org/10.1016/J.FORSCIINT.2006.08.023.

[88] R.H. Bremmer, K.G. De Bruin, M.J.C. Van Gemert, T.G. Van Leeuwen, M.C.G. Aalders, Forensic quest for age determination of bloodstains, Forensic Sci. Int. 216 (2012) 1–11. https://doi.org/10.1016/j.forsciint.2011.07.027.

[89] G. Zadora, A. Menżyk, In the pursuit of the holy grail of forensic science – Spectroscopic studies on the estimation of time since deposition of bloodstains, TrAC Trends in Analytical Chemistry 105 (2018) 137–165. https://doi.org/10.1016/J.TRAC.2018.04.009.

[90] H. Sun, Y. Dong, P. Zhang, Y. Meng, W. Wen, N. Li, Z. Guo, Accurate age estimation of bloodstains based on visible reflectance spectroscopy and chemometrics methods, IEEE Photonics J. 99 (2017) 1. https://doi.org/10.1109/JPHOT.2017.2651580.

[91] G. Edelman, T.G. van Leeuwen, M.C.G. Aalders, Hyperspectral imaging for the age estimation of blood stains at the crime scene, Forensic Sci. Int. 223 (2012) 72–77. https://doi.org/10.1016/J.FORSCIINT.2012.08.003.

[92] K.C. Doty, G. McLaughlin, I.K. Lednev, A Raman “spectroscopic clock” for bloodstain age determination: the first week after deposition, Anal. Bioanal. Chem. 408 (2016) 3993–4001. https://doi.org/10.1007/s00216-016-9486-z.

[93] A. Menżyk, A. Damin, A. Martyna, E. Alladio, M. Vincenti, G. Martra, G. Zadora, Toward a novel framework for bloodstains dating by Raman spectroscopy: How to avoid sample photodamage and subsampling errors, Talanta 209 (2020) 120565. https://doi.org/10.1016/J.TALANTA.2019.120565.

[94] R. Kumar, K. Sharma, V. Sharma, Bloodstain age estimation through infrared spectroscopy and Chemometric models, Science and Justice 60 (2020) 538–546. https://doi.org/10.1016/J.SCIJUS.2020.07.004.

[95] C. Manis, C. Malegori, E. Alladio, M. Vincenti, P. Garofano, F. Barni, A. Berti, P. Oliveri, Non-destructive age estimation of biological fluid stains: An integrated analytical strategy based on near-infrared hyperspectral imaging and multivariate regression, Talanta 245 (2022) 123472. https://doi.org/10.1016/J.TALANTA.2022.123472.

[96] S. Gariglio, C. Malegori, A. Menżyk, G. Zadora, M. Vincenti, M. Casale, P. Oliveri, Determination of time since deposition of bloodstains through NIR and UV–Vis spectroscopy – A critical comparison, Talanta 278 (2024) 126444. https://doi.org/10.1016/J.TALANTA.2024.126444.

[97] G. Edelman, V. Manti, S.M. Van Ruth, T. Van Leeuwen, M. Aalders, Identification and age estimation of blood stains on colored backgrounds by near infrared spectroscopy, Forensic Sci. Int. 220 (2012) 239–244. https://doi.org/10.1016/J.FORSCIINT.2012.03.009.

[98] A. Menżyk, A. Martyna, A. Damin, M. Vincenti, G. Zadora, Breaking with trends in forensic dating: A likelihood ratio-based comparison approach, Forensic Sci. Int. 349 (2023). https://doi.org/10.1016/j.forsciint.2023.111763.

[99] A. Menzyk, Toward a spectroscopy - based approach for estimating time elapsed since bloodstains deposition. Development of a novel framework for blood evidence evaluation., 2021.

[100] O. Leers, Die forensische Blutuntersuchung., JAMA: The Journal of the American Medical Association 55 (1910) 41–87. https://doi.org/10.1001/jama.1910.04330020055034.

[101] D. Patterson, Use of reflectance measurements in assessing the colour changes of ageing bloodstains, Nature 187 (1960) 688–689. https://doi.org/10.1038/187688a0.

[102] S.S. Kind, D. Patterson, G.W. Owen, Estimation of the age of dried blood stains by a spectrophotometric method, Forensic Sci. 1 (1972) 27–54. https://doi.org/10.1016/0300-9432(72)90146-X.

[103] H. Inoue, F. Takabe, M. Iwasa, Y. Maeno, Identification of fetal hemoglobin and simultaneous estimation of bloodstain age by high-performance liquid chromatography, Int. J. Legal Med. 104 (1991) 127–131. https://doi.org/10.1007/BF01369715.

[104] Botonjic-Sehic, E.; Brown, C.W.; Lamontagne, M.; Tsaparikos, Mary, Forensic application of near-infrared spectroscopy: Aging of bloodstains, 24 (2009) 42–47.

[105] H. Lin, Y. Zhang, Q. Wang, B. Li, S. Fan, Z. Wang, Species identification of bloodstains by ATR-FTIR spectroscopy: the effects of bloodstain age and the deposition environment, Int. J. Legal Med. 132 (2018) 667–674. https://doi.org/10.1007/s00414-017-1634-2.

[106] R.H. Bremmer, A. Nadort, T.G. van Leeuwen, M.J.C. van Gemert, M.C.G. Aalders, Age estimation of blood stains by hemoglobin derivative determination using reflectance spectroscopy, Forensic Sci. Int. 206 (2011) 166–171. https://doi.org/10.1016/J.FORSCIINT.2010.07.034.

[107] B. Li, P. Beveridge, W.T. O'Hare, M. Islam, The age estimation of blood stains up to 30 days old using visible wavelength hyperspectral image analysis and linear discriminant analysis, Science and Justice 53 (2013) 270–277. https://doi.org/10.1016/J.SCIJUS.2013.04.004.

[108] T. Bergmann, F. Heinke, D. Labudde, Towards substrate-independent age estimation of blood stains based on dimensionality reduction and k-nearest neighbor classification of absorbance spectroscopic data, Forensic Sci. Int. 278 (2017) 1–8. https://doi.org/10.1016/j.forsciint.2017.05.023.

[109] T. Seki, Y.Y. Hsiao, F. Ishizawa, Y. Sugano, Y. Takahashi, Establishment of a random forest regression model to estimate the age of bloodstains based on temporal colorimetric analysis, Leg. Med. 69 (2023) 102343. https://doi.org/10.1016/J.LEGALMED.2023.102343.

[110] S. Boyd, M.F. Bertino, S.J. Seashols, Raman spectroscopy of blood samples for forensic applications, Forensic Sci. Int. 208 (2011) 124–128. https://doi.org/10.1016/j.forsciint.2010.11.012.

[111] A. Takamura, D. Watanabe, R. Shimada, T. Ozawa, Comprehensive modeling of bloodstain aging by multivariate Raman spectral resolution with kinetics, Commun. Chem. 2 (2019) 115. https://doi.org/10.1038/s42004-019-0217-1.

[112] R. Zhang, P. Wang, J. Chen, Y. Tian, J. Gao, Age estimation of bloodstains based on Raman spectroscopy and chemometrics, Spectrochim. Acta A Mol. Biomol. Spectrosc. 290 (2023). https://doi.org/10.1016/j.saa.2022.122284.

[113] H. Lin, Y. Zhang, Q. Wang, B. Li, P. Huang, Z. Wang, Estimation of the age of human bloodstains under the simulated indoor and outdoor crime scene conditions by ATR-FTIR spectroscopy, Sci. Rep. 7 (2017) 1–9. https://doi.org/10.1038/S41598-017-13725-1.

[114] N.F.N. Hassan, D.D. Sandran, M. Mohamad, Y. Zakaria, N.Z.M. Muslim, Estimation of the age of bloodstains on soil matrices by ATR-FTIR spectroscopy and chemometrics,

International Journal of Innovative Technology and Exploring Engineering 9 (2019) 4750–4755. https://doi.org/10.35940/IJITEE.A4454.119119.

[115] E.K. Hanson, J. Ballantyne, A blue spectral shift of the hemoglobin Soret band correlates with the age (time since deposition) of dried bloodstains, PLoS One 5 (2010) 12830. https://doi.org/10.1371/journal.pone.0012830.

[116] J. Workman, L. Weyer, Practical guide to interpretive near-infrared spectroscopy, Practical Guide to Interpretive Near-Infrared Spectroscopy (2007) 1–333. https://doi.org/10.1201/9781420018318.

[117] F. Shihana, D.M. Dissanayake, N.A. Buckley, A.H. Dawson, A simple quantitative bedside test to determine methemoglobin, Ann. Emerg. Med. 55 (2010) 184–189. https://doi.org/10.1016/J.ANNEMERGMED.2009.07.022.

[118] A. Hofmann, A. Simon, T. Grkovic, M. Jones, UV-Vis spectroscopy, in: A. Hofmann, A. Simon, T. Grkovic, M. Jones (Eds.), Methods of Molecular Analysis in the Life Sciences, Cambridge University Press, Cambridge, 2014: pp. 15–37. https://doi.org/10.1017/CBO9781107045224.

[119] Å. Rinnan, F. van den Berg, S.B. Engelsen, Review of the most common pre-processing techniques for near-infrared spectra, TrAC - Trends in Analytical Chemistry 28 (2009) 1201–1222. https://doi.org/10.1016/j.trac.2009.07.007.

[120] R.J. Barnes, M.S. Dhanoa, S.J. Lister, Standard normal variate transformation and de-trending of near-infrared diffuse reflectance spectra, Appl. Spectrosc. 43 (1989) 772–777. https://doi.org/10.1366/0003702894202201.

[121] B. Li, P. Beveridge, W.T. O'Hare, M. Islam, The estimation of the age of a blood stain using reflectance spectroscopy with a microspectrophotometer, spectral pre-processing and linear discriminant analysis, Forensic Sci. Int. 212 (2011) 198–204. https://doi.org/10.1016/J.FORSCIINT.2011.05.031.

[122] A.A. Gowen, G. Downey, C. Esquerre, C.P. O'Donnell, Preventing over-fitting in PLS calibration models of near-infrared (NIR) spectroscopy data using regression coefficients, J. Chemom. 25 (2011) 375–381. https://doi.org/10.1002/cem.1349.

[123] A.M. Tarone, D.R. Foran, Generalized additive models and Lucilia sericata growth: Assessing confidence intervals and error rates in forensic entomology, in: J. Forensic Sci., 2008. https://doi.org/10.1111/j.1556-4029.2008.00744.x.

[124] E. Giles, L.L. Klepinger, Confidence intervals for estimates based on linear regression in forensic anthropology, J. Forensic Sci. 33 (1988) 1218–1222. https://doi.org/10.1520/jfs12555j.

[125] G.W. Beecham, B.S. Weir, Confidence interval of the likelihood ratio associated with mixed stain DNA evidence, J. Forensic Sci. 56 (2011) 166–171. https://doi.org/10.1111/j.1556-4029.2010.01600.x.

[126] R. Chakraborty, M.R. Srinivasan, S.P. Daiger, Evaluation of standard error and confidence interval of estimated multilocus genotype probabilities, and their implications in DNA forensics, Am. J. Hum. Genet. 52 (1993) 60–70.

[127] M. Hubig, H. Muggenthaler, S. Schenkl, G. Mall, Temperature-based death time estimation in near equilibrium: Asymptotic confidence interval estimation, Forensic Sci. Int. 290 (2018). https://doi.org/10.1016/j.forsciint.2018.07.010.

[128] M. Hubig, H. Muggenthaler, G. Mall, Confidence intervals in temperature-based death time determination, Leg. Med. 17 (2015) 48–51. https://doi.org/10.1016/j.legalmed.2014.08.002.

[129] L. Valderrama, P. Valderrama, Nondestructive identification of blue pen inks for documentoscopy purpose using iPhone and digital image analysis including an approach for interval confidence estimation in PLS-DA models validation, Chemometrics and Intelligent Laboratory Systems 156 (2016) 188–195. https://doi.org/10.1016/J.CHEMOLAB.2016.06.009.

[130] M. Forina, S. Lanteri, M. Casale, Multivariate calibration, J. Chromatogr. A 1158 (2007). https://doi.org/10.1016/j.chroma.2007.03.082.

[131] P. Oliveri, C. Malegori, R. Simonetti, M. Casale, The impact of signal pre-processing on the final interpretation of analytical outcomes – A tutorial, Anal. Chim. Acta 1058 (2019) 9–17. https://doi.org/10.1016/J.ACA.2018.10.055.

[132] A. Savitzky, M.J.E. Golay, Smoothing and differentiation of data by simplified least squares procedures, Anal. Chem. 36 (1964) 1627–1639. https://doi.org/10.1021/ac60214a047.

[133] Eigenvector Research, Classcenter, Eigenvector Research Documentation Wiki (2013).

[134] P. Oliveri, C. Malegori, M. Casale, Chemometrics: multivariate analysis of chemical data, in: Chemical Analysis of Food: Techniques and Applications, Second Edition, 2020: pp. 33–76. https://doi.org/10.1016/B978-0-12-813266-1.00002-4.

[135] S. Wold, A. Ruhe, H. Wold, W.J. Dunn, III, The collinearity problem in linear regression. The partial least squares (PLS) approach to generalized inverses, SIAM Journal on Scientific and Statistical Computing 5 (1984) 735–743. https://doi.org/10.1137/0905052.

[136] Eigenvector Research, Advanced preprocessing: sample normalization, Eigenvector Research Documentation Wiki (2021). https://www.eigenvectordocs.com/index.php?title=Advanced_Preprocessing:_Sample_Normalization (accessed December 13, 2025).

[137] H. van der Voet, Comparing the predictive accuracy of models using a simple randomization test, Chemometrics and Intelligent Laboratory Systems 25 (1994) 313–323. https://doi.org/10.1016/0169-7439(94)85050-X.

[138] Eigenvector Research, Tools: permutation test, Eigenvector Research Documentation Wiki (2014). https://www.eigenvectordocs.com/index.php?title=Tools:_Permutation_Test (accessed December 13, 2025).

[139] F. Castanedo, A review of data fusion techniques, The Scientific World Journal 2013 (2013) 704504. https://doi.org/10.1155/2013/704504.

[140] G.J. Edelman, M. Roos, A. Bolck, M.C. Aalders, Practical implementation of blood stain age estimation using spectroscopy, IEEE JOURNAL OF SELECTED TOPICS IN QUANTUM ELECTRONICS 22 (n.d.). https://doi.org/10.1109/JSTQE.2016.2536655.

[141] M. Mengual-Pujante, A.J. Perán, A. Ortiz, M.D. Pérez-Cárceles, Estimation of human bloodstains time since deposition using ATR-FTIR spectroscopy and chemometrics in simulated crime conditions, Chemometrics and Intelligent Laboratory Systems 251 (2024) 105172. https://doi.org/10.1016/J.CHEMOLAB.2024.105172.

[142] R. Gautam, D. Peoples, K. Jansen, M. O'Connor, G. Thomas, S. Vanga, I.J. Pence, A. Mahadevan-Jansen, Feature selection and rapid characterization of bloodstains on different substrates, Appl. Spectrosc. 74 (2020) 1238–1251. https://doi.org/10.1177/0003702820937776.

[143] K. Rampete, C.I. Elliott, T. Stotesbury, Monitoring the solid-state VIS profiles of degrading bloodstains, Forensic Chemistry 35 (2023) 100507. https://doi.org/10.1016/J.FORC.2023.100507.

[144] H. Sun, Y. Meng, P. Zhang, Y. Li, N. Li, C. Li, Z. Guo, Non-invasive prediction of bloodstain age using the principal component and a back propagation artificial neural network, Laser Phys. Lett. 14 (2017). https://doi.org/10.1088/1612-202X/AA7C48.

[145] R. Leardi, Experimental design in chemistry: A tutorial, Anal. Chim. Acta 652 (2009) 161–172. https://doi.org/10.1016/J.ACA.2009.06.015.

[146] J. Jansen, J. Engel, ASCA: The implementation of design of experiments into multivariate modelling in chemometrics, Comprehensive Analytical Chemistry 82 (2018) 301–335. https://doi.org/10.1016/bs.coac.2018.08.007.

[147] C. Chatfield, A.J. Collins, The Multivariate analysis of variance, in: C. Chatfield, M. Tanner, J. Zidek (Eds.), Introduction to Multivariate Analysis, Chapman & Hall/CRC, 1981: pp. 140–160. https://doi.org/10.2307/3616628.

[148] J. Engel, K.J. Houthuijs, V. Vasiliou, G. Charkoftaki, Regularized multivariate analysis of variance, Comprehensive Chemometrics: Chemical and Biochemical Data Analysis, Second Edition: Four Volume Set 1 (2020) 479–494. https://doi.org/10.1016/B978-0-12-409547-2.14577-9.

[149] L. Sthle, S. Wold, Multivariate analysis of variance (MANOVA), Chemometrics and Intelligent Laboratory Systems 9 (1990) 127–141. https://doi.org/10.1016/0169-7439(90)80094-M.

[150] C. Bertinetto, J. Engel, J. Jansen, ANOVA simultaneous component analysis: A tutorial review, Anal. Chim. Acta X 6 (2020) 100061. https://doi.org/10.1016/J.ACAX.2020.100061.

[151] P. Firmani, R. Vitale, C. Ruckebusch, F. Marini, ANOVA-simultaneous component analysis modelling of low-level-fused spectroscopic data: A food chemistry case-study, Anal. Chim. Acta 1125 (2020) 308–314. https://doi.org/10.1016/J.ACA.2020.05.059.

[152] M. Ryckewaert, N. Gorretta, F. Henriot, F. Marini, J.M. Roger, Reduction of repeatability error for analysis of variance-simultaneous component analysis (REP-ASCA): Application to NIR spectroscopy on coffee sample, Anal. Chim. Acta 1101 (2020) 23–31. https://doi.org/10.1016/J.ACA.2019.12.024.

[153] C. Buvé, W. Saeys, M.A. Rasmussen, B. Neckebroeck, M. Hendrickx, T. Grauwet, A. Van Loey, Application of multivariate data analysis for food quality investigations: An example-based review, Food Research International 151 (2022) 110878. https://doi.org/10.1016/J.FOODRES.2021.110878.

[154] C.G. Bertinetto, R. Spijkerman, L. Hesselink, G.H. Tinnevelt, C.C.W.G. Bongers, G.J. Postma, M.T.E. Hopman, L. Koenderman, J.J. Jansen, Comprehensive multivariate evaluation of the effects on cell phenotypes in multicolor flow cytometry data using ANOVA simultaneous component analysis, J. Chemom. 37 (2023) e3402. https://doi.org/10.1002/CEM.3402.

[155] Y. Sefid-Sefidehkhan, A. Jouyban, M. Khoshkam, M. Amiri, E. Rahimpour, Application of ASCA as a multivariate statistical tool for identification of critical parameters for spectroscopic determination of dexamethasone, Iranian Journal of Chemistry and Chemical Engineering 42 (2023) 2175–2186. https://doi.org/10.30492/IJCCE.2022.560104.5515.

[156] A. Rust, F. Marini, M. Allsopp, P.J. Williams, M. Manley, Application of ANOVA-simultaneous component analysis to quantify and characterise effects of age, temperature, syrup adulteration and irradiation on near-infrared (NIR) spectral data of honey, Spectrochim. Acta A Mol. Biomol. Spectrosc. 253 (2021) 119546. https://doi.org/10.1016/J.SAA.2021.119546.

[157] K.C. Doty, C.K. Muro, I.K. Lednev, Predicting the time of the crime: Bloodstain aging estimation for up to two years, Forensic Chemistry 5 (2017) 1–7. https://doi.org/10.1016/J.FORC.2017.05.002.

[158] P. Lemler, W.R. Premasiri, A. DelMonaco, L.D. Ziegler, NIR Raman spectra of whole human blood: Effects of laser-induced and in vitro hemoglobin denaturation, Anal. Bioanal. Chem. 406 (2014) 193–200. https://doi.org/10.1007/S00216-013-7427-7.

[159] N.M. Htun, Y.C. Chen, B. Lim, T. Schiller, G.J. Maghzal, A.L. Huang, K.D. Elgass, J. Rivera, H.G. Schneider, B.R. Wood, R. Stocker, K. Peter, Near-infrared autofluorescence induced by intraplaque hemorrhage and heme degradation as marker for high-risk atherosclerotic plaques, Nat. Commun. 8 (2017). https://doi.org/10.1038/S41467-017-00138-X.

[160] E. Nagababu, J.M. Rifkind, Heme degradation during autoxidation of oxyhemoglobin, Biochem. Biophys. Res. Commun. 273 (2000) 839–845. https://doi.org/10.1006/bbrc.2000.3025.

[161] U. Neugebauer, A. März, T. Henkel, M. Schmitt, J. Popp, Spectroscopic detection and quantification of heme and heme degradation products, Anal. Bioanal. Chem. 404 (2012) 2819–2829. https://doi.org/10.1007/S00216-012-6288-9.

[162] R. Dasgupta, S. Ahlawat, R.S. Verma, A. Uppal, P.K. Gupta, Hemoglobin degradation in human erythrocytes with long-duration near-infrared laser exposure in Raman optical tweezers, J. Biomed. Opt. 15 (2010) 055009. https://doi.org/10.1117/1.3497048.

[163] B.R. Wood, L. Hammer, L. Davis, D. McNaughton, Raman microspectroscopy and imaging provides insights into heme aggregation and denaturation within human erythrocytes, J. Biomed. Opt. 10 (2005) 014005. https://doi.org/10.1117/1.1854678.

[164] P.H.C. Eilers, H.F.M. Boelens, Baseline correction with asymmetric least squares smoothing, Leiden, 2005. https://www.researchgate.net/publication/228961729_Baseline_Correction_with_Asymmetric_Least_Squares_Smoothing (accessed May 28, 2025).

[165] H. Parastar, P. Weller, Feature selection and extraction strategies for non-targeted analysis using GC-MS and GC-IMS: A tutorial, Anal. Chim. Acta 1343 (2025) 343635. https://doi.org/10.1016/J.ACA.2025.343635.

[166] S. Sharifzadeh, A. Ghodsi, L.H. Clemmensen, B.K. Ersbøll, Sparse supervised principal component analysis (SSPCA) for dimension reduction and variable selection, Eng. Appl. Artif. Intell. 65 (2017) 168–177. https://doi.org/10.1016/J.ENGAPPAI.2017.07.004.

[167] B. Ghojogh, M.N. Samad, S.A. Mashhadi, T. Kapoor, W. Ali, F. Karray, M. Crowley, Feature Selection and Feature Extraction in Pattern Analysis: A Literature Review, (2019). https://doi.org/10.48550/arXiv.1905.02845.

[168] L.C. Lee, C.Y. Liong, A.A. Jemain, Partial least squares-discriminant analysis (PLS-DA) for classification of high-dimensional (HD) data: a review of contemporary practice strategies and knowledge gaps, Analyst 143 (2018) 3526–3539. https://doi.org/10.1039/C8AN00599K.

[169] X.S. Gan, J.S. Duanmu, J.F. Wang, W. Cong, Anomaly intrusion detection based on PLS feature extraction and core vector machine, Knowl. Based. Syst. 40 (2013) 1–6. https://doi.org/10.1016/J.KNOSYS.2012.09.004.

[170] T. Pham-Gia, Exact distribution of the generalized Wilks's statistic and applications, J. Multivar. Anal. 99 (2008) 1698–1716. https://doi.org/10.1016/J.JMVA.2008.01.021.

[171] S.S. Wilks, Certain generalizations in the analysis of variance, Biometrika 24 (1932) 471. https://doi.org/10.2307/2331979.

[172] R.A. Armstrong, When to use the Bonferroni correction, Ophthalmic Physiol. Opt. 34 (2014) 502–508. https://doi.org/10.1111/OPO.12131.

[173] S. Willis, ENFSI guideline for evaluative reporting in forensic science - Strengthening the evaluation of forensic results across Europe (STEOFRAE), 2015.

[174] A. Weber, A. Wójtowicz, I.K. Lednev, Post deposition aging of bloodstains probed by steady-state fluorescence spectroscopy, J. Photochem. Photobiol. B 221 (2021) 112251. https://doi.org/10.1016/j.jphotobiol.2021.112251.

[175] M. Rubio-Salcedo, S. Merinero, I. Martínez, Tree species and microhabitat influence the population structure of the epiphytic lichen Lobaria pulmonaria, Fungal Ecol. 18 (2015). https://doi.org/10.1016/j.funeco.2015.08.002.

[176] G. Palmer, P.J. Platts, T. Brereton, J.W. Chapman, C. Dytham, R. Fox, J.W. Pearce-Higgins, D.B. Roy, J.K. Hill, C.D. Thomas, Climate change, climatic variation and extreme biological responses, Philosophical Transactions of the Royal Society B: Biological Sciences 372 (2017). https://doi.org/10.1098/RSTB.2016.0144.

[177] C.F. Dormann, M. Bobrowski, D.M. Dehling, D.J. Harris, F. Hartig, H. Lischke, M.D. Moretti, J. Pagel, S. Pinkert, M. Schleuning, S.I. Schmidt, C.S. Sheppard, M.J. Steinbauer, D. Zeuss, C. Kraan, Biotic interactions in species distribution modelling: 10 questions to guide interpretation and avoid false conclusions, Global Ecology and Biogeography 27 (2018) 1004–1016. https://doi.org/10.1111/GEB.12759.

[178] P. De Frenne, F. Zellweger, F. Rodríguez-Sánchez, B.R. Scheffers, K. Hylander, M. Luoto, M. Vellend, K. Verheyen, J. Lenoir, Global buffering of temperatures under forest canopies, Nat. Ecol. Evol. 3 (2019). https://doi.org/10.1038/s41559-019-0842-1.

[179] L. Di Nuzzo, R. Benesperi, J. Nascimbene, A. Papini, P. Malaspina, G. Incerti, P. Giordani, Little time left. Microrefuges may fail in mitigating the effects of climate change on epiphytic lichens, Science of the Total Environment 825 (2022). https://doi.org/10.1016/j.scitotenv.2022.153943.

[180] S. Pincebourde, C.C. Murdock, M. Vickers, M.W. Sears, Fine-scale microclimatic variation can shape the responses of organisms to global change in both natural and urban environments, Integr. Comp. Biol. 56 (2016) 45–61. https://doi.org/10.1093/ICB/ICW016.

[181] V. Vandvik, O. Skarpaas, K. Klanderud, R.J. Telford, A.H. Halbritter, D.E. Goldberg, Biotic rescaling reveals importance of species interactions for variation in biodiversity responses to climate change, Proc. Natl. Acad. Sci. U. S. A. 117 (2020) 22858–22865. https://doi.org/10.1073/PNAS.2003377117.

[182] M.C.F. Proctor, Desiccation tolerance in some British ferns, Fern Gazette 18 (2009).

[183] M.C.F. Proctor, Z. Tuba, Poikilohydry and homoihydry: Antithesis or spectrum of possibilities?, New Phytologist 156 (2002). https://doi.org/10.1046/j.1469-8137.2002.00526.x.

[184] P.W. Rundel, The role of morphology in the water relations of desert lichens, Journ. Hattori Bot. Lab. No 53 (1982) 315–320.

[185] T.H.I. Nash, T. Friedl, B. Büdel, R. Honegger, C. Scheidegger, S. Scherrer, J.A. Elix, E. Stocker-Wörgötter, R.P. Beckett, I. Kranner, F. V. Minibayeva, T.G.A. Green, O.L. Lange, K. Palmqvist, L. Dahlman, A. Jonsson, D. Fahselt, M.R.D. Seaward, D.J. Galloway, A. Tehler, M. Wedin, A. Hager, Introduction, in: T.H.I. Nash (Ed.), LichenBiology, 2nd ed., Cambridge University Press, Cambridge, 2008.

[186] Y. Gauslaa, Rain, dew, and humid air as drivers of morphology, function and spatial distribution in epiphytic lichens, The Lichenologist 46 (2014) 1–16. https://doi.org/10.1017/S0024282913000753.

[187] L. Song, W.Y. Liu, Potential impacts of global changes on epiphytic bryophytes in subtropical montane moist evergreen broad-leaved forests, SW China, in: Treetops at Risk: Challenges of Global Canopy Ecology and Conservation, 2013. https://doi.org/10.1007/978-1-4614-7161-5_16.

[188] P. Porada, J.T. Van Stan, A. Kleidon, Significant contribution of non-vascular vegetation to global rainfall interception, Nature Geoscience 2018 11:8 11 (2018) 563–567. https://doi.org/10.1038/s41561-018-0176-7.

[189] K. Sales, L. Kerr, J. Gardner, Factors influencing epiphytic moss and lichen distribution within Killarney National Park, Bioscience Horizons: The International Journal of Student Research 9 (2016). https://doi.org/10.1093/BIOHORIZONS/HZW008.

[190] J.H.D. Wolf, Diversity patterns and biomass of epiphytic bryophytes and lichens along an altitudinal gradient in the Northern Andes, Annals of the Missouri Botanical Garden 80 (1993). https://doi.org/10.2307/2399938.

[191] J.T. Van Stan, E. Gutmann, J. Friesen, Precipitation partitioning by vegetation: A global synthesis, Precipitation Partitioning by Vegetation: A Global Synthesis (2020) 1–281. https://doi.org/10.1007/978-3-030-29702-2.

[192] F. Gasulla, P.G. De Nova, A. Esteban-Carrasco, J.M. Zapata, E. Barreno, A. Guéra, Dehydration rate and time of desiccation affect recovery of the lichenic algae Trebouxia erici: Alternative and classical protective mechanisms, Planta 231 (2009). https://doi.org/10.1007/s00425-009-1019-y.

[193] Y. Gu, T. Liu, G. Gao, G. Ren, Y. Ma, J. Chanussot, X. Jia, Multimodal hyperspectral remote sensing: an overview and perspective, Science China Information Sciences 64 (2021). https://doi.org/10.1007/s11432-020-3084-1.

[194] M. Gerhards, M. Schlerf, K. Mallick, T. Udelhoven, Challenges and future perspectives of multi-/Hyperspectral thermal infrared remote sensing for crop water-stress detection: A review, Remote Sens. (Basel). 11 (2019). https://doi.org/10.3390/rs11101240.

[195] M.L. Nordberg, A. Allard, A remote sensing methodology for monitoring lichen cover, Canadian Journal of Remote Sensing 28 (2002) 262–274. https://doi.org/10.5589/m02-026.

[196] M.L. Belov, A. Belov, V. Gorodnichev, S. Alkov, A. Shkarupilo, Evaluation of the hyperspectral monitoring method capabilities for forests areas, in: O.A. Romanovskii (Ed.), 29th International Symposium on Atmospheric and Ocean Optics: Atmospheric Physics, SPIE, 2023: p. 128. https://doi.org/10.1117/12.2690227.

[197] N. Kuusinen, J. Juola, B. Karki, S. Stenroos, M. Rautiainen, A spectral analysis of common boreal ground lichen species, Remote Sens. Environ. 247 (2020) 111955. https://doi.org/10.1016/j.rse.2020.111955.

[198] B. Weber, C. Olehowski, T. Knerr, J. Hill, K. Deutschewitz, D.C.J. Wessels, B. Eitel, B. Büdel, A new approach for mapping of Biological Soil Crusts in semidesert areas with hyperspectral imagery, Remote Sens. Environ. 112 (2008). https://doi.org/10.1016/j.rse.2007.09.014.

[199] I. Palmroos, V. Norros, S. Keski-Saari, J. Mäyrä, T. Tanhuanpää, S. Kivinen, J. Pykälä, P. Kullberg, T. Kumpula, P. Vihervaara, Remote sensing in mapping biodiversity – A case study of epiphytic lichen communities, For. Ecol. Manage. 538 (2023). https://doi.org/10.1016/j.foreco.2023.120993.

[200] C. Malegori, J. Muncan, E. Mustorgi, R. Tsenkova, P. Oliveri, Analysing the water spectral pattern by near-infrared spectroscopy and chemometrics as a dynamic multidimensional biomarker in preservation: rice germ storage monitoring, Spectrochim. Acta A Mol. Biomol. Spectrosc. 265 (2022). https://doi.org/10.1016/J.SAA.2021.120396.

[201] M. Barták, K.B. Mishra, M. Marečková, Spectral reflectance indices sense desiccation induced changes in the thalli of Antarctic lichen Dermatocarpon polyphyllizum, Czech Polar Rep. 8 (2018). https://doi.org/10.5817/CPR2018-2-21.

[202] M. Barták, K. Trnková, E.S. Hansen, J. Hazdrová, K. Skácelová, J. Hájek, M. Forbelská, Effect of dehydration on spectral reflectance and photosynthetic efficiency in Umbilicaria arctica and U. hyperborea, Biol. Plant. 59 (2015). https://doi.org/10.1007/s10535-015-0506-1.

[203] B. Miloš, H. Josef, M. Jana, S. Kateřina, K. Alica, Dehydration-induced changes in spectral reflectance indices and chlorophyll fluorescence of Antarctic lichens with different thallus color, and intrathalline photobiont, Acta Physiol. Plant. 40 (2018). https://doi.org/10.1007/s11738-018-2751-3.

[204] L. Granlund, S. Keski-Saari, T. Kumpula, E. Oksanen, M. Keinänen, Imaging lichen water content with visible to mid-wave infrared (400–5500 nm) spectroscopy, Remote Sens. Environ. 216 (2018) 301–310. https://doi.org/10.1016/j.rse.2018.06.041.

[205] P. Stefansson, T. Thiis, L.R. Gobakken, I. Burud, Hyperspectral NIR time series imaging used as a new method for estimating the moisture content dynamics of thermally modified Scots pine, Wood Mater. Sci. Eng. 16 (2021). https://doi.org/10.1080/17480272.2020.1772366.

[206] L.M. Kandpal, H. Lee, M.S. Kim, C. Mo, B.K. Cho, Hyperspectral reflectance imaging technique for visualization of moisture distribution in cooked chicken breast, Sensors (Switzerland) 13 (2013). https://doi.org/10.3390/s131013289.

[207] D. Wu, S. Wang, N. Wang, P. Nie, Y. He, D.W. Sun, J. Yao, Application of time series hyperspectral imaging (TS-HSI) for determining water distribution within beef and spectral kinetic analysis during dehydration, Food Bioproc. Tech. 6 (2013). https://doi.org/10.1007/s11947-012-0928-0.

[208] C. Malegori, P. Oliveri, E. Mustorgi, M.A. Boggiani, G. Pastorini, M. Casale, An in-depth study of cheese ripening by means of NIR hyperspectral imaging: Spatial mapping of dehydration, proteolysis and lipolysis, Food Chem. 343 (2021). https://doi.org/10.1016/j.foodchem.2020.128547.

[209] K. Yu, Y. Zhao, X. Li, Y. He, NIR hyperspectral imaging for mapping of moisture content distribution in tea buds during dehydration, International Agricultural Engineering Journal 24 (2015). https://doi.org/10.5772/intechopen.86095.

[210] X. Lin, D.-W. Sun, Investigation of moisture distribution of ginger slices and splits during hot-air drying and rehydration procedures by NIR hyperspectral imaging, in: 2020. https://doi.org/10.1117/12.2558213.

[211] K. Mägdefrau, Life-forms of Bryophytes, Bryophyte Ecology (1982) 45–58. https://doi.org/10.1007/978-94-009-5891-3_2.

[212] R.A. Armstrong, T. Bradwell, Growth of foliose lichens: A review, Symbiosis 53 (2011) 1–16. https://doi.org/10.1007/S13199-011-0108-4.

[213] R. Armstrong, T. Bradwell, Growth of crustose lichens: A review, Geografiska Annaler: Series A, Physical Geography 92 (2010) 3–17. https://doi.org/10.1111/J.1468-0459.2010.00374.X.

[214] G. Squeo, D. De Angelis, R. Leardi, C. Summo, F. Caponio, Background, applications and issues of the experimental designs for mixture in the food sector, Foods 10 (2021). https://doi.org/10.3390/foods10051128.

[215] P. Porada, P. Giordani, Bark water storage plays key role for growth of mediterranean epiphytic lichens, Frontiers in Forests and Global Change 4 (2021). https://doi.org/10.3389/ffgc.2021.668682.

[216] M. Lakatos, U. Rascher, B. Büdel, Functional characteristics of corticolous lichens in the understory of a tropical lowland rain forest, New Phytologist 172 (2006) 679–695. https://doi.org/10.1111/J.1469-8137.2006.01871.X.

[217] F. Valladares, Texture and hygroscopic features of the upper surface of the thallus in the lichen family umbilicariaceae, Ann. Bot. 73 (1994) 493–500. https://doi.org/10.1006/ANBO.1994.1061.

[218] J. Workman Jr., L. Weyer, Practical Guide and Spectral Atlas for Interpretive Near-Infrared Spectroscopy, Practical Guide and Spectral Atlas for Interpretive Near-Infrared Spectroscopy (2012). https://doi.org/10.1201/B11894.

[219] Y. Gauslaa, K.A. Solhaug, S. Longinotti, Functional traits prolonging photosynthetically active periods in epiphytic cephalolichens during desiccation, Environ. Exp. Bot. 141 (2017) 83–91. https://doi.org/10.1016/J.ENVEXPBOT.2017.07.005.

[220] T.J.K. Dilks, M.C.F. Proctor, Photosynthesis, respiration and water content in bryophytes, New Phytologist 82 (1979) 97–114. https://doi.org/10.1111/J.1469-8137.1979.TB07564.X.

[221] B.J. Crandall-Stotler, S.E. Bartholomew-Began, Morphology of Mosses (Phylum Bryophyta), (2007).

[222] M.O.. Hill, BRYOATT : attributes of British and Irish mosses, liverworts and hornworts, (2007) 88. https://www.researchgate.net/publication/240641510_BRYOATT_Attributes_of_British_and_Irish_Mosses_Liverworts_and_Hornworts_With_Information_on_Native_Status_Size_Life_Form_Life_History_Geography_and_Habitat (accessed September 28, 2024).

[223] M.C.F. Proctor, Z. Nagy, Z. Csintalan, Z. Takács, Water-content components in bryophytes: analysis of pressure-volume relationships, J. Exp. Bot. 49 (1998) 1845–1854. https://doi.org/10.1093/JXB/49.328.1845.

[224] M. Lakatos, Lichens and bryophytes: habitats and species, (2011) 65–87. https://doi.org/10.1007/978-3-642-19106-0_5.

[225] M.A. Bowker, S. Soliveres, F.T. Maestre, Competition increases with abiotic stress and regulates the diversity of biological soil crusts, Journal of Ecology 98 (2010) 551–560. https://doi.org/10.1111/J.1365-2745.2010.01647.X.

[226] S. Longinotti, K.A. Solhaug, Y. Gauslaa, Hydration traits in cephalolichen members of the epiphytic old forest genus Lobaria (s. lat.), The Lichenologist 49 (2017) 493–506. https://doi.org/10.1017/S0024282917000445.

[227] R. Rocha de Oliveira, C. Malegori, G. Sciutto, P. Oliveri, PoliBrush – A user-friendly software to aid multivariate image analysis dissemination, Chemometrics and Intelligent Laboratory Systems 240 (2023). https://doi.org/10.1016/j.chemolab.2023.104918.

[228] A.C. Olivieri, N.M. Faber, J. Ferré, R. Boqué, J.H. Kalivas, H. Mark, Uncertainty estimation and figures of merit for multivariate calibration: (IUPAC technical report), Pure and Applied Chemistry 78 (2006). https://doi.org/10.1351/pac200678030633.

[229] J.M. Amigo, H. Babamoradi, S. Elcoroaristizabal, Hyperspectral image analysis. A tutorial, Anal. Chim. Acta 896 (2015) 34–51. https://doi.org/10.1016/J.ACA.2015.09.030.

[230] Z. Shi, C.A. Anderson, Application of Monte Carlo simulation-based photon migration for enhanced understanding of near-infrared (NIR) diffuse reflectance. Part I: Depth of penetration in pharmaceutical materials, J. Pharm. Sci. 99 (2010) 2399–2412. https://doi.org/10.1002/JPS.22013.

[231] L. Lin, H. He, R. Xue, Y. Zhang, Z. Wang, S. Nie, J. Ye, Direct and quantitative assessments of near-infrared light attenuation and spectroscopic detection depth in biological tissues using surface-enhanced Raman scattering, Med-X 2023 1:1 1 (2023) 9-. https://doi.org/10.1007/S44258-023-00010-2.

[232] L.O. Svaasand, R. Ellingsen, Optical properties of human brain, Photochem. Photobiol. 38 (1983) 293–299. https://doi.org/10.1111/J.1751-1097.1983.TB02674.X.

[233] F.B. Haeussinger, S. Heinzel, T. Hahn, M. Schecklmann, A.C. Ehlis, A.J. Fallgatter, Simulation of near-infrared light absorption considering individual head and prefrontal cortex

anatomy: Implications for optical neuroimaging, PLoS One 6 (2011) e26377. https://doi.org/10.1371/JOURNAL.PONE.0026377.

[234] J. Yadav, A. Rani, V. Singh, B.M. Murari, Prospects and limitations of non-invasive blood glucose monitoring using near-infrared spectroscopy, Biomed. Signal Process. Control 18 (2015) 214–227. https://doi.org/10.1016/J.BSPC.2015.01.005.

[235] M. V. Padalkar, N. Pleshko, Wavelength-dependent penetration depth of near infrared radiation into cartilage, Analyst 140 (2015) 2093–2100. https://doi.org/10.1039/C4AN01987C.

[236] F.C. Clarke, S. V. Hammond, R.D. Jee, A.C. Moffat, Determination of the information depth and sample size for the analysis of pharmaceutical materials using reflectance near-infrared microscopy, Appl. Spectrosc. 56 (2002) 1475–1483. https://doi.org/10.1366/00037020260377797.

[237] C.S.C. Yang, F. Jin, S.R. Swaminathan, S. Patel, E.D. Ramer, S.B. Trivedi, E.E. Brown, U. Hommerich, A.C. Samuels, Comprehensive study of solid pharmaceutical tablets in visible, near infrared (NIR), and longwave infrared (LWIR) spectral regions using a rapid simultaneous ultraviolet/visible/NIR (UVN) + LWIR laser-induced breakdown spectroscopy linear arrays detection system and a fast acousto-optic tunable filter NIR spectrometer, Opt. Express 25 (2017) 26885. https://doi.org/10.1364/OE.25.026885.

[238] M. Longoni, B. Genova, A. Marzanni, D. Melfi, C. Beccaria, S. Bruni, FT-NIR spectroscopy for the non-invasive study of binders and multi-layered structures in ancient paintings: artworks of the lombard renaissance as case studies, Sensors 22 (2022). https://doi.org/10.3390/S22052052.

[239] C. Cucci, J.K. Delaney, M. Picollo, Reflectance hyperspectral imaging for investigation of works of art: old master paintings and illuminated manuscripts, Acc. Chem. Res. 49 (2016) 2070–2079. https://doi.org/10.1021/ACS.ACCOUNTS.6B00048.

[240] E. Catelli, Z. Li, G. Sciutto, P. Oliveri, S. Prati, M. Occhipinti, A. Tocchio, R. Alberti, T. Frizzi, C. Malegori, R. Mazzeo, Towards the non-destructive analysis of multilayered samples: A novel XRF-VNIR-SWIR hyperspectral imaging system combined with multiblock data processing, Anal. Chim. Acta 1239 (2023) 340710. https://doi.org/10.1016/J.ACA.2022.340710.

[241] M. Vega-Castellote, M.T. Sánchez, J.P. Wold, N.K. Afseth, D. Pérez-Marín, Near infrared light penetration in watermelon related to internal quality evaluation, Postharvest Biol. Technol. 204 (2023) 112477. https://doi.org/10.1016/J.POSTHARVBIO.2023.112477.

[242] G. Staufenberg, N. Graupner, J. Müssig, C. V Greensill, K.B. Walsh, A remote acceptance probe and illumination configuration for spectralassessment of internal attributes of intact fruit, Meas. Sci. Technol. 11 (2000) 1674. https://doi.org/10.1088/0957-0233/11/12/304.

[243] A. Laborde, B. Jaillais, R. Bendoula, J.M. Roger, D. Jouan-Rimbaud Bouveresse, L. Eveleigh, D. Bertrand, A. Boulanger, C.B.Y. Cordella, A partial least squares-based approach to assess the light penetration depth in wheat flour by near infrared hyperspectral imaging, J. Near Infrared Spectrosc. 28 (2020) 25–36. https://doi.org/10.1177/0967033519891594.

[244] M. Almeida, K.E. Torrance, A.K. Datta, Measurement of optical properties of foods in near- and mid-infrared radiation, Int. J. Food Prop. 9 (2006) 651–664. https://doi.org/10.1080/10942910600853667.

[245] M. Dagerskog, L. Österström, Infra-red radiation for food processing, in: Food Processing Operations and Modeling, CRC Press, 2008. https://doi.org/10.1201/9781420055542.ch5.

[246] A.L. Pomerantsev, O.Y. Rodionova, A.N. Skvortsov, Diffuse reflectance spectroscopy of hidden objects. Part II: Recovery of a target spectrum, Appl. Spectrosc. 71 (2017) 1773–1784. https://doi.org/10.1177/0003702817695288.

[247] A.L. Pomerantsev, O.Y. Rodionova, A.N. Skvortsov, Diffuse reflectance spectroscopy of hidden objects, Part I: Interpretation of the reflection–absorption-scattering fractions in near-infrared (NIR) spectra of polyethylene films, Appl. Spectrosc. 71 (2017) 1760–1772. https://doi.org/10.1177/0003702817694182.

[248] J. Workman, L. Weyer, Practical guide to interpretive near-infrared spectroscopy, Practical Guide to Interpretive Near-Infrared Spectroscopy (2007) 1–333. https://doi.org/10.1201/9781420018318.

[249] S. Muroga, Y. Hikima, M. Ohshima, Near-Infrared spectroscopic evaluation of the water content of molded polylactide under the effect of crystallization, Appl. Spectrosc. 71 (2017) 1300–1309. https://doi.org/10.1177/0003702816681011.

[250] S. Gariglio, R.R. de Oliveira, G. Canali, C. Malegori, P. Malaspina, M. Casale, P. Oliveri, P. Giordani, NIR hyperspectral imaging combined with chemometrics for mapping water patterns during dehydration of nonvascular epiphytic communities, J. Anal. Test. (2025) 1–17. https://doi.org/10.1007/S41664-025-00384-9.

[251] B.M. Zacour, B. Igne, J.K. Drennen, C.A. Anderson, Efficient near-infrared spectroscopic calibration methods for pharmaceutical blend monitoring, J. Pharm. Innov. 6 (2011) 10–23. https://doi.org/10.1007/S12247-011-9096-4.

[252] L.C. Pacheco-Londoño, J.A. Aparicio-Bolaño, N.J. Galán-Freyle, A.D. Román-Ospino, J.L. Ruiz-Caballero, S.P. Hernández-Rivera, Classical least squares-assisted mid-infrared (MIR) laser spectroscopy detection of high explosives on fabrics, Appl. Spectrosc. 73 (2019) 17–29. https://doi.org/10.1177/0003702818780414.

[253] G.H. Golub, C.F. Van Loan, Matrix computations, Matrix Computations (2022). https://doi.org/10.56021/9781421407944.

[254] J.C.A. Barata, M.S. Hussein, The Moore-Penrose pseudoinverse: A tutorial review of the theory, Brazilian Journal of Physics 42 (2012) 146–165. https://doi.org/10.1007/S13538-011-0052-Z.

[255] Ian Goodfellow, Aaron Courville, Yoshua Bengio, Deep learning, The MIT Press, Cambridge, 2016. http://www.deeplearningbook.org (accessed September 26, 2025).

[256] J. Schmidhuber, Deep learning in neural networks: An overview, Neural Networks 61 (2015) 85–117. https://doi.org/10.1016/J.NEUNET.2014.09.003.

[257] J. Wahl, M. Sjödahl, K. Ramser, Single-Step preprocessing of Raman spectra using convolutional neural networks, Appl. Spectrosc. 74 (2020) 427–438. https://doi.org/10.1177/0003702819888949.

[258] J. Acquarelli, T. van Laarhoven, J. Gerretzen, T.N. Tran, L.M.C. Buydens, E. Marchiori, Convolutional neural networks for vibrational spectroscopic data analysis, Anal. Chim. Acta 954 (2017) 22–31. https://doi.org/10.1016/J.ACA.2016.12.010.

[259] V. Nair, G.E. Hinton, Rectified linear units improve restricted boltzmann machines, in: International Conference on Machine Learning, 2010: pp. 807–814. https://doi.org/10.5555/3104322.3104425.

[260] C. Blake, C. Ford, B. Manner, B. Webb, Improving the Adam optimizer using time delays, Nonlinearity 38 (2025). https://doi.org/10.1088/1361-6544/adeb39.

CONFERENCES, COURSES AND COLLABORATIONS LISTS

CONFERENCES

Oral contributions as an invited speaker at national and international conferences

- Konferencja Chemometria i Metrologia w Analityce (Chemometrics and Metrology in Analytical Chemistry Conference), 6-8/03/2024, Poznan (Poland). “Dating of forensic bloodstains through spectroscopic techniques – a critical comparison towards a multiplatform approach.”

Oral and poster contributions at national and international conferences

Note: only conference where the candidate was the presenting author are reported

- International conference Colloquium Chemiometricum Mediterraneum (CCM2025), 8-12/09/2025, Porquerolle (France). “Dealing with non-linearity in the study of near infrared light penetration through matter” - **oral presentation**
- National conference of the Italian society of Analytical Forensic Chemistry (CAF2025), 26-27/06/2025, Turin (Itay). “Applicazione di RMANOVA su dati spettroscopici per valutare l’effetto delle condizioni ambientali e del substrato di deposizione sull’invecchiamento di macchie di sangue.” (translated title: Application of RMANOVA on spectroscopic data to evaluate the effect of environmental conditions and deposition substrate on forensic bloodstains ageing”) – **oral presentation**
- 22nd International Conference on Near Infrared Spectroscopy (NIR2025), 8-13/06/2025, Rome (Italy). “Investigating the penetration depth of NIR radiation through hyperspectral imaging and chemometrics” – **poster presentation**
- National conference of the Italian Chemical Society (SCI2024), 26-30/08/2024, Milan (Italy). “The effect of environmental conditions and deposition substrate on bloodstains ageing: a spectroscopic approach to target a forensic analytical problem” – **poster presentation**
- International conference on Spectral Imaging (IASIM2024), 6-10/07/2024, Bilbao (Spain). “Mapping water patterns during dehydration of nonvascular epiphytic communities through NIR hyperspectral imaging” – **oral presentation**
- National Italian conference on Near Infrared Spectroscopy (NIR Italia), 26-28/06/2024, Turin (Italy). “Le potenzialità della spettroscopia NIR in chimica

forense: la datazione delle macchie di sangue" (Translated title: "The power of NIR spectroscopy in forensic chemistry: bloodstains dating") – **oral presentation**

- Italian-French days 2024 (Giornate Italofrancesi della Chimica 2024), 04-05/04/2024, Turin (Italy). "Exploiting spectroscopy and chemometrics for bloodstain dating in forensic chemistry." – **oral presentation**
- Third European Aquaphotomics Conference (3EAC), 2-4/09/2023, Rome (Italy). "NIR hyperspectral imaging for monitoring water patterns during dehydration of nonvascular epiphytic communities: the power of water absorption bands." – **oral presentation**
- 21st International Conference on Near Infrared Spectroscopy (NIR2023), 20-24/08/2023, Innsbruck (Austria). "Bloodstains dating by means of NIR and UV-Vis spectroscopy – a critical comparison." – **flash oral + poster presentation**

COURSES ATTENDED

- PrusaSlicer masterclass – beginner to advanced, held online by "Prusa Academy" – October 2025
- "Machine learning with Python" held by prof. Sergey Kucheryavskiy at Aalborg University (Esbjerg) – October 2024
- "Hyperspectral Image Analysis" online course held online by Eigenvector Research Incorporated – May 2024
- "School of Aquaphotomics" organised by the Italian Society or NIR Spectroscopy (SISNIR) in the context of the 3rd European Aquaphotomics Conference – 1st-2nd September 2023, Rome (Italy)
- "School of Chemometrics – Design of Experiment" organised by the Analytical Chemistry and Chemometrics group at Università degli Studi di Genova – 15-19th May 2023, Genoa (Italy).
- "School of Chemometrics – Multivariate analysis" organised by the Analytical Chemistry and Chemometrics group at Università degli Studi di Genova – 16-20th January 2023, Genoa (Italy).

COLLABORATIONS

- Department of Chemistry, University of Turin, Via Pietro Giuria 7, Torino (Italy)
- Institute of Forensic Research in Krakow, Westerplatte 9, Krakow (Poland)
- Department of Chemistry and Bioscience, Aalborg University, Niels Bohrs Vej 8, Esbjerg (Denmark)

- School of Biosystems and Engineering, University College Dublin, Belfield, Dublin (Ireland)

PUBLICATION LIST

IN PEER-REVIEWED JOURNALS

Related to the PhD topic

1. **Gariglio, S.**, Malegori, C., Menżyk, A., Zadora, G., Vincenti, M., Casale, M., & Oliveri, P. (2024). Determination of time since deposition of bloodstains through NIR and UV–Vis spectroscopy – A critical comparison. *Talanta*, *278*, 126444. https://doi.org/10.1016/J.TALANTA.2024.126444
2. **Gariglio, S.**, de Oliveira, R. R., Canali, G., Malegori, C., Malaspina, P., Casale, M., Oliveri, P., & Giordani, P. (2025). NIR Hyperspectral Imaging Combined with Chemometrics for Mapping Water Patterns During Dehydration of Nonvascular Epiphytic Communities. *Journal of Analysis and Testing*, 1–17. https://doi.org/10.1007/S41664-025-00384-9
3. Barbera, M., **Gariglio, S.**, Malegori, C., Oliveri, P., Saiano, F., Scalenghe, R., & Piazzese, D. (2025). Multivariate Strategy for Understanding Soil Features from Rare-Earth Element Profiles: A Focus on Data Normalization. *ACS Measurement Science Au*, *5*(2), 189–198. https://doi.org/10.1021/ACSMEASURESCIAU.4C00084
4. Canali, G., Hurtado, P., **Gariglio, S.**, de Oliveira, R. R., Malegori, C., & Giordani, P. (2025). How Thermal Patterns Change During Dehydration in Non-Vascular Epiphytic Communities. *Ecology and Evolution*, *15*(7). https://doi.org/10.1002/ECE3.71756
5. **Gariglio, S.**, Malegori, C., Menżyk, A., Zadora, G., Vincenti, M., Casale, M., & Oliveri, P. (2026). Effect of environmental conditions and deposition substrate on bloodstain ageing studied by means of Raman and near infrared spectroscopies coupled with chemometrics. *Microchemical Journal*, *220*, 116381. https://doi.org/10.1016/J.MICROC.2025.116381
6. Li, Z., Scagliarini, C., Mazzoleni, A., **Gariglio, S.**, Catelli, E., Malegori, C., Prati, S., Alladio, E., Sciutto, G., & Oliveri, P. (2026). Exploiting the penetration depth of XRF and NIR radiation: from 2D to 3D spectral imaging, *TrAC Trends in Analytical Chemistry*, *197*, 118693. https://doi.org/10.1016/J.TRAC.2026.118693

Unrelated to the PhD topic

7. Manetti, F., David, M. C., **Gariglio, S.**, Consalvo, F., Padovano, M., Scopetti, M., Grande, A., & Santurro, A. (2023). Atypical Fentanyl Transdermal Patch Consumption and Fatalities: Case Report and Literature Review. *Toxics*, *11*(1). https://doi.org/10.3390/toxics11010046

8. Fiore, M., Minni, A., Cavalcanti, L., Raponi, G., Puggioni, G., Mattia, A., **Gariglio, S.**, Colizza, A., Meliante, P. G., Zoccali, F., Tarani, L., Barbato, C., Lucarelli, M., Ceci, F. M., Francati, S., Ferraguti, G., Ceccanti, M., & Petrella, C. (2023). The Impact of Alcohol Consumption and Oral Microbiota on Upper Aerodigestive Tract Carcinomas: A Pilot Study. *Antioxidants*, *12*(6). https://doi.org/10.3390/antiox12061233
9. **Gariglio, S.**, David, M. C., Mattia, A., Consalvo, F., Scopetti, M., Padovano, M., D’Errico, S., Morena, D., Frati, P., Santurro, A., & Fineschi, V. (2024). Evaluation of Spontaneous Overtime Methemoglobin Formation in Post-Mortem Blood Samples from Real Cases in Critical Storage Conditions. *Toxics*, *12*(9), 670. https://doi.org/10.3390/toxics12090670

IN NON-PEER REVIEWED JOURNALS

10. Calvini, R., **Gariglio, S.**, Grassi, S., Malegori, C., Casale, M., & Marini, F. (2024). NIR2025: The 22nd International Conference on Near Infrared Spectroscopy is to be held in Rome, Italy. *NIR News*, *35*(5–6), 3–3. https://doi.org/10.1177/09603360241296655
11. Marini, F., Casale, M., Calvini, R., Malegori, C., **Gariglio, S.**, & Grassi, S. (2025). Highlights from the 22nd International Conference of Near Infrared Spectroscopy – NIR 2025. *NIR News, 0(0)*, 1-4. https://doi.org/10.1177/09603360251407449

RINGRAZIAMENTI

Chi mi conosce sa che questa è stata probabilmente la pagina più difficile da scrivere all'interno di questa tesi di dottorato; non già per una mancanza di gratitudine, quanto per la mia difficoltà intrinseca nell'esternare sentimenti. Eppure, questa è la chiusura di un capitolo cruciale della mia vita, e so che merita un momento di riflessione e di condivisione con le persone che lo hanno reso tale.

Se considero la mia carriera accademica e lavorativa in genere, il primo pensiero che mi viene in mente è quanto io sia stata fortunata. Per molti, il dottorato è un periodo tanto formativo quanto stressante, frustrante, e spesso solitario. Non per me. I tre anni di dottorato sono stati probabilmente i più belli della mia vita, e se è stato così lo devo in primo luogo alle mie tutor, Monica e Cristina.

Monica, grazie per la tua umanità e la tua comprensione, e per avermi ricordato, anche senza saperlo, che una carriera brillante non deve necessariamente annullare tutti gli altri aspetti di una persona. Grazie per essere sempre stata pronta a sostenermi, sia con le scadenze burocratiche (con cui so di essere un disastro) sia con l'attenta revisione di tutti i testi e le presentazioni che ho preparato in questi anni.

Cristina, non saprei scegliere una cosa specifica per cui ringraziarti. Hai creduto in me dal giorno zero (anzi, forse da prima), mi hai presa con i miei pregi e i miei difetti e mi hai aiutata a mettere in luce i primi e a smussare i secondi, senza mai chiedermi di essere una persona diversa da quella che sono. Mi hai spinta a mettermi alla prova e superarmi ogni giorno, e so che se oggi sono dove sono lo devo in buona parte a te, che sei stata sprone ed esempio negli ultimi tre anni della mia vita, e spero che lo sarai anche negli anni a venire.

Un grazie speciale va anche a Paolo, che, anche se non rientra formalmente tra i tutor, lo è stato di fatto. Grazie per i tuoi validissimi consigli su come muovermi nel mondo accademico e per il tuo incessante impegno nel valorizzare il mio lavoro di ricerca attraverso sfide sempre nuove.

Tra le figure accademiche, la mia gratitudine va anche a tutti i professori internazionali che hanno supervisionato il mio lavoro con professionalità e attenzione durante i miei periodi all'estero: il professor Grzegorz Zadora del Centro di Ricerca Forense di Cracovia, la professoressa Aoife Gowen dello University College Dublin, il professor Sergey Kucheryavskiy della Alborg University. In particolare, grazie a Sergey per la stima che mi ha dimostrato durante tutta la nostra collaborazione e per l'impegno che sta ancora mettendo nel supportarmi nella mia carriera accademica post-dottorato. Menzione speciale anche ad Alicja Menżyk: anche tu non risulti sulla carta come tutor, ma se ho amato così tanto il mio periodo in Polonia è stato soprattutto grazie a te. Ti sono grata per essere qui oggi e per essere diventata per me più di una collega (anche se ti rifiuti tassativamente di farti chiamare amica).

Grazie anche ai miei colleghi, con cui nel tempo ho sviluppato un rapporto di amicizia e che spero di non perdere dopo la fine di questo percorso. Grazie Riccardo: per la tua simpatia, la tua emotività, il tuo essere così diverso da me e allo stesso tempo esattamente la persona di cui avevo bisogno per condividere questo cammino. Non sarebbe stato lo stesso senza di te. Grazie a Giulia, collega per caso e amica per scelta, e a Michele: siete diventati un appoggio costante. Grazie anche a Elisa: sei arrivata quasi alla fine dell'avventura, ma ti sei dimostrata una persona interessante e di grande aiuto. Ti auguro tutto il bene all'inizio di questo percorso che io sto ora chiudendo. Grazie anche a Giorgia, con la sua umanità, vitalità e allegria a dispetto di tutto: sei un esempio di resilienza e forza rare. Grazie a tutti quelli che sono passati per il DIFAR e mi hanno lasciato un pezzetto di sé: Rodrigo, Larissa, Mateus, Yves.

Grazie a tutti gli altri professori, dottorandi, assegnisti e studenti del DIFAR che hanno in qualche modo contribuito al mio lavoro e alla mia crescita: Riccardo Leardi, Paolo Giordani, Raffaella Boggia, Federica Turrini, Emanuele Farinini, Federica Grasso, Valentina Orlandi, Giulia Ferrari, Rebecca Bassoli, e sicuramente avrò dimenticato qualcuno

Menzione d'onore poi per tutti i colleghi che ho conosciuto tramite i convegni, che mi hanno accolta e accompagnata in questo mondo magico. In particolare, grazie a Elena Cazzaniga, un'amica di cui non sapevo di avere bisogno.

Ed eccoci giunti alla famiglia. Mamma, papà: mi avete vista nascere, crescere e poi volare. Sono una figlia testarda e non sempre semplice; grazie per permettermi di essere chi sono e di scegliere con la mia testa, anche quando faccio l'esatto contrario di ciò che mi avevate consigliato. Grazie per avermi sempre sostenuta durante questi tre anni, per avermi ascoltato parlare di progetti di ricerca che magari non capivate, per tutti i bagagli trascinati, gli aerei a cui mi avete accompagnata e le domeniche in cui la mia presenza è stata solo una faccia in una videochiamata su WhatsApp. Grazie al nonno Gianni: nell'ultimo anno in particolare sei stato per me un esempio di forza e determinazione, il punto fisso e il volto sorridente ad accogliermi ogni volta che tornavo dai miei viaggi. Se c'è una cosa che ho capito nella vita, è che voglio arrivare alla tua età con la tua gioia e la tua meraviglia per il mondo. Grazie anche a nonna Puccia. Anche se non posso abbracciarti oggi, spero tu possa leggere le mie parole, dovunque tu sia. Sono sicura che anche le tue mani oggi mi applaudano insieme a quelle di tutti gli altri.

Grazie ad Arianna, cugina, sorella, twin, amica. Spesso ci separano chilometri e mondi, ma ti ho sempre sentita vicina. Grazie per i tuoi consigli, per essermi venuta a trovare un po' ovunque e per essere sempre qui per me. Grazie anche ad Aurora, la piccola non più piccola, con la sua dolcezza, e agli zii, i cugini e i parenti tutti, che si sono sempre interessati alle mie numerosissime avventure.

Grazie ai miei amici, colonna portante della mia persona. Grazie a Cassy, Eli, Anna e Malvina per le serate “donne” in videochiamata che mi hanno sempre fatta sentire coinvolta. Grazie a tutti i ragazzi dell’Uni per non esserci persi e per continuare a far parte della mia vita. Grazie a Gioppi: da quando ti ho ritrovata la mia vita è più luminosa. Grazie per esserci sempre e per trovare tempo per me anche quando passo in Piemonte solo due giorni in un mese.

Per finire, grazie a Kevin, Talos e Tiamat, la mia famigliola genovese. Grazie alle due piccole belve pelose per il supporto emotivo e per non permettere mai alla vita di diventare noiosa. Kevin, sei il compagno di vita migliore che si possa desiderare. Grazie per non lamentarti mai di tutti i miei viaggi, per essere sempre pronto a seguirmi. Tu forse non te ne rendi conto, ma il tuo supporto incondizionato è ciò che più mi aiuta ad affrontare con il sorriso la precarietà che mi aspetta in questa carriera che mi sono scelta. Grazie per le chiamate fino a tarda notte, per tutte le volte che mi hai aiutata con quelle cose burocratiche che tanto mi stressano, per l’impegno che metti ogni giorno nel coltivare la nostra relazione. Grazie per la tua profondità emotiva e l’aiuto che mi dai quando non riesco a capire e condividere le mie emozioni: se sono stata in grado di aprirmi così in questi ringraziamenti è anche grazie a ciò che ho imparato da te.

E in ultimo, anche se questo probabilmente infrangerà non so quante leggi non scritte dei ringraziamenti, grazie a me, per aver creduto in me stessa e per essermi rimboccata le maniche quando è stato necessario.

A un nuovo capitolo, pieno di soddisfazioni come lo è stato questo.

ACKNOWLEDGEMENTS

Those who know me are aware that this has probably been the most difficult page to write in this doctoral thesis; not because of a lack of gratitude, but rather because of my intrinsic difficulty in expressing emotions. And yet, this marks the closing of a crucial chapter of my life, and I know it deserves a moment of reflection and sharing with the people who made it what it was.

When I look back at my academic and professional career as a whole, the first thought that comes to mind is how fortunate I have been. For many, a PhD is a period that is as formative as it is stressful, frustrating, and often lonely. Not for me. The three years of my PhD have probably been the best of my life, and if that is the case, I owe it first and foremost to my supervisors, Monica and Cristina.

Monica, thank you for your humanity and understanding, and for reminding me, often without even realising it, that a brilliant career does not necessarily have to erase all other aspects of a person’s life. Thank you for always being ready to support me, both with bureaucratic deadlines (which I know I am terrible at) and with the careful revision of all the texts and presentations I prepared over these years.

Cristina, I would not know how to choose one specific thing to thank you for. You believed in me from day zero (or perhaps even before), you accepted me with my strengths and my flaws, and you helped me highlight the former and smooth out the latter, without ever asking me to be someone different from who I am. You pushed me to challenge myself and to grow every single day, and I know that if I am where I am today, I owe a large part of it to you. You have been both a driving force and a role model over the past three years of my life, and I hope you will continue to be so in the years to come.

A special thank you also goes to Paolo, who, even if not formally listed as a supervisor, truly was one in practice. Thank you for your invaluable advice on how to navigate the academic world and for your constant effort to enhance my research work by offering ever new challenges.

Among the academic figures, I would also like to express my gratitude to all the international professors who supervised my work with professionalism and care during my periods abroad: Professor Grzegorz Zadora from the Forensic Research Centre in Kraków, Professor Aoife Gowen from University College Dublin, and Professor Sergey Kucheryavskiy from Aalborg University. In particular, thank you to Sergey for the esteem you have shown me throughout our collaboration and for the commitment you are still demonstrating in supporting me in my post-PhD academic career. A special mention also goes to Alicja

Menżyk: even if, on paper, you are not listed as a supervisor, the fact that I loved my time in Poland so much is largely thanks to you. I am grateful to have you here today, and for having become more than just a colleague to me (even if you firmly refuse to be called a friend).

Thanks also go to my colleagues, with whom over time I have built relationships of friendship that I hope will continue beyond the end of this journey. Thank you, Riccardo, for your humour, your emotional openness, and for being so different from me while at the same time being exactly the person I needed to share this path with. It would not have been the same without you. Thank you to Giulia, colleague by chance and friend by choice, and to Michele: you have become a constant source of support. Thank you also to Elisa: you joined almost at the very end of the adventure, but you proved to be an interesting person and a great help. I wish you all the best at the beginning of the journey that I am now bringing to a close. Thank you as well to Giorgia, with her humanity, vitality, and cheerfulness in spite of everything: you are a rare example of resilience and strength. Thanks to everyone who passed through DIFAR and left me a small part of themselves: Rodrigo, Larissa, Mateus, Yves.

Thanks also to all the other professors, PhD students, postdoctoral researchers, and students at DIFAR who, in one way or another, contributed to my work and to my growth: Riccardo Leardi, Paolo Giordani, Raffaella Boggia, Federica Turrini, Emanuele Farinini, Federica Grasso, Valentina Orlandi, Giulia Ferrari, Rebecca Bassoli, and I am sure I have forgotten someone.

An honourable mention then goes to all the colleagues I met through conferences, who welcomed me and accompanied me in this fascinating world. In particular, thank you to Elena Cazzaniga, a friend I did not know I needed.

And here we are, at family. Mum, Dad: you have seen me be born, grow up, and then take flight. I am a stubborn daughter and not always an easy one; thank you for allowing me to be who I am and to make my own choices, even when I do exactly the opposite of what you advised. Thank you for always supporting me over these three years, for listening to me talk about research projects you might not have fully understood, for all the suitcases you carried, the flights you took me to, and the Sundays when my presence was reduced to a face on a WhatsApp video call. Thank you to Nonno Gianni: over the past year in particular, you have been an example of strength and determination for me, a fixed point and a smiling face welcoming me every time I returned from my travels. If there is one thing I have learned in life, it is that I want to reach your age with your joy and your sense of wonder for the world. Thank you also to Nonna Puccia. Even though I cannot hug you today, I hope you can read my words, wherever you may be. I am sure that today your hands are applauding together with everyone else's.

Thank you to Arianna: cousin, sister, twin, friend. Kilometres and worlds often separate us, but I have always felt you close. Thank you for your advice, for coming to visit me wherever I was, and for always being there for me. Thank you also to Aurora, the little one who is no longer so little, with her sweetness, and to all my aunts, uncles, cousins, and relatives, who have always taken an interest in my countless adventures.

Thank you to my friends, the backbone of who I am. Thank you to Cassy, Eli, Anna, and Malvina for the "girls' nights" on video calls that always made me feel included. Thank you to all my university friends for not losing touch and for continuing to be part of my life. Thank you, Gioppi: since finding you again, my life has been brighter. Thank you for always being there, and for making time for me even when I only pass through Piedmont for two days in a month.

Finally, thank you to Kevin, Talos, and Tiamat, my little Genoese family. Thank you to the two small furry beasts for the emotional support and for never letting life become boring. Kevin, you are the best life partner one could wish for. Thank you for never complaining about all my travels, and for always being ready to follow me. You may not realise it, but your unconditional support is what most helps me face with a smile the uncertainty that awaits me in the career I have chosen. Thank you for the late-night calls, for all the times you helped me with the bureaucratic matters that stress me so much, and for the effort you put every day into nurturing our relationship. Thank you for your emotional depth and for the help you always give me when I struggle to understand and share my emotions: if I have been able to open up like this in these acknowledgements, it is also thanks to what I have learned from you.

And lastly, even if this probably breaks more than a few unwritten rules of acknowledgements, thank you to myself, for believing in myself and for rolling up my sleeves when it was necessary.

To a new chapter, hopefully as full of fulfilment as this one has been.